

QUANTUM LIQUIDS AND QUANTUM CRYSTALS

On the theory of dynamic properties of semiquantum helium

V. V. Ignatyuk, I. M. Mryglod, and M. V. Tokarchuk

*Institute for Physics of Condensed Systems, National Academy of Sciences of the Ukraine, 290011 Lviv, Ukraine**

(Submitted December 8, 1998)

Fiz. Nizk. Temp. **25**, 407–416 (May 1999)

A general theoretical approach is developed for describing the dynamic properties of semiquantum fluids on the basis of the nonequilibrium statistical operator technique. A set of equations of generalized hydrodynamics is derived and the particular case of thermo-viscoelastic model of a fluid is analyzed in details in the hydrodynamic limit. The case of intermediate and large values of the wave vector is also discussed. The Markov approximation for transport kernels is used to obtain a closed set of equations for dynamic correlation functions. The problem is considered in the context of relation with the experimental data on neutron scattering and the theoretical results known previously in the literature. © 1999 American Institute of Physics. [S1063-777X(99)00105-X]

1. INTRODUCTION

Liquid ^4He is a classical example of a quantum liquid which has drawn the attention of experimental and theoretical scientists for a long time.^{1–3} Being an object obeying Bose–Einstein statistics, liquid ^4He requires, like many other Bose- and Fermi-systems, the application of the quantum-mechanical apparatus for describing its thermodynamic and nonequilibrium (dynamic) properties.^{3,4}

It is well known that any quantum system can be characterized by specifying certain effective parameters that are important for understanding its properties. One of such characteristic parameters is the quantum degeneracy temperature $T_d = \hbar/\tau$ which depends on the number density n of particles and the effective mass m^* of a particle: $T_d \propto n^{2/3}/m^*$. The quantity τ can be treated as the quantum delocalization time of the particle. Another characteristic temperature describing the role of phonon processes in a quantum system is the Debye temperature $T_D = \hbar\Omega_D$.³ It can be estimated through the relation $T_D \propto cn^{1/3}$, where c is the adiabatic velocity of sound.

Quantum systems usually obey the inequality $T_d \leq T_D$. Depending on the value of the equilibrium temperature T , all quantum fluid (whose melting point is much lower than T_D) can be divided into two main classes:

- (a) fluids for which $T < T_D$, and hence the quantum effects play a dominating role in them;
- (b) liquids (and gases) for which $T_d < T \leq T_D$.

According to Frenkel's model,⁵ a significant point in the description of kinetic processes in liquids belonging to class (a) is that the vibrational frequency ω of the atoms around their equilibrium position is much higher than the reciprocal τ^{-1} of "hopping" of the particle between two adjacent states. Thus, we can use the phenomenological model for a system of particles having a fairly high vibrational frequency and located at the bottom of the potential well, which pass

over to the nearest equilibrium state after a time τ . In Frenkel's description, transitions of particles of a liquid in an asymmetric potential well play the role of elementary excitations. Such phonon-type excitations have been defined quite adequately under the condition $\omega\tau \gg 1$, and must contribute to the thermodynamics as well as dynamics of the system. Since long-range order does not exist in a liquid and the local equilibrium positions are distributed unevenly, such liquids must possess a number of properties characteristic of low-temperature glasses, the only difference being that all barriers are penetrable in the case of a quantum system. Such a phenomenological description enabled Andreev to introduce in scientific terminology the concept of "semiquantum" fluids and to determine a number of thermodynamic⁶ and kinetic⁷ properties of such systems. In particular, he obtained a linear temperature dependence of specific heat in the interval characteristic for fluids belonging to class (b), which differs from the phonon behavior $c_v(T) \propto T^3$ which is characteristic for quantum objects of class (a) (e.g., for a degenerate nonideal Bose gas⁸). As regards the dynamic properties of semiquantum liquids, the following dependences were obtained⁷ in the frequency range $\hbar\omega \ll T$ for viscosity η and thermal conductivity λ : $\eta \propto T^{-1}$, and $\lambda \propto T$. The absorption of ultrasound in semiquantum liquids was also studied in Ref. 9. The frequency dependence of the absorption coefficient was estimated under the assumption of a weak dependence of the density of states on the excitation energy.

Naturally, it can be asked whether such weakly disperse excitations can be detected in experiments on scattering, and in which range of wave vectors k can they be expected. In this context, we can mention that Crevecoeur *et al.*^{10,11} carried out their investigations for two thermodynamic states of ^4He , viz., $T = 4$ K, $p = 1$ bar and $T = 8$ K, $p = 18.7$ bar, the object of investigation being the symmetrized dynamic structural factor $S_{\text{sym}}(k, \omega)$. The results of these investigations

will be described in detail in subsequent sections. For the present, we merely remark that these authors used the concept of generalized modes to construct a semi-phenomenological model for describing the experimental data using the formalism of two (damped harmonic oscillator model) or three variables (hydrodynamic model). In these models, the unknown parameters for $S_{\text{sym}}(k, \omega)$ played the role of fitting parameters. These models do not explain fully the essence of dynamic processes occurring in a system, hence we can accept the statement of Griffin¹² that the spectrum of strongly damped phonons may quite turn out to be an artifact of a certain fitting.

In another important publication from the point of view of the dynamics of semiquantum systems, Montfrooij *et al.*¹³ have presented the experimental data for gaseous helium at $T=13.3$ K, $p=203$ bar in the interval $3 \text{ nm}^{-1} \leq k \leq 11 \text{ nm}^{-1}$, as well as results of calculations obtained in the five-variable formalism (thermoviscous model). The generalized dynamic matrix was determined for intermediate values of the wave vector as well as in the hydrodynamic limit $k \rightarrow 0$ where the corresponding nondissipative elements tend to their thermodynamic values while the transport coefficients can be treated as experimental values. It was also shown that unlike classical liquids, the dynamic structural factor in this case has a clearly traceable side resonance in the region of intermediate wave vectors. However, the conclusion drawn by the authors¹³ about the purely thermal origin of propagator excitation which is transformed into ordinary sound in the limit $k \rightarrow 0$ seems to be quite strange.

The present paper aims at studying the nature of collective excitations in semiquantum ⁴He proceeding from microscopic premises. For this purpose, we use the concept of generalized collective modes, which was found to be quite effective for studying dense classical liquids.^{14–16} Analyzing the spectrum of a simple Lennard–Jones liquid,¹⁷ it can be assumed that weakly disperse excitations observed experimentally in semiquantum helium are actually kinetic propagator modes emerging as a result of interaction between viscous and thermal processes. These modes are strongly damped in classical liquids, but can be observed in a number of cases in simple liquids^{15,16} as well as binary mixtures^{18–20} in which they generate interesting phenomena named “fast sound.”

The material of this paper is divided into the following sections. Dynamic correlation functions and their interrelation with experimentally observed quantities are defined in Sec. 2. Equations for dynamic correlation functions as well as expressions for generalized thermodynamic quantities and transport kernels are presented in Sec. 3 in terms of the corresponding microscopic densities and fluxes. Section 4 is devoted to an analysis of the spectrum of collective excitations in the hydrodynamic limit. Certain problems emerging while studying the intermediate region of wave vectors and short-wave limit are also considered. The obtained results are discussed in Conclusion.

2. CORRELATION FUNCTIONS AND EXPERIMENTALLY OBSERVED QUANTITIES

The object of our investigation are time correlation functions (TCF) $\Phi_{AB}(k, t)$ which can be defined as follows:

$$\begin{aligned} \Phi_{AB}(k, t) &= (\hat{A}(\mathbf{k}, t), \hat{B}(-\mathbf{k}))_0 \\ &= \int_0^1 d\tau \text{Sp}[\Delta \hat{A}(\mathbf{k}, t) \rho_0^\tau \Delta \hat{B}(-\mathbf{k}) \rho_0^{1-\tau}], \\ \Delta \hat{A}(\mathbf{k}, t) &= \hat{A}(\mathbf{k}, t) - \text{Sp}[\rho_0 \hat{A}(0, 0)], \end{aligned} \quad (1)$$

where ρ_0 is the equilibrium statistical operator, while the time dependence is introduced in terms of Heisenberg representation.

The functions $\Phi_{AB}(k, t)$ emerge naturally in the method of nonequilibrium statistical operator²¹ and are directly connected with Green’s correlation functions. The Fourier transform $\Phi_{nn}(k, \omega)$ of the function $\Phi_{nn}(k, t)$ formed by using the operators \hat{n}_k of the number density of particles, i.e.,

$$\Phi_{AB}(k, \omega) = \frac{1}{2\pi} \int_{-\infty}^{\infty} dt \exp(i\omega t) \Phi_{AB}(k, t), \quad A, B = n, \quad (2)$$

can be connected with the experimentally observed dynamic structural factor

$$S(k, \omega) = \frac{1}{2\pi} \int_{-\infty}^{\infty} dt \exp(i\omega t) \text{Sp}[\rho_0 \hat{n}_k(t) \hat{n}_{-k}] \quad (3)$$

through the relation

$$\Phi_{nn}(k, \omega) \equiv S_{\text{sym}}(k, \omega) = \frac{1 - \exp(-\beta \hbar \omega)}{\beta \hbar \omega} S(k, \omega), \quad (4)$$

where $S_{\text{sym}}(k, \omega)$ is the symmetrized dynamic structural factor^{10,11} and $\beta = 1/k_B T$, where k_B is the Boltzmann constant. Note that the identity (4) follows directly from the definition (1) of TCF. In the following analysis, we shall deal only with symmetric TCF defined by formulas (1) and (2).

Let us write the relation between symmetrized static structural factor $S_{\text{sym}}(k)$ and $S_{\text{sym}}(k, \omega)$:

$$S_{\text{sym}}(k) = \int_{-\infty}^{\infty} d\omega S_{\text{sym}}(k, \omega). \quad (5)$$

It can be shown easily that in the limit $k \rightarrow 0$, the familiar relation $S_{\text{sym}}(k \rightarrow 0) = k_B T \kappa_T$ (where κ_T is the isothermal compressibility of the system) from the theory of classical liquids holds just for $S_{\text{sym}}(k)$.

3. EQUATIONS FOR TIME CORRELATION FUNCTIONS

In order to describe thermodynamic and dynamic properties of semiquantum ⁴He, we define a set of basic dynamic variables including the hydrodynamic number density \hat{n}_k of particles, longitudinal component \mathbf{J}_k of momentum, and the generalized enthalpy \hat{h}_k :

$$\hat{n}_k = \frac{1}{\sqrt{N}} \sum_{\mathbf{p}} \hat{a}_{\mathbf{p}-\mathbf{k}/2}^+ \hat{a}_{\mathbf{p}+\mathbf{k}/2}, \quad (6)$$

$$\hat{\mathbf{J}}_{\mathbf{k}} = \frac{1}{\sqrt{N}} \sum_{\mathbf{p}} \frac{\mathbf{k}\mathbf{k} \cdot \mathbf{p}}{\mathbf{k}^2} a_{\mathbf{p}-\mathbf{k}/2}^+ \hat{a}_{\mathbf{p}+\mathbf{k}/2}, \quad (7)$$

$$\hat{h}_{\mathbf{k}} = \hat{\varepsilon}_{\mathbf{k}} - (\hat{\varepsilon}_{\mathbf{k}}, \hat{n}_{-\mathbf{k}})_0 (\hat{n}_{\mathbf{k}}, \hat{n}_{-\mathbf{k}})_0^{-1} \hat{n}_{\mathbf{k}}, \quad (8)$$

where

$$\begin{aligned} \hat{\varepsilon}_{\mathbf{k}} = & \frac{1}{\sqrt{N}} \sum_{\mathbf{p}} \left(\frac{\mathbf{p}^2}{2m} - \frac{\mathbf{k}^2}{8m} \right) \hat{a}_{\mathbf{p}-\mathbf{k}/2}^+ \hat{a}_{\mathbf{p}+\mathbf{k}/2} \\ & + \frac{1}{2V} \sum_{\mathbf{p}} \sum_{\mathbf{q}} \nu(\mathbf{q}) a_{\mathbf{p}+(\mathbf{q}-\mathbf{k})/2}^+ \hat{n}_{\mathbf{q}} \hat{a}_{\mathbf{p}-(\mathbf{q}-\mathbf{k})/2} \end{aligned}$$

is the energy density, as well as ‘‘kinetic’’ variables defined by the expressions

$$\hat{\pi}_{\mathbf{k}} = (1 - \mathcal{P}_0) \hat{J}_{\mathbf{k}}, \quad (9)$$

$$\hat{Q}_{\mathbf{k}} = (1 - \mathcal{P}_0) \hat{h}_{\mathbf{k}}. \quad (10)$$

As usual, $\hat{a}_{\mathbf{p}}^+$ and $\hat{a}_{\mathbf{p}}$ in Eqs. (6)–(10) are the creation and annihilation operators for quasiparticles with momentum \mathbf{p} , which satisfy the transposition relations $[\hat{a}_{\mathbf{p}}^+, \hat{a}_{\mathbf{q}}] = \delta_{\mathbf{p}\mathbf{q}}$, $[\hat{a}_{\mathbf{p}}, \hat{a}_{\mathbf{q}}] = [\hat{a}_{\mathbf{p}}^+, \hat{a}_{\mathbf{q}}^+] = 0$; $\nu(\mathbf{q}) = \int \exp(i\mathbf{q}\mathbf{r}) \Phi(|\mathbf{r}|) \times d\mathbf{r}$ is the Fourier transform of the potential $\Phi(|\mathbf{r}|)$ of interaction between particles, V is the volume of the system, and N the number of particles. The quantities $(\hat{\varepsilon}_{\mathbf{k}}, \hat{n}_{-\mathbf{k}})_0$, $(\hat{n}_{\mathbf{k}}, \hat{n}_{-\mathbf{k}})_0$ in formula (8) are equilibrium (static) quantum correlation functions (SCF) defined as follows:

$$\begin{aligned} \Phi_{AB}(k) = (\hat{A}(\mathbf{k}), \hat{B}(-\mathbf{k}))_0 = & \text{Sp} \left(\Delta \hat{A}(\mathbf{k}) \int_0^1 d\tau \rho_0^\tau \Delta \hat{B} \right. \\ & \left. \times (-\mathbf{k}) \rho_0^{1-\tau} \right). \quad (11) \end{aligned}$$

The operators $\hat{\pi}_{\mathbf{k}}$ and $\hat{Q}_{\mathbf{k}}$ are connected with the microscopic stress tensor and the enthalpy flux projected onto the space of hydrodynamic variables $\hat{B}(\mathbf{k}) = \{\hat{n}_{\mathbf{k}}, \hat{J}_{\mathbf{k}}, \hat{h}_{\mathbf{k}}\}$. In this respect, $\hat{\pi}_{\mathbf{k}}$ and $\hat{Q}_{\mathbf{k}}$, being fast variables, are defined as kinetic variables. In Eqs. (9) and (10), \mathcal{P}_0 is Mori’s projection operator constructed on hydrodynamic variables, and its action is defined as

$$\mathcal{P}_0 \hat{A} = \sum_{l=1}^3 \sum_{\mathbf{k}} (\hat{A}, \hat{B}_l(-\mathbf{k}))_0 (\hat{B}_l(\mathbf{k}), \hat{B}_l(-\mathbf{k}))_0^{-1} \hat{B}_l(\mathbf{k}). \quad (12)$$

The Liouville operator $i\hat{L}$ is defined in the standard manner:

$$\hat{A} \equiv i\hat{L}\hat{A} = \frac{i}{\hbar} [\hat{A}, \hat{H}], \quad (13)$$

where

$$\hat{H} = \sum_{\mathbf{p}} \frac{\mathbf{p}^2}{2m} \hat{a}_{\mathbf{p}}^+ \hat{a}_{\mathbf{p}} + \frac{1}{2V} \sum_{\mathbf{k}} \sum_{\mathbf{p}} \nu(\mathbf{k}) \hat{a}_{\mathbf{p}+\mathbf{k}/2}^+ \hat{n}_{\mathbf{k}} \hat{a}_{\mathbf{p}-\mathbf{k}/2}. \quad (14)$$

The nonequilibrium statistical operator technique²¹ can be used to obtain²² a system of equations for Laplace trans-

forms of TCF $\tilde{\Phi}_{AB}(k, z) = \int_0^\infty \exp(-zt) \Phi_{AB}(k, t) dt (z = i\omega + \varepsilon, \varepsilon = +0)$, which can be presented in matrix form as follows:

$$z\Phi(k, z) - i\Omega(k)\Phi(k, z) + \bar{\varphi}(k, z)\Phi(k, z) = \Phi(k), \quad (15)$$

where the notation

$$\begin{aligned} i\Omega_{ij}(k) = & (i\hat{L}\hat{Y}_i(\mathbf{k}), \hat{Y}_j(-\mathbf{k}))_0 (\hat{Y}_j(\mathbf{k}), \hat{Y}_j(-\mathbf{k}))_0^{-1}, \\ \hat{Y}_i(\mathbf{k}) = & \{\hat{n}_{\mathbf{k}}, \hat{J}_{\mathbf{k}}, \hat{h}_{\mathbf{k}}, \hat{\pi}_{\mathbf{k}}, \hat{Q}_{\mathbf{k}}\} \end{aligned} \quad (16)$$

has been used for elements of the frequency matrix $i\Omega(k)$ and

$$\begin{aligned} \bar{\varphi}_{ij}(k, z) = & \left((1 - \mathcal{P}) \hat{Y}_i(\mathbf{k}), \frac{1}{z - (1 - \mathcal{P})i\hat{L}} (1 - \mathcal{P}) \hat{Y}_j(-\mathbf{k}) \right) \\ & \times (\hat{Y}_j(\mathbf{k}), \hat{Y}_j(-\mathbf{k}))_0^{-1} \end{aligned} \quad (17)$$

for elements of the matrix of memory functions $\bar{\varphi}(k, z)$. The projection operator \mathcal{P} acts in the same manner as (12), but is defined on the complete set of base variables $\{\hat{Y}_i(\mathbf{k})\}$, $i = 1, \dots, 5$. It can be shown easily that the only nonzero elements of the matrix of memory functions are $\bar{\varphi}_{\pi\pi}(k, z)$, $\bar{\varphi}_{\pi Q}(k, z)$, $\bar{\varphi}_{Q\pi}(k, z)$, and $\bar{\varphi}_{QQ}(k, z)$, which are constructed on kinetic variables (9) and (10). The system of equations (15) (or a similar system of transport equations) can be solved in kinetic variables and the initial problem can be reduced to the three-variable formalism after substitution of the obtained results into the first equations. The generalized transport coefficients, which depend on the modulus of wave vector and frequency, will be expressed in terms of higher-order memory functions constructed on kinetic transport coefficients.²³ In turn, the elements of the frequency matrix for longitudinal fluctuations can be written in terms of generalized thermodynamic functions

$$\begin{aligned} i\Omega_{Jn}(k) = \frac{ik}{n\kappa_T(k)}, \quad i\Omega_{nJ}(k) = \frac{ik}{m}, \\ i\Omega_{Jh}(k) = \frac{ik}{nc_V(k)} \frac{\alpha(k)}{\kappa_T(k)}, \quad i\Omega_{hJ}(k) = \frac{ik}{mn\beta} \frac{\alpha(k)}{\kappa_T(k)}, \end{aligned} \quad (18)$$

where the following notation has been used: $c_V(k) = 1/k_B T^2 \times (\hat{h}_{\mathbf{k}}, \hat{h}_{-\mathbf{k}})_0$ for the generalized specific heat at constant volume, $\alpha(k)$ for the generalized thermal expansion coefficient, and $\kappa_T(k)$ for the generalized compressibility.

The following remarks can be made regarding the connection between our results and those obtained by Crevecoeur:¹¹

- (1) the explicit form of the hydrodynamic matrix in Ref. 11 follows directly from Eq. (15) in the Markov approximation;
- (2) nondiagonal elements of the matrix of memory functions $\bar{\varphi}_{\pi Q}(k, z)$ and $\bar{\varphi}_{Q\pi}(k, z)$, which were disregarded by Crevecoeur,¹¹ are quite important in the intermediate regions of k and ω . This is confirmed by computations made for a Lennard–Jones liquid;^{14,15}
- (3) transition from a five-variable description to three- or two-variable description was carried out not quite correctly in Ref. 11. As a matter of fact, the disregard of

“superfluous” variables results in the emergence of space and time dispersion of transport coefficients, which is quite important for describing the dynamics of a system for finite k and ω .^{16,17}

4. SPECTRUM OF COLLECTIVE EXCITATIONS

In order to close the chain of equations (15) for DCF, we use the Markov approximation for the memory function (17):

$$\tilde{T}(k) = \begin{bmatrix} 0 & -i\Omega_{nJ} & 0 & 0 & 0 \\ -i\Omega_{Jn} & 0 & -i\Omega_{Jh} & -i\Omega_{J\pi} & 0 \\ 0 & -i\Omega_{hJ} & 0 & 0 & -i\Omega_{hQ} \\ 0 & -i\Omega_{\pi J} & 0 & \tilde{\varphi}_{\pi\pi} & -i\Omega_{\pi Q} + \tilde{\varphi}_{\pi Q} \\ 0 & 0 & -i\Omega_{Qh} & -i\Omega_{Q\pi} + \tilde{\varphi}_{Q\pi} & \tilde{\varphi}_{QQ} \end{bmatrix}. \tag{21}$$

In the Markov approximation, the solution of the system of equations for DCF can be written in an analytic form in terms of the eigenvalues z_α and eigenvectors $X_\alpha = ||X_{i\alpha}||$ of the matrix $\tilde{T}(k)$,^{15,22} i.e.,

$$\tilde{\varphi}_{il}(k, z) = \sum_{\alpha=1}^5 \frac{G_\alpha^{il}(k)}{z + z_\alpha(k)}, \tag{22}$$

where the amplitudes $G_\alpha^{il}(k)$ can be presented in the form

$$G_\alpha^{il}(k) = X_{i\alpha}(k)[X(k)^{-1}]_{l\alpha}\Phi_{ll}(k, 0), \tag{23}$$

X^{-1} is the matrix inverse to $X = ||X_{i\alpha}||$. In the time representation, we obtain

$$\Phi_{ij}(k, t) = \sum_{\alpha=1}^5 G_\alpha^{ij}(k) \exp\{-z_\alpha(k)t\}, \tag{24}$$

and hence DCF are a sum of weighted exponents, each term corresponding to some collective mode.

We shall now analyze the spectrum of collective excitations for different values of the wave vector.

4.1. Hydrodynamic region

In the limit $k \rightarrow 0$, we have the following collective excitation modes:

the *thermal mode* defined by

$$z_h(k) = D_T \mathbf{k}^2 + o(\mathbf{k}^4); \tag{25}$$

two complex conjugate *acoustic modes*

$$z_\pm(k) = \pm i c k + \Gamma \mathbf{k}^2 + o(k^3); \tag{26}$$

and two *kinetic modes* that do not vanish at $k = 0$:

$$z_\pi(k) = \varphi_{\pi\pi}(0, 0) + o(k^2), \tag{27}$$

$$z_Q(k) = \varphi_{QQ}(0, 0) + o(k^2). \tag{28}$$

The following notation has been used in formulas (25)–(28): D_T is the thermal diffusion defined as coefficient defined as

$$\tilde{\varphi}_{ij}(k, z) \approx \tilde{\varphi}_{ij}(k, 0) = \int_0^\infty \varphi_{ij}(k, t) dt. \tag{19}$$

The system of equations (15) can then be presented in the form

$$z\tilde{\Phi}(k, z) + \tilde{T}(k)\tilde{\Phi}(k, z) = \Phi(k), \tag{20}$$

where the generalized hydrodynamic matrix $\tilde{T}(k)$ has the following structure:

$$D_T = \frac{1}{mk_B T^2 c_p(0)} \frac{\tilde{\Phi}_{QQ}(0, 0)}{\tilde{\varphi}_{QQ}(0, 0)} = \frac{\lambda(0, 0)}{nm c_p(0)}; \tag{29}$$

$c_p(0)$ is the specific heat at constant pressure (the zero in parentheses indicates the thermodynamic limit $c_p(k \rightarrow 0)$), $\lambda(0, 0)$ is the generalized thermal conductivity for $k = 0$, $z = 0$, $c = \gamma/mnT\kappa_T$ is the adiabatic velocity of sound, where $\gamma = c_p(0)/c_v(0)$,

$$\Gamma = \frac{1}{2}(\gamma - 1)D_T + \frac{1}{2}\eta^\parallel \tag{30}$$

is the sound attenuation coefficient, where

$$\eta^\parallel = \frac{\tilde{\Phi}_{\pi\pi}(0, 0)}{mn\tilde{\varphi}(0, 0)} = \left(\frac{4}{3} \eta(0, 0) + \zeta(0, 0) \right) / nm, \tag{31}$$

$\eta(0, 0)$ and $\zeta(0, 0)$ being the shear and bulk viscosity respectively.

An analysis of Eqs. (25)–(28) readily shows that nondiagonal elements of the matrix of memory functions are not manifested in the limit $k \rightarrow 0$ (it can be shown that they are proportional to k). However, as mentioned above, they may be quite significant in an analysis of the experimental data even for small values of k . For example, having presented the expression for the dynamic structural factor at zero frequency in an explicit form, we can see that the term $(-i\Omega_{Q\pi} + \tilde{\varphi}_{Q\pi})$ appears in $S_{\text{sym}}(k, 0)$ in the same order in k ($\sim k^0$) as the quantity $\tilde{\varphi}_{\pi\pi}$. On the other hand, thermal processes (associated with a consideration of $\tilde{\varphi}_{QQ}$) dominate in the limit of small values of the wave vector and make a contribution $\sim 1/k^2$ to the function $S_{\text{sym}}(k, 0)$. Going over to an analysis of the experimental data, we note that a correct

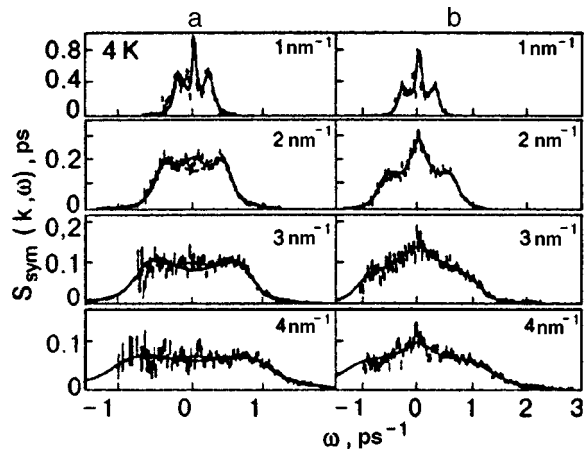


FIG. 1. Symmetrized dynamic structural factor $S_{\text{sym}}(k, \omega)$ for ${}^4\text{He}$ at $T=4$ K (a) and $T=8$ K (b) for $k=1, 2, 3, 4$ nm^{-1} . The vertical lines correspond to the experimental results, the solid curve shows the results of fitting for three-variable formalism, while the dashed line corresponds to two-variable formalism (borrowed from Ref. 11).

description of the behavior of the dynamic structural factor for small values of k and ω is possible only if we take into consideration all nonzero elements of the matrix of the memory functions $\tilde{T}(k)$.

The experimental data for $S_{\text{sym}}(k, \omega)$ obtained by Crevecoeur¹¹ for $k=1-4$ nm^{-1} are shown in Fig. 1. It can be seen that a purely hydrodynamic behavior typical of classical fluids is observed for small values of k ($k < 2$ nm^{-1}): $S_{\text{sym}}(k, \omega)$ consists of the Rayleigh–Brillouin triplet whose central line characterizes the entropy fluctuations, while the side peaks are associated with the processes of sound propagation. The central line vanishes for $k > 3$ nm^{-1} . It is interesting to note that at $T=8$ K, the thermal peak vanishes at higher values of the wave vector. Helium remains nondegenerate at both temperatures, and no Bose-condensate is formed. It should be remarked, however, that on the dynamic level, the system begins to feel the “approaching” phase transition even at these temperatures, which is indeed observed in the behavior of the central peak. The cluster sizes corresponding to the emerging asymmetry are naturally larger at $T=4$ K. Hence a transition at this temperature from the Rayleigh–Brillouin triplet to a more complex form of the dynamic structural factor occurs for lower values of k .

On the other hand, an increase in k leads to a change in the form of the dynamic structural factor due to the effect of kinetic modes also. In particular, it is well known that starting from a certain value k^* , the kinetic processes in a Lennard–Jones liquid lead to the emergence of a new propagator excitation with a weak dispersion for large values of k .¹⁷ Depending on the form of the interaction potential and the thermodynamic point, these excitations may be manifested in the dynamic structural factor in the form of new side peaks. Such an effect is known in literature as “fast” sound.¹⁵ A similar picture was also observed in binary mixtures.²⁰ The value of k^* corresponding to a transition from two relaxation kinetic modes (27) and (28) to a pair of kinetic propagator modes is often defined as the limit of applicability of hydrodynamic description.

In order to verify the assumption concerning the effect of kinetic propagator excitations on the behavior of the dynamic structural factor in semiquantum helium, we carried out computations whose results are presented in Fig. 2. We proceed from expressions (20) and (21) in the limit of small but finite values of k . The figure shows the contributions of thermal, acoustic, and kinetic modes to $S_{\text{sym}}(k, \omega)$ which can be defined using formulas (22) and (23). For the initial data for the matrix $\tilde{T}(k)$, we chose thermodynamic parameters associated with the elements of the frequency matrix (18) in the limit of small k , as well as transport coefficients borrowed from Ref. (11). The three unknown quantities $\tilde{\varphi}_{\pi\pi}$, $\tilde{\varphi}_{QQ}$ and $-i\Omega_{\pi Q} + \tilde{\varphi}_{\pi Q}$ were determined by a self-consistent solution of the system of equations for three experimental points at $k=1$ nm^{-1} , viz., the values of $S_{\text{sym}}(k, \omega)$ for $\omega=0$ as well as the points of maximum and minimum values of $S_{\text{sym}}(k, \omega)$ for ω . Further, the results for the next two values of the wave vector $k=2, 3$ nm^{-1} were also obtained by assuming the quasi-hydrodynamic nature of $S_{\text{sym}}(k, \omega)$.

Figure 3 shows the dispersion of propagator excitations at $T=4$ and 8 K. In order to analyze the origin of collective excitations and their contribution to the dynamic structural factor, let us consider in greater detail Figs. 2 and 3.

First, it follows from Fig. 3 that the behavior of kinetic propagator excitation of gaseous ${}^4\text{He}$ at $T=8$ K has a closer resemblance to that of classical liquids.¹⁵ Although the kinetic propagator excitation appears at this temperature for lower values of k , its dispersion curve lies below the acoustic curve. At $T=4$ K, a typical “fast sound” behavior is observed even at $k \sim 2.7$ nm^{-1} , i.e., the kinetic propagator mode intersects the dispersion curve of acoustic excitation and remains much higher upon a further increase in the value of k . On the other hand, it can also be seen from Fig. (2) that the amplitude of this mode falls rapidly at $T=4$ K for $k=3$ nm^{-1} . The situation becomes entirely opposite at $T=8$ K, when the contribution of the kinetic mode becomes dominant for $k=3$ nm^{-1} in the interval of small ω .

Second, it should be interesting to observe the characteristic behavior of the thermal mode whose amplitude at $T=4$ K decreases sharply with increasing k and which makes a small contribution, even for $k=2$ nm^{-1} , to the dynamic structural factor whose shape is determined mainly by the acoustic excitation. It is the actual vanishing of the thermal mode that is responsible for the emergence of a “plateau” on the dynamic structural factor at $T=4$ K, serving as a precursor of the emerging violation of symmetry of the Bose system. At $T=8$ K, the contribution of the thermal excitation can be traced for all values of wave vectors, and the behavior of $S_{\text{sym}}(k, \omega)$ is more classical.

Note that the procedure for determining the parameters $\tilde{\varphi}_{\pi\pi}$, $\tilde{\varphi}_{QQ}$ and $-i\Omega_{\pi Q} + \tilde{\varphi}_{\pi Q}$ is quite sensitive to variation in the values of the dynamic structural factor at reference points. However, our computations are in good agreement with the experimental data within the accuracy of the experiment (see Fig. 1).

4.2. Intermediate values of k

In order to study the dynamic structural factor in the intermediate region, we must know the dependence of all

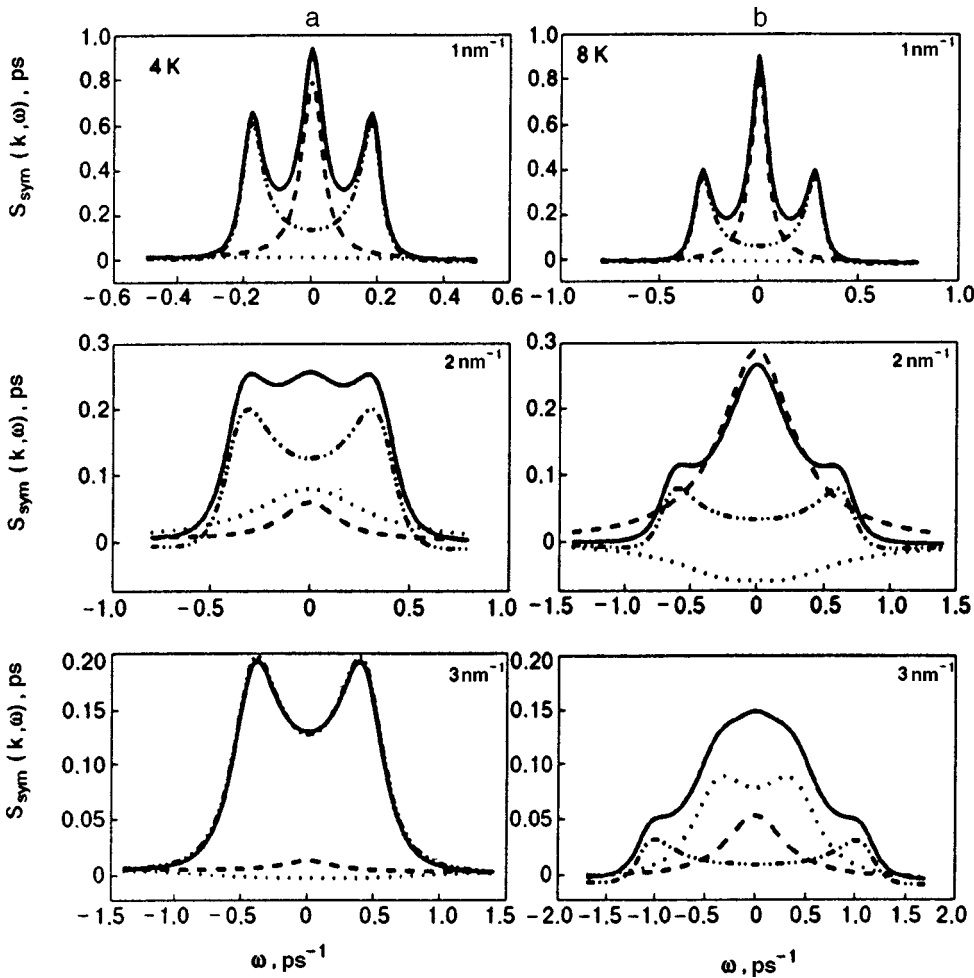


FIG. 2. Symmetrized dynamic structural factor $S_{sym}(k, \omega)$ for ${}^4\text{He}$ at $T=4\text{ K}$ (a) and $T=8\text{ K}$ (b) for $k=1, 2, 3\text{ nm}^{-1}$ for five-variable formalism (solid curve). The dashed, dot-and-dash, and dotted curves show the contributions from the thermal mode, acoustic mode, and kinetic modes respectively to $S_{sym}(k, \omega)$.

matrix elements (21) on k . While carrying out specific calculations, these data can be obtained either from computer experiments¹⁵⁻¹⁷ or by approximation based on some phenomenological approach.^{13,24}

Figure 4 shows the results of neutron scattering experiments obtained for intermediate values of the wave vector.¹¹ The following characteristic features are worth noting:

- (1) the central line vanishes at both temperatures upon an increase in k . The side peaks are associated with the strongly damped propagator mode and form two broad lines which merge practically for $k > 10\text{ nm}^{-1}$;

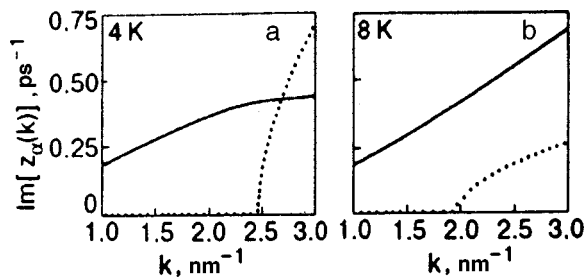


FIG. 3. Dispersion of propagator excitations of ${}^4\text{He}$ at $T=4\text{ K}$ (a) and $T=8\text{ K}$ (b). The solid and dotted curves correspond to the acoustic and kinetic modes respectively.

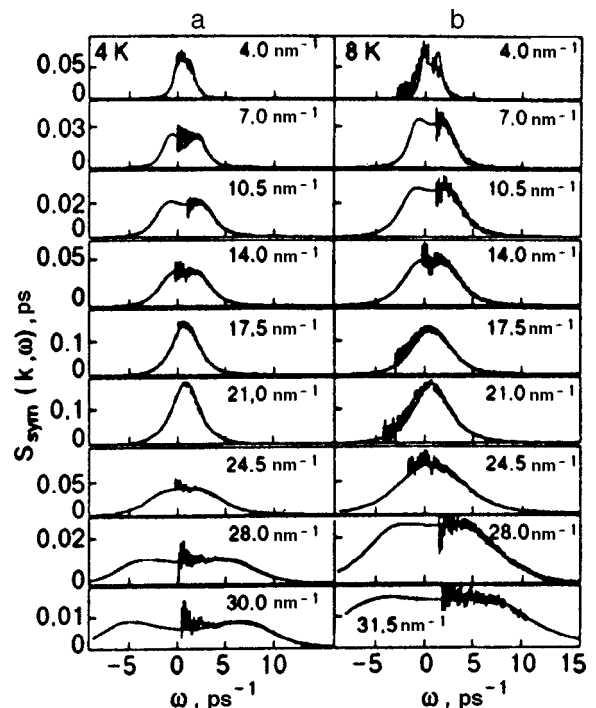


FIG. 4. The same as in Fig. 1 for $k \geq 4\text{ nm}^{-1}$.

- (2) in the region of the static structural factor maximum $k=20\text{ nm}^{-1}$, de Gennes narrowing characteristic of classical liquids is observed;
- (3) upon a further increase in k , the secondary peaks are formed once again, their localization depending weakly on k . Thus, we observe new weakly disperse propagator excitations which, unlike classical liquids, are clearly separated.

A somewhat different picture was observed in experiments on scattering at $T=13.3\text{ K}$.¹³ The behavior of the dynamic structural factor in this case is more like in the case of a classical liquid. The behavior of side peaks in the region $k=3-10\text{ nm}^{-1}$ is especially interesting. Two pairs of complex conjugate propagator excitations are encountered in this range, one of them being associated the generalized sound, and the other being the kinetic propagator mode. Montfrooij *et al.*¹³ tried to identify both types of excitations with specific physical processes. In particular, an analysis of the contributions from various excitations in the “density–density,” “momentum–momentum” and “energy–energy” TCF led the authors to the conclusion that the propagator mode with a higher frequency can be identified with thermal processes. Although such an interpretation is quite interesting in itself, the transformation of a thermal wave into an acoustic wave in the hydrodynamic limit seems to be quite strange.

4.3. Shortwave limit

For large values of k and ω , scattering experiments provide information about the movement of atoms over small distances and time intervals.²⁵ In this case, the wavelength of an impinging neutron is small in comparison with the atomic spacing, and hence the neutron can effectively interact with just one atom, the scattering becomes incoherent, and one-particle effects are observed. The incoherence limit in liquid helium is attained at $k\geq 15\text{ \AA}^{-1}$, although the effect of the atomic surroundings also becomes significant for quite large values of k . Andersen *et al.*²⁶ have derived expressions for the nonsymmetrized dynamic structural factor on the basis of cumulative expansion in (3). The authors took into account both the environment effect (through moments of the interparticle interaction potential) and the deviation from Maxwell distribution of particles in the momentum space. The emergence of nonzero odd moments of purely quantum origin shifts the $S(k, \omega)$ resonance by the free recoil frequency $\omega_r = \hbar \mathbf{k}^2/2m$ of a ^4He particle. Note that the results of short-wave scattering are normally used for determining the distribution function $n(\mathbf{p})$ in the momentum space.²⁶

The dynamics of semiquantum ^4He can also be studied in a different manner by using formulas (20) and (21). In the limit $k\rightarrow\infty$, the matrix elements $\tilde{T}(k)$ attain their asymptotic values for which we can obtain the necessary analytic expressions. The analysis for simple liquids shows^{14,15} that in the shortwave limit, all modes acquire a linear dependence: $z_\alpha \propto k$. Moreover, it was shown²⁷ that within the concept of generalized collective modes, there exists a one- to-one correspondence between the set of dynamic variables used in the analysis, and the first frequency moments. In particular, in the thermoviscous model considered in our work, the first

five frequency moments for the dynamic structural factor are reproduced correctly. Naturally, the odd moments are equal to zero in the case of the symmetrized dynamic structural factor.

CONCLUSION

In this work, we have studied the spectrum of collective excitations of semiquantum ^4He . The thermoviscous model is used to obtain the results for the dispersion of propagator excitations as well as the expressions for $S_{\text{sym}}(k, \omega)$, and to analyze the contributions from all collective modes. Calculations show that the quasihydrodynamic description is still applicable for values $\sim 2-3\text{ nm}^{-1}$ of the wave vector, although the contribution of kinetic excitations becomes quite significant. The behavior of the contribution from the thermal mode clearly indicates that the system begins to “feel” the impending phase transition to the superfluid state even in the high-temperature phase.

As the value of k increases, we must have a knowledge about the spatial dispersion of the matrix elements $\tilde{T}(k)$ over the entire range of values of k . In the analysis of classical liquids, the authors of Refs. 15–17, 20 used the results of computer experiment for this purpose. Such an analysis becomes more complicated in the quantum case, since computer techniques have not been worked out so well for calculating higher-order TCF. The importance of investigations in the region of intermediate and high values of k is associated with the fact that this is the only way in which reliable information can be obtained about the role of kinetic propagator excitations and the dominant physical processes singled out.

Note that as a rule, one-particle and many-particle resonances can be separated in superfluid helium. This was observed clearly in experiments,^{1,25} the coupling between hydrodynamic and one-particle variables $\hat{a}_{\mathbf{k}}$ and $\hat{a}_{\mathbf{k}}^+$ due to the presence of Bose condensate occurring at the level of SCF.^{1,8,25} In the case of semiquantum ^4He , however, such a coupling can also be obtained on dissipative levels only by decoupling memory functions in the framework of the mode coupling theory.²⁸ This leads to a set of equations for TCF of hydrodynamic levels together with equations for the one-particle nonequilibrium function ($\hat{a}_{\mathbf{k}}^+; \hat{a}_{\mathbf{k}}$).

We plan to continue the analysis of the above problems in our subsequent publications.

One of the authors (VVI) is grateful to the President of Ukraine for financial support. The research of another author (IMM) was financed by the Fonds für Forderung der Wissenschaftlichen Forschung, Project P12423 TPH.

*E-mail: ignat@icmp.lviv.ua

¹ A. Griffin, D. E. Snoke, and S. Stringari, *Bose–Einstein Condensation*, Cambridge University Press, New York (1993).

² E. M. Lifshitz and L. P. Pitaevskii, *Statistical Physics*, Part II [in Russian], Nauka, Moscow (1978).

³ J. Wilks, *An Introduction to Liquid Helium*, Clarendon Press, Oxford (1970).

⁴ D. Vollhardt and P. Wölfle, *The Superfluid Phases of Helium 3*, Taylor and Francis, London (1990).

- ⁵ Ya. I. Frenkel' *Kinetic Theory of Liquids* [in Russian], Academy of Sciences, Moscow (1945).
- ⁶ A. F. Andreev, Pis'ma Zh. Éksp. Teor. Fiz. **28**, 603 (1978) [JETP Lett. **28**, 556 (1978)].
- ⁷ A. F. Andreev and Yu. A. Kosevich, Zh. Éksp. Teor. Fiz. **77**, 2518 (1979) [Sov. Phys. JETP **50**, 1218 (1979)].
- ⁸ Yu. A. Tserkovnikov, Teor. Mat. Fiz. **93**, 412 (1992).
- ⁹ L. L. Buishvili and A. I. Tugushi, Zh. Éksp. Teor. Fiz. **84**, 970 (1983) [Sov. Phys. JETP **57**, 563 (1983)].
- ¹⁰ R. M. Crevecoeur, R. Verberg, I. M. de Schepper *et al.*, Phys. Rev. Lett. **74**, 5052 (1995).
- ¹¹ R. M. Crevecoeur, *Analogies in the Microscopic Behavior of Superfluid and Classical Helium Studied by Neutron Scattering*, Ph.D. Thesis, Delft (1996).
- ¹² A. Griffin, Phys. Rev. Lett. **76**, 1759 (1996).
- ¹³ W. Montfrooij, L. A. de Graaf, and I. M. de Schepper, Phys. Rev. B **45**, 3111 (1992).
- ¹⁴ I. P. Omelyan and I. M. Mryglod, Condens. Matter Phys. **4**, 128 (1994).
- ¹⁵ I. M. Mryglod, I. P. Omelyan, and M. V. Tokarchuk, Mol. Phys. **84**, 235 (1995).
- ¹⁶ I. M. Mryglod and I. P. Omelyan, Mol. Phys. **90**, 91 (1997); *ibid.* **92**, 913 (1997).
- ¹⁷ I. M. Mryglod and I. P. Omelyan, Phys. Lett. A **205**, 401 (1995).
- ¹⁸ J. Bosse, G. Jacucci, M. Ronchetti, and W. Schirmacher, Phys. Rev. Lett. **57**, 3277 (1986).
- ¹⁹ P. Westerhuijs, W. Montfrooij, L. A. de Graaf, and I. M. de Schepper, Phys. Rev. A **45**, 3749 (1992).
- ²⁰ T. M. Bryk, I. M. Mryglod, and G. Kahl, Phys. Rev. E **56**, 2903 (1997).
- ²¹ D. Zubarev, V. Morozov, and G. Röpke, *Statistical Mechanics of Non-equilibrium Processes*, Akademie Verlag, Berlin (1996).
- ²² V. V. Ignatyuk, I. M. Mryglod, and M. V. Tokarchuk, Preprint ICMP-98-08E, Lviv (1998).
- ²³ I. M. Mryglod and A. M. Hachkevych, Condens. Matter Phys. **5**, 105 (1995).
- ²⁴ P. Goldstein and L. S. Garcia-Colin, J. Chem. Phys. **99**, 3913 (1993).
- ²⁵ H. R. Glyde, *Excitations in Liquid and Solid Helium*, Clarendon Press, Oxford (1994).
- ²⁶ K. H. Andersen, W. G. Stirling, and H. R. Glyde, Phys. Rev. B **56**, 8978 (1997).
- ²⁷ I. M. Mryglod, Ukr. Fiz. Zh. **43**, 252 (1998).
- ²⁸ V. G. Morozov, Physica A **110**, 201 (1982); *ibid.* **117**, 511 (1983).

Translated by R. S. Wadhwa

On phase transitions in a Fermi liquid. II. Transition associated with translational symmetry breaking

A. S. Peletminsky

Scientific Research Center of Electrophysical Treatment, National Academy of Sciences of the Ukraine, 310002 Kharkov, Ukraine

S. V. Peletminsky, and Yu. V. Slyusarenko

*National Science Center "Kharkov Institute of Physics and Technology," 310108 Kharkov, Ukraine**

(Submitted December 24, 1998)

Fiz. Nizk. Temp. **25**, 417–431 (May 1999)

The phase transition in a Fermi liquid, associated with translational symmetry breaking and the formation of periodic structures is considered. Special attention is paid to the formation of one-dimensional long-periodic structures in a three-dimensional Fermi liquid. The relation between the formation of such structures and kinetic and thermodynamic stability of the normal state of the Fermi liquid is analyzed. © 1999 American Institute of Physics. [S1063-777X(99)00205-4]

1. INTRODUCTION

The term “normal Fermi liquid” is traditionally applied to a degenerate (charged or neutral) Fermi liquid possessing main properties of a system of noninteracting fermions in the case of a quasiparticle description. Such a definition of a normal Fermi liquid presumes that the equilibrium state of the Fermi liquid is the most symmetric, i.e., the distribution function describing this state is invariant to spatial translations and rotations in the spin and momentum spaces.

In spite of natural differences in the behavior of charged and neutral Fermi liquids, basic concepts of the Landau–Silin theory of the normal Fermi liquid^{1,2} studying low-lying excitations against the background of the equilibrium state make it possible to disregard the electric charge of quasiparticles in the description of some phenomena in charged and neutral systems of interacting fermions. Apart from the main condition of applicability of the theory of the normal Fermi liquid, i.e., the smallness of temperature T as compared to the Fermi energy $\varepsilon_F (T \ll \varepsilon_F)$, the main postulate of the theory which is common for neutral and charged systems concerns the functional dependence of the energy of the system on the fermion distribution function $f(\mathbf{p}, \mathbf{r})$.¹⁾ This energy can be expanded into a functional Taylor series in the distribution function:

$$E(f(\mathbf{p}, \mathbf{r})) = \sum_{n=1}^{\infty} E_n((\mathbf{p}, \mathbf{r})),$$

where the quantity

$$E_n(f(\mathbf{p}, \mathbf{r})) = \frac{(2S+1)^{n-1}}{n! V^n} \sum_{\mathbf{p}_1, \dots, \mathbf{p}_n} \int d^3 r_1 \dots d^3 r_n \times F(\mathbf{p}_1, \dots, \mathbf{p}_n; \mathbf{r}_1 - \mathbf{r}_2, \dots, \mathbf{r}_1 - \mathbf{r}_n) \times f(\mathbf{p}_1, \mathbf{r}_1) \dots f(\mathbf{p}_n, \mathbf{r}_n)$$

can be treated as an n -quasiparticle interaction. In this case, the quasiparticle energy which is a functional of the distribution function is defined as

$$\varepsilon(\mathbf{p}, \mathbf{r}) = V \frac{\delta E(f)}{\delta f(\mathbf{p}, \mathbf{r})}.$$

Neglecting interactions between three and more quasiparticles, we have

$$\varepsilon(\mathbf{r}, \mathbf{p}) = \varepsilon_p + \frac{2}{V} \sum_{\mathbf{p}'} \int d\mathbf{r}' F(\mathbf{r} - \mathbf{r}'; \mathbf{p}, \mathbf{p}') f(\mathbf{r}', \mathbf{p}'),$$

$$S = 1/2, \tag{1}$$

where $F(\mathbf{r} - \mathbf{r}', \mathbf{p}, \mathbf{p}')$ is the Landau amplitude characterizing two-particle interactions, and $\varepsilon_p \equiv F(\mathbf{p})$ is the fermion energy in the absence of interaction between quasiparticles. In the absence of magnetic ordering, the existence of the fermion spin $S = 1/2$ is important only for the calculation of the fermion density of states, which is reflected in the factor $2S + 1 = 2$ in the second term of formula (1) The equilibrium state of the normal Fermi liquid is described by the Fermi–Dirac distribution function

$$f(\mathbf{p}, \mathbf{r}) \equiv f_0(p) = [\exp \beta(\varepsilon(p) - \mu) + 1]^{-1} \tag{2}$$

($\beta^{-1} = T$ is the reciprocal temperature and μ the chemical potential). Together with Eq. (1), this equation determines the dispersion relation $\varepsilon(\mathbf{p}, \mathbf{r}) \equiv \varepsilon(p)$ for quasiparticles in the equilibrium state.

Strictly speaking, in the construction of thermodynamics of a normal Fermi liquid, the Landau amplitude is defined as the second variational derivative of the energy functional with respect to the distribution function in equilibrium at $T = 0$. However, second variational derivatives are insufficient for an analysis of the new phase structure, and higher-order variational derivatives must be introduced. The disregard of such derivatives in our analysis is equivalent to the neglect of the interaction between quasiparticles of an order higher than the second.

An important aspect of the theory is the determination of the stability conditions for an equilibrium state of a normal Fermi liquid. This problem was solved for the first time in the spatially homogeneous case by Pomeranchuk³ who formulated the stability criterion for the normal state down to the temperature $T=0$:

$$1 + \frac{\nu(\mu)F_l}{2l+1} > 0, \quad (3)$$

where F_l are the coefficients of the l th harmonic in the expansion of the spatially homogeneous Landau amplitude

$$F(\mathbf{p}, \mathbf{p}') = \int d\mathbf{r}' F(\mathbf{r} - \mathbf{r}'; \mathbf{p}, \mathbf{p}') \quad (4)$$

into a series in Legendre polynomials near the Fermi surface ($p \approx p' \approx p_F$). The quantity $\nu(\varepsilon)$ appearing in formula (3) is the density of energy states defined as

$$\nu(\varepsilon) = \frac{2}{(2\pi)^3} \int d^3p \delta(\varepsilon - \varepsilon(p)). \quad (5)$$

Another important circumstance is worth noting. Pomeranchuk's criteria (3) were obtained at zero temperature. For this reason, it cannot be generally stated that the equilibrium state of the normal Fermi liquid (2) is obviously unstable at any temperature when conditions (3) are violated, i.e., when $\nu(\mu)F_l \leq -(2l+1)$. On the contrary, we can prove (which will be done later) that the state of statistical equilibrium of a normal Fermi liquid in the case when Pomeranchuk's criteria are violated is stable down to a certain temperature T_0 and becomes unstable at lower temperatures $T < T_0$ (naturally, we presume that the main condition $T \ll \mu$ for the applicability of the theory of a normal Fermi liquid is fulfilled). Such an instability of the ground state indicates the possibility of phase transitions in the Fermi liquid, which are associated with the violation of Pomeranchuk's stability criteria.

This research is devoted to an analysis of such a phase transition, i.e., the transition involving the violation of the stability condition (3) for the zeroth harmonic ($l=0$), for which the following relation holds:

$$\nu(\mu)F_0 \leq -1. \quad (6)$$

We shall prove that condition (6) characterizes a phase transition in a Fermi liquid, associated with translational symmetry breaking for the equilibrium state. It will be clear from the subsequent analysis that the solution of this problem requires a modification of basic concepts of the theory of a normal Fermi liquid considered here.

However, before going over to a description of a spatially periodic structures formed as a result of a phase transition in a Fermi liquid associated with violation of condition (6), we shall consider in greater detail some aspects of the behavior of the Fermi liquid in the case when the temperature of the system approaches the critical value on the side of the normal phase, i.e., $T \geq T_0$.

2. ON KINETIC AND THERMODYNAMIC THEORY OF STABILITY OF THE NORMAL STATE

First of all, we shall illustrate the connection between the violation of stability of the equilibrium state of a normal Fermi liquid and the attenuation of zeroth sound. Zeroth sound in a normal Fermi liquid is the term applied to the high-frequency collective longitudinal mode associated with density fluctuations of the substance.^{1,2} Zero sound can exist in the frequency range $\omega \tau_r \gg 1$ (τ_r is the relaxation time). For this reason, we can analyze the dispersion of zeroth sound by using the kinetic equation for the nonequilibrium distribution function $f(\mathbf{r}, \mathbf{p}, t)$ in the collisionless approximation:

$$\frac{\partial}{\partial t} f(\mathbf{r}, \mathbf{p}, t) + \frac{\partial \varepsilon(\mathbf{r}, \mathbf{p}, f)}{\partial \mathbf{p}} \frac{\partial f(\mathbf{r}, \mathbf{p}, t)}{\partial \mathbf{r}} - \frac{\partial \varepsilon(\mathbf{r}, \mathbf{p}, f)}{\partial \mathbf{r}} \frac{\partial f(\mathbf{r}, \mathbf{p}, t)}{\partial \mathbf{p}} = 0. \quad (7)$$

In order to simplify calculations, we assume here that the Landau amplitude is independent of momenta, i.e.,

$$F(\mathbf{r} - \mathbf{r}'; \mathbf{p}, \mathbf{p}') \equiv F(\mathbf{r} - \mathbf{r}'), \quad (8)$$

and hence the dispersion relation (1) for quasiparticles assumes the form

$$\varepsilon(\mathbf{r}, \mathbf{p}, f) = \varepsilon_p + \frac{2}{V} \int d\mathbf{r}' F(\mathbf{r} - \mathbf{r}') \sum_{\mathbf{p}'} f(\mathbf{r}', \mathbf{p}', t). \quad (9)$$

The inclusion the dependence of the Landau amplitude on momenta in (8) and (9) would not lead to fundamental difficulties, but would make calculations more cumbersome without changing significantly the final results.

Linearizing the kinetic equation (7) taking into account (9) near the equilibrium state (2) and going over in the linearized equation to Fourier transforms in time and coordinates in accordance with formulas

$$\delta f(\mathbf{r}, \mathbf{p}, t) = \frac{1}{(2\pi)^3} \int d\mathbf{k} \int_{-\infty}^{\infty} d\omega \exp(i\mathbf{k}\mathbf{r} - i\omega t) \delta f(\mathbf{k}, \mathbf{p}, \omega),$$

$$F(\mathbf{r}) = \frac{1}{(2\pi)^3} \int d\mathbf{k} \exp(i\mathbf{k}\mathbf{r}) F(\mathbf{k}) \quad (10)$$

we obtain

$$\delta f(\mathbf{k}, \mathbf{p}, \omega) (-\omega + \mathbf{k}\mathbf{v}) - F_0 \mathbf{k} \frac{\partial f_0(\mathbf{p})}{\partial \mathbf{p}} \frac{2}{V} \sum_{\mathbf{p}'} \delta f(\mathbf{k}, \mathbf{p}', \omega) = 0, \quad (11)$$

where the following notation has been introduced:

$$\mathbf{v} \equiv \frac{\partial \varepsilon(p)}{\partial \mathbf{p}}, \quad F_0 \equiv F(\mathbf{k}=0) = \int d\mathbf{r} F(\mathbf{r}). \quad (12)$$

According to (1), the quantity $\varepsilon(p)$ appearing in the definition of \mathbf{v} in formula (12) satisfies the relation

$$\varepsilon(p) = \varepsilon_p + F_0 \frac{2}{V} \sum_{\mathbf{p}'} f_0(p'), \quad (13)$$

which is the self-consistency equation for a normal Fermi liquid in the spatially homogeneous case. The presence of

the quantity F_0 and not $F(\mathbf{k})$ in formula (11) (see formulas (9) and (10)) reflects the fact that zeroth sound represents long-wave oscillations with small wave vectors \mathbf{k} . It should also be noted that if we include the momentum dependence of the Landau amplitude (see (4)), the quantity F_0 corresponds to the zeroth harmonic in the expansion of the Landau amplitude in the Legendre polynomials near the Fermi surface in the spatially homogeneous case, i.e., coincides with the quantity appearing in relation (6).

The solution of Eq. (11) can be presented in the form (see, for example, Ref. 4 in this connection)

$$\begin{aligned} \delta f(\mathbf{k}, \mathbf{p}, \omega) = & \delta A(\mathbf{p}, \mathbf{k}) \delta(\omega - \mathbf{k}\mathbf{v}) - F_0 \Xi^{-1}(\mathbf{k}, \omega) \\ & \times \frac{\partial f_0(\varepsilon)}{\partial \varepsilon} \frac{\mathbf{k}\mathbf{v}}{\omega - \mathbf{k}\mathbf{v} + i\eta} \frac{2}{V} \sum_{\mathbf{p}'} \\ & \times \delta A(\mathbf{p}', \mathbf{k}) \delta(\omega - \mathbf{k}\mathbf{v}'), \end{aligned} \quad (14)$$

where $\delta A(\mathbf{p}, \mathbf{k})$ is an arbitrary function which is restricted only by the conditions that the value of the quantity $\delta f(\mathbf{r}, \mathbf{p}, t)$ calculated according to (10) and (14) must be smaller than the equilibrium distribution function (2). The quantity $\Xi(\mathbf{k}, \omega)$ appearing in (14) and defined as

$$\Xi(\mathbf{k}, \omega) = 1 + F_0 \frac{2}{V} \sum_{\mathbf{p}} \frac{\partial f_0(\varepsilon)}{\partial \varepsilon} \frac{\mathbf{k}\mathbf{v}}{\omega - \mathbf{k}\mathbf{v} + i\eta}, \quad (15)$$

is the permittivity of the system in the case of a charged Fermi liquid (see, for example, Ref. 5). The dispersion relation for zeroth sound obtained from the equation $\Xi(\mathbf{k}, \omega_0) = 0$ has the form

$$\omega_0 = skv_F, \quad (16)$$

where k is the magnitude of the wave vector and v_F the value of the velocity $\mathbf{v}(\varepsilon) = \mathbf{v}(\varepsilon(p))$ (see (12)) at the Fermi surface (we assume that the Fermi surface is isotropic), and the quantity s can be found from the equation

$$1 - \frac{1}{2} F_0 \int_0^\infty d\varepsilon v(\varepsilon) \frac{\partial f(\varepsilon)}{\partial \varepsilon} \int_0^\pi \frac{d(\cos \theta) [v(\varepsilon)/v_F] \cos \theta}{s - [v(\varepsilon)/v_F] \cos \theta + i\eta} = 0. \quad (17)$$

After the evaluation of integrals with respect to momentum, the parameter η in formulas (14), (15), and (17) taking into account attenuation of oscillations with the dispersion relation (16) must tend to zero from the side of positive values taking into account the formula

$$\frac{1}{z+i0} = P \frac{1}{z} - i\pi \delta(z)$$

(P is the symbol of the principal value of integral).

In the range of positive values of the Landau amplitude ($F_0 > 0$), Eq. (17) for determining the parameter s has the well-known form

$$1 + \nu(\mu)F_0 = \nu(\mu)F_0 \frac{s}{2} \ln \frac{s+1}{s-1}, \quad (18)$$

and the decrement of collisionless attenuation of zeroth sound becomes noticeable (nevertheless remaining smaller than the frequency ω_0) only for small $F_0 > 0$, $F_0 \nu(\mu) \ll 1$.⁴

In the range of negative values of the Landau amplitude satisfying the relation

$$-1 < \nu(\mu)F_0 < 0,$$

zeroth sound attenuates strongly, and the parameter s becomes complex-valued with the real and imaginary components of the same order of magnitude. In this range of values of the quantity F_0 , Eq. (18) should be used with care (see Ref. 6 in this connection). It can be stated, however, that the magnitude of the coefficient s determining the dispersion of zeroth sound becomes small for $F_0 \nu(\mu) \approx -1$ and vanishes for $F_0 \nu(\mu) = -1$, i.e., at the point where Pomeranchuk's criterion is violated. It should be noted that in view of the smallness of the parameter s for $\nu(\mu)F_0 \approx -1$, we must generally take into account in Eq. (18) thermal corrections that can be of the same order of magnitude as the quantity $\nu(\mu)F_0 + 1$. But it can be easily seen that the inclusion of these corrections for $\nu(\mu)F_0 \geq -1$ does not lead to a qualitatively new result since the system is stable down to zero temperature under these conditions. However, the inclusion of thermal corrections in Eq. (18) in the case when Pomeranchuk's criterion is violated and relation (6) is valid leads to the vanishing of the parameter s for a certain nonzero temperature. Such a vanishing of some thermodynamic and kinetic parameters at a certain (critical) temperature is a typical effect in the theory of phase transitions (see, for example, Ref. 7).

In this connection, let us analyze in greater detail the behavior of the dispersion relation for zeroth sound in the case when Pomeranchuk's criterion is violated, i.e., the Landau amplitude F_0 satisfies relation (6). The latter circumstance suggests the smallness of the parameter s in Eq. (17). Expanding the second term in Eq. (17) in small s taking into account thermal corrections determined by the temperature dependence of the equilibrium distribution function, we arrive in the main approximation to the following equation for determining the parameter s :

$$1 + \nu(\mu)F_0 + \frac{\pi^2}{6} \nu''(\mu)F_0 T^2 = -i \frac{\pi}{2} s \nu(\mu)F_0. \quad (19)$$

It can be seen from this equation that the parameter s vanishes at a temperature T_0 defined as

$$T_0^2 = -\frac{6}{\pi^2} \frac{1 + \nu(\mu)F_0}{F_0 \nu''(\mu)},$$

or, considering that $\nu(\mu)F_0 \approx -1$,

$$T_0^2 = \frac{6}{\pi^2} \frac{\nu(\mu)}{\nu''(\mu)} [1 + \nu(\mu)F_0], \quad (20)$$

where the quantity $\nu(\mu)$ is defined by formula (5) as before. The positive value of the right-hand side of (20) is ensured by the fulfillment of condition (6) and the fact that $\nu''(\mu) < 0$. In the vicinity of the temperature T_0 , the quantity s obtained from (19) taking into account formula (20) has the form

$$s = i \frac{2\pi}{3} \frac{\nu''(\mu)}{\nu(\mu)} T_0 (T - T_0), \quad (21)$$

i.e., the parameter s determining the dispersion relation for zeroth sound in accordance with (16) is purely imaginary in the given approximation. Formula (21) taking into account (16) and (10) readily shows that zeroth sound at $T > T_0$ becomes a purely attenuating mode ($\text{Im } s < 0$). In other words, the state of the system remains stable even when the Pomeranchuk's criterion is violated at $T > T_0$, but naturally under the main condition $T \ll \mu$ of the applicability of the theory of the normal Fermi liquid.

At $T < T_0$, the imaginary component of s becomes positive, which corresponds to "building-up" of zeroth sound, i.e., the state of the system becomes unstable. It was noted above, however, that such an instability can indicate a transition of the system to a new stable state, i.e., a phase transition with the critical temperature T_0 defined by formula (20).

Let us now consider the region of existence of solutions of the self-consistent equation corresponding to the normal state of a Fermi liquid in the plane of parameters T, μ . We assume that the rotational symmetry is not broken in the momentum space, i.e., the quasiparticle energy $\varepsilon(p)$ and the distribution function $f_0(p)$ in Eq. (13) are independent of the direction of the momentum \mathbf{p} . The case associated with rotational symmetry breaking in the momentum space is analyzed in detail in Ref. 8.

Taking into account what has been said above and introducing the quantity $\varepsilon = \varepsilon(p) - \varepsilon_p$, we can write Eq. (13) in the form

$$\varepsilon = \frac{2F_0}{V} \sum_{\mathbf{p}'} \{ \exp \beta(\varepsilon + \varepsilon_{\mathbf{p}'} - \mu) + 1 \}^{-1}$$

or

$$n(\beta, \mu_0) = \frac{\mu - \mu_0}{F_0}, \tag{22}$$

where

$$n(\beta, \mu_0) = \frac{2}{V} \sum_{\mathbf{p}'} \{ \exp \beta(\varepsilon_{\mathbf{p}'} - \mu_0) + 1 \}^{-1},$$

$$\mu_0 = \mu - \varepsilon. \tag{23}$$

For testing the self-consistent equation (22) for the existence of solutions corresponding to the normal state of the Fermi liquid, we consider the following two cases: $F_0 > 0$ and $F_0 < 0$. Noting that $(\partial n(\beta, \mu_0))/\partial \mu_0 > 0$ and $n(\beta, -\infty) = 0$, in accordance with (13), we find that the self-consistent equation (22) for positive F_0 always has a solution in the plane of the parameters T and μ corresponding to the normal state of the system (see Fig. 1). In the case of negative F_0 , the region of existence of the normal state [normal solutions of Eq. (22)] is determined by the inequality (see Fig. 2)

$$-\frac{1}{F_0} > \frac{\partial n(\beta, \mu_0)}{\partial \mu_0}. \tag{24}$$

Carrying out the low-temperature expansion for the function $n(\beta, \mu_0)$ for $\beta^{-1} = T \ll \mu$, i.e.,

$$n(\beta, \mu_0) = n(0, \mu_0) + \frac{\pi^2}{6} T^2 \nu'_0(\mu_0) + \dots, \tag{25}$$

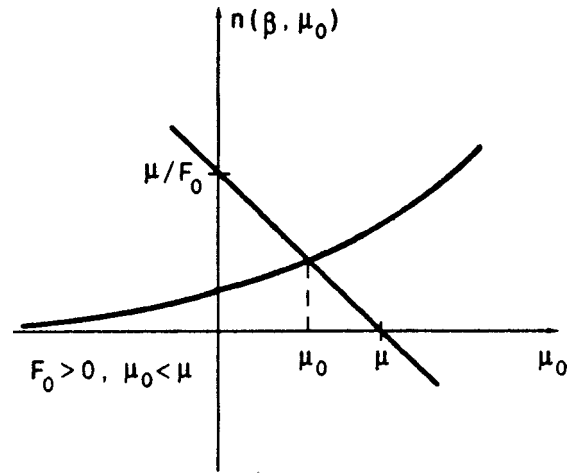


FIG. 1. Definition of the region of existence of normal solutions of Eq. (22) for $F_0 > 0$.

where $\nu_0(\mu_0)$ is the density of states of a Fermi gas with the dispersion relation ε_p and the chemical potential μ_0 and noting that

$$\frac{\partial n(\infty, \mu_0)}{\partial \mu_0} = \nu_0(\mu_0),$$

$$\frac{\partial n(\beta, \mu_0)}{\partial \mu_0} = \nu_0(\mu_0) + \frac{\pi^2}{6} T^2 \nu''_0(\mu_0), \tag{26}$$

we can write condition (24) for the existence of normal solutions of the self-consistent equation (22) for $F_0 < 0$ in the form

$$\frac{1}{F_0} + \nu_0(\mu_0) < -\frac{\pi^2}{6} \nu''_0(\mu_0)(\mu_0) T^2. \tag{27}$$

(It should be emphasized that the density of states $\nu_0(\mu_0) = \nu_0(\mu - \varepsilon) \equiv \nu(\mu)$ coincides with the density of states $\nu(\mu)$ corresponding to the true dispersion relation $\varepsilon(p) = \varepsilon_p + \varepsilon$;

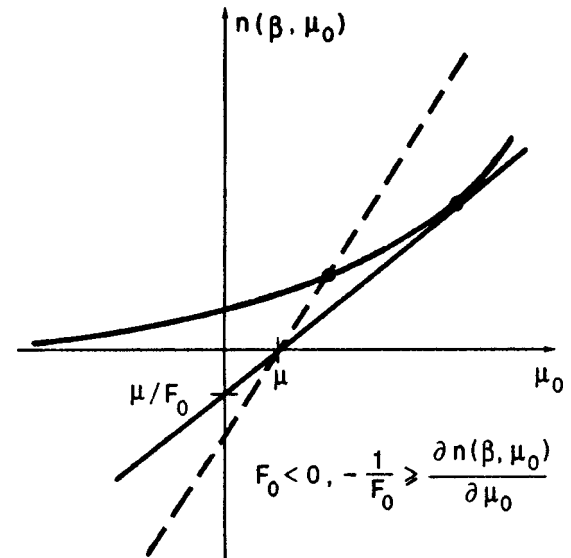


FIG. 2. Definition of the region of existence of normal solutions of Eq. (22) for $F_0 < 0$.

see formula (5).) If $1/F_0 + \nu(\mu) = (1 + F_0\nu(\mu))/F_0 < 0$, which corresponds to the fulfillment of Pomeranchuk's stability criterion $1 + F_0\nu(\mu) > 0$ for the normal state for $l=0$, inequality (27) always holds since $\nu''(\mu) < 0$, and hence normal solutions exist in the entire range of the parameters μ and T . If, however, $1/F_0 + \nu(\mu) = (1 + F_0\nu(\mu))/F_0 > 0$ which corresponds to the violation of Pomeranchuk's criterion $1 + F_0\nu(\mu) < 0$ for $l=0$, normal solutions exist, according to (27) in the temperature range defined by the condition

$$T^2 > T_0^2 = -\frac{6}{\pi^2} \frac{1 + F_0\nu(\mu)}{F_0\nu''(\mu)} > 0. \quad (28)$$

It should be emphasized that Eq. (22) has no solutions at temperatures that do not satisfy condition (28). Thus, the thermodynamic and kinetic stability criteria coincide for the normal state.

Let us illustrate the above arguments by an example of quadratic dispersion relation $\varepsilon_p = p^2/2m$ for quasiparticles. In this case, the density (5) of energy states is given by

$$\nu_0(\mu_0) = \frac{m\sqrt{2m\mu_0}}{\pi^2}, \quad (29)$$

and the self-consistent equation (22) taking into account the low-temperature expansion (25) as well as (26) and (29) acquires the form

$$\frac{2m\sqrt{2m}}{3\pi^2} \mu_0^{3/2} + \frac{\pi^2}{6} T^2 \frac{m\sqrt{2m}}{2\pi^2 \mu_0^{1/2}} = \frac{\mu - \mu_0}{F_0}. \quad (30)$$

The condition starting with which solutions of Eq. (22) ("point of tangency," see Fig. 2) appear can be written in the form

$$\frac{1}{F_0} + \frac{m\sqrt{2m\mu_0}}{\pi^2} = \frac{\pi^2}{6} T^2 \frac{m\sqrt{2m}}{2\pi^2 \mu_0^{3/2}}. \quad (31)$$

Introducing instead of μ , μ_0 , and T the dimensionless quantities $\tilde{\mu}$, $\tilde{\mu}_0$, and \tilde{T} defined as

$$\mu = \frac{\pi^4}{m^3 F_0^2} \tilde{\mu}, \quad \mu_0 = \frac{\pi^4}{m^3 F_0^2} \tilde{\mu}_0, \quad T = \frac{\pi^4}{m^3 F_0^2} \tilde{T},$$

we can write Eqs. (30) and (31) in the following simple form:

$$\tilde{\mu} = \tilde{\mu}_0 - \frac{2\sqrt{2}}{3} \tilde{\mu}_0^{3/2} - \frac{\pi^2}{6\sqrt{2}} \frac{\tilde{T}^2}{\tilde{\mu}_0^{1/2}}, \quad (32)$$

$$1 - \sqrt{2\tilde{\mu}_0} = -\frac{\pi^2}{12\sqrt{2}} \frac{\tilde{T}^2}{\tilde{\mu}_0^{3/2}}. \quad (33)$$

Let us consider the case when $T=0$. In this case, the self-consistent equation (32) $\tilde{\mu} = \tilde{\mu}_0 - (2\sqrt{2}/3)\tilde{\mu}_0^{3/2}$ has a solution only for $\tilde{\mu} \leq 1/6$. The point of tangency (see Fig. 2) is defined by Eq. (33) which gives $\tilde{\mu}_0 = 1/2$. Consequently, $\tilde{\mu} = 1/6$ at this point. Thus, the region of existence of solutions of the self-consistent equation (32) for $T=0$ is determined by the inequality $\tilde{\mu} \leq 1/6$.

For $T \neq 0$ ($\tilde{T} \ll 1$), the solution of Eqs. (32) and (33) has the form

$$\tilde{\mu}_0 = \frac{1}{2} + \frac{\pi^2}{6} \tilde{T}^2, \quad \tilde{\mu} = \frac{1}{6} - \frac{\pi^2}{6} \tilde{T}^2.$$

The last equation describes a curve in the plane of parameters $\tilde{\mu}$, \tilde{T} separating the region in which the self-consistent equation (22) has a solution from the region in which no solution exists. Since a solution for $T=0$ exists for $\tilde{\mu} \leq 1/6$, the region $\tilde{\mu} < 1/6 - \pi^2 \tilde{T}^2/6$ is the region of existence of normal solutions for $\tilde{T} \ll 1$. It will be proved below that the region $\tilde{\mu} > 1/6 - \pi^2 \tilde{T}^2/6$ corresponds to spatially periodic solutions at $\tilde{T} \ll 1$.

3. PHASE TRANSITION ASSOCIATED WITH VIOLATION OF TRANSLATIONAL INVARIANCE

This section is devoted to an analysis of violation of Pomeranchuk's stability criterion (see (6)) for the harmonic $l=0$. The violation of this criterion will be put in correspondence with a phase transition of the Fermi liquid to a state with spontaneously broken translational symmetry, i.e., a state with a spatially periodic structure.

The self-consistent equation for determining spatially periodic solutions can be obtained from Eq. (1) by substituting into it a Fermi-Dirac distribution function with the spatially inhomogeneous dispersion relation

$$\varepsilon(\mathbf{r}, \mathbf{p}) = \varepsilon_{\mathbf{p}} + \frac{2}{V} \sum_{\mathbf{p}'} \int d^3 r' F(\mathbf{r} - \mathbf{r}'; \mathbf{p}, \mathbf{p}') f_0(\mathbf{p}', \mathbf{r}'),$$

$$f_0(\mathbf{r}, \mathbf{p}) = \{\exp \beta(\varepsilon(\mathbf{r}, \mathbf{p}) - \mu) + 1\}^{-1}. \quad (34)$$

We shall seek the solution of Eq. (34) in the form of functions periodic in \mathbf{r} , i.e.,

$$\varepsilon(\mathbf{r}, \mathbf{p}) = \sum_{\mathbf{q}} \varepsilon_{\mathbf{q}}(\mathbf{p}) e^{i\mathbf{q}\mathbf{r}} = \varepsilon_0(\mathbf{p}) + \tilde{\varepsilon}(\mathbf{r}, \mathbf{p}),$$

where

$$\tilde{\varepsilon}(\mathbf{r}, \mathbf{p}) = \sum_{\mathbf{q} \neq 0} \varepsilon_{\mathbf{q}}(\mathbf{p}) e^{i\mathbf{q}\mathbf{r}}, \quad \varepsilon_0(\mathbf{p}) = \langle \varepsilon(\mathbf{r}, \mathbf{p}) \rangle$$

and the angle brackets $\langle \dots \rangle$ denote the averaging over periods. Consequently, Eqs. (34) can be written in the form

$$\varepsilon_0(\mathbf{p}) = \varepsilon_{\mathbf{p}} + \frac{2}{V} \sum_{\mathbf{p}'} F_0(\mathbf{p}, \mathbf{p}') \times \left(\frac{1}{\exp\{\beta(\varepsilon_0(\mathbf{p}') + \tilde{\varepsilon}(\mathbf{r}', \mathbf{p}') - \mu)\} + 1} \right)_0, \quad (35)$$

$$\tilde{\varepsilon}_{\mathbf{q}}(\mathbf{p}) = \frac{2}{V} \sum_{\mathbf{p}'} F_{\mathbf{q}}(\mathbf{p}, \mathbf{p}') \times \left(\frac{1}{\exp\{\beta(\varepsilon_0(\mathbf{p}') + \tilde{\varepsilon}(\mathbf{r}', \mathbf{p}') - \mu)\} + 1} \right)_{\mathbf{q}},$$

$$q \neq 0, \quad (36)$$

where $F_{\mathbf{q}}(\mathbf{p}, \mathbf{p}') = \int^3 r F(\mathbf{p}, \mathbf{p}'; \mathbf{r}) e^{i\mathbf{q}\mathbf{r}}$ is the Fourier component of the Landau amplitude. We shall assume that the dependence of the amplitude $F_{\mathbf{q}}(\mathbf{p}, \mathbf{p}')$ on the direction of vectors \mathbf{p} and \mathbf{p}' is determined only by their dot product $\mathbf{p} \cdot \mathbf{p}'$.

In this case, the solution of Eq. (36) can be sought in the form for which the quantity $\varepsilon_q(\mathbf{p}) \equiv \varepsilon_q(\mathbf{p})$ is independent of the direction of vector \mathbf{p} . Besides, we assume that the functions $F_q(\mathbf{p}, \mathbf{p}')$ vary slowly with \mathbf{p} and \mathbf{p}' , and hence the quantity $\tilde{\varepsilon}_q(p)$ also varies slowly with the variable p . Since the function $(\exp\{\beta(\varepsilon_0(p') + \tilde{\varepsilon}(\mathbf{r}', \mathbf{p}') - \mu)\} + 1)^{-1}$ has a sharp peak at $p' = p_F$ for $q \neq 0$, we can put $p' = p_F$ in the quantity $F_q(\mathbf{p}, \mathbf{p}')$ appearing in Eq. (36), which gives

$$\tilde{\varepsilon}_q(p) = \frac{F_q(p, p_F)}{F_q(p_F, p_F)} \tilde{\varepsilon}_q(p_F),$$

$$F_q(p, p') \equiv \frac{1}{4\pi} \int d\Omega F_q(\mathbf{p}, \mathbf{p}'), \quad (37)$$

where $\tilde{\varepsilon}_q(p_F) \equiv \tilde{\varepsilon}_q$ satisfies the equation

$$\tilde{\varepsilon}_q = F_q \{n(\beta, \mu - \tilde{\varepsilon}(\mathbf{r}, p))\}_q,$$

$$F_q = F_q(p_F, p_F), \quad \mathbf{q} \neq 0, \quad (37a)$$

and the function $n(\beta, \mu)$ is defined by the expression

$$n(\beta, \mu) = \frac{2}{V} \sum_{\mathbf{p}} [\exp \beta(\varepsilon_0(p) - \mu) + 1]^{-1}. \quad (38)$$

For the sake of simplicity, we shall confine our subsequent analysis to one-dimensional periodic structures in a three-dimensional Fermi liquid. We assume that the periodic structure appearing in this case has a period a along the x -axis, so that

$$\tilde{\varepsilon}_q(p) = \delta_{q_y, 0} \delta_{q_x, 0} \tilde{\varepsilon}_q(p), \quad q_x = q = \frac{2\pi n}{a}$$

(n are integers). In this case, Eq. (37a) acquires the form

$$\tilde{\varepsilon}_q = F_q \{n(\beta, \mu - \tilde{\varepsilon}(x, p))\}_q, \quad q \neq 0, \quad (39)$$

where

$$F_q = \int d^3r e^{iqx} F_0(p_F, p_F; \mathbf{r}).$$

Equation (39) obtained in the approximation of a slow variation of the amplitude $F(\mathbf{p}, \mathbf{p}')$ with \mathbf{p} and \mathbf{p}' is in complete accord with the model (8) used by us earlier for analyzing the properties of the normal state.

Let us now go over to the solution of Eq. (39) near the phase-transition point, where the quantity $\tilde{\varepsilon}_q$ describing the order parameter is small. Expanding Eq. (39) into a power series in $\tilde{\varepsilon}(x)$ as well as in $(\beta - \beta_c)$ taking into account (38) ($\beta_c^{-1} \equiv T_c$ is the transition temperature), we obtain

$$\tilde{\varepsilon}_q = F_q \left(-\frac{\partial n(\beta_c, \mu)}{\partial \mu} \tilde{\varepsilon}_q - \frac{\partial^2 n(\beta_c, \mu)}{\partial \beta_c \partial \mu} (\beta - \beta_c) \tilde{\varepsilon}_q + \frac{1}{2} \frac{\partial^2 n(\beta_c, \mu)}{\partial \mu^2} (\tilde{\varepsilon}^2(x))_q - \frac{1}{6} \frac{\partial^3 n(\beta_c, \mu)}{\partial \mu^3} \times (\tilde{\varepsilon}^3(x))_q + \dots \right). \quad (40)$$

We shall seek the solution of this equation in the form $\varepsilon_q = \tilde{\varepsilon}_q^{(0)} + \tilde{\varepsilon}_q^{(1)} + \dots$, where

$$\tilde{\varepsilon}_q^{(0)} = \tilde{\varepsilon}_q^{(0)} \{ \Delta(q - q_0) + \Delta(q + q_0) \} \quad (41)$$

($\Delta(q)$ is the Kronecker symbol). In the main approximation, we have

$$1 + F_{q_0} \frac{\partial n(\beta_c, \mu)}{\partial \mu} = 0. \quad (42)$$

This equation determines the transition temperature $\beta_c = \beta_c(q_0)$. Carrying out in this equation the low-temperature expansion (25), we obtain

$$T_c^2 = -\frac{6}{\pi^2} \frac{1 + F_{q_0} \nu(\mu)}{F_{q_0} \nu''(\mu)}. \quad (43)$$

Since $\nu''(\mu) < 0$, it can be easily seen that the inequality $T_c^2 > 0$ holds only when the relation

$$1 + \nu(\mu) F_{q_0} < 0,$$

reflecting the violation of the criterion of stability of the equilibrium state of a normal Fermi liquid is valid.

Let us now find the expression for the order parameter $\tilde{\varepsilon}$. Noting in this connection that

$$(\tilde{\varepsilon}(x))_q = \tilde{\varepsilon}_q,$$

$$(\tilde{\varepsilon}(x))_q = \sum_{q', q''} \tilde{\varepsilon}_{q'} \tilde{\varepsilon}_{q''} \Delta(q' + q'' - q),$$

$$(\tilde{\varepsilon}^3(x))_q = \sum_{q', q'', q'''} \tilde{\varepsilon}_{q'} \tilde{\varepsilon}_{q''} \tilde{\varepsilon}_{q'''} \Delta(q' + q'' + q''' - q),$$

and taking into account the fact that the relations

$$(\tilde{\varepsilon}^2(x))_{q_0} \approx 2 \tilde{\varepsilon}_{q_0}^{(0)} \tilde{\varepsilon}_{q_0}^{(1)}, \quad (\tilde{\varepsilon}^3(x))_{q_0} \approx 3 (\tilde{\varepsilon}_{q_0}^{(0)})^3,$$

hold in the main nonvanishing approximation, we can write Eq. (40) taking into account (41) and (42) for $q = q_0$ in the form

$$-\frac{\partial^2 n(\beta_c, \mu)}{\partial \beta_c \partial \mu} (\beta - \beta_c) \tilde{\varepsilon}_{q_0}^{(0)} + \frac{\partial^2 n(\beta_c, \mu)}{\partial \mu^2} \tilde{\varepsilon}_{q_0}^{(0)} \tilde{\varepsilon}_{2q_0}^{(1)} - \frac{1}{2} \frac{\partial^3 n(\beta_c, \mu)}{\partial \mu^3} (\tilde{\varepsilon}_{q_0}^{(0)})^3 = 0. \quad (44)$$

It can be easily seen that along with Eq. (44), we must also write Eq. (40) for $q \neq \pm q_0$:

$$\tilde{\varepsilon}_q = F_q \left(-\frac{\partial n(\beta_c, \mu)}{\partial \mu} \tilde{\varepsilon}_q + \frac{1}{2} \frac{\partial^2 n(\beta_c, \mu)}{\partial \mu^2} (\tilde{\varepsilon}^2(x))_q \right).$$

Putting $q = 2q_0$ in this equation, we obtain

$$\tilde{\varepsilon}_{2q_0} = F_{2q_0} \left(-\frac{\partial n(\beta_c, \mu)}{\partial \mu} \tilde{\varepsilon}_{2q_0} + \frac{1}{2} \frac{\partial^2 n(\beta_c, \mu)}{\partial \mu^2} (\tilde{\varepsilon}^2(x))_{2q_0} \right). \quad (45)$$

Noting further that in the main approximation we have

$$(\tilde{\varepsilon}^2(x))_{2q_0} \approx (\tilde{\varepsilon}_{q_0}^{(0)})^2, \quad \tilde{\varepsilon}_{2q_0} \approx \tilde{\varepsilon}_{2q_0}^{(1)},$$

we write Eq. (45) in the form

$$\tilde{\varepsilon}_{2q_0}^{(1)} = F_{2q_0} \left(-\frac{\partial n(\beta_c, \mu)}{\partial \mu} \tilde{\varepsilon}_{2q_0}^{(1)} + \frac{1}{2} \frac{\partial^2 n(\beta_c, \mu)}{\partial \mu^2} (\tilde{\varepsilon}_{q_0}^{(0)})^2 \right),$$

whence

$$\tilde{\varepsilon}_{2q_0}^{(1)} = \frac{F_{2q_0}}{2} \frac{\partial^2 n(\beta_c, \mu)}{\partial \mu^2} \left(1 + F_{2q_0} \frac{\partial n(\beta_c, \mu)}{\partial \mu} \right)^{-1} (\tilde{\varepsilon}_{q_0}^{(0)})^2.$$

Substituting the expression obtained for $\tilde{\varepsilon}_{2q_0}^{(1)}$ into (44), we obtain the following equation for determining $\tilde{\varepsilon}_{q_0}^{(0)}$:

$$\begin{aligned} & \frac{F_{2q_0}}{2} \left(\frac{\partial^2 n(\beta_c, \mu)}{\partial \mu^2} \right)^2 \left(1 + F_{2q_0} \frac{\partial n(\beta_c, \mu)}{\partial \mu} \right)^{-1} (\tilde{\varepsilon}_{q_0}^{(0)})^2 \\ & - \frac{1}{2} \frac{\partial^3 n(\beta_c, \mu)}{\partial \mu^3} (\tilde{\varepsilon}_{q_0}^{(0)})^2 = \frac{\partial^2 n(\beta_c, \mu)}{\partial \beta_c \partial \mu} (\beta - \beta_c). \end{aligned} \quad (46)$$

Taking into account the low-temperature expansion (25) as well as (42), we obtain

$$\tilde{\varepsilon}_{q_0}^{(0)} = A(2q_0) \sqrt{1 - T/T_c}, \quad (47)$$

where

$$A(2q_0) = \left\{ \frac{2n^2}{3} \frac{T_c^2 \nu''(\mu)}{\nu''(\mu) - F_{2q_0} (\nu'(\mu))^2 (1 - F_{2q_0}/F_{q_0})^{-1}} \right\}^{-1/2}.$$

The quantity $\tilde{\varepsilon}_{q_0}(p)$ is defined by formula (37).

It should be noted now that the perturbation theory developed by us becomes inapplicable in the region of small q_0 . This follows even from the fact that the quantity $1 - F_{2q_0}/F_{q_0}$ appearing in the denominator of Eq. (46) and formula (47) vanishes for $q_0 \rightarrow 0$. For this reason, the case of small q_0 corresponding to a large period of spatially periodic functions analyzed by us requires a separate analysis. Since all quantities vary slowly with x in the case of a large lattice period (low gradients), it is more convenient to solve the problem in the coordinate representation.

We shall proceed from the equation

$$\begin{aligned} \tilde{\varepsilon}(x) &= \int dx F(x-x') \{ n(\beta, \mu - \tilde{\varepsilon}(x')) \\ & - \langle n(\beta, \mu - \tilde{\varepsilon}(x')) \rangle \}, \\ \tilde{\varepsilon}(\mathbf{p}, x) &\equiv \tilde{\varepsilon}(x), \end{aligned} \quad (48)$$

where

$$F(x-x') = \int F_q e^{iq(x-x')} dq$$

and the angle brackets $\langle \dots \rangle$ denote the averaging of a quantity over the lattice period, while the quantity $n(\beta, \mu - \tilde{\varepsilon}(x))$ is defined by the formula (38). This equation is equivalent to Eqs. (35) and (36) if we consider that $\langle \tilde{\varepsilon}(x) \rangle = 0$. Noting that the quantity $F(x-x')$ has a sharp peak at $x=x'$ and also considering that the quantity $\tilde{\varepsilon}(x)$ varies slowly on account of the large lattice period, we can write Eq. (48) in the form

$$\begin{aligned} \tilde{\varepsilon}(x) &= F_0 \{ n(\beta, \mu - \tilde{\varepsilon}(x)) - \langle n(\tilde{\beta}, \mu - \tilde{\varepsilon}(x)) \rangle \} \\ & + F_2 \frac{\partial^2 n(\beta, \mu - \tilde{\varepsilon}(x))}{\partial x^2}, \end{aligned} \quad (49)$$

where

$$\begin{aligned} & \int dx' F(x-x') = F_0, \\ & \frac{1}{2} \int dx' F(x-x') (x-x')^2 = F_2 \end{aligned} \quad (50)$$

(while deriving Eq. (49), we assumed that the function $F(x-x')$ is even). Carrying out the power expansion in $\tilde{\varepsilon}(x)$ and $(\beta - \beta_0)$ in the last equation (β_0 corresponds to the transition temperature for $q=0$) and taking into account the equation for determining β_0

$$1 + F_0 \frac{\partial n(\beta_0, \mu)}{\partial \mu} = 0 \quad (51)$$

as well as the fact that $\langle \tilde{\varepsilon}(x) \rangle = 0$, we obtain

$$\begin{aligned} F_0 \left\{ -(\beta - \beta_0) \frac{\partial^2 n(\beta_0, \mu)}{\partial \beta \partial \mu} \tilde{\varepsilon}(x) + \frac{1}{2} \frac{\partial^2 n(\beta_0, \mu)}{\partial \mu^2} (\tilde{\varepsilon}^2(x) \right. \\ \left. - \langle \tilde{\varepsilon}^2(x) \rangle) \right\} - F_2 \frac{\partial n(\beta_0, \mu)}{\partial \mu} \frac{\partial^2 \tilde{\varepsilon}(x)}{\partial x^2} = 0. \end{aligned} \quad (52)$$

It was proved above that the equation for determining the transition temperature as a function of q has the form

$$1 + F_q \frac{\partial n(\beta_c, \mu)}{\partial \mu} = 0.$$

Considering that $F_q = F(q^2)$ and $F'(0) = -F_2$, $F_0 = F(0)$ (see (49) and (50)), we can write this equation for small q in the form

$$1 + (F_0 - F_2 q^2) \left(\frac{\partial n(\beta_0, \mu)}{\partial \mu} + (\beta_c - \beta_0) \frac{\partial^2 n(\beta_0, \mu)}{\partial \beta \partial \mu} \right) = 0$$

or, taking into account (51),

$$\begin{aligned} \beta_c - \beta_0 &= q^2 \frac{F_2}{F_0} \frac{\partial n(\beta_0, \mu)}{\partial \mu} \bigg/ \frac{\partial^2 n(\beta_0, \mu)}{\partial \beta \partial \mu} \\ &= -q^2 \frac{F_2}{F_0^2} \bigg/ \frac{\partial^2 n(\beta_0, \mu)}{\partial \beta \partial \mu}. \end{aligned} \quad (53)$$

This equation defines the transition temperature as a function of q in the range of small q . Making the natural assumption that $\beta_0 < \beta_c$ (a long-periodic structure branches at higher temperatures) and considering that $(\partial^2 n(\beta_0, \mu))/\partial \beta \partial \mu > 0$ (see the low-temperature expansion (25)), we obtain $F_2 < 0$, which corresponds to attraction between fermions. Equation (52) used for defining the quantity $\tilde{\varepsilon}(x)$ can be written in another form more convenient for the subsequent analysis. For this purpose, we introduce the quantity $\varepsilon(x) = -\tilde{\varepsilon}(x)$ that can be regarded as a correction to chemical potential (see (35) and (36)). Then Eq. (52) assumes the form

$$\begin{aligned} & \frac{\partial^2 \varepsilon(x)}{\partial x^2} + g(\varepsilon(x)) = 0, \\ & g(\varepsilon(x)) = A \varepsilon(x) + B(\varepsilon^2(x) - \langle \varepsilon^2(x) \rangle), \end{aligned} \quad (54)$$

where

$$A = -\frac{F_0^2}{F_2} (\beta - \beta_0) \frac{\partial^2 n(\beta_0, \mu)}{\partial \beta_0 \partial \mu},$$

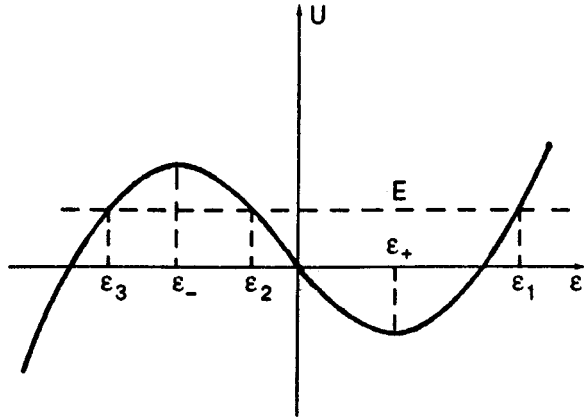


FIG. 3. Schematic dependence of "potential" $U(\varepsilon)$ on the order parameter ε .

$$B = -\frac{1}{2} \frac{F_0^2}{F_2} \frac{\partial^2 n(\beta_0, \mu)}{\partial \mu^2}. \quad (55)$$

We shall seek periodic solutions of Eq. (54) which gives

$$\varepsilon' = \pm \sqrt{2(E - U(\varepsilon))}, \quad x = \pm \int_{\varepsilon}^{\varepsilon} \frac{d\varepsilon}{\sqrt{2(E - U(\varepsilon))}}, \quad (56)$$

where

$$U(\varepsilon) = \int_0^{\varepsilon} g(\varepsilon) d\varepsilon = \frac{1}{3} B \varepsilon^3 + \frac{1}{2} A \varepsilon^2 - B d^2 \varepsilon,$$

$$d^2 = \langle \varepsilon^2(x) \rangle$$

and E is the integration constant. The cubic polynomial $E - U(\varepsilon)$ can be written in the form

$$\begin{aligned} E - U(\varepsilon) &= E - \frac{1}{3} B \varepsilon^3 - \frac{1}{2} A \varepsilon^2 + B d^2 \varepsilon \\ &= -\frac{1}{3} B (\varepsilon - \varepsilon_1)(\varepsilon - \varepsilon_2)(\varepsilon - \varepsilon_3) > 0. \end{aligned} \quad (57)$$

The points of extrema of the function $U(\varepsilon)$ are defined as

$$\varepsilon_{\pm} = -\frac{A}{2B} \pm \sqrt{A^2/4B^2 + d^2}, \quad \varepsilon_+ > 0, \quad \varepsilon_- < 0.$$

Figure 3 shows schematically the function $U(\varepsilon)$ (we take into account the fact that $B > 0$). Since $E - U > 0$, periodic solutions of Eq. (54) correspond to the region $\varepsilon_2 < \varepsilon < \varepsilon_1$, and since $\langle \varepsilon \rangle = 0$, we have $\varepsilon_2 < 0$ and $\varepsilon_1 > 0$. Consequently, we have

$$\begin{aligned} x(\varepsilon) &= -\int_{\varepsilon}^{\varepsilon_1} \frac{d\varepsilon}{\sqrt{2(E - U(\varepsilon))}}, \quad x < 0, \\ x(\varepsilon) &= \int_{\varepsilon}^{\varepsilon_1} \frac{d\varepsilon}{\sqrt{2(E - U(\varepsilon))}}, \quad x > 0 \end{aligned} \quad (58)$$

(see Fig. 4 showing a period of the function $\varepsilon(x)$). The period of this function is defined by the formula

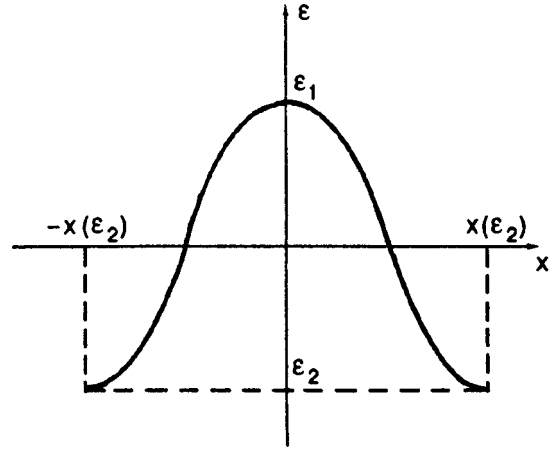


FIG. 4. Dependence of the order parameter ε on the coordinate x .

$$X = 2 \int_{\varepsilon_2}^{\varepsilon_1} \frac{d\varepsilon}{\sqrt{2(E - U(\varepsilon))}} = 2x(\varepsilon_2). \quad (59)$$

Substituting expression (57) for $E - U(\varepsilon)$ into the formula (58) for $x(\varepsilon)$ for $x > 0$ and transforming the corresponding integral, we obtain

$$\begin{aligned} x(\varepsilon) &= \sqrt{6/B} \frac{1}{\sqrt{\varepsilon_1 - \varepsilon_3}} \int_0^{\varphi} \frac{d\varphi}{\sqrt{1 - k^2 \sin^2 \varphi}}, \\ k^2 &= \frac{\varepsilon_1 - \varepsilon_2}{\varepsilon_1 - \varepsilon_3}, \quad \varphi = \arcsin \sqrt{(\varepsilon_1 - \varepsilon)/(\varepsilon_1 - \varepsilon_2)}. \end{aligned}$$

Taking into account the definition of the first-order elliptical integral

$$\mathcal{F}(k, \varphi) = \int_0^{\varphi} \frac{d\varphi}{\sqrt{1 - k^2 \sin^2 \varphi}}, \quad (60)$$

we can write $x(\varepsilon)$ in the form

$$x(\varepsilon) = \sqrt{6/B} \frac{1}{\sqrt{\varepsilon_1 - \varepsilon_3}} \mathcal{F}(k, \varphi). \quad (61)$$

In accordance with (59), in this case we have

$$X = \sqrt{6/B} \frac{2}{\sqrt{\varepsilon_1 - \varepsilon_3}} \mathcal{F}(k), \quad \mathcal{F}(k) \equiv \mathcal{F}(k, \pi/2). \quad (62)$$

Let us now determine the quantities ε_1 , ε_2 , and ε_3 . For this purpose, we note that

$$\begin{aligned} \langle \varepsilon(x) \rangle &= \frac{1}{X} \int_0^{X/2} \varepsilon(x) dx + \frac{1}{X} \int_{X/2}^X \varepsilon(x) dx \\ &= \frac{2}{X} \int_0^{X/2} \varepsilon(x) dx, \end{aligned}$$

or, going over to integration with respect to ε ,

$$\langle \varepsilon(x) \rangle = \frac{2}{X} \int_{\varepsilon_2}^{\varepsilon_1} \varepsilon \frac{d\varepsilon}{\sqrt{2(E - U)}}. \quad (63)$$

Equation (54) implies that $\langle \varepsilon \rangle = 0$. Transforming the integral appearing in (63) and taking into account (57), we obtain

$$\int_0^{\pi/2} d\varphi \frac{\varepsilon_1 - (\varepsilon_1 - \varepsilon_2) \sin^2 \varphi}{\sqrt{1 - k^2 \sin^2 \varphi}} = 0, \quad k^2 = \frac{\varepsilon_1 - \varepsilon_2}{\varepsilon_1 - \varepsilon_3}.$$

Using the definition of the second-order elliptical integral

$$E(k) = \int_0^{\pi/2} d\varphi \sqrt{1 - k^2 \sin^2 \varphi}, \quad (64)$$

we obtain

$$E(k) + \left(k^2 \frac{\varepsilon_1}{\varepsilon_1 - \varepsilon_3} - 1 \right) \mathcal{F}(k) = 0.$$

This expression can also be written in the form

$$\frac{\varepsilon_1}{\varepsilon_1 - \varepsilon_2} = \frac{\mathcal{F}(k) - E(k)}{k^2 \mathcal{F}(k)},$$

$$\frac{\varepsilon_1}{\varepsilon_1 - \varepsilon_3} = \frac{\mathcal{F}(k) - E(k)}{\mathcal{F}(k)}. \quad (65)$$

These formulas indicate that the ratios $\varepsilon_1/\varepsilon_2$, $\varepsilon_1/\varepsilon_3$, $\varepsilon_2/\varepsilon_3$ can be expressed only in terms of the parameter k . Let us now find the expression for the quantity ε_1 in terms of k . For this purpose, we note that, according to (56),

$$\varepsilon_1 + \varepsilon_2 + \varepsilon_3 = -\frac{3}{2} \frac{A}{B} \equiv \gamma(\beta - \beta_0), \quad (66)$$

where

$$\gamma = -3 \frac{\partial^2 n(\beta_0, \mu)}{\partial \beta \partial \mu} \bigg/ \frac{\partial^2 n(\beta_0, \mu)}{\partial \mu^2} \quad (67)$$

in accordance with (55). Using further formulas (65), we obtain the following expression for the quantity ε_1 :

$$\varepsilon_1 = \frac{\gamma(\beta - \beta_0)}{3 - (1 + k^2) \mathcal{F}(k) / [\mathcal{F}(k) - E(k)]}. \quad (68)$$

Taking into account this relation and (65), we can easily determine the quantity $1/\sqrt{\varepsilon_1 - \varepsilon_3}$ appearing in the expression (62) for the period:

$$\frac{1}{\sqrt{\varepsilon_1 - \varepsilon_3}} = \left[\left(3 \frac{\mathcal{F}(k) - E(k)}{\mathcal{F}(k)} - k^2 - 1 \right) \bigg/ \gamma(\beta - \beta_0) \right]^{1/2}. \quad (69)$$

Noting that $k^2 = (\varepsilon_1 - \varepsilon_2)/(\varepsilon_1 - \varepsilon_3)$, and introducing the new variable $\varepsilon \equiv \varepsilon_1 - \varepsilon_3$, we obtain

$$\varepsilon_1 - \varepsilon_2 = \varepsilon k^2, \quad \varepsilon_1 = \varepsilon \frac{\mathcal{F}(k) - E(k)}{\mathcal{F}(k)}$$

or

$$\varepsilon_1 = \varepsilon \left(1 - \frac{E(k)}{\mathcal{F}(k)} \right),$$

$$\varepsilon_2 = \varepsilon \left(1 - k^2 - \frac{E(k)}{\mathcal{F}(k)} \right),$$

$$\varepsilon_3 = -\varepsilon \frac{E(k)}{\mathcal{F}(k)}. \quad (70)$$

Since $\varepsilon > 0$ and $\gamma(\beta - \beta_0) < 0$ (see (66) and (67)), the inequality $3[(\mathcal{F} - E)/\mathcal{F}] - k^2 - 1 < 0$, must hold in accordance with (69), which gives $k < k_0 \approx 0.95$.

The period X of the function $\varepsilon(x)$ is connected with the quantity q through the formula

$$X = \frac{2\pi}{q} = 2\sqrt{6/B} \frac{1}{\sqrt{\varepsilon}} \mathcal{F}(k). \quad (71)$$

The variables k and ε can be taken as independent thermodynamic variables instead of β and q . The phase curve in the β, q space, separating the regions of the normal phase and the spatially periodic phase is given by formula (53). It can be easily seen from formulas (69) and (70) taking into account (60) and (64) that the same curve in the space of the variables k and ε has the form

$$k = 0. \quad (72)$$

Let us now find the expression for $\varepsilon(x)$. The definitions (60) and (62) of the functions $\mathcal{F}(k, \varphi)$ and $\mathcal{F}(k)$ lead to the relation

$$\mathcal{F}(k, \varphi + \pi) = 2\mathcal{F}(k) + \mathcal{F}(k, \varphi). \quad (73)$$

Since $\mathcal{F}(k, \varphi)$ is a monotonically increasing function of φ , we can introduce the reciprocal function $\varphi(k, y)$ such that

$$\mathcal{F}(k, \varphi(k, y)) = y.$$

Taking into account (73), we have

$$\mathcal{F}(k, \varphi(k, y) + \pi) = y + 2\mathcal{F}(k),$$

$$\sigma(k, y) + \pi = \varphi(k, y + 2\mathcal{F}(k)),$$

whence

$$\sin^2 \varphi(k, y) = \sin^2 \varphi(k, y + 2\mathcal{F}(k)).$$

Thus, the function $\sin^2 \varphi(k, y)$ is a periodic function of y with the period $2\mathcal{F}(k)$. Noting further that

$$2\mathcal{F}(k) \frac{x}{X} = \mathcal{F}(k, \varphi),$$

$$\varphi = \arcsin \sqrt{(\varepsilon_1 - \varepsilon)/(\varepsilon_1 - \varepsilon_2)},$$

in accordance with (61) and (62), we obtain

$$\varepsilon(x) = \varepsilon_1 - (\varepsilon_1 - \varepsilon_2) \sin^2 \varphi \left(k, 2\mathcal{F}(k) \frac{x}{X} \right)$$

or, taking into account (70), we finally get

$$\varepsilon(x) = \varepsilon \left(1 - \frac{E(k)}{\mathcal{F}(k)} - k^2 \sin^2 \varphi \left(k, 2\mathcal{F}(k) \frac{x}{X} \right) \right), \quad (74)$$

where the quantity X is defined by (71). It should be noted that the function $\sin \varphi(k, u)$ is connected with the elliptical sine $\text{sn}(u, k)$ through the relation

$$\sin \varphi(k, u) = \text{sn}(u, k).$$

Formula (74) determines the long-periodic structure of the system under investigation at temperatures close to the transition temperature T_0 .

4. STRUCTURE OF LONG-PERIODIC SOLUTIONS AT $T=0$

Let us find one-dimensional periodic solutions of the self-consistent equation (34) far away from the phase-transition point, namely, at $T=0$. In this case, it is not expedient to use the parameter $\tilde{\varepsilon}(x)$ since this quantity is not small at $T=0$. Thus, we shall seek the solution of Eq. (34) in the form

$$\varepsilon(p, x) = \varepsilon(x) + \varepsilon_p,$$

where $\varepsilon(x)$ is a periodic function of the variable x . In the approximation of small gradients (large period, see below), Eq. (34) can be written in the form

$$\varepsilon(x) = F_0 n(\beta, \mu - \varepsilon(x)) + F_2 \frac{\partial^2 n(\beta, \mu - \varepsilon(x))}{\partial x^2}, \quad (75)$$

where

$$F_0 = \int d^3 r F(\mathbf{r}), \quad F_2 = \frac{1}{2} \int d^3 r x^2 F(\mathbf{r}).$$

Introducing the quantity $\underline{\mu}(x) = \mu - \varepsilon(x)$ and considering Eq. (75) as an equation for determining the function $n(n(\underline{\mu}(x)) = n(x), \underline{\mu} = \underline{\mu}(n))$, we obtain

$$\frac{\partial^2 n}{\partial x^2} = \frac{1}{F_2} (\mu - \underline{\mu}(n) - F_0 n).$$

Integration of the last equation leads to the following expression for $x = x(n)$:

$$x = \pm \int^n \frac{dn}{\sqrt{E - U}}, \quad (76)$$

where

$$U = \frac{2}{F_2} \int^n dn (\underline{\mu}(n) - \mu + F_0 n) \quad (77)$$

and E is the integration constant. Noting that

$$n(\underline{\mu}) = \frac{2}{(2\pi)^3} \int d^3 p \theta(\underline{\mu} - \varepsilon(p, x)), \quad \frac{\partial n}{\partial \underline{\mu}} = \nu(\underline{\mu}),$$

at $T=0$, we obtain

$$n = \int_{-\infty}^{\underline{\mu}} \nu(\varepsilon) d\varepsilon, \quad n(-\infty) = 0$$

and hence, in accordance with (77), we obtain

$$U = \frac{2}{F_2} \left(\int_{-\infty}^{\underline{\mu}} \varepsilon \nu(\varepsilon) d\varepsilon - \mu \int_{-\infty}^{\underline{\mu}} \nu(\varepsilon) d\varepsilon + \frac{1}{2} F_0 \left(\int_{-\infty}^{\underline{\mu}} \nu(\varepsilon) d\varepsilon \right)^2 \right) \quad (78)$$

(we consider in this case that

$$\int^n \mu(n) dn = \int^{\underline{\mu}} \mu(dn/d\underline{\mu}) d\underline{\mu} = \int^{\underline{\mu}} \mu \nu(\underline{\mu}) d\underline{\mu},$$

and choose the integration constant in a quite definite form in view of the arbitrariness of the integration constant E in formula (76)). Thus, we can finally write

$$x = \pm \int^{\underline{\mu}} \frac{\nu(\varepsilon) d\varepsilon}{\sqrt{E - U(\varepsilon)}}, \quad (79)$$

where $U(\varepsilon)$ is defined by (78).

Let us now consider the algorithm of determining the period X of the function $\varepsilon(x)$ for a quadratic dispersion relation. In this case, the quantity $\nu(\varepsilon)$ is defined by formula (29), and the quantity $U(\varepsilon)$ defined by relation (78) assumes the form

$$U(\varepsilon) = \frac{2}{F_2} \frac{\sqrt{2} m^{3/2}}{\pi^2} \left\{ \frac{2}{5} \varepsilon^{5/2} - \frac{2}{3} \mu \varepsilon^{3/2} + \frac{2}{9} F_0 \frac{\sqrt{2} m^{3/2}}{\pi^2} \varepsilon^3 \right\}, \quad (80)$$

It can be easily proved that the function $U(\varepsilon)$ defined by formula (80) has one maximum and two minima for $F_0 < 0$ and $F_2 < 0$; One minimum corresponds to the point $\varepsilon = 0$, while the point ε_0 corresponding to the second minimum satisfies the equation

$$a \varepsilon_0^{3/2} + \varepsilon_0 = \mu, \quad a = F_0 \frac{(2m)^{3/2}}{3\pi^2} < 0. \quad (81)$$

In order to find the period X of the function $\varepsilon(x)$, we can find the roots of the equations $E - U(\varepsilon) = 0$ defining the so-called turning points. The equation for determining the turning points near the minimum ε_0 of the function $U(\varepsilon)$ can be written in the form

$$\begin{aligned} \tilde{E} - (\varepsilon - \varepsilon_0)^2 &= 0, \\ \tilde{E} &= \frac{2(E - U(\varepsilon_0))}{\partial^2 U(\varepsilon_0) / \partial \varepsilon_0^2} > 0, \end{aligned}$$

whence

$$\varepsilon_{\pm} = \varepsilon_0 \pm \sqrt{\tilde{E}}, \quad \varepsilon_+ > \varepsilon_-.$$

On the other hand, the period of the function $\varepsilon(x)$ is defined, in accordance with (79), by the formula

$$X = 2 \int_{\varepsilon_-}^{\varepsilon_+} \frac{\nu(\varepsilon_0) d\varepsilon}{\sqrt{E - U(\varepsilon_0) - 1/2 [\partial^2 U(\varepsilon_0) / \partial \varepsilon_0^2] (\varepsilon - \varepsilon_0)^2}},$$

$$\nu(\varepsilon_0) = \frac{\sqrt{2} m^{3/2}}{\pi^2} \sqrt{\varepsilon_0}.$$

After evaluating the integral appearing in this formula, we find that

$$X = 2 \left[\frac{F_2 (2m)^{3/2}}{2 \varepsilon_0^{-1/2} + 3a} \right]^{1/2},$$

or, introducing the dimensionless quantity $\tilde{\varepsilon}_0$ through the relation

$$\varepsilon_0 = \frac{\pi^4}{m^3 F_0^2} \tilde{\varepsilon}_0,$$

we finally obtain

$$X = 2 \pi \sqrt{F_2 / F_0} \left[\frac{1}{(2\tilde{\varepsilon}_0)^{-1/2} - 1} \right]^{1/2},$$

where, in accordance with (81), $\tilde{\varepsilon}_0$ satisfies the following equation:

$$\tilde{\mu} = \tilde{\varepsilon}_0 - \frac{2\sqrt{2}}{3} \tilde{\varepsilon}_0^{3/2}, \quad \tilde{\mu} = \frac{m^3 F_0^2}{\pi^4} \mu.$$

This equation has a solution only for $\tilde{\mu} < 1/6$, and $\tilde{\varepsilon}_0 = 1/2$ for $\tilde{\mu} = 1/6$. According to the definition of the quantity F_2 , we have $F_2 \approx x_0^2 F_0$, where x_0 determines the region in which the function $F(x) = \int dy dz F(\mathbf{r})$ differs from zero. The slow variation of the function $\varepsilon(x)$ (small values of the gradients) presumed above means that $x_0 \ll X$ or $\sqrt{2} \tilde{\varepsilon}_0 \approx 1$. This means that the approximation used by us is valid only in the vicinity of $\tilde{\mu} = 1/6$.

5. CONCLUSION

It should be noted that the description of spatially periodic structures formed in strongly interacting systems was proposed for the first time by Vlasov⁹ by using the method based on the application of the self-consistent field approximation. Actually, he made an attempt to construct a classical (and not quantum-mechanical) theory of crystal since the analysis was based on determining spatially periodic solutions of the equation for the self-consistent interaction potential with the help of Boltzmann's equilibrium distribution. Such an approach disregarding the quantum-mechanical nature of crystallization was criticized by many authors, and there is no need to do this again. It should only be noted that the conditions for the existence of spatially periodic structures obtained by Vlasov⁹ presume that attractive forces acting between particles of the system dominate over repulsive forces, which is observed for normal crystals.

Crystalline structures can also be formed in the case when neighboring particles (or quasiparticles) forming such a periodic structure repel and not attract one another. However, in this case there must be some external (relative to the given system) agencies compensating the effect of repulsive forces. The possibility of the existence of such crystal structures was illustrated by Wigner¹⁰ as early as in 1934 for the crystallization of a three-dimensional low-density electron gas in the field of a spatially homogeneous positive charge. The role of the agency compensating the action of repulsive forces is played in this case just by the field of the homogeneous positive charge. The description of phenomena associated with three-dimensional Wigner crystallization remains an important problem in spite of the fact that the conditions for experimental observation of this effect have not been created yet (see, for example, Ref. 11).

It should be noted in this connection that the conditions for the formation of spatially periodic structures in a Fermi liquid, which were analyzed by us here, also presume the

domination of attractive forces acting between quasiparticles over repulsive forces (the condition of violation of Pomeranchuk's criterion; see (6)). Since the explicit form of the Landau amplitude is not specified in our analysis, we can assume that the Landau function plays the role of effective potential of interaction between quasiparticles, which takes into account the action of attractive as well as repulsive forces without specifying their origin, but with predominant contribution of attraction. Such conditions are most likely for electron liquids in various metals. For this reason, we can expect that our results can be used in a description of three-dimensional Wigner crystallization (naturally taking into account the difference between the model of Fermi liquid used by us in order to simplify calculations and the electron liquid in real metals).

It is well known that the conditions of two-dimensional Wigner crystallization can be created quite easily for the electron gas over the surface of liquid helium.¹¹ However, the approach developed by us requires a certain modification to be applied for describing spatial lattices formed in a two-dimensional Fermi liquid, which is beyond the scope of this paper.

This research was carried out under financial support of the Ukrainian State Foundation for Fundamental Studies (Grant No. 2.4/378), as well as in collaboration with the Rostock University, Germany.

*E-mail: slusarenko@kipt.kharkov.ua,
spelet@kipt.kharkov.ua

¹We are using the system of units in which Boltzmann's constant k and Planck's constant \hbar are equal to unity.

¹L. D. Landau, Zh. Éksp. Teor. Fiz. **30**, 1058 (1956) [Sov. Phys. JETP **3**, 920 (1956)]; Zh. Éksp. Teor. Fiz. **32**, 59 (1957) [Sov. Phys. JETP **5**, 101 (1957)].

²V. P. Silin, Zh. Éksp. Teor. Fiz. **33**, 495 (1957) [Sov. Phys. JETP **6**, 387 (1957)]; Zh. Éksp. Teor. Fiz. **35**, 1243 (1958) [Sov. Phys. JETP **8**, 870 (1958)].

³I. Ya. Pomeranchuk, Zh. Éksp. Teor. Fiz. **35**, 524 (1958) [Sov. Phys. JETP **8**, 361 (1958)].

⁴Yu. V. Slyusarenko, Fiz. Nizk. Temp. **24**, 291 (1998) [Low Temp. Phys. **24**, 219 (1998)].

⁵A. I. Akhiezer and S. V. Peletminskii, *Methods of Statistical Physics* [in Russian], Nauka, Moscow (1977).

⁶D. Pines and Ph. Nozière, *The Theory of Quantum Liquids*, New York (1966).

⁷H. Stanley, *Introduction to Phase Transitions and Critical Phenomena*, Pergamon Press, Oxford (UK) (1971).

⁸A. S. Peletminskii, S. V. Peletminskii, and Yu. V. Slyusarenko, Fiz. Nizk. Temp. **25**, 211 (1999) [Low Temp. Phys. **25**, 153 (1999)].

⁹A. A. Vlasov, *Theory of Many Particles* [in Russian], Gostekhizdat, Moscow-Leningrad (1950).

¹⁰E. P. Wigner, Phys. Rev. **40**, 1002 (1934).

¹¹Yu. P. Monarkha and V. V. Shikin, Fiz. Nizk. Temp. **8**, 583 (1982) [*sic*].

Translated by R. S. Wadhwa

SUPERCONDUCTIVITY, HIGH-TEMPERATURE SUPERCONDUCTIVITY

Conductivity of normal metal with phase-coherent excitations in the presence of NS boundary

Yu. N. Chiang and O. G. Shevchenko

*B. Verkin Institute for Low Temperature Physics and Engineering, National Academy of Sciences of the Ukraine, 310164 Kharkov, Ukraine**

(Submitted April 22, 1998; revised November 12, 1998)

Fiz. Nizk. Temp. **25**, 432–448 (May 1999)

Resistive properties of 3D systems formed by a normal metal and type I superconductor (Cu–Sn) with a large electron mean free path in the normal metal are investigated in the liquid-helium temperature region. A number of new types of temperature behavior of the normal metal conductivity is revealed at temperatures below the superconducting transition temperature of the superconductor in contact with the normal metal for distances commensurate with a typical mesoscopic scale of electron transport trajectories in the normal metal, in which the phase memory of wave functions is retained. © 1999 American Institute of Physics.

[S1063-777X(99)00305-9]

1. INTRODUCTION

The resistance of a metal is a parameter reflecting the averaging of conduction electron scattering over the distributions of scatterers within a chosen spatial scale, e.g., between measuring probes or in the entire sample in the case of contactless methods of measurements. At low temperatures, the scale within which the coherence of electron wave functions is preserved in metals with predominantly elastic scatterers plays a special role, leading to quantum-interference effects (QIE) in conductivity. Its characteristic length is the inelastic electron mean free path $l_{N,inel}$ (phase-break length for wave functions) associated with inelastic processes in electron-phonon scattering or with attenuation due to Fermi-liquid effects. The quantity $l_{N,inel}$ and another characteristic length, viz., elastic (ballistic) mean free path $l_{N,el}$, can attain macroscopic values in a pure metal at low temperatures, which makes it possible to install measuring probes for experimental investigation of the contribution of quantum-interference effects to the conductivity of a metal within these lengths.

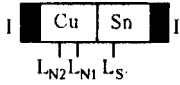
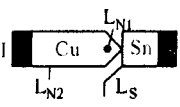
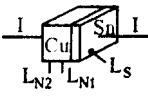
Till now, “macroscopic” experiments have not been carried out in this field. Quantum-interference phenomena were studied on samples with a size of the order of 1 μm . Samples of this size and the effects observed in them are referred to as mesoscopic according to the classification based on the ratio $\Delta\varepsilon/k_B T$ ($\Delta\varepsilon$ is the separation between energy levels and k_B Boltzmann’s constant). The size of a system is regarded as mesoscopic if the value of the ratio for it is of the order of unity or slightly smaller (the system is microscopic if $\Delta\varepsilon/k_B T \gg 1$ and macroscopic if $\Delta\varepsilon/k_B T \ll 1$). Since the mean free paths, and hence the phase coherence lengths in metals can attain macroscopic values, the entire class of possible quantum-interference effects in zero and nonzero magnetic field cannot be studied on samples of a mesoscopic size. This especially applies to the ballistic

scale which is very small ($\sim l_{N,el} \sim 10^{-2} \mu\text{m}$) as a rule for such samples in view of specific methods of their preparation.

In our samples with macroscopically long mean free paths $l_{N,el} \sim 10\text{--}100 \mu\text{m}$ and sizes L satisfying the criterion of 3D systems ($L \gg l_{N,el}$), almost entire characteristic region in which quantum-interference phenomena are manifested was accessible for experimental investigations since the size of this region was large enough for installation of measuring probes at distances of the order of inelastic as well as ballistic mean free paths from one to another. The samples were singly connected. The existence of phase-coherent excitations (electrons and “Andreev’s holes”) in zero magnetic field was ensured by the presence of the NS boundary, viz., the junction of a normal metal (copper) with a superconductor (tin). The formation and scattering properties of the junction were controlled by temperature variation near the superconducting transition temperature in tin.

In the presence of the NS boundary, new anomalies in the temperature dependence of the resistivity of the normal metal in the QIE mode with the help of precision measurements were registered. A peculiar mesoscopic effect was observed in the conductivity of the region of the normal metal in the immediate vicinity of the NS boundary when the separation between measuring probes in copper and their separation from the interface with the superconductor were comparable with the ballistic mean free path: after the transition of tin to the superconducting state, the resistance of such a layer of ballistic thickness increased abruptly (up to 60%) upon cooling, while the resistance of copper decreased as usual when tin was in the normal state. The quantum-interference nature of this effect follows from the restoration of the classical temperature dependence of resistance when the measuring probes were removed from the NS boundary to

TABLE I. Schematic diagram of samples and arrangement of experimental probes relative to the NS boundaries.

Sample No.	Sample configuration	NS-junction area, μm^2	Separation of N-probes from the boundary μm		Separation of S-bands from the boundary $L_S, \mu\text{m}$
			L_{N1}	L_{N2}	
Sp 1		200×200	13	45	31
Sp 2//.....	150×1500	36	414	375
Sp 3		10×10	20	2600	<10
Sp 4		1000×2500	70	100	<5;20

the bulk of the normal metal over distances exceeding the inelastic mean free path.

If the probes are mounted in the normal metal at macroscopic distances from the NS boundary, which are smaller than the inelastic mean free path, but much larger than the ballistic length, another effect of quantum interference origin, i.e., a strong decrease in resistance with temperature, was observed. The change in the resistance in the same temperature range was an order of magnitude stronger than the classical change measured by probes separated by distances exceeding the inelastic mean free path.

In a series of experiments, measuring probes were installed on different sides of the contact in the geometry normally used for studying the conductivity of NS systems. In this case, the contribution of mesoscopic effects to the conductivity of normal regions is difficult to observe against the background of accompanying effects including primarily the excess boundary resistance (BR), especially near T_c where the BR has the maximum value. A method of estimating of accompanying effects was proposed in order to analyze the contribution of mesoscopic effects in the normal region for such an arrangement of probes.

Special measurements with probes located in the superconductor at distances from the NS boundary of the order of the elastic mean free path did not reveal any resistive contribution of the superconductor to the excess resistance of NS systems with a developed area of the NS junction, indicating the affiliation of the origin of excess resistance to the NS boundary itself.

2. SAMPLES AND EXPERIMENTAL TECHNIQUE

The basis of the bimetallic NS systems under investigation was a copper single crystal with a “macroscopically” large elastic mean free path $l_{N,el}$. The single crystal was in contact with a type I superconductor (tin). Tunnel properties were not manifested in view of the large area of the junction.

Copper and tin used as initial materials were characterized by $RRR=300$ ($l_{N,el}\approx 10-20\ \mu\text{m}$) and 10^3 ($l_{S,el}\approx 100\ \mu\text{m}$) respectively. Bimetallic samples were obtained by spreading molten tin over a face of monocrystalline cop-

per. The size and configuration of NS samples are given in Table I (shaded regions highlight the equality of cross sections of samples and current leads for all samples except Sp4). Table I gives two values of L_S for sample Sp4. The first value corresponds to the case when the thickness of the superconductor layer $t_{Sn}<\xi_{Cu}$ ($T<0.9T_c$), while the second value corresponds to the case when $t_{Sn}>\xi_{Cu}$ (ξ_{Cu} is the coherence length in the normal metal). Measuring probes were fixed to the samples by a fusible superconducting solder with $T_c\gg 4.2\ \text{K}$. The transverse size of contact areas of probes was 20–30 μm (the distances given in Table I are measured from the boundaries of area elements.)

A reliable recording of mesoscopic conductivity, including the conductivity of a layer of the normal metal of thickness of the order of $l_{N,el}$ for the given geometric parameters of the samples and separations between probes, required the measurements of resistance with an accuracy to within one percent of $R_N\sim 10^{-9}\ \Omega$ (characterizing the sample with the largest area of the NS junction). For currents whose values ruled out the emergence of nonlinear effects ($\leq 1\ \text{A}$), the required accuracy in the measurements of potential difference at a level of $10^{-11}\ \text{V}$ was ensured by a superconducting modulator.¹

3. EXPERIMENT

3.1. Results of measurements with NS probes

Figure 1 shows the temperature dependences of resistance $R_{NS}(T)/R_{NS}(4.2\ \text{K})$ of samples Sp1–Sp3 (rectangles) (for Sp4, the dependences of $\delta R_{NS}(T)/R_{NS}(2\ \text{K})$) for $t_{Sn}>\xi_{Cu}$ (curve 1) and $t_{Sn}<\xi_{Cu}$ which were measured by pairs of probes embracing the NS boundaries. Triangles in Fig. 1 illustrate the temperature variation of resistance of the superconductor proper in samples Sp1–Sp3, measured by a pair of probes which are separated from the boundary by distances $L_{S1}=0-50\ \mu\text{m}$ ($\sim l_{S,el}\ll l_{S,inel}$) and L_{S2} (indicated in Table I) respectively. Circles represent the initial resistance of the normal region (copper) at the boundaries [$L_{N1}; x=0$] prior to the contact with the superconductor. All the three curves for each sample in the region below T_c are shown on the

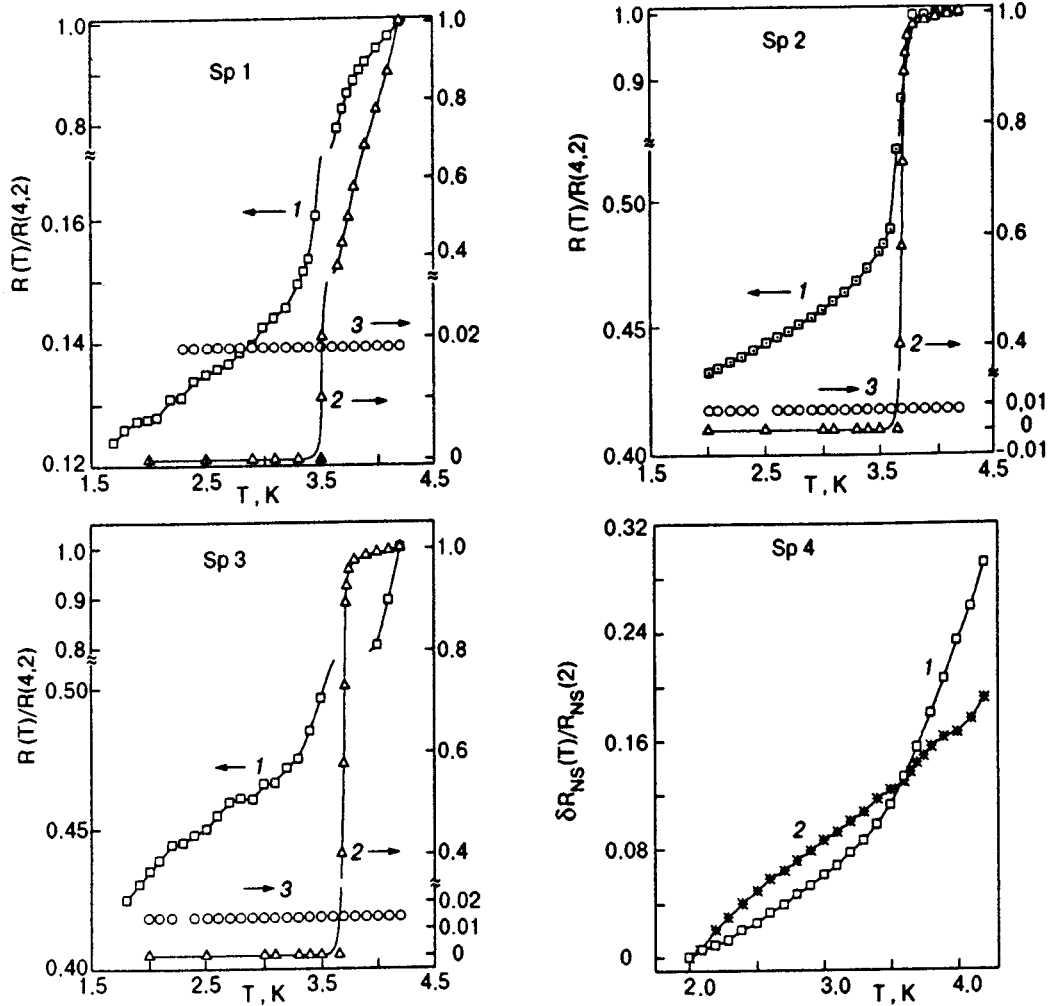


FIG. 1. Temperature dependences of the resistance of the NS system copper-tin and its individual regions normalized to the resistance of the system at 4.2 K (at 2 K for Sp4); probes $[L_{N1}; L_S]$ including the NS boundary (\square ; *); probes $[0; L_S]$ on the tin side (Δ), and probes $[L_{N1}; 0]$ in copper regions before its contact with tin (\circ). $R_{[L_{N1}; L_S]}(4.2 \text{ K}) = 8.057 \times 10^{-7} \Omega$ (Sp1), $1.546 \times 10^{-6} \Omega$ (Sp2), $3.137 \times 10^{-7} \Omega$ (Sp3), $2.44 \times 10^{-8} \Omega$ (Sp4) ($t_{Sn} > \xi_{Cu}$), $3.06 \times 10^{-8} \Omega$ (Sp4) ($t_{Sn} < \xi_{Cu}$), $R_{[L_{N1}; 0]}(4.2 \text{ K}) = 6.03 \times 10^{-9} \Omega$ (Sp1), $5.88 \times 10^{-9} \Omega$ (Sp2), and $2.063 \times 10^{-7} \Omega$ (Sp3).

same scale; it can be seen that ordinary temperature dependences of the superconductor and of the normal metal which is not in contact with the former virtually make no contribution to the $R_{NS}(T)$ dependence below T_c : $R_N(T_c) - R_N(0) \approx 10^{-2} R_N \leq 10^{-3} (R_{ONS} + R_N)$. Here R_{ONS} is the temperature-independent contact resistance, which is at least an order of magnitude higher than the resistance of normal regions for all the NS systems under investigation, including sample Sp4. The position of T_c on the temperature scale corresponded to the position of the jump in the normalized derivatives dR_{NS}/dT shown in Fig. 2.

In spite of simple method of preparing the NS junction (by spreading molten metals), there were no indications of the existence of a nonzero potential in a three-dimensional superconductor at distances from the NS boundary even of the order of the elastic mean free path.

3.2. Results of measurements with NN probes

Figure 3 shows temperature dependences of copper resistance in the NS systems with tin under investigation,

which was measured outside the NS boundary in the normal region by pairs of probes $[L_{N1}; L_{N2}]$ with L_{N1} and L_{N2} separated from the NS junction by distances of one and two orders of magnitude respectively relative to $l_{N,el}$ (see Table I), i.e., in the limits of the ballistic and inelastic mean free paths (according to estimates, $l_{N,inel} \approx 10^2 l_{N,el}$). It can be seen that the temperature below which the resistance $R_N(T)$ of the normal part of the system with such an arrangement of probes relative to the NS boundary displays a behavior differing from the known variation, correlates with the superconducting transition temperature for tin (with the position of the jump in the derivative dR_{NS}/dT in Fig. 2). Moreover, for such an arrangement of probes, $R_N(T)$ behaves in a peculiar way not observed earlier in the pure normal metal: as the temperature decreases below T_c for tin, the values of $R_N(T)$ increases abruptly in the interval $\sim 0.1T_c$ ($\sim 0.3 \text{ K}$), continuing to increase slowly or decrease depending on the value of L_{N2} upon a further decrease in temperature. It should be recalled that the temperature dependence of the resistance of copper in the absence of the NS boundary could

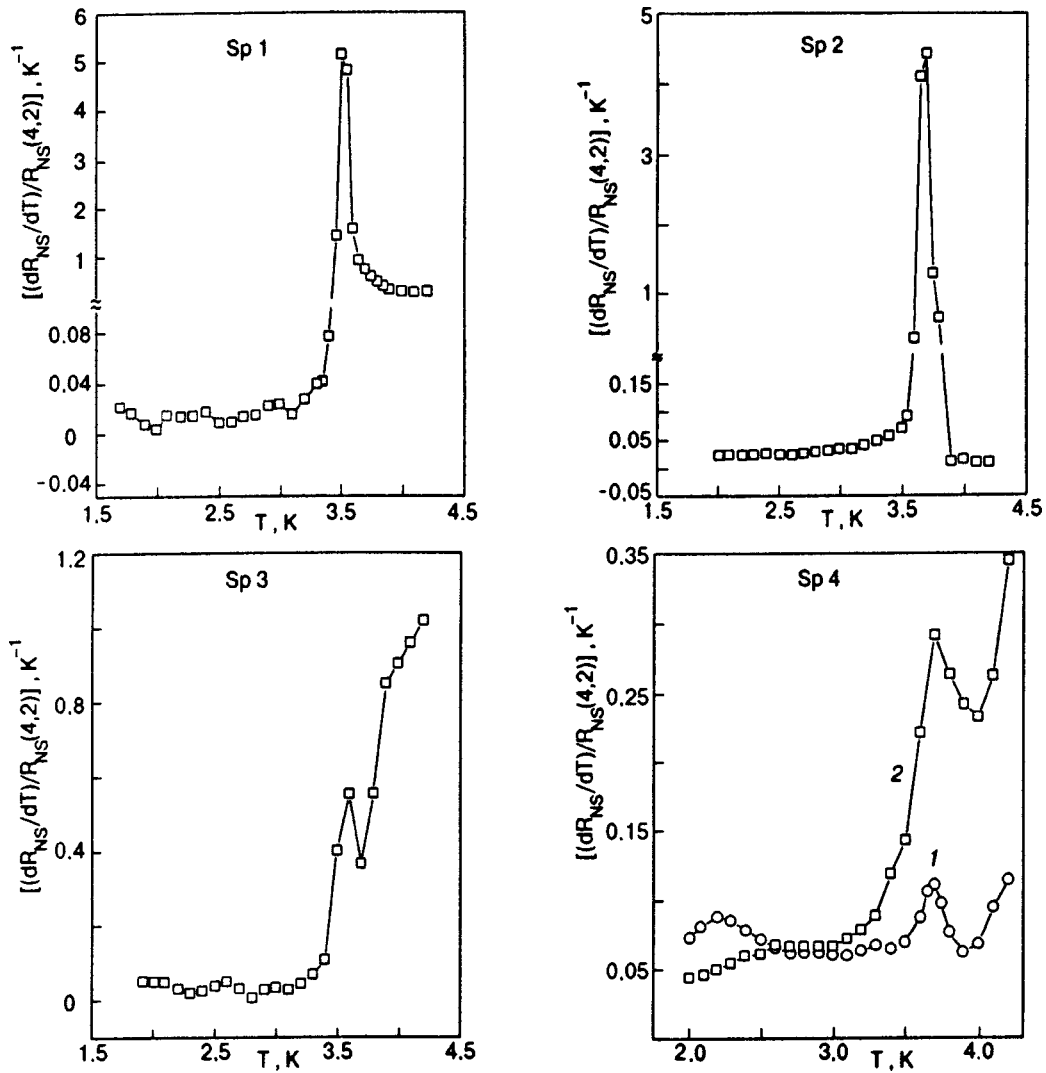


FIG. 2. Temperature dependence of the derivatives of $R_{NS}(T) \equiv R_{[L_{N1}, L_S]}(T)$ with respect to temperature for samples Sp1–Sp4.

be neglected completely on a scale comparable with observed variations (as well as in the case of *NS* probes; see Sec. 3.1).

Some experimental results were reported in Ref. 2.

4. DISCUSSION

A comparison of the temperature dependences $R_{NS}(T)$ of the resistance of *NS* systems measured with the help of *NS* probes in all samples with the form of corresponding dependences for individual parts of the system (see Sec. 3.1) undoubtedly indicates the leading role of the *NS* boundary in the formation of the temperature dependence of conductivity of bimetallic *NS* systems after a transition of one of the metals to the superconducting state. The points T_c for $R_{NS}(T)$ corresponding to the positions of jumps on the derivatives dR_{NS}/dT (see Fig. 2) are typical points at which one temperature dependence is replaced by another (this follows from the strong difference in the values of the derivatives before the jump and after it). The results obtained for sample Sp4 are most remarkable in this respect. In the case when $t_{Sn} < \xi_{Cu}$, when the proximity of the normal metal suppresses the order parameter in a thin layer of the superconductor, the values of

the derivative before and after the jump are practically identical (see curve 1 in Fig. 2), indicating the absence of a resistive transition. The curves acquire the shape typical of curves with a point of cessation only after an increase in the thickness t_{SN} of the superconducting layer in the sample Sp4 to values $\sim \xi_{Cu}$ (curve 2 in Fig. 2). For Sp1–Sp3 samples for which $t_{Sn} \gg \xi_{Cu}$, peculiarities in the temperature behavior of the resistance of the normal metal measured with *NV* probes mounted at mesoscopic distances from the *NS* boundary are observed just in the region below T_c .

The role of the *NS* boundary in the emergence of the peculiarities in question can be clarified if we take into account the fact that the *NS* boundary plays the role of a mirror reflecting multiply phase-coherent excitations (electrons and Andreev holes), thus creating the conditions for their interaction with one another and with impurities in a certain region in the normal metal near the boundary. This region can be referred to as a region of mesoscopic phenomena. Accord-

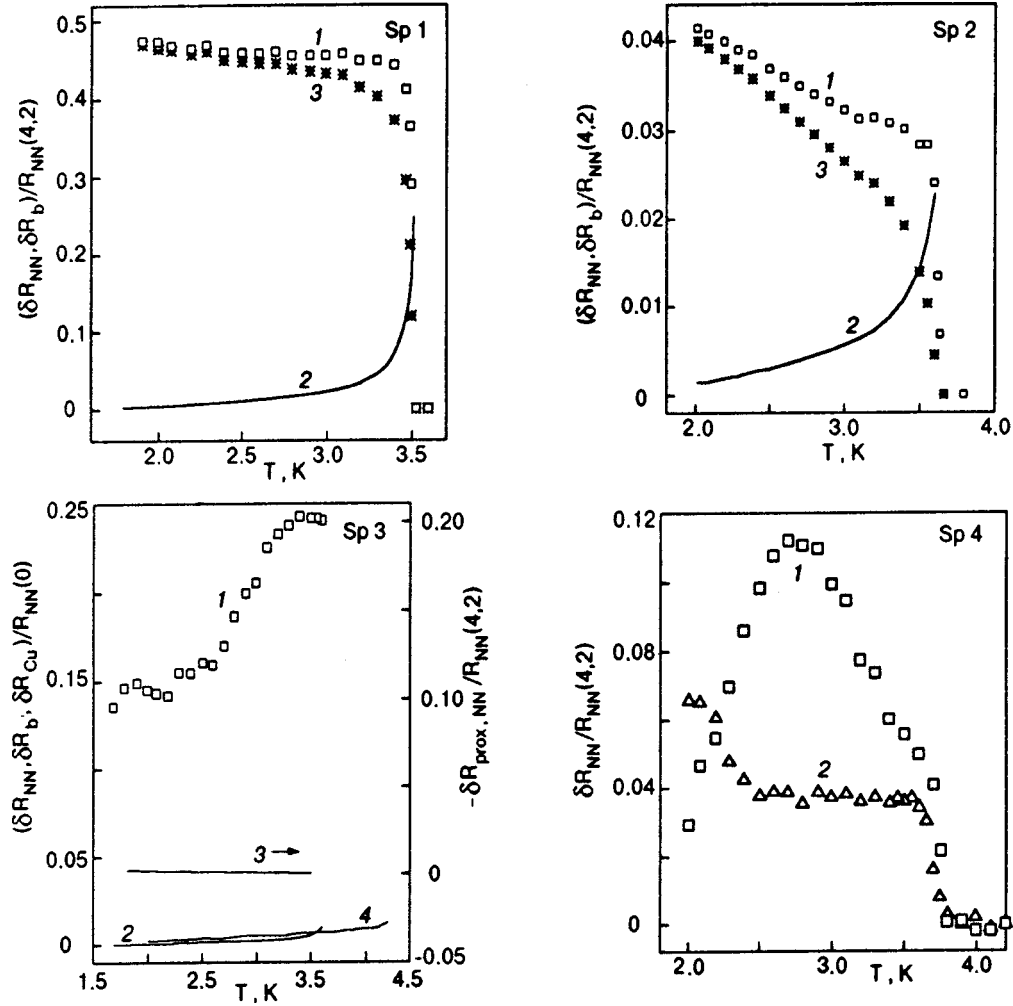


FIG. 3. Temperature dependence of the copper resistance in the copper-tin system measured with the NN probes $[L_{N1}; L_{N2}]$: \square and \triangle correspond to experimental results, curves 2 for Sp1–Sp3 describe the calculated boundary resistance, curves 3 for Sp1 and Sp2 correspond to the difference between curves 1 and 2 for Sp3 (proximity effect), and curve 4 describes copper resistance in the absence of the NS boundary. $R_{[L_{N1}; L_{N2}]}(4.2\text{ K}) = 1.59 \times 10^{-8} \Omega$ (Sp1), $9.36 \times 10^{-8} \Omega$ (Sp2), $4.421 \times 10^{-6} \Omega$ (Sp3), and $2.04 \times 10^{-9} \Omega$ (Sp4).

ing to experiments, its scale can also be macroscopic for macroscopic mean free paths. The condition $l_{N,S} \gg \xi_{N,S}$ of pure limit required for manifestation of interaction of phase-coherent excitations in conductivity ($\xi_{N,S}$ is the coherence length in the normal metal in contact with the superconductor and in the superconductor respectively) can also be realized easily for large mean free paths.

Let us write the temperature-dependent component of the resistance of the normal metal within mesoscopic distances from the NS boundary ($T < T_c$) for an arbitrary arrangement of a pair of probes relative to the boundary in the form

$$\overline{\delta R_N(T)} = \overline{\delta R_b(T)} + \overline{\delta R_N^{\text{mes}}(T)} - \overline{\delta R_N^{\text{prox}}(T)}, \quad (1)$$

where $\overline{\delta R_b(T)}$ is the contribution from the boundary resistance, $\overline{\delta R_N^{\text{mes}}(T)}$ the mesoscopic contribution to the resistance of the normal metal, associated with the presence of phase-coherent excitations near the NS boundary, and $\overline{\delta R_N^{\text{prox}}(T)}$ the contribution from the proximity effect; the bar indicated averaging. The most general considerations con-

cerning the temperature dependence of the boundary resistance (BR) and proximity effect imply that as we move from T_c towards lower temperatures, the resistance of the normal metal can only decrease due to the BR and proximity effect (excluding the singularity at the point T_c itself; see below). Consequently, the increase in $R_N(T)$ upon cooling observed by us (see Sec. 3.2) directly indicates the presence and predominant contribution of a special mechanism of variation of conductivity of the normal metal in the region of mesoscopic effects near the NS boundary. According to Eq. (1), a quantitative estimate of such a contribution ($\overline{\delta R_N^{\text{mes}}(T)}$) can be obtained by subtracting the contributions of the BR and proximity effect from the experimental results, which is especially important for the results of measurements with a pair of NS probes $[L_{N1}; L_S]$ for which $\overline{\delta R(T)} > \overline{\delta R_N^{\text{mes}}(T)}$ in the entire temperature range below T_c . Calculations show that for the results obtained with NN probes $[L_{N1}; L_{N2}]$ installed beyond the NS boundary, $\overline{\delta R_b(T)} \ll \overline{\delta R_N^{\text{mes}}(T)}$ in the most part of the same temperature region excluding a narrow region in the immediate vicinity of T_c ($\sim 0.1T_c$). The

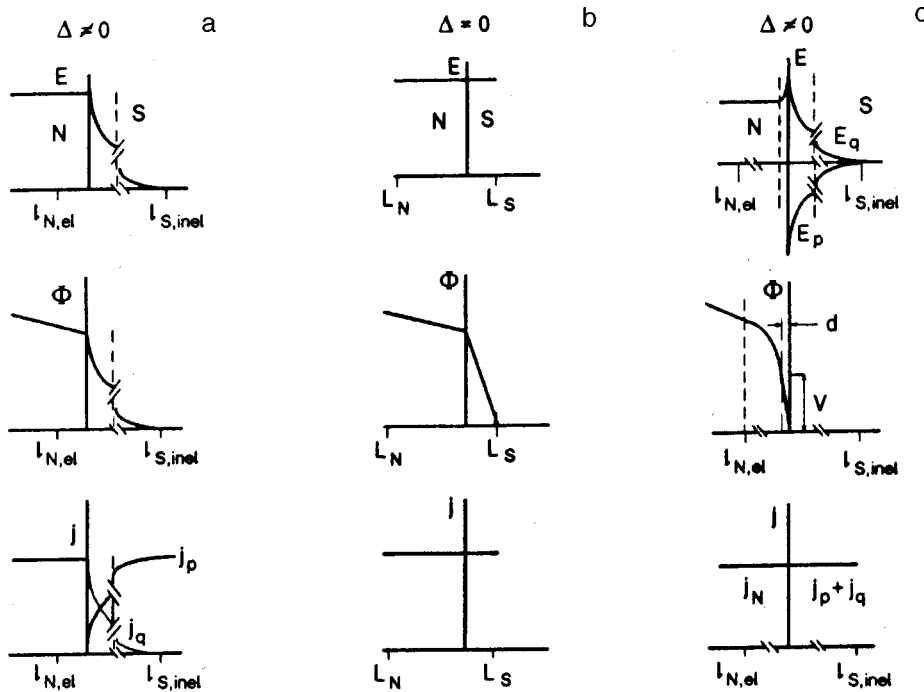


FIG. 4. Variation of the electric field E and electrochemical potential Φ in the given current mode j as a result of intersection of the NS boundary for the energy gap $\Delta=0$ (b) and $\Delta \neq 0$ (a,c) for the results obtained in Ref. 4 (a) and for our results (c).

boundary resistance and proximity effect will be calculated below for the three-dimensional NS systems under investigation.

4.1. Excess boundary resistance and proximity effect

It was noted long ago³ that the temperature behavior of the resistance of a system formed by a normal metal and a type I superconductor does not correlate with the form of temperature dependences of the resistances of the individual metals constituting the system at temperatures below the superconducting transition temperature T_c for the superconductor. In the absence of experimental data on three-dimensional samples of NS systems for which any dimension of the superconducting component is larger than the bulk mean free path typical of high-purity metals (including our samples), an opinion was subsequently formed concerning the existence of a nonzero potential attenuating exponentially towards the bulk of the superconductor in the direction perpendicular to the NS boundary even in type I superconductor under stationary nonequilibrium conditions and for a finite gap Δ . It was assumed that the effect is observed at macroscopic distances \bar{l}_S of the order of the root-mean-square elastic and inelastic mean free path in the superconductor and exceeding considerably the characteristic scale of variation of the order parameter $\xi(T)$ in the Ginzburg–Landau theory (Fig. 4a). This led to the concept of boundary resistance as the resistive contribution of the superconducting layer extended over the distance \bar{l}_S from the NS boundary in the indicated direction. Our experimental results for SS probes (curves 2 In Fig. 1) did not confirm this opinion: *no potential difference is observed in the superconductor in three-dimensional samples in a direction perpendicular to the NS boundary even at distances from the boundary of the order of the elastic mean free path.* These results are in complete accord with the remark made in Ref. 5 that the phenomenol-

ogy of superconductors must be conserved under nonequilibrium conditions also: the current in the bulk of the superconductor must be zero in the direction perpendicular to the NS boundary beyond the Meissner layer, although the total current *along* this boundary is determined by the mechanism of transformation of the normal current to supercurrent suppressing the initial current, which is manifested in the form of *boundary resistance* rather than *excess resistance on the side of the superconductor*.

Boundary resistance can be calculated by using various methods. We follow the method proposed by Blonder *et al.*⁶ and based on the thermodynamic approach in which only the jump in potential V is taken into account for a transition from the normal metal to superconductor at the boundary between them in a region of width d (Fig. 4c). Although this approach appears as speculative when applied to large-area NS junctions, its application can be justified by the ratio of V to the potential difference in the normal part, whose value was $10\text{--}10^2$ for our samples. For this reason, while estimating the BR, the distribution function $f_0(\varepsilon)$ (ε is the energy measured from the Fermi level) in the normal metal can be regarded as an equilibrium function to a high degree of accuracy. In this case, the value of BR is determined only by the probabilities of intersection of the NS boundary by excitations with different energies under nonequilibrium conditions emerging as a result of passage of current (a similar approach was used, for example, by Harding *et al.*⁷).

We shall first assume that the superconductor is in the normal state. In this case, the unified electrochemical potential of the system in thermal equilibrium does not possess a spatial gradient in view of electroneutrality and is constant over the coordinate. When an external source of electrostatic field is connected to opposite ends of the bimetallic system, so that its thermodynamic equilibrium is violated, the electrochemical potential of the system is not constant any

longer, so that the voltages measured with a pair of probes at any region of the system will be a measure of the difference between local electrochemical potentials at corresponding test points. We shall assume that fields are small enough to leave the density of states unchanged at any point including the contact region since we were dealing with exactly such fields. As one of the metals in the system goes over to the superconducting state, the gradient of electrochemical potential of this metal beyond the Meissner layer must vanish for any finite value of the order parameter in accordance with the electrostatics of type I superconductors.

It is well known that the constancy of electrochemical potential over the coordinate in a superconductor follows from the London equation⁸

$$\frac{\partial \mathbf{v}_s}{\partial t} = \frac{e}{m} \mathbf{E} - \text{grad} \left[\Psi + \frac{v_s^2}{2} \right], \quad (2)$$

where \mathbf{v}_s is the velocity of the superfluid component of current, \mathbf{E} the electric field strength, $m\Psi$ the thermodynamic potential per electron, which is a function of concentrations of the normal ($n - n_s$) and superconducting (n_s) electrons (n is the total electron concentration), momentum of the system, and temperature, t the time, and e and m electron charge and mass. According to (2), the stationary mode of current flow in the superconductor, which is determined by the constancy of electrochemical potential

$$m\Psi + \frac{1}{2}mv_s^2 + e\Phi = \text{const}(\propto n/n_s) \quad (3)$$

(Φ is the electrostatic potential), of intensity $(1/2)\nabla v_s^2$ sets in due to the mutual compensation of gradients of the concentration of the normal and superconducting electrons:

$$\nabla(n\Psi) = -\frac{1}{2}\nabla(n_s v_s^2). \quad (4)$$

The energy corresponding to these fields (zeroth approximation of the Bernoulli potential) near T_c is given by

$$e\Phi_B = -\frac{1}{2} \frac{n_s}{n} m v_s^2 \approx \frac{\Delta^2}{\varepsilon_F}$$

(ε_F is the Fermi energy).⁹⁻¹¹ This is just the quantity by which the ground-state energy of the normal metal changes upon its transition to the superconducting state:¹²

$$\varepsilon_s - \varepsilon_n = -\frac{1}{2} N_n(\varepsilon_F) \Delta^2 \approx \frac{\Delta^2}{\varepsilon_F} \quad (5)$$

(ε_n and $N_n(\varepsilon_F)$ are the energy and density of states of the metal in the normal state, and ε_s is the energy of the metal in the superconducting state.)

Thus, condition (3) in the superconductor at an arbitrary temperature must be satisfied due to the temperature variation of the level of its electrochemical potential in accordance with formula (5). It is well known that a variation of chemical potential of one of the metals in contact leads to a change in the initial level of the contact potential difference. This circumstance was noted earlier during the study of Bernoulli's effect.^{13,14} Since the field in the junction experiences a jump, the emerging correction to the contact potential difference is concentrated in the junction. In this case, we have complete analogy with the situation with a semiconductor-

metal junction, leading to the formation of a Schottky barrier. The possibility of the emergence of such a barrier in the case of a normal metal-superconductor system is ensured by the magnitude of the correction to the field corresponding to the variation of the ground-state energy (5) of the superconductor: at atomic distances, energies of the order of $\Delta^2(0)/\varepsilon_F$ correspond to the field strength of the order of tens V/cm, which is quite sufficient for the formation of a potential barrier of the Schottky type, which cannot be disregarded in large-area junctions with a low distributed resistance in spite of a comparatively low barrier height.

Thus, in addition to other barriers at the NS boundary in bimetallic NS systems with a large contact area, it is also reasonable to take into account an energy barrier of the Schottky type with the height

$$|\Delta\Phi| \delta(x) = \frac{1}{2} N_n(\varepsilon_F) \Delta^2(T), \quad (6)$$

where $\delta(x)$ is the delta-function reflecting the barrier localization at the boundary (x is the coordinate along the field).

We shall follow further the computational method developed by Blonder *et al.*⁶ and based on the probabilistic ratios for quasiparticle states in the formalism of the Bogoliubov equation and the boundary conditions of Andreev's and normal reflection at the NS boundary. For a nonequilibrium mode of current flow, the "probabilistic" current through the NS boundary must obviously meet the ordinary requirement

$$A(\varepsilon) + B(\varepsilon) + C(\varepsilon) + D(\varepsilon) = 1, \quad (7)$$

where A , B , C , and D are the probabilities of filling the corresponding branches of quasiparticle spectrum in the normal (A, B) and superconducting (C, D) half-spaces. After the mutually consistent determination of these probabilities from the conservation laws and electroneutrality condition in accordance with (7), the calculation of total current in the nonequilibrium region ($l_{N,el} + l_S$) containing the boundary becomes independent of the choice of the half-space in which it is carried out.

For example, the expression for current calculated on the side of the normal half-space within the ballistic distance from the NS junctions and depending only on the probabilities of Andreev's (A) and ordinary (B) reflection of individual quasiparticles in the absence of supercurrent can be written in the form

$$J_{NS} = 2N_n(\varepsilon_F) e v_F \int_{-\infty}^{+\infty} [f_0(\varepsilon - eV) - f_0(\varepsilon)] [1 + A(\varepsilon) - B(\varepsilon)] d\varepsilon, \quad (8)$$

where v_F is the Fermi velocity and $f_0(\varepsilon - eV)$ is the distribution function in the boundary region of the normal metal whose potential experiences a jump V (see Fig. 4c) at the NS boundary (it should be recalled that this method of calculation is valid only in the approximation $V \gg V_N$, where V_N is the potential difference in the boundary region of the normal metal). For $eV \ll k_B T$ observed in experiments with pure metals, the first factor in the integrand in (8) can be replaced by $(eV)(-df_0/\partial\varepsilon)$. The second integrand is referred to as

the ‘‘current transmission coefficient’’ K_j which, according to Blonder *et al.*,⁶ is a function of Δ , ε , and z , where z the potential barrier height in the dimensionless normalization: $z = k_F H / 2\varepsilon_F$. Here k_F is the Fermi wave vector, H the repulsive potential localized at the boundary, e.g., $|\Delta\Phi|$ from formula (6). At $T=0$, we have $|\Delta\Phi| \sim 10^{-3}$ K·cm which corresponds to $z \approx 1$ for the copper–tin pair.

The calculation of (8) leads to the following most typical results.

In the normal state of the superconductor ($T \geq T_c$), in the absence of Andreev’s reflection, $A=0$, $K_j = (1+z^2)^{-1}$ (see Ref. 6 for details), and

$$J_{NS} = J_{NN} = 2N_n(\varepsilon_F) e^2 v_F V (1+z^2)^{-1} \quad (9)$$

In the region near T_c , $T \leq T_c$ and $\Delta/k_B T \rightarrow 0$, $K_j(\varepsilon < \Delta) \rightarrow 0$, $K_j(\varepsilon > \Delta) \rightarrow (1+z^2)^{-1}$, and

$$\frac{J_{NS}}{J_{NN}} \rightarrow \int_{\Delta}^{+\infty} \left(-\frac{\partial f_0}{\partial \varepsilon} \right) K_j d\varepsilon = \frac{1}{2},$$

i.e., for a transition to temperatures below T_c , the boundary resistance $R_b = V/I_{NS}$ ($I_{NS} = J_{NS}S$, where S is the cross-sectional area of the boundary) increases jumpwise by a factor of two.

At low temperatures, in the limit $k_B T / \Delta \rightarrow 0$ and $z \gg 1$, $K_j(\varepsilon > \Delta) \rightarrow 0$, $K_j(\varepsilon < \Delta) \rightarrow z^{-2} [1 + (\varepsilon/\Delta)^2]$ and

$$\frac{J_{NS}}{J_{NN}} = \int_{-\infty}^{\Delta} \left(-\frac{\partial f_0}{\partial \varepsilon} \right) K_j d\varepsilon \approx \frac{e^{\Delta/k_B T}}{1 + e^{\Delta/k_B T}} + \left(\frac{k_B T}{\Delta} \right)^2. \quad (10)$$

The boundary resistance decreases upon cooling to its value in the normal state of the superconductor.

The limit of applicability of approximation (8) for samples with a large area of the NS junction follows directly from (9). For $z=0$, formula (9) can be reduced to the expression $I_{NS} = J_{NS}S \equiv V/R_b$ which leads to the existence (even in the absence of a barrier) of a certain finite boundary resistance R_b with voltage V across it, which is higher than the potential difference in the boundary layer of the normal metal. Since the current I_{NS} increases with the contact area, the value of R_b is obviously limited by the value of resistance R_{N0} of the layer of the normal metal: $R_b^* = R_{N0} [1 + R_b/R_{N0}]$, which leads to the condition restricting current to the preset level I_0 :

$$\frac{1}{I_b^*} = \frac{1}{I_0} + \frac{1}{I_{NS}}. \quad (11)$$

The physical meaning of expression (8) in contrast to that of the boundary resistance in other theories is that it associates the excess resistance of the region of an NS system with a boundary mainly with the type of conductivity of the boundary itself. It should be recalled that the initial assumption of the computational model used by us is the assumption on complete compensation of the field $E_q = |2eN_s^N(\varepsilon_F)|^{-1} \nabla a$, transported to the superconductor by excitations with energy $\varepsilon > \Delta$ and the total nonequilibrium charge q by the gradient of the chemical potential of superconducting electrons $E_p = -(1/e) \nabla \mu_S$ beyond the Meissner layer in the direction normal to the NS boundary. In other words, although the BR can be evaluated numerically as the

contribution of nonequilibrium region of the superconductor, the results of our experiments proved that the real change in the potential along x corresponding to the boundary resistance can be fixed only in the normal half-space at distances of the order of elastic mean free paths (nonequilibrium region on the ballistic scale), i.e., incommensurately smaller than the predicted size of the region of nonequilibrium charge in the superconductor (Fig. 4c).

The contribution of the NS boundary to limitation of current in the system can be regarded as a result of reflection of a certain electron flow from the boundary to the bulk of the normal metal in the direction opposite to that of the initial current. Consequently, we can expect that this contribution is also reflected in the resistance of the normal metal at distances L_N from the boundary with a weight $\exp(-L_N/l_{N,el})$ (L_N is the distance between the NS boundary and the corresponding measuring probe).

Formally, the decrease in current in the presence of the NS boundary can be presented in the form

$$I_b^* = I_0 - I_{0,ref}, \quad (12)$$

where $I_{0,ref}$ is the flux of particles reflected from the boundary in the immediate vicinity from it (for $x=0$), which can be determined from condition (11).

Taking into account the exponential nature of attenuation of the current $I_{0,ref}(T)$ with increasing distance from the boundary, we can write the following expression for the region of normal half-space with the coordinate x along the current:

$$I_{ref}(T, x) = \alpha(x) I_{0,ref}(T);$$

$$\alpha(x) = 1 - \exp\left(-\frac{I_{N,el}}{x}\right).$$

As a result, the local value of current in the normal half-space in the region of a probe located at the distance x from the boundary decreases to

$$I_b^*(T, x) = I_0 - \alpha(x) I_{0,ref}(T),$$

which corresponds to an increase in the resistance of the normal metal in this region.

In actual practice, the effective (averaged) resistance \bar{R} is measured. In the region confined between a pair of probes, its value exceeds the initial value R_0 by a factor of

$$\begin{aligned} \frac{\bar{R}}{R_0} &\approx \frac{I_0}{I_b(T, x)} = I_0(x_i - x_k) \left[\int_0^{x_i} I_b^*(T, x) dx \right. \\ &\quad \left. - \int_0^{x_k} I_b^*(T, x) dx \right]^{-1} = \left\{ 1 - \frac{I_{0,ref}}{I_0} \left[1 - (x_i \right. \right. \\ &\quad \left. \left. - x_k)^{-1} \int_{x_k}^{x_i} \exp\left(-\frac{l_{N,el}}{x}\right) dx \right] \right\}^{-1} \end{aligned} \quad (13)$$

(i and k correspond to different probes in the pair). For a pair of probes with $x_i, x_k > 0$, $R_0 = R_N(T_c)$, while for a pair with $x_i > 0$, $x_k < 0$ we have $R_0 = R_{NS}(T_c) - R_S^N = R_{ONS} + R_N(T_c)$, where R_{NS} is the resistance of the bimetallic system between the probes embracing the boundary, R_S^N the value of the re-

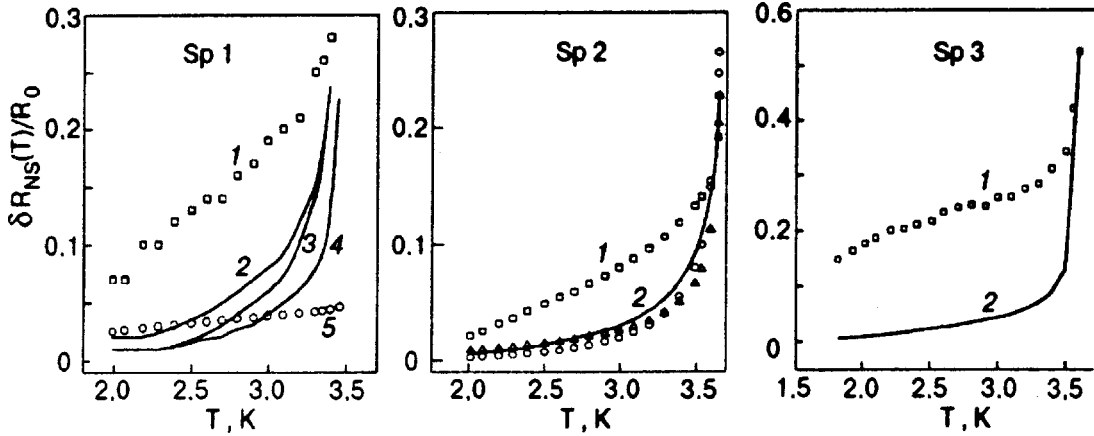


FIG. 5. Temperature dependences of the resistances of Cu-Sn systems in the temperature range $T < T_c$ for probes $[L_{N1}; L_S]$: experiment (curve 1, boundary resistance calculated for $z(T) \neq 0$ (curve 2), curve 3 (for Sp1) and Δ (for Sp2) is the same with $z=0$, curve 4 (for Sp1) and \circ (for Sp2) is the boundary resistance calculated according to the theories,^{4,5} and curve 5 describes the proximity effect.

sistance of the superconductor immediately before the transition to the superconducting state, R_N the resistance of the normal region between the probes outside the boundary, and R_{0NS} the residual resistance of a narrow contact region formed during the preparation of the bimetallic sample. The condition $R_{0NS} \gg R_N(0)$ was satisfied for all the samples investigated by us. As in the model of a “small-area channel,” R_{0NS} is just the maximum resistance in the system at $T < T_c$ at which almost the entire voltage V applied to the bimetallic sample and undergoing a jump as we go over to the superconducting half-space is concentrated (Fig. 4c). We shall assume that the effect of barriers at the boundary is completely taken into account in the parameter z^2 so that the transmission coefficient for this layer is taken equal to unity.

Expression (13) implies that the correction to the boundary resistance in the normal state of the superconductor has the maximum value for $T \rightarrow T_c$ when only the normal reflection takes place ($I_{0,ref} \rightarrow I_0$) and tends to zero in the case of total Andreev’s reflection ($I_{0,ref} \rightarrow 0$). The arrangement of probes relative to the boundary and one another is taken into account by the expression in the second brackets in (13).

It can easily be verified that the contribution of the NS boundary to the resistance of the system considered above must be noticeable if at least one of the probes is separated from the boundary by a distance of the order of a few mean free paths. For large values of $l_{N,el}$, this distance becomes macroscopically large, the magnitude of the effect increasing in the presence of additional barriers at the boundary.

Along with the change in the resistance of the normal half-space considered above, strictly speaking, we must take into account a slight decrease in the same resistance upon cooling below T_c due to the “expansion” of the NS boundary associated with the proximity effect, especially in the case when a pair of probes embraces the NS boundary, and the normal probe is separated from it by a distance commensurate with the coherence length ξ_N . Estimating the current in the perturbed layer of the normal metal on the basis of the microscopic theory of the effect,¹² we find that this contribution to the resistance of the normal half-space below T_c for the superconductor must be of the order of

$$\begin{aligned} \overline{|\delta R_N^{\text{prox}}(T, x_N)|} = R_N \frac{1 - \exp(-\Delta/k_B T)}{1 + \exp(-\Delta/k_B T)} \frac{\xi_N(T)}{\xi_S(T) + \xi_N(T)} \\ \times \frac{1}{x_N} \int_0^{x_N} \exp[-x/\xi_N(T)] dx. \end{aligned} \quad (14)$$

The first two fractional factors are associated with the temperature variation of the order parameter in the normal half-space in the diffusion region of Cooper pairs, while the third factor is the result of averaging of the spatial distribution of the order parameter in this region. If we take into account the fact that the region of Andreev’s transformation (physical NS boundary) is a region of the size $\xi_N(T) + \xi_S(T)$, the inclusion of the proximity effect in the form (14) indicates that the displacement of the boundary between the purely normal region and the “NS region,” i.e., the change in the size of the normal region confined between the N-probe and the normal region boundary, is taken into account.

Attempts made to describe the temperature dependences $R_{NS}(T)$ of the samples under investigation using the conclusions of the theory of boundary resistance revealed noticeable systematic discrepancy between the experimental and theoretical data for BR. This follows from a comparison of curves 1 and 2 in Fig. 5, where the regions of curves 1 from Fig. 1 in the temperature range below T_c are shown on a magnified scale for each of the samples Sp1–Sp3. The discrepancy persists for any theory used for the boundary resistance. Curves 2 in Fig. 5 are calculated in accordance with formula (13) taking into account the temperature-dependent contribution of the NS Schottky barrier $z(T)$. Besides, the results of calculations of the boundary resistance for samples Sp1 and Sp2 disregarding this contribution are also presented (curve 3 for Sp1 and triangles for Sp2) as well as the results of calculation of the same quantity on the basis of the Artemenko–Volkov–Zaitsev–Hsiang–Clarke theory^{4,5} (curve 4 for Sp1 and circles for Sp2) and the contribution of the proximity effect in the normal region of sample Sp1 calculated by formula (14) (curve 5, circles).

The coefficients for calculating the BR curves were determined by the universal method from the normalization to

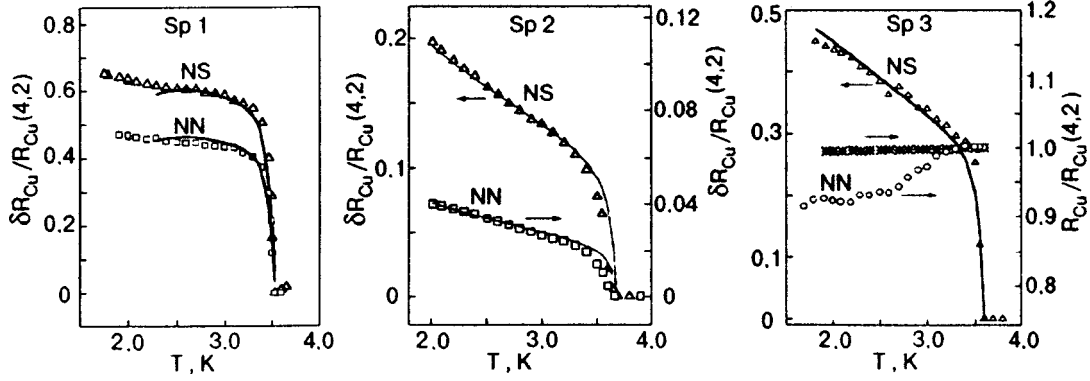


FIG. 6. Temperature dependence of the correction of the resistance of the normal metal (Cu) corresponding to the mesoscopic effect associated with the difference in the efficiencies of scattering of normal electrons and holes undergoing Andreev's reflection at impurities located within the ballistic mean free path from the NS boundary: NS curves are calculated on the basis of experimental data for NS probes [$L_{N1}; L_S$], NN curves are calculated for Sp1 and Sp2 on the basis of data obtained by using NN probes [$L_{N1}; L_{N2}$] (the same as curves 3 for Sp1 and Sp2 in Fig. 3. Solid curves correspond to the theory (formula (17)), and* mark the temperature dependence of the resistance of the copper single crystal used in the samples.

the value $\delta\bar{R}_b(T_c)$ calculated from the condition $\delta\bar{R}_b(T_c)I_0 = R_S^N I_0$ of continuity of the potential at the boundary at $T = T_c$.

A comparison of experimental and theoretical curves for probes embracing the NS boundary (Fig. 5) leads to the conclusion that the inclusion of the well-known effects changing the conduction of the NS system, such as the boundary resistance (irrespective of the method of its estimation) and the proximity effect is insufficient for describing the actual temperature behavior of the resistance of three-dimensional NS systems with long mean free paths below T_c , indicating the presence of additional mechanisms of conductivity associated with the NS boundary in such systems. Figure 5 shows that the contributions of the BR and proximity effect are small over a considerably large temperature region for the geometry of the arrangement of probes under consideration. The absolute value of the above-mentioned contributions for NN probes in the same temperature region is still smaller (see curves 2 (BR) for Sp1–Sp3 and curve 3 (proximity effect) for Sp3 in Fig. 3). Thus, we have all grounds to assume that the temperature region far away from T_c is the region of manifestation of mesoscopic effects analyzed below. However, it is just the jump in the boundary resistance near T_c that explains the astonishingly sharp increase in the resistance of the normal metal measured with NN probes after the transition of the metal in contact to the superconducting state.

4.2. Conductivity in the presence of phase-coherent excitations

The hypothesis resulting from the data obtained with probes embracing the NS boundary were confirmed in experiments on the resistance of the normal metal with the probes [$L_{N1}; L_{N2}$] installed only in the normal region at mesoscopic distances from the NS boundary.

4.2.1. Ballistic scale

Curves 3 in Fig. 3 show the results of subtraction of the boundary resistance (curves 2) from the experimental data (curve 1) normalized from the values of the resistance mea-

sured by the same pair of probes at $T > T_c$ for samples Sp1 and Sp2 in units of $\delta R_{NN}(T)$. Temperature dependences of BR (curves 2) were calculated by formula (13). The contribution of the proximity effect for the investigated values of L_{N2} for all the samples does not exceed its contribution for sample Sp3 shown in the same figure (curve 3). It can be seen that the theoretical curves (*) for samples Sp1 and Sp2 are similar to the experimental curves 1 except in the narrow temperature region near T_c . A distinguishing feature of these samples is that the values of L_{N1} for them is of the order of (for Sp2) or even smaller than (for Sp1) the ballistic (elastic) mean free path, while the values of L_{N2} remain much smaller than the inelastic mean free path.

The results of measurements with the probes [$L_{N1}; L_{N2}$] for sample Sp4 are presented in the form in which they were obtained (without subtracting BR).

Curves NS in Fig. 6 show the results of the same operation of subtraction for the results of measurements with the probes [$L_{N1}; L_S$] for samples Sp1–Sp3, while NN curves correspond to measurements with the probes [$L_{N1}; L_{N2}$] (similar to curves 3 in Fig. 3 for Sp1 and Sp2). While calculating NS curves, we took into account the fact that

$$\overline{\delta R_N^{mes}(T)} \equiv \delta R_{Cu}^{L_{N1};0}(T) = \delta R^{L_{N1};L_S}(T)[1 + \gamma]^{-1}, \quad (15)$$

where $\gamma = R_{0NS}^{L_{N1};L_S}/R_{Cu}^{L_{N1};0}(T_c)$ ($\gamma_{Sp1} = 17$; $\gamma_{Sp2} = 1.1 \times 10^2$; $\gamma_{Sp3} = 41.3$).

For sample Sp3 with the largest value of L_{N2} , the contribution of the BR as well as of the proximity effect to the resistance of the region [$L_{N1}; L_{N2}$] is negligibly small (see Fig. 3).

A comparison of the data presented in Figs. 3, 5, and 6 shows that in spite of the apparent difference in the form of temperature dependences of resistance measured with the probes arranged in different ways relative to the NS boundary in a bimetallic sample, a general regularity in the behavior of the resistance of normal regions adjoining the NS boundary and having a mesoscopic size is revealed when accompanying effects are taken into account, i.e., the presence of a contribution to resistance with a temperature de-

pendence closely related to the temperature dependence of the gap in the superconductor in contact.

The existence of effects such as the increase in the resistance of a layer of the normal metal contacting the superconductor and having a thickness of the order of the thermal length $\lambda_T \approx \hbar v_F / k_B T$ or the increase in the conduction of a layer of thickness of the order of the inelastic mean free path upon cooling below T_c was predicted in Refs. 15 and 16 respectively. Among other things, it was proved in Ref. 15 and later in Ref. 17 that the mesoscopic correction $\delta R_N^{\text{mes}}(T)$ to the normal resistance (subsequently referred to as δR_N^{Andr}) leading to an increase in the metal resistance upon cooling within ballistic distances from the NS boundary can be due to the increase in the cross section of electron scattering by impurities during multiple interaction of phase-coherent electron and Andreev excitations with impurities and with the NS boundary. The calculations made in the publications mentioned above give doubled value of this cross section.

We shall use the results obtained by Kadigrobov *et al.*¹⁷ who obtained the solution of kinetic equation for the latter case in order to present the expected temperature dependence of the resistance of a layer of the metal at a mesoscopic distance from the NS boundary and to compare it with the experimentally observed dependence. According to Kadigrobov *et al.*,¹⁷ the relative increase in the resistance of a layer of thickness L_N measured from the NS boundary and having a resistance R_N prior to the formation of this boundary must be equal to

$$\frac{\delta R_N^{\text{Andr}}}{R_N} = \frac{l_{N,\text{el}}}{L_N} \{T_p\}, \quad (16)$$

where $\{T_p\}$ is the effective probability of electron scattering by a layer of thickness of the order of ‘‘coherence length’’ λ_l taking into account Andreev reflection and the conditions $\lambda_T \leq l_{N,\text{el}} < L_N$. The quantity $\{T_p\}$ can be obtained¹⁸ by integrating $T_p = \hbar v_F / \varepsilon l_{N,\text{el}}$, viz., the probability that the particle is scattered by impurity and reflected as an Andreev particle with energy ε (the energy is measured from the Fermi level), making a contribution to the resistance over the length $l_{N,\text{el}}$, in the entire energy range from the minimum energy $\varepsilon_{\text{min}} = \hbar v_F / l_{N,\text{el}}$ to the maximum energy of the order of the gap energy $\Delta(T)$:

$$\{T_p\} = \int_{\hbar v_F / l_{N,\text{el}}}^{\Delta(T)} \left(- \frac{\partial f_0}{\partial \varepsilon} \right) T_p d\varepsilon.$$

Integration to within the second approximation gives the following analytic result for the correction to the resistance of the layer under investigation as a function of temperature:

$$\begin{aligned} \frac{\delta R_N^{\text{Andr}}}{R_N} = \frac{1}{2} \frac{\lambda_T}{L_N} \left\{ 1 + \ln \frac{\Delta(T) l_{N,\text{el}}}{T \lambda_T} + \left[\frac{\tanh(\Delta(T)/2T)}{\Delta(T)/2T} \right. \right. \\ \left. \left. - \frac{\tanh(\lambda_T/2l_{N,\text{el}})}{\lambda_T/2l_{N,\text{el}}} \right] - \frac{1}{6} \left[\left(\frac{\Delta(T)}{2T} \right)^2 \right. \right. \\ \left. \left. - \left(\frac{\lambda_T}{2l_{N,\text{el}}} \right)^2 \right] \right\} = \alpha_N F(T), \quad (17) \end{aligned}$$

where $\alpha_N = L_N/2$.

For a pair of probes $[L_{N1}; L_{N2}] (L_{N1,2} > l_{N,\text{el}})$, we have

$$\begin{aligned} \frac{\delta R_{L_{N1}; L_{N2}}^{\text{Andr}}}{R_{L_{N1}; L_{N2}}} \approx \frac{F(T)}{L_{N2} - L_{N1}} \int_{L_{N1}}^{L_{N2}} \frac{dL}{L} = F(T) \frac{\ln(L_{N2}/L_{N1})}{L_{N2} - L_{N1}} \\ = \alpha_{N-N} F(T). \quad (18) \end{aligned}$$

The approximation $L_{N1,2} > l_{N,\text{el}} \geq \lambda_T$ of the theory is valid for both values of L_N for sample Sp2 and the value of L_{N1} for sample Sp3. Solid curves in Fig. 6 are calculated by formulas (17) and (18) for Sp2 with $l_{N,\text{el}} = 10 \mu\text{m}$ and (17) for Sp3 with $l_{N,\text{el}} = 20 \mu\text{m}$, while the symbols correspond to experimental data.

In the case when a probe is separated from the NS boundary by a distance smaller than the ballistic path ($L_N < l_{N,\text{el}}$), the estimates of $R_N(L_N)$, and hence of the coefficients α can only be approximate. We shall assume that $R_N(L_N) \approx (L_N/l_{N,\text{el}}) R_N(l_{N,\text{el}})$, so that $\alpha_N \approx L_N/2$ and $\alpha_{N-N} \approx (l_{N,\text{el}}/L_N) - 1$. The temperature dependences $\delta R_{L_{N1}}^{\text{Andr}}/R_{L_{N1}}$ and $\delta R_{L_{N1}; L_{N2}}^{\text{Andr}}/R_{L_{N1}; L_{N2}}$, calculated with these coefficients for sample Sp1 with $l_{N,\text{el}} = 20 \mu\text{m}$ are also shown in Fig. 6 by solid curves.

Thus, it can be seen that the theory of scattering of phase-coherent excitations at ballistic distance from the NS boundary considered above is confirmed both qualitatively and quantitatively in our experiments.

4.2.2. Phase coherence length scale

A quite different behavior of resistance is observed in the region of the normal metal of sample Sp3 bounded by the probe separated from the boundary by a distance L_{N2} of the order of $l_{N,\text{inel}} \approx 10^2 l_{N,\text{el}}$ for $L_{N2} \gg L_{N1} \approx l_{N,\text{el}}$ and for sample Sp4 whose normal region confined between L_{N1} and L_{N2} ($L_N \approx 5 l_{N,\text{el}}$) in other two measurements has the same scale $\sim l_{N,\text{inel}}$ with nonzero current components along these directions in view of the small cross section of current leads (see Table I). The results obtained for these geometrical situations indicate the emergence of another mesoscopic conductivity mechanism reducing the resistance of the normal metal on the scale of inelastic mean free path upon cooling under the condition when this mechanism obviously dominates as for Sp4 sample with probes separated by distances of the order of the ballistic mean free path (curve 1 in Fig. 3), or remains in fact the only mechanism in the case when the contribution from all other mechanisms changing the conductivity of the metal is negligibly small as in the case of sample Sp3 and its probe L_{N2} (NN curve in Fig. 6). The results obtained for the probes $[L_{N1}; L_{N2}]$ in sample Sp2, for which $\delta R_N^{\text{Andr}}/R_N$ has the lowest value (only 4%; see Fig. 6) apparently reflect the intermediate situation.

The existence of such a mesoscopic conductivity mechanism was predicted by van Wees *et al.*¹⁶ on the basis of the assumption concerning the interference of phase-coherent excitations on trajectories formed as a result of multiple coherent reflections at the NS boundary and having the relaxation (diffusion) length $\lambda_{\text{diff}} = (\hbar D / k_B T)^{1/2}$ of the order of the inelastic mean free path. It is assumed that the interaction of excitations with impurities on these trajectories is elastic without a loss in the phase memory. Van Wees *et al.*¹⁶ ob-

tained an expression for differential conductivity of the boundary region in the normal metal, from which it follows that the correction to the resistance in this mesoscopic region can be presented in the form

$$\delta R_N^{\text{mes}}(T)/R_N(T_c) \approx - \frac{\Sigma}{1 + \Sigma} \quad (19)$$

for

$$\Sigma = \sum_{m=1}^{\infty} P(m) I(m, Z(T), \Delta/k_B T), \quad (20)$$

where m is the number of reflections of phase-coherent excitations at the NS boundary, and $P(m)$ the fraction of interference trajectories with such reflections (which will be henceforth referred to as m -trajectories) reaching the boundary of the equilibrium region located within the inelastic mean free path from the NS boundary, i.e., relaxing along \mathbf{E} over a distance $\sim l_{N,\text{inel}}$:

$$P(m) = \begin{cases} 1 - T_p & (m=0) \\ T_p^2 (1 - T_p)^{m-1} & (m \neq 0) \end{cases} \quad (21)$$

Here $T_p \sim l_{N,\text{el}}/l_{N,\text{inel}}$ is the probability of traversing the distance $l_{N,\text{inel}}$ by an electron reflected from the NS boundary provided that the transverse dimension of the NS junction is not smaller than this scale, and $I[m, Z(T), (\Delta/k_B T)]$ is the quantity reflecting the temperature-dependent mean contribution to the current from a charge on the m -trajectory in the presence of a barrier of height Z at the NS boundary (this quantity has the same meaning as the integrand in (8) upon the substitution $A \rightarrow A(m)$ and $B \rightarrow B(m)$). Van Wees *et al.*¹⁶ considered the limiting case of $I(T=0)$. The form of the temperature dependence $I(T)$ is similar to that of the temperature dependence of expression (10) corresponding to $m=1$. A decrease in temperature ‘‘shifts’’ the boundary of the equilibrium region from the NS junction and increases the number of excitations undergoing Andreev reflection due to the temperature dependence of the gap. Thus, the contribution to the current from trajectories elevating the conductivity of a metal layer of the order of the inelastic (e.g., electron–phonon) mean free path increases effectively due to multiple coherent reflections of electrons at the NS boundary and interference of phase-coherent excitations on these trajectories (the weight of m -trajectories with large values of m increases: the value of P from (21) increases upon cooling at $T \sim \Delta$ and upon a decrease in T_p at the expense of the second factor).

Although the calculation by formula (19) can be carried out only by using a numerical method in the random walk model, the qualitative pattern is obvious. The contribution of the mechanism in question to the change in the conductivity must be negligibly small for measurements with the probes $L_{N,\text{ball}}$ installed at a ballistic distance from the boundary ($L_{N,\text{ball}} \sim l_{N,\text{el}} \ll l_{N,\text{inel}}$) (contribution (19) decreases by a factor of $l_{N,\text{inel}}/L_{N,\text{ball}}$) as compared to contribution (16). This situation corresponds to the conditions of measurements with all combinations of pairs of probes in samples Sp1 and Sp2 (see Table I and NN and NS curves in Fig. 6, although one of the transverse dimensions of sample Sp2 is commensurate

with $l_{N,\text{inel}}$, but in a direction orthogonal to \mathbf{E}) and in sample Sp3 with a pair of probes $[L_{N1}; L_{N2}]$ (NS curve in Fig. 6). For $L_N \sim l_{N,\text{inel}}$, when, conversely, the contribution (16) is negligibly small, the correction to the resistance of a layer of metal of the order of $l_{N,\text{inel}}$ must behave in accordance with (19). In particular, since $T_p \sim l_{N,\text{el}}/l_{N,\text{inel}} \ll 1$, $P(T) \propto T_p^2 \propto T^6$ in the temperature range $\sim (0.8T_c - T_c)$ in which the probability of Andreev reflection is small, and the maximum contribution to current comes from trajectories with small values of m , while the value of $I[m, Z(T), (\Delta/k_B T)]$ increases exponentially upon cooling (see formula (10)). In this connection, we could expect that both dependences $P(T)$ and $I(T)$ compensate each other significantly in this temperature range. At lower temperatures, when $I[m, Z(T), (\Delta/k_B T)]$ attains saturation and the contribution from m -trajectories with large m increases, the temperature dependence $\delta R_N^{\text{mes}}(T) \approx -\Sigma(T) + \Sigma^2(T)$ is mainly determined by the temperature dependence $P(T) \propto (1 - T_p)^{m-1}$, which corresponds to a decrease in $\delta R_N^{\text{mes}}(T)$ upon cooling for $\Sigma(T) < 1$. This situation is observed most clearly in the results obtained for the probes $[L_{N1}; L_{N2}]$ in sample Sp4 with a large area of the NS junction and nonzero components of the field \mathbf{E} along all three dimensions of the normal region due to incommensurate areas of current leads and sample cross section (see the configuration in Table I). Since the value of \bar{L}_N in this sample along E_x is of the order of $l_{N,\text{el}}$, both effects ((16) and (19)) should generally be added in this situation. Then we obtain the following temperature dependence of the correction to resistance at temperatures $\sim (0.7-0.8)T_c$ and below:

$$\frac{\delta R_N(T)}{R_N(T_c)} \approx \begin{cases} \lambda_T / \bar{L}_N, & 0.8T_c < T < T_c \\ (\lambda_T / \bar{L}_N) - \Sigma(T) + \Sigma^2(T) = K_1 T^{-1} \\ \quad - K_2 (1 - DT^3)^{m-1} + K_2^2 (1 - DT^3)^{2(m-1)}, & \\ T < 0.7T_c \end{cases} \quad (22)$$

(K_1 is a constant), which satisfactorily corresponds to the results obtained for sample Sp4 (curve I in Fig. 3) with a peak near $(0.7-0.8)T_c$, $m=100$, and $K_2 \approx 2$.

A somewhat different behavior which can also be easily explained is observed for a pair of probes $[L_{N1}; L_{N2}]$ in sample Sp3. The characteristic size r of contact cross section in sample Sp3 is commensurate with $l_{N,\text{el}}$ so that the probability of passage of m -trajectories to the equilibrium region along \mathbf{E} should be reduced to a value of the order of $T_p(1 - l_{N,\text{el}}/r)$ under the assumption of diffusive scattering at the lateral faces in the normal region near the contact (the configuration of sample Sp3 (see Table I) ensured the fulfillment of the condition $r \gg l_{N,\text{el}}$ at distances from the contact exceeding $l_{N,\text{el}}$). This noticeably suppresses the temperature dependence $\Sigma(T)$ in the region below $0.8T_c$ without affecting, however, the general tendency in the behavior of the effect following from formula (22), which is probably manifested in the sample under investigation (curve NN in Fig. 6).

Nature of anomalous behavior of the surface resistance of $\text{YBa}_2\text{Cu}_3\text{O}_{7-\delta}$ films in a microwave field

V. G. Prokhorov and G. G. Kaminsky

*Institute for Metal Physics, National Academy of Sciences of the Ukraine, 252142 Kiev, Ukraine**

Yong Pak Lee

*Sunmoon University, 100 Galsan-Ri, Tangjeong-Myeon Asan, Chongnam, Korea**

(Submitted September 25, 1998; revised November 24, 1998)

Fiz. Nizk. Temp. **25**, 449–454 (May 1999)

The temperature dependence of the surface resistance of overdoped YBCO films is studied experimentally. It is shown that the observed unusual behavior of the surface resistance can be described within the framework of spin-flip scattering of carriers, which leads to pair-breaking and the emergence of the gapless state. © 1999 American Institute of Physics. [S1063-777X(99)00405-3]

The interest towards the investigation of physical properties of HTSC films in a microwave field is associated with the possibility of their potential application in radioelectronic devices. Above all, this concerns the development of passive elements in mobile, cellular, and satellite communication. A high value of the residual resistance at low temperatures and a strong field dependence of the impedance even for relatively low values of the incident radiation intensity are the main factors obstructing immediate practical application of these elements.

In spite of the fact that a large number of works have been devoted to the study of microwave losses in HTSC compounds, the physical nature of this phenomenon continues to defy a complete understanding. Among the approaches used for describing the unusual behavior of the surface impedance $Z(H, T, \omega)$, the following two are the most widespread. The first one is based on the concepts about the $d_{x^2-y^2}$ symmetry of the superconducting order parameter.^{1–3} In the second case, the HTSC materials are treated as spatially nonhomogeneous superconductors with weak links between crystallites^{4–6} or with a nonsuperconducting thin layer at their surface.⁷

However, a strong effect of the oxygen concentration on the form of temperature dependence of the surface resistance $R_s(T)$ was observed in many experiments.^{6,8} In this case, the mechanism of microwave losses cannot be explained in the framework of the weak-link model, or d-wave pairing. The perfection of crystal structure of HTSC compounds is determined by the mechanisms of nucleation and growth, while the type of symmetry of the order parameter must remain unchanged over the entire concentration range of the superconducting state.

In the present work, we describe the results of experimental measurements of the temperature dependence of surface resistance for $\text{YBa}_2\text{Cu}_3\text{O}_{7-\delta}$ films obtained by magnetron sputtering technique in an atmosphere of pure oxygen. The $R_s(T)$ dependence displays a number of peculiarities which cannot be explained correctly by any of the existing

theoretical models. A new concept for the emergence of microwave losses in HTSC compounds based on breaking of superconducting electron pairs as a result of spin-flip scattering at magnetic impurities is proposed.⁹

2. EXPERIMENTAL RESULTS

We used the dc magnetron sputtering technique to obtain $\text{YBa}_2\text{Cu}_3\text{O}_{7-\delta}$ films in an elevated pressure of the working gas in the chamber. This was done in order to reduce the effect of bombardment of the substrate by negative oxygen ions and to avoid backsputtering of the growing film layers.

The sputtering device was based on the commercial complex VUP-5M. Pressed ceramic disks of diameter 58 mm and thickness 5 mm made of $\text{YBa}_2\text{Cu}_3\text{O}_{7-\delta}$ of stoichiometric composition were used as targets. For a better thermal contact with cooled cathode, the target was soldered to the cathode by using Wood's alloy. Standard magnetrons comprising the device VUP-5M were used for sputtering. Sputtering of films was carried out under a pressure of 2–3 Torr, a cathode voltage 300–350 V, and in a plasma current of about 20 mA. The separation between the target and the substrate was 8–10 mm. The substrate temperature during film deposition was 720–750 °C. The substrate was made of monocrystalline SrTiO_3 with a working surface (100). The average deposition rate was 0.1–0.5 nm/min. Unlike the case of magnetron sputtering of HTSC films, where a mixture of argon and oxygen was used as the working gas, we used pure oxygen for film deposition. The investigated films had a thickness of 100–120 nm.

X-ray diffraction studies revealed that all the obtained films had an excess oxygen concentration $\delta \approx 0.04$ –0.05.

The superconducting transition temperature of the obtained samples was $T_c \approx 91$ K, the transition width $\Delta T_c = 1$ –2 K, and the room-temperature resistivity $\rho_{300} = 200$ –250 $\mu\Omega \cdot \text{cm}$ (in the best samples).

The surface resistance of the obtained films was measured by using the resonance technique with H_{011} mode. In this method, film samples of diameter 8–10 mm replaced

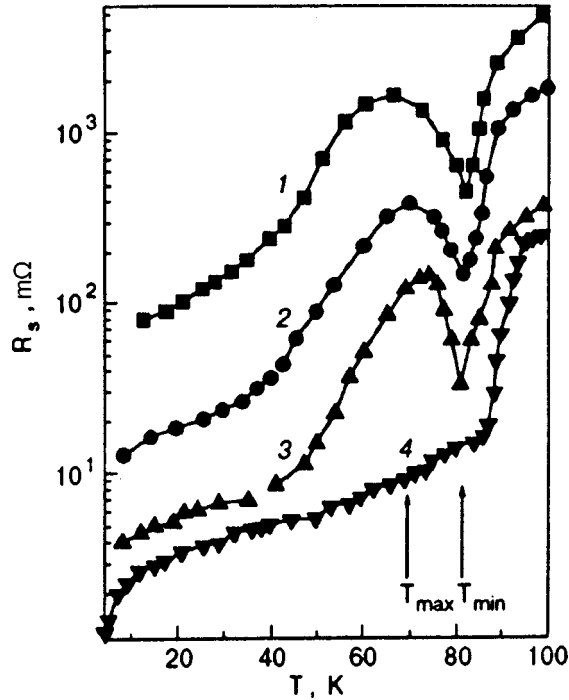


FIG. 1. Temperature dependences of the surface resistance for three $\text{YBa}_2\text{Cu}_3\text{O}_{7-\delta}$ films with different residual resistivities ρ_0 , $\approx 3.5 \text{ m}\Omega \cdot \text{cm}$: (curve 1), ~ 1.1 (curve 2), ~ 0.1 (curve 3), and ~ 0 (curve 4).

one of the end faces of a cylindrical copper cavity. All measurements were made at a frequency of 32.4 GHz.

It can be seen from Fig. 1 that the curves $R_s(T)$ have a well-defined nonmonotonic nature with a sharp minimum at a temperature close to T_c and a broad peak at lower temperatures. Such a behavior of the surface resistance is basically different from the experimental dependences obtained for monocrystalline samples⁷ and most of the films.^{3,6} By way of an example, the dependence $R_s(T)$ is plotted for a $\text{YBa}_2\text{Cu}_3\text{O}_{7-\delta}$ film with parameter $\delta \approx 0.09$, i.e., with a chemical composition quite close to the optimal oxygen concentration.

3. DISCUSSION OF RESULTS

The temperature dependence of the surface resistance in a microwave field is usually described by the empirical relation

$$R_s(T) = R_{st}(T) + R_{\text{res}}, \quad (1)$$

where $R_s(T)$ and $R_{st}(T)$ are the experimental and theoretical surface resistance respectively, and R_{res} is the residual surface resistance associated with the presence of various defects and impurities in the sample. The quantity $R_{st}(T)$ can be obtained either in the BCS theory or by using the Gorter-Casimir two-liquid phenomenological model.

Near the superconducting transition temperature, we can use a local approximation of the BCS theory which does not take into consideration the variation in the number of quasiparticles, and the expression for the surface impedance can be written in the form¹⁰

$$Z_{st} = R_n \{ 2i / [1 + i \delta_n^2 / 2\lambda(T)^2] \}^{1/2}, \quad (2)$$

where R_n and δ_n denote the surface resistance in the normal state and the classical skin-depth respectively.

The temperature dependence of the magnetic field penetration depth for the entire temperature range can be presented in integral form as follows:

$$\lambda(T)^{-2} = \lambda(0)^{-2} \left\{ 1 - 2 \int_{\Delta}^{\infty} - \frac{\partial f_F}{\partial E} \frac{E}{\sqrt{E^2 - \Delta^2}} dE \right\}, \quad (3)$$

where $\lambda(0)$ is the magnetic field penetration depth at zero temperature, Δ the energy gap, and f_F the Fermi function.

In this case, the surface resistance can be presented in the form

$$R_{st}(T) = R_n \frac{2\lambda(T)}{\delta_n}, \quad (4)$$

while its temperature dependence is determined completely by the temperature dependence of λ . For the skin depth, we obtain the expression

$$\delta_n = (2\rho_n / \mu_0 \omega)^{1/2}. \quad (5)$$

Generally speaking, the condition $d \ll \delta_n$ must be satisfied for thin films, where d is the sample thickness. In this case, the resistivity can be determined from the simple relation $\rho_n = R_n d$. However, it would be appropriate to use a more rigorous expression by assuming that in this case we determine, instead of surface resistivity, the bulk resistivity which takes into account the interference of the incident microwave:

$$R_n = (\mu_0 \omega \rho_n / 2)^{1/2}. \quad (6)$$

Here μ_0 is the permeability of the vacuum, and ω is the microwave radiation frequency.

In order to describe the temperature dependence of the surface resistance with the help of Eqs. (3) and (4), we use $\lambda(0)$ and $\Delta(0)$ as fitting parameters. All the remaining characteristics can be obtained from the experimental data. For one of the investigated films (curve 3 in Fig. 1), the following values were obtained with the help of formulas (5) and (6): $\rho_n = 59.5 \mu\Omega \cdot \text{cm}$, $\delta_n = 54 \mu\text{m}$. Note that the obtained value of ρ_n is in good agreement with the results obtained by Jacobs *et al.* for single crystals of $\text{YBa}_2\text{Cu}_3\text{O}_{7-\delta}$.⁸

The solid curve in Fig. 2 shows the theoretical dependence $R_{st}(T)$ obtained from formulas (3) and (4) by computer analysis taking into account the temperature dependence of the energy gap and the following values of fitting parameters: $\lambda(0) = 140 \text{ nm}$, $\Delta(0) = 2.1 k_B T_c$.

The real part of the impedance can be presented in terms of the two-liquid model parameters:¹¹

$$R_{st}(T) = \frac{2\pi\omega\lambda(T)^2}{c^2} \frac{n_n}{n_s} \tau, \quad (7)$$

where n_n and n_s are the numbers of normal and superconducting electrons respectively, $\tau^{-1} = v_F / l$ is the frequency of electron collisions, v_F the electron velocity at the Fermi surface, and l the electron mean free path. Naturally, $n = n_n + n_s$ is the total number of conduction electrons.

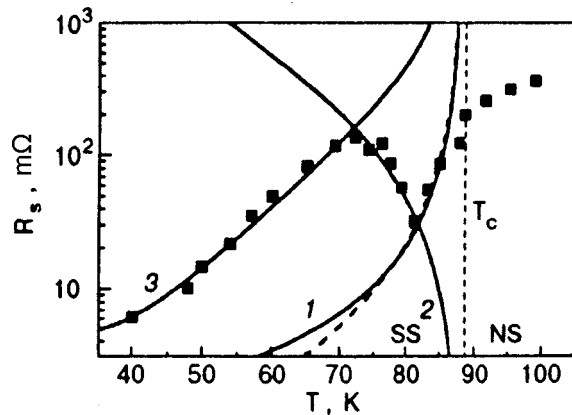


FIG. 2. Temperature dependence of the surface resistance for a $\text{YBa}_2\text{Cu}_3\text{O}_{7-\delta}$ film with $\rho_0 \approx 100 \text{ m}\Omega\cdot\text{cm}$: theoretical curves obtained in the BCS theory (solid curve) and in the two-liquid model (dashed curve) (curve 1), the theoretical curve obtained for scattering of carriers at magnetic impurities with spin flip (curve 2), and the theoretical curve obtained for scattering of carriers at correlated magnetic impurities (curve 3).

Using the well-known empirical expression for the magnetic field penetration depth $\lambda(T) = \lambda(0)(1 - t^4)^{-1/2}$, which is valid for temperature interval close to T_c , we arrive at a simple expression for $R_{st}(T)$:

$$R_{st}(T) = \frac{2\pi\omega^2 l}{c^2} \lambda(0) \frac{t^4}{(1 - t^4)^{3/2}}, \quad (8)$$

where $t = T/T_c$.

The electron velocity at the Fermi surface is determined from the formula $v_F = k_B T_c \xi_0 / (0.18\hbar)$, assuming the coherence length $\xi_0 = 2 \text{ nm}$.⁶ The electron mean free path l for these compounds is put equal to 5 nm .⁶

The dashed curve in Fig. 2 shows the theoretical dependence $R_{st}(T)$ obtained from formula (8) for the magnetic field penetration depth $\lambda(0) = 140 \text{ nm}$ and superconducting transition temperature $T_c = 88 \text{ K}$. It can be seen from the figure that both theoretical approaches lead to almost identical results which can be used to explain the decrease in surface resistance at temperatures close to T_c . However, neither the BCS theory nor the Gorter–Casimir approximation can explain the sharp increase in resistance upon an increase in temperature.

Many authors (see, for example, Refs. 4–6) associate the emergence of a sharp peak on the $R_s(T)$ dependence with the microstructural inhomogeneity of the investigated objects and the existence of weak links, where superconductivity may be suppressed or completely destroyed. As a rule, grain or twin boundaries are often treated as weak links. However, a reliable experimental confirmation has not been obtained so far showing the direct influence of the density of crystal defects on the observed effect. On the other hand, the peak on the $R_s(T)$ curves may be observed in monocrystalline $\text{YBa}_2\text{Cu}_3\text{O}_{7-\delta}$ samples as well as on films prepared by different methods and having various degrees of perfection of their microstructure. However, it was shown by Jacobs *et al.*⁶ that the above-mentioned peak on the $R_s(T)$ dependence appears in $\text{YBa}_2\text{Cu}_3\text{O}_{7-\delta}$ films prepared by nonaxial magnetron sputtering technique only after holding them in

air for two weeks. It is hard to believe that such a low-temperature treatment can lead to noticeable variations in the microstructure of the film. Hence it can be concluded that the observed anomalies in the behavior of $R_s(T)$ shown in Fig. 1 are probably not related to microstructural inhomogeneities and the formation of weak bonds.

For the same reasons, the attempt to attribute the observed increase in $R_s(T)$ to d -wave mechanism of electron pairing seems to be quite controversial.^{1–3} The change in the conditions of sample preparation can hardly lead to a change in the type of symmetry of the superconducting order parameter. On the other hand, an analysis of the temperature dependence of the surface resistance for monocrystalline $\text{YBa}_2\text{Cu}_3\text{O}_{7-\delta}$ samples based on the d -wave pairing model³ shows a poor agreement with the experimental data.

Apparently, the existence of residual surface resistance in the superconducting state can be explained by the mechanism of emergence of losses in a microwave field associated with the interference of incident waves due to interface reflection proposed by some authors.²¹ However, this mechanism presumes a strong dependence of the effect on the geometrical size of the samples, which is not observed in actual practice.

Many experimental facts indicate that the residual surface resistance and the temperature dependence $R_s(T)$ are quite sensitive to the concentration of oxygen atoms in these compounds. It is well known that the optimal concentration of oxygen atoms in $\text{YBa}_2\text{Cu}_3\text{O}_{7-\delta}$ corresponds to $\delta = 0.08$. The excess or deficiency of oxygen atoms can lead to peculiar variations in the electron properties of the material associated with the possibility of charge transport. The physical nature of this phenomenon is still unclear on account of an extreme complexity of the electronic structure of these compounds. It was shown by Koldis *et al.*¹² that in $\text{YBa}_2\text{Cu}_3\text{O}_{7-\delta}$ compounds overdoped with oxygen (for $0.05 < \delta < 0.03$), two superconducting phases can emerge with critical temperatures differing by just 2.5 K. According to Gusakov,¹³ an increase in oxygen concentration is accompanied by a change in the magnitude and sign of charge at the O(4) position from -2.07 to 0.67 , which must lead to the formation of uncompensated magnetic moments localized in the Ba–O layer. The recently discovered phase separation effect (see, for example, Ref. 14) can also lead to the formation of tiny spin-polarized clusters in compounds of this type.

Taking into consideration all that has been stated above, we can propose an entirely different explanation for the unusual behavior of the $R_s(T)$ dependence on the basis of the following assumptions.

- (1) Two superconducting energy gaps, say, in Cu–O planes and Cu–O chains, can appear in HTSC compounds. However, other versions for the formation of the two-phase superconducting state are also possible. At temperatures close to T_c , a strong increase in the coherence length and overlapping of the wave functions of superconducting electrons in adjacent planes and chains transform both gaps into a single gap which determines the superconducting transition temperature of the compound. The overlapping of wave functions weakens

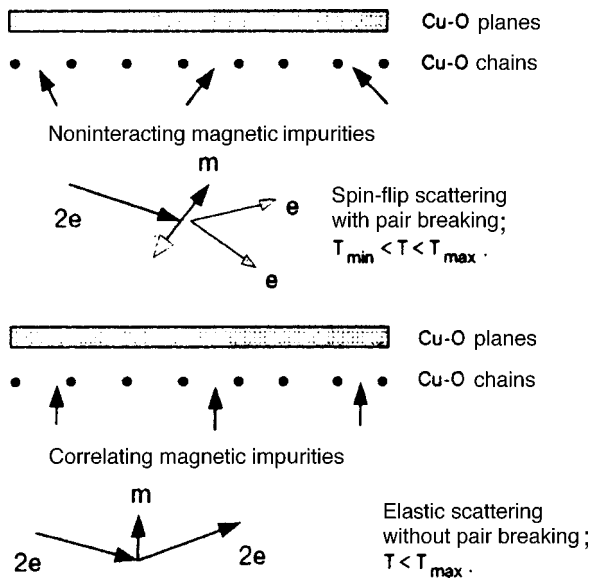


FIG. 3. Schematic diagram for scattering of charge carriers at magnetic impurities with and without spin flip.

upon a decrease in temperature (the manifestation of the proximity effect becomes less pronounced), and the behavior of the two gaps can be treated independently.

- (2) The excess or deficiency of oxygen atoms in the compound $\text{YBa}_2\text{Cu}_3\text{O}_{7-\delta}$ can lead to the formation of magnetic impurities. At high temperatures (close to T_c), the magnetic impurities can be treated as independent centers at which spin-flip scattering of carriers takes place.¹⁵⁻¹⁷ This process is accompanied by depairing of electrons due to the law of conservation of total spin, and leads to the emergence of gapless superconducting state.^{9,18}
- (3) A decrease in temperature can lead to the enhancement of interaction between impurities and a tendency towards ordering of the magnetic subsystem. In this case, the spin-flip scattering of carriers becomes less probable, and the electron pair breaking effects become impossible.⁹ Ordering of magnetic impurities may be of the type of phase transition at the final temperature, or of continuous type with a transition to the spin-glass state. It can be hoped that the mechanism of formation of magnetic order in cuprates will not differ significantly from that proposed for doped manganites which became quite popular after the discovery of ‘‘giant magnetoresistance’’ in them.^{19,20} For example, such a mechanism may emerge owing to indirect anisotropic exchange through oxygen orbitals.

The situation described above is presented schematically in Fig. 3.

In this work, we do not specify the physical nature of magnetic ordering, but rather assume that the magnetic subsystem may exist in two states, viz., high-temperature non-correlated state (in which the impurities can be treated as independent), and the low-temperature correlated state (in which magnetic ordering sets in). In this case, the number N_m of noncorrelated magnetic impurities will decrease with

temperature to zero according to the simple law

$$N_m(T) \propto N_{m0} \exp(-T_0/T), \quad (9)$$

where N_{m0} is the number of independent magnetic impurities at high temperatures, T_0 the energy of impurity interaction leading to magnetic ordering (or the correlation energy of magnetic impurities).

Thus, a decrease in temperature may lead to the emergence of three successive processes in the superconducting compound $\text{YBa}_2\text{Cu}_3\text{O}_{7-\delta}$, resulting in a considerable rearrangement of the energy spectrum and affecting losses in the microwave field. In the close proximity of T_c , the entire sample is in the phase-coherent state and begins to go over to the superconducting state as a single entity. In this case, the temperature behavior of the surface resistance can be described quite correctly by the BCS theory or the Gorter-Casimir two-liquid model as shown by the solid curve and dashed curve 1 in Fig. 2. Further decrease in temperature must lead to the separation of superconducting energy gaps in Cu–O planes and chains due to a sharp decrease in the coherence length. Hence a situation may arise in which the concentration of magnetic impurities that are invariably present in the compound exceeds the critical concentration for the superconducting component of electrons localized along the Cu–O chains. In this case, the spin-flip scattering of carriers results in the transition of a part of the sample to the gapless superconducting state. Since this process is accompanied by breaking of superconducting electron pairs, the temperature dependence of the surface resistance can be presented in a form inverse to formula (7). Indeed, the number of normal electrons in this case will increase with decreasing temperature, while the number of superconducting electrons will decrease. Taking into account the temperature dependence of the electron mean free path⁶ and assuming that the magnetic field penetration depth varies weakly in the temperature range in which we are interested, we calculated the theoretical dependence $R_{st}(T)$ keeping in view the pair-breaking of a part of the superconducting electrons (see curve 2 in Fig. 2). It can be seen from the plot that the sharp minimum observed experimentally on the $R_{st}(T)$ dependence (see Fig. 1) may be described by the given model without the introduction of any additional fitting parameters. Upon a further decrease in temperature, the resulting correlation between magnetic impurities leads to a termination of the spin-flip scattering of electrons and to a restoration of the superconducting energy gap along the Cu–O chains. In this case, the expression for the temperature dependence of surface resistance must contain two cofactors, viz., the temperature dependence of the number of the normal and superconducting electrons, which can again be expressed in terms of the BCS theory (2) and (3) or the Gorter–Casimir model (7), and the probability of existence of independent magnetic impurities described by formula (9):

$$R_{st}(T) \approx R_0 \exp(-T_0/T) \left[\frac{t^4}{1-t^4} \right] + R_1, \quad (10)$$

where R_0 is a constant parameter which can be determined from formulas (7) and (9), and R_1 is the residual surface resistance.

The best agreement with the experiment is obtained (curve 3 in Fig. 2) by choosing the parameter $T_0=130$ K, which can characterize the correlation energy of spin interaction of impurity atoms.

4. CONCLUSION

In this work, we have shown that the frequently observed peculiar temperature dependence of the surface resistance of HTSC materials in a microwave field can be associated with the concentration and the extent of ordering of oxygen atoms, and not with the structural inhomogeneities or nontraditional type of electron pairing. The idea of the existence of magnetic impurities and mechanism of inelastic spin-flip scattering of carriers is used to propose a qualitative model of the emergence and peculiar temperature dependence of the microwave losses in HTS films at low temperatures.

The authors are pleased to thank V. Kresin and Yu. Ovchinnikov for fruitful discussions.

This research was supported by the Ukrainian Ministry of Science and Technology (project No. 2/573).

*E-mail: pvg@imp.kiev.ua

*E-mail: yplee@omea.sunmoon.ac.kr

- ¹D. A. Bonn, P. Liang, and W. N. Hardy, Phys. Rev. Lett. **68**, 2390 (1992).
- ²J. Mao, D.-H. Wu, J. Peng *et al.*, Phys. Rev. B **51**, 3316 (1995).
- ³T. Jacobs, S. Sridhar, Qiang Li *et al.*, Phys. Rev. Lett. **75**, 4516 (1995).
- ⁴J. Halbritter, J. Appl. Phys. **68**, 6315 (1992).
- ⁵J. Halbritter, J. Supercond. **8**, 691 (1995).
- ⁶T. Jacobs, K. Nurnssen, R. Schwab *et al.*, IEEE Trans. Appl. Supercond. **7**, 1917 (1997).
- ⁷V. F. Tarasov, V. F. Taborov, V. G. Prokhorov, and V. M. Pan, Czech. J. Phys. **46**, 1067 (1996).
- ⁸T. Jacobs, S. Sridhar, C. T. Rieck *et al.*, J. Chem. Phys. Solids **56**, 1945 (1995).
- ⁹Yu. Ovchinnikov and V. Kresin, Phys. Rev. B **54**, 1251 (1996).
- ¹⁰S. Sridhar, D.-H. Wu, and W. Kennedy, Phys. Rev. Lett. **63**, 1873 (1989).
- ¹¹V. V. Shmidt, *Introduction to Superconductor Physics* [in Russian], Nauka, Moscow (1982).
- ¹²E. Kaldis, J. Röhrler, E. Liarokapis *et al.*, Phys. Rev. Lett. **79**, 4894 (1997).
- ¹³V. Gusakov, Physica C **239–240**, 813 (1994).
- ¹⁴A. A. Gorbatsevich, Yu. A. Kopaev, and L. V. Tokatly, Physica C **223**, 95 (1994).
- ¹⁵A. Abrikosov and L. Gor'kov, Zh. Éksp. Teor. Fiz. **39**, 1781 (1961) [Sov. Phys. JETP **12**, 1243 (1961)].
- ¹⁶S. Skalski, O. Betleder, and P. Weiss, Phys. Rev. A **134**, 1500 (1964).
- ¹⁷A. Abrikosov, *Fundamentals of the Theory of Metals*, North Holland, Amsterdam (1988).
- ¹⁸V. Kresin and S. Wolf, Phys. Rev. B **51**, 1229 (1995).
- ¹⁹L. P. Gor'kov, Usp. Fiz. Nauk **168**, 665 (1998) [*sic*].
- ²⁰D. Khomskii and G. Sawatzky, Solid State Commun. **102**, 87 (1997).
- ²¹V. V. Eremenko, D. E. Zhrebchevskii, T. N. Moiseeva, and V. V. Chabanenko, Fiz. Nizk. Temp. **15**, 695 (1989) [Sov. J. Low Temp. Phys. **15**, 389 (1989)].

Translated by R. S. Wadhwa

Spectrum of Andreev states in asymmetric S_1NS_2 junction

Yu. G. Peisakhovich and A. A. Shtygashev

*Novosibirsk State Educational University, 630068 Novosibirsk, Russia**

(Submitted October 20, 1998; revised January 4, 1999)

Fiz. Nizk. Temp. **25**, 455–458 (May 1999)

A completely asymmetric S_1NS_2 junction with different Fermi surfaces in the layers is considered. The transfer matrix is constructed, and the spectrum of localized states is obtained. The weakening of the phase dependence with increasing difference in the Fermi momenta in the layers is of a slow power type. © 1999 American Institute of Physics.
[S1063-777X(99)00505-8]

It is well known that the formation of discrete Andreev's levels is the main mechanism determining the phase dependence of superconducting current flowing through an SNS junction under the conditions of stationary Josephson effect.^{1–5}

The spectrum of the junction is usually determined from an analysis of the one-dimensional scattering problem by joining solutions for three regions with piecewise-constant values of physical parameters. Starting from the fundamental work by A. F. Andreev,² it is assumed that the values of the Fermi momentum components k_{F_x} normal to the interfaces between the media are the same for all waves participating in joining. In Ref. 2, this was dictated by physical conditions of the problem on the intermediate state of a homogeneous sample. In subsequent publications on SNS junctions and SN superlattices,^{6–9} this condition is presumed automatically, which should be regarded as an essentially model assumption (Andreev approximation⁷).

In actual broad asymmetric S_1NS_2 junctions formed by different metals, the Fermi surfaces corresponding to different regions obviously have different sizes and shapes, which must be taken into account in joining the corresponding solutions and for determining current. Old theories based on the model of tunnel Hamiltonian⁴ described this circumstance just by the product of energy densities of states of junctions with reciprocal root singularities at their superconducting gap thresholds. In recent publications on ballistic Josephson junctions,^{6,9} asymmetric S_1NS_2 junctions were considered, in which the absolute values Δ_1 and Δ_2 of the pairing potential on the left and on the right were assumed to be different for the same Fermi momentum k_{F_x} , and the spectrum of such junctions as well as the current through them were analyzed. In the presence of additional dielectric barriers at the boundaries of the N region, ordinary scattering of quasiparticles and the situation not covered by Andreev's approximation must be taken into account along with Andreev scattering.¹⁰

In this communication, we study and analyze numerically the equation for the spectrum of Andreev states for a completely asymmetric S_1NS_2 junction taking into account the difference in transverse Fermi momenta in the layers. In addition of Andreev reflection which by definition involves a

small change in the quasiparticle momentum $\delta k \sim k_F \Delta / \mu$, where μ is the Fermi energy, ordinary reflection of quasiparticles at the boundary between metals occurs with a large change of momentum $\delta k \sim k_F$. This scattering channel is always present in actual systems, and we must take it into account in order to describe completely the phase dependence of current. We shall prove that the dependence of the energy of Andreev states on the coherent phase difference disappears smoothly with increasing difference in the Fermi momenta in the layers. It follows hence that the phase-dependent contribution to the superconducting current through such junctions is proportional to the product of the areas of quasi-cylindrical strips with the same value of k_{F_x} on the Fermi surfaces for different media.

In real metals, conduction electrons have a complex dispersion relation $E = E(\mathbf{k})$, where \mathbf{k} is the quasimomentum, and the Fermi surface may have an intricate shape.^{11,12} In order to describe quasiparticles in a superconductor with a complex topology of conduction bands, we write the Bogoliubov–de Gennes equation in the form¹¹

$$\begin{pmatrix} \hat{H}(-i\hbar\nabla + \mathbf{p}_s) - \mu - \varepsilon & -\Delta \\ \Delta & \hat{H}(-i\hbar\nabla - \mathbf{p}_s) - \mu + \varepsilon \end{pmatrix} \begin{pmatrix} u \\ v \end{pmatrix} = 0. \quad (1)$$

Here we replace the electron kinetic energy operator $(-\hbar^2\nabla^2/2m)$ by the Hamiltonian operator $\hat{H}(-i\hbar\nabla)$ whose eigenfunctions are plane waves enveloping Bloch functions, i.e.,

$$\hat{H}(-i\hbar\nabla)e^{i\mathbf{k}\mathbf{r}} = E(\mathbf{k})e^{i\mathbf{k}\mathbf{r}}. \quad (2)$$

Such a substitution for metals is justified with the help of the Wannier representation¹² or in analogy with the description of optical spatial dispersion in the electromagnetic wave equation if the phase velocity of light is a function of wavelength. A weak magnetic field in crystals can be described by the vector potential $\mathbf{A} = \mathbf{A}(\mathbf{r})$ through the Peierls substitution¹² into the dispersion relation of quasimomentum. In this connection, we have introduced in (1) the gauge-invariant superfluid momentum $\mathbf{p}_s = \hbar\nabla\Phi/2 - e\mathbf{A}/c$, and the calibration of \mathbf{A} is chosen so that the pairing potential $\Delta = \Delta(\mathbf{r})$ is real-valued, i.e., its phase Φ is equal to zero.

In a one-particle spectral problem, we can often assume (for $a \gg \xi$, where a is the width of the N region and ξ the correlation length) that $E(\mathbf{k}), \Delta$ and \mathbf{p}_s are preset piecewise-constant functions in the relevant regions, and Eq. (1) is a linear differential equation. We direct the x -axis at right angles to the layers along the current \mathbf{p}_s so that the left boundary of the N region corresponds to $x=0$ and the right boundary to $x=a$. Particular solutions of the one-dimensional problem have the form e^{ikx} . We confine our analysis to a typical case when the Fermi surfaces have only one cavity and have an inversion center $E(\mathbf{k}_F) = E(-\mathbf{k}_F)$, and the characteristic equation for (1) in each medium has four roots (this is obvious for a spherical Fermi surface):

$$\begin{aligned} k_{1,3} &= k_f \pm (\hbar v_F)^{-1} \sqrt{(\varepsilon - v_F p_s)^2 - \Delta^2}, \\ k_{2,4} &= -k_f \mp (\hbar v_F)^{-1} \sqrt{(\varepsilon + v_F p_s)^2 - \Delta^2}. \end{aligned} \quad (3)$$

Here k_1 and k_2 correspond to electron-type and k_3 and k_4 to hole-type excitations, and the transverse Fermi momentum k_F can be determined from the equation $E(k_F, \mathbf{k}_\parallel) = \mu$, where \mathbf{k}_\parallel is the Fermi momentum parallel to the boundaries, the transverse group velocity $v_F = \partial E(k_F, \mathbf{k}_\parallel) / \partial k_F$, and $v_F, k_F \gg \varepsilon, \Delta, v_F p_s$ almost on the entire Fermi surface.

The solution at an arbitrary point can be written with the help of the transfer matrix $\Psi(x) = M_x \Psi(0)$, where $\Psi(x) = \text{col}(u, du/dx, v, dv/dx)$ and $\Psi(0)$ is the column of boundary conditions at the point $x=0$.¹³ The transfer matrix M_x in a homogeneous layer has the form

$$M_x = L M_{D_x} L^{-1}, \quad (4)$$

where L is the diagonalization matrix, i.e., $\Psi(x) = L \Psi_D(x)$, and $\Psi_D(x) = \text{col}(A_1 e^{ik_1 x}, A_2 e^{ik_2 x}, A_3 e^{ik_3 x}, A_4 e^{ik_4 x})$, $M_{D_x} = \text{diag}(e^{ik_1 x}, e^{ik_2 x}, e^{ik_3 x}, e^{ik_4 x})$ in the diagonal representation. The continuity of the current density implies that the superfluid momentum \mathbf{p}_s of particles is large in the N region, where the condensate density is low, and conversely, can be approximately put equal to zero in the S regions. Then the modulus of phase lead of the wave functions for quasiparticles in the normal region, which predominantly determines the disbalance of spectra of forward and backward currents, is $\varphi/2 = p_s a$.³ This parameter automatically appears in the exponential factors of the transfer matrix through the N region, which allow us (for the chosen simple calibration (1)) to use only the ordinary continuity conditions for wave functions and their derivatives at the boundaries instead of the Kulik condition¹ introduced for equations with a complex-valued $\Delta(x)$. In this approximation ($\Delta_1 \neq 0$, $\mathbf{p}_s = 0$), matrices L_j in S_j regions ($j=1,2$) are given by the direct product

$$L_j = \begin{pmatrix} 1 & l_j \\ l_j & 1 \end{pmatrix} \otimes \begin{pmatrix} 1 & 1 \\ ik_{Fj} & -ik_{Fj} \end{pmatrix}, \quad (5)$$

where $l_j = (\gamma_j - \varepsilon) / \Delta_j = -\Delta_j / (\gamma_j + \varepsilon)$ are coherence factors for partial u - and v -waves, and $\gamma_j = \sqrt{\varepsilon^2 - \Delta_j^2}$. In the N regions, matrices L can be obtained from (5) for $\Delta_j = l_j = 0$, $k_{Fj} = k_{F0}$; in this case, the transfer matrix (4) has the form

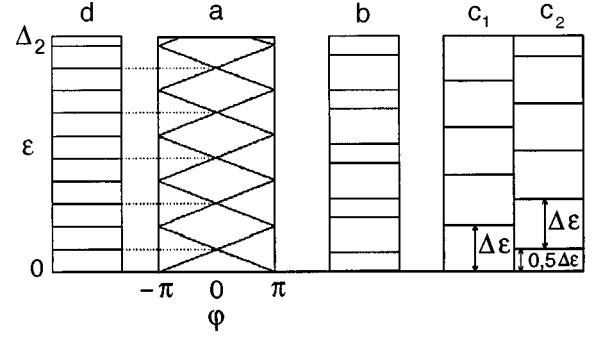


FIG. 1. Characteristic asymptotic forms of Andreev states in N region.

$$\begin{aligned} M_{Nx} &= \begin{pmatrix} N_1 e^{-ip_s x} & 0 \\ 0 & N_3 e^{ip_s x} \end{pmatrix}, \\ N_{1,3} &= \begin{pmatrix} \cos \kappa_{1,3} x & \frac{1}{k_{F0}} \sin \kappa_{1,3} x \\ -k_{F0} \sin \kappa_{1,3} x & \cos \kappa_{1,3} x \end{pmatrix}, \end{aligned} \quad (6)$$

where $\kappa_{1,3} = k_{F0} \pm \varepsilon / \hbar v_{F0}$.

Specifying the boundary conditions $\Psi(a)$ at the second point $x=a$ also, we arrive at the equation $\Psi(a) = M_a \Psi(0)$. For subbarrier states of an asymmetric $S_1 N S_2$ junction $\Delta_1 > \Delta_2 > \varepsilon$, retaining at the boundaries only the waves $\Psi(0) = L_1 \text{col}(0, A_2, A_3, 0)$, $\Psi(a) = L_2 \text{col}(A_1, 0, 0, A_4)$, attenuating to the left and right, we obtain the following four equations for amplitudes:

$$\begin{pmatrix} A_1 \\ 0 \\ 0 \\ A_4 \end{pmatrix} = L_2^{-1} M_{Na} L_1 \begin{pmatrix} 0 \\ A_2 \\ A_3 \\ 0 \end{pmatrix}. \quad (7)$$

Equating the determinant to zero, we obtain the required equation for the spectra of Andreev states coupled in the junction:

$$\begin{aligned} \Delta_1 \Delta_2 \cos \varphi &= \frac{1}{4} \tilde{\gamma}_1 \tilde{\gamma}_2 \tau_1 \tau_2 \cos 2k_{F0} a \\ &+ \left(\varepsilon^2 - \frac{1}{4} \tilde{\gamma}_1 \tilde{\gamma}_2 \eta_1 \eta_2 \right) \cos \frac{2\varepsilon a}{\hbar v_{F0}} \\ &+ \frac{\varepsilon}{2} (\tilde{\gamma}_1 \eta_1 + \tilde{\gamma}_2 \eta_2) \sin \frac{2\varepsilon a}{\hbar v_{F0}}, \end{aligned} \quad (8)$$

where

$$\begin{aligned} \tau_i &= \frac{k_{F0}}{k_{Fi}} - \frac{k_{Fi}}{k_{F0}}, & \eta_i &= \frac{k_{F0}}{k_{Fi}} + \frac{k_{Fi}}{k_{F0}}, \\ \tilde{\gamma}_i &= \sqrt{\Delta_i^2 - \varepsilon^2}, & i &= 1, 2. \end{aligned} \quad (9)$$

For $k_{F1} = k_{F2} = k_{F0}$, this equation is transformed into the equation obtained in Refs. 6 and 9 (Fig. 1a). Besides the additional asymmetry $\tau_1 \neq \tau_2 \neq 0$, $\eta_1 \neq \eta_2 \neq 2$, the first term on the right-hand side of (8), which oscillates with the variation of the parameter $k_{F0} a$ and is especially significant near the bottom of the well $\varepsilon \ll \Delta_2 < \Delta_1$, is new qualitatively. The emergence of this term is in fact associated with the

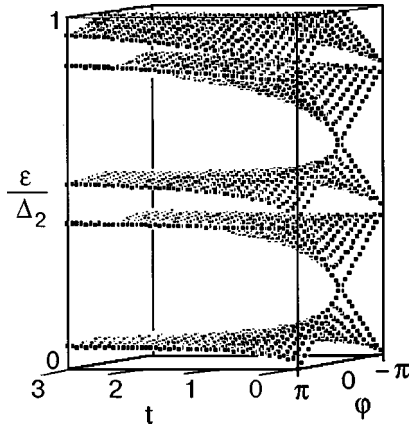


FIG. 2. Evolution of the phase dependence of the energy of states with increasing difference between transverse Fermi momenta in S - and N -regions (calculations were made by using formula (8)).

inclusion of the ordinary scattering channel at the potential barriers of SN boundaries. It can be seen that the behavior of the spectrum strongly depends on the structure of the Fermi surface in all the three regions. If $\tau_i \sim \eta_i \gg 1$, the dependence of the energy of Andreev's levels on φ disappears, bands contract to discrete levels, but the asymptotic form can be different. For example, for processes with $k_{F1} = k_{F2} \neq k_{F0}$ (Fig. 2), where $t = \eta_1/2 - 1$, the calculations based on formula (8) for $\Delta_1 = \Delta_2 = 10^{-3}$, $a = 3 \cdot 10^{-7}$ m, $k_{F0} = 5.8 \cdot 10^8$ m $^{-1}$, $v_{F0} = \hbar k_{F0}/m$, $\tau_1 = \tau_2 \gg 1$ and $\eta_1 = \eta_2 \gg 1$ we obtain the spectrum $\kappa_{1,3}a = n\pi$ ($n = 0, \pm 1, \pm 2, \dots$) consisting of equidistant doublets (see Fig. 1b) of standing waves with $k = \kappa_{1,3}$ confined in a rectangular well. If $k_{F0}a = n\pi/2$, the lines in the doublets merge: we have $\varepsilon = l\Delta\varepsilon$ for even n (Fig. 1c $_1$) and $\varepsilon = (l+1/2)\Delta\varepsilon$ for odd n (Fig. 1c $_2$), where $\Delta\varepsilon = \pi\hbar v_F/a$ and l is an integer. For processes with $k_{F1} \neq k_{F2} = k_{F0}$ ($\tau_2 = 0, \eta_2 = 2$) for $\eta_1 \gg 1$, we have Andreev's spectrum with zero current $\varphi = 0^{1-3}$ in a well of double width $2a$:

$$\tan \frac{2\varepsilon a}{\hbar v_{F0}} = \frac{\tilde{\gamma}_2}{\varepsilon}. \quad (10)$$

According to the Bohr–Sommerfeld quantization rule, this corresponds to specular reflection of the wave incident from the right at the left well, the separations between lines being almost identical (Fig. 1d). Pay attention to the fact that these asymptotic forms are independent of the relation between k_{Fi} and of the signs of τ_i . The dependence of the spectrum on φ disappears quite smoothly in the phase space for values of the parameters

$$\eta \sim \tau \sim t \sim \frac{\Delta}{\tilde{\gamma}} = \begin{cases} 1, & \varepsilon \ll \Delta_2 \\ \sqrt{\frac{1}{2} \frac{\Delta_2}{\Delta_2 - \varepsilon}} \gg 1, & \varepsilon \leq \Delta_2 \end{cases} \quad (11)$$

near the top of the well at a much lower rate than near the bottom.

The spectral equation (8) derived by us takes into account the difference in the transverse Fermi momenta of particles in all regions along with the difference in pairing potentials at the S banks of the junction. Besides Andreev's

scattering channel, the ordinary scattering at the SN boundaries is also taken into account. The method of transfer matrix¹³ allows us to automatize the procedure of joining the solutions and to leave easily the limits of Andreev's approximation.

For determining the current through the junction, the summation over the states involves the integration over phase volumes near Fermi surfaces in all the three media. The estimate (11) and Figs. 1 and 2 show that the calculation of the phase-dependent component of current (both subbarrier and above the barrier) must be carried out with the help of careful numerical summation. Our analysis shows, however, that this current component is determined roughly by the presence of regions with the same value of k_{Fx} , i.e., strips of a quasi-cylindrical shape with a height determined by the surface with the smallest area on all the three Fermi surfaces and gives information on the area of these strips and their orientation relative to crystallographic axes.

The results obtained for taking into account additional scattering channels can be easily generalized to the case of a more complex topology of the Fermi surface (the absence of inversion center, nonconvexity, lack of simple connectivity, self-intersection, magnetic splitting, and so on), when the roots of the characteristic equation for (1) in a layer have different values of k_F and v_F , or the number of these roots is greater than four. In the latter case, we must supplement the vector of state $\Psi(x)$ with rows containing higher-order derivatives corresponding to the number of the roots, and the matrices M_x and L have dimensions equal to the number of the roots.

*E-mail: ygpe@ngpi.nsk.su

¹I. O. Kulik, Zh. Éksp. Teor. Fiz. **57**, 1745 (1969) [Sov. Phys. JETP **30**, (1969)].

²A. I. Andreev, Zh. Éksp. Teor. Fiz. **46**, 1823 (1964) [Sov. Phys. JETP **19**, (1964)].

³J. Bardeen and J. L. Johnson, Phys. Rev. B **5**, 72 (1972); A. V. Svidzinskii, *Spatially Inhomogeneous Problems in the Theory of Superconductivity* [in Russian], Nauka, Moscow (1982).

⁴V. Ambegaokar and A. Baratoff, Phys. Rev. Lett. **10**, 486 (1963); E. L. Volf, *Principles of Electron Tunnel Spectroscopy* [in Russian], Naukova Dumka, Kiev (1990).

⁵C. J. Lambert and R. Raimondi, J. Phys.: Condens. Matter **10**, 901 (1998).

⁶P. F. Bagwell, Phys. Rev. B **46**, 12 573 (1992); R. A. Riedel and P. F. Bagwell, Phys. Rev. B **48**, 15 198 (1993).

⁷R. Kummel, Phys. Rev. B **16**, 1979 (1977); M. Hurd and G. Wendin, Phys. Rev. B **49**, 15 258 (1994).

⁸Y. Tanaka and M. Tsukada, Phys. Rev. B **44**, 7578 (1991); S. V. Kuplevakhskii and I. I. Falko, Fiz. Nizk. Temp. **18**, 203 (1992) [Sov. J. Low Temp. Phys. **18**, 140 (1992)]; H. Plehn, O. J. Wacker, and R. Kummel, Phys. Rev. B **49**, 12 140 (1994).

⁹S. V. Kuplevakhskii and I. I. Falko, Fiz. Nizk. Temp. **17**, 961 (1991) [Sov. J. Low Temp. Phys. **17**, 501 (1991)].

¹⁰G. A. Gogadze and A. M. Kosevich, Fiz. Nizk. Temp. **24**, 716 (1998) [Low Temp. Phys. **24**, 540 (1998)].

¹¹Y. G. Peisakhovich, J. Supercond. **9**, 579 (1996).

¹²I. M. Lifshits, M. Ya. Azbel, and M. I. Kaganov, *Electronic Theory of Metals* [in Russian], Nauka, Moscow (1971).

¹³Yu. G. Peisakhovich, J. Phys. A **29**, 5103 (1996).

Dynamics of electronic excitations in YBCO at low temperatures

I. Ya. Fugol, V. N. Samovarov, and M. Yu. Libin

Verkin Institute for Low Temperature Physics and Engineering, National Academy of Sciences of Ukraine, Lenin Ave. 47, Kharkov, 310164, Ukraine

(Submitted November 11, 1998; revised December 24, 1998)

Fiz. Nizk. Temp. **25**, 459–468 (May 1999)

We present the results of low-temperature optical experiments (absorption and reflection) in visible and middle infrared frequency regions with epitaxial films of copper oxide materials like a $\text{Y}_1\text{Ba}_2\text{Cu}_3\text{O}_{6+x}$. Based on our data and reference data, we consider the anomalous spectral effects in HTSC having no analogy with conventional BCS superconductors: (1) the optical response to superconducting transition at T_c ; (2) the spectral weight redistribution induced by chemical doping and temperature; (3) the drastic enhancement of low-temperature photodoping; (4) the long spin-structure relaxation via temperature variations seen in the optical spectra.

The thorough analysis of the results obtained is fully compatible with the concept of two-component system of light and heavy carriers (holes), being in dynamical coexistence with each other. The dynamical coexistence of the intraband carriers occurs on the background of strongly correlation interrelation of the heavy quasiparticles with the optical interband (charge transfer) excitations. © 1999 American Institute of Physics. [S1063-777X(99)00605-2]

INTRODUCTION

In recent years the optical spectroscopy of HTSC at frequencies much higher than the superconducting gap, $\hbar\omega \gg \Delta$, has been found to be informative for understanding the nature of high- T_c superconductivity, in particular, for studying the anomaly of the normal-state properties of HTSC. With regards to room temperature (RT) optical experiments, the following distinct features of the HTSC spectra, which were originally associated with the unusual electron structure, deserve mention: (i) the pronounced optical effect of strongly correlated electrons (holes) under doping, manifesting itself in spectral weight redistribution between the high-energy (interband) region of spectra and the low-energy (intraband) one; (ii) the declination of the optical conductivity from the Drude-like behavior (standard for free carriers) and the appearance of an additional band in the middle infrared region; (iii) the inherent potentiality of photodoping, which results in pumping of carriers under irradiation with light quanta at the frequencies of interband charge transfer transitions above the optical gap $\hbar\omega > \hbar\omega_g \cong 1.6$ eV; (iv) the optical relaxation of the reflection coefficient in the course of aging and the oxygen ordering of HTSC samples after cooling from high temperature ($T \leq 450$ K) to RT.

The mentioned important results for different HTSC are presented, for example, in.^{1–6} All the above features were measured in the optical range from 10^{-2} to 5 eV with different doping regimes of $\text{Y}_1\text{Ba}_2\text{Cu}_3\text{O}_{6+x}$: the dielectric phase, $x < 0.3$; the strange metal phase at underdoping, $0.35 < x < 0.8$; the metal at optimal doping, $x \approx 0.9$; the overdoped metal with depressed superconductivity, $x > 0.95$. Because there are two different cuprate structures in the ab geometry of $\text{Y}_1\text{Ba}_2\text{Cu}_3\text{O}_{6+x} - \text{CuO}_2$ (active plane and CuO_x (chain structure along the b axis), it is essential that the

contributions from these planes to absorption and reflection should be separated in experiments with light polarization. This can be most easily done in polarization experiments with $E \parallel a$ and $E \parallel b$ on untwinned crystals. In this respect most intriguing are the data of polarization spectrum measurements on untwinned single crystals of YBaCuO for a and b axes.^{2,6} For example, the optical conductivity spectrum of $\text{Y}_1\text{Ba}_2\text{Cu}_3\text{O}_{6+x}$ for different doping amounts at RT according² is shown in Fig. 1. Below the energy of the charge transfer optical gap, $E \cong 1.6$ eV, separating the lower valent and the upper Hubbard bands there are intraband transitions. Above this energy, $E > E_g$, one can observe interband absorption bands with charge transfer from O^{2-} to Cu^{2+} —CT1, CT3, CT4 which are most prominent at low doping. Still higher in energy, at $E = 4.1$ eV, there is a band which belongs to the transition ($d-p$) in the local center of Cu^+ of CuO_x plane. Figure 1 clearly shows the evolution of optical conductivity spectra with doping from the dielectric to a superconducting state. The correlation effect in the spectra with doping is revealed in the form of integral spectral weight redistribution from the interband charge transfer (CT) transitions in the visible (VIS) region to the intraband transitions in the middle infrared one (MIR). The spectral change indicates that the conduction and valence band states of YBCO insulator are redistributed by doping to construct new states which give rise to low-energy excitations below crossover point $\hbar\omega_{\text{cr}}$. As seen from Fig. 1, there is the crossover point ω_{cr} at which $\sigma_1(\omega)$ is constant with doping. It should be mentioned that in general the existence of the doping-independent crossover point ω_{cr} suggests that the optical gap in $\text{Y}_1\text{Ba}_2\text{Cu}_3\text{O}_{6+x}$ is not generated by the charge density wave (the spectrum of optical excitations associated with the charge density wave shifts dramatically to a red region as a whole on doping). The optical spectra of YBaCuO in the vicinity of intraband transitions have a Drude peak, centered

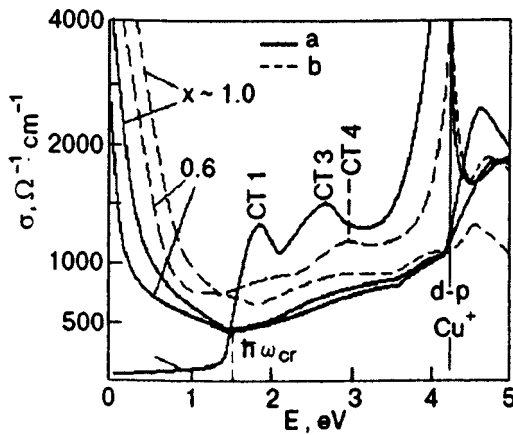


FIG. 1. Optical conductivity of untwinned YBCO crystals for various composition x at RT:² along a axis (—); along b axis (---).

at $\omega=0$ with width of $1/T$ and additional spectral weight in the MIR region (with the MIR maximum at 0.6 eV). It is the occurrence of additional absorption in the MIR region that results in the difference of the frequency dependence $\sigma(\omega)$ from the law $\sigma(\omega) \sim \omega^{-2}$ expected for the ordinary Fermi liquid. And that once entailed the need for development of new concepts of HTSC electronic spectrum (for instance, the concept of “marginal” and “nesting” Fermi-liquid⁷). It should be emphasized that in conventional BCS-superconductors no radically new optical effect were observed at low temperatures (LT) as compared to RT in the region $\hbar\omega \gg \Delta$, moreover, no optical response to the emergence of the SC state was detected. In the case of HTSC the LT dynamics of charges displays new effects which would signaled on precursory processes to superconductivity.

This paper presents the experimental results of later years on some nonordinary spectral properties of the normal phase of $Y_1Ba_2Cu_3O_{6+x}$ in VIS and MIR, revealed at different regimes of doping and temperature variations within the LT range below $T=200$ K down to 20 K. In the main these are the data of investigations under the Program of the National Academy of Sciences of Ukraine. All optical measurements were carried out on thin epitaxial films $l \approx 2000\text{--}3000$ Å in thickness oriented parallel to the ab plane. The films were grown in German scientific centers (University of Erlangen; Munich Technical University). The films were tested for their electrical, magnetic and structure characteristics. Some details of the LT optical measurements were described in.⁸

At present it can be said with confidence that the hole subsystem dynamics in HTSC materials is largely determined by the Fermi-liquid effects and the strong correlation interaction between intra- and interband transitions. However, up to now the correlation redistribution along spectra has been studied only for the doping effect at RT and has not been considered for other processes of charge dynamics. According to the data⁸ and the results presented here, the integral redistribution of spectral weight in HTSC also occurs in experiments with temperature variations, in photoinduced spectra, in experiments with provocation of spin-structure instability and so on. Therefore, the LT spectral data should

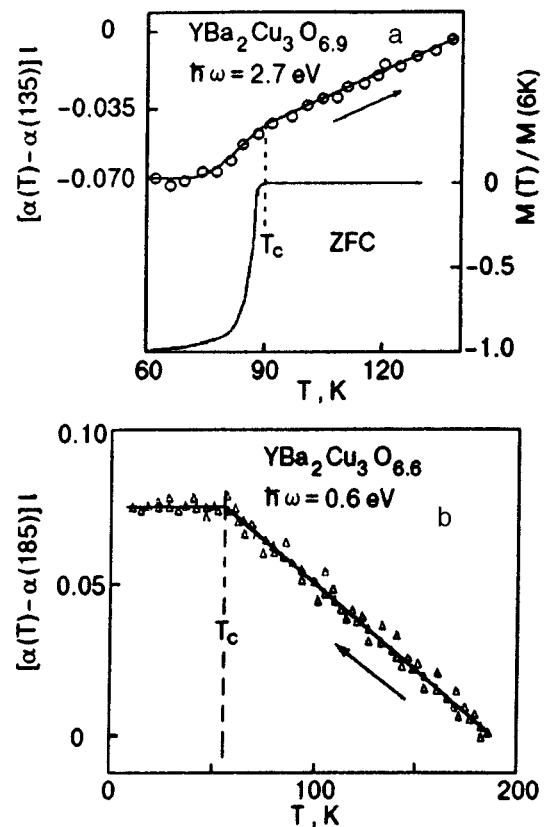


FIG. 2. Temperature dependences of the differential absorption coefficient for VIS (a) and MIR (b) with different x (in (a) shown are magnetic measurements of the film for ZFC regime also).

be analyzed from the general viewpoint. We would like to stress that all LT features in the MIR and VIS spectra can be naturally examined in terms of the Mott-Hubbard model of 2D strongly correlated electrons with taking into account the intense spin fluctuations at LT.

OPTICAL RESPONSE TO SC TRANSITION AT T_c AND TEMPERATURE DEPENDENCES OF SPECTRAL FUNCTIONS

One of the unexpected spectroscopic results in copper oxides was the finding of sensitivity to the onset of superconductivity for the transmitted electromagnetic field of optical frequencies $\hbar\omega \gg \Delta$. The optical response in absorption and reflection to T_c was detected both in VIS and MIR.^{9–12} The subsequent experiments confirmed the occurrence of this peculiar effect in YBaCuO and other HTSC in a wide range of doping. It was shown that the response arose under optical transitions belonging to the conducting plane of CuO_2 . The T dependence of the differential absorption coefficient at fixed frequency $\Delta\alpha_\omega(T)l = [\alpha_\omega(T) - \alpha_\omega(T_0)]l$ (for the CT maxima at 2.6 eV) is shown in Fig. 2a and that for the differential absorption coefficient of the MIR maximum at 0.6 eV is shown in Fig. 2b. As it can be seen, the T_c point coincides closely with the kink of the functions $\alpha_\omega(T)$. Note that the optical response to the SC transition in HTSC was also detected in luminescence spectra on oxygen F centers at frequencies near 2–3 eV.¹³

The temperature behavior of the optical spectra in YBaCuO was found to be uncommon. Below T_c one can

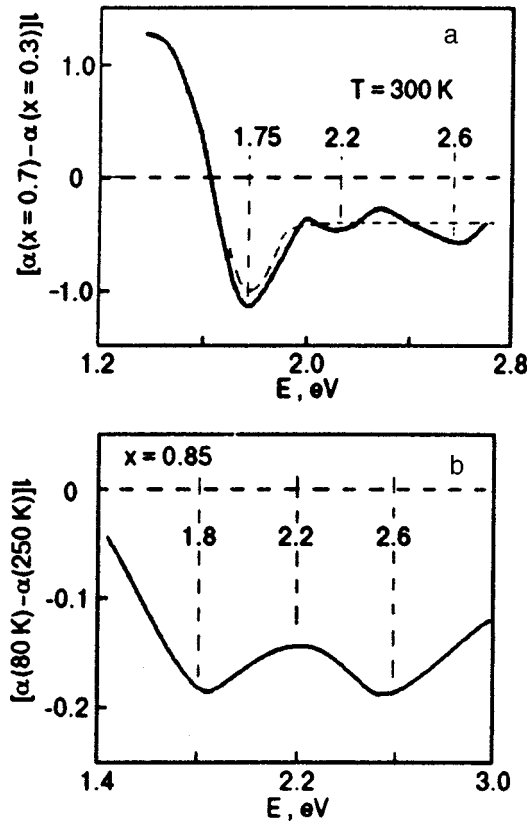


FIG. 3. The differential absorption spectra in YBCO in the CT interband region of frequencies: on doping from $x=0.3$ to 0.7 at RT (a); on cooling from $T=250$ K to 80 K for $x=0.85$ (b).

observe a continuous freezing of the T dependences. Particularly striking is the T behavior of $\alpha_\omega(T)$ and $R_\omega(T)$ for the normal state at $T > T_c$: for the regimes of underdoping and optical doping the T dependences of the absorption and reflection coefficients have different signs in the VIS and MIR region: both $\alpha_\omega(T)$ and $R_\omega(T)$ are increasing functions of T in VIS and they are decreasing ones of T in MIR (see Fig. 2a and b and Refs. 8 and 10). However, in the overdoping regime ($x=0.95$) the CT transitions in VIS undergo fundamental changes with temperature and the VIS spectral function (T) measured decreases with temperature similar to the MIR one.⁸ It is like that the correlation spectral weight redistribution is terminated in the overdoping regime where YBaCuO becomes an uncorrelated metal, in which the upper and lower Hubbard bands are merged together.

Take note that the dependences $\alpha_\omega(T)$ and $R_\omega(T)$ have no selective character in frequency and the T changes touch on the whole wide region in the VIS and MIR spectra. The differential absorption spectra $\Delta\alpha(\omega)l = (\alpha^f(\omega) - \alpha^i(\omega))l$ (where f and i mark the final and initial conditions of the measurements) are shown in Fig. 3a for doping and in Fig. 3b for cooling from 250 to 80 K (for comparison). In both cases one can observe a decrease in the integral spectral weight of the CT absorption in favor of the MIR absorption under cooling as well as under doping (but the scale of the T effect is much smaller than that of the doping one). Another remarkable common feature of the spectral evolution under doping and T variations is the existence of the crossover

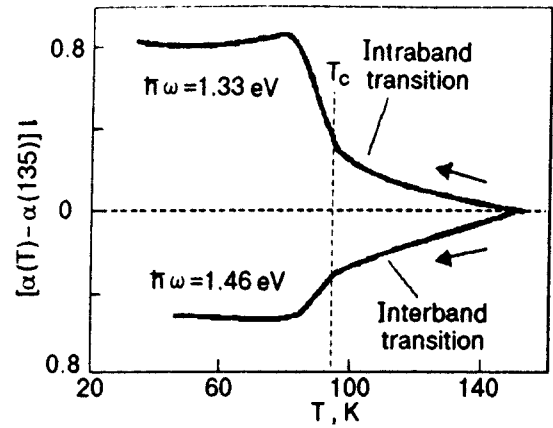


FIG. 4. Temperature dependences of the differential absorption coefficient for two frequencies in the vicinity of the crossover point (the upper curve for $\hbar\omega < \hbar\omega_{cr}$, the lower curve for $\hbar\omega > \hbar\omega_{cr}$).

point ω_{cr} positioning near E_g and dividing the VIS interband and the MIR intraband transitions: $\omega_{cr}=1.55$ eV at doping and $\omega_{cr}=1.4$ eV at T variations (Fig. 4). It is seen that the overall integral spectral weight redistribution from VIS to MIR occurs on around the crossover point at which $\Delta\alpha_\omega = 0$.

The above data on sensitivity of spectral functions to T_c and on their different signs of the temperature dependences above and below the crossover point are in agreement with the results in Ref. 14. In this work the ratio of reflection coefficients for the superconducting and the normal phases near T_c was measured by applying the temperature modulation of HTSC samples. The data of the measurements are shown in Fig. 5 for a BiCaCuO film. As is evident, the response of the reflection spectra to the SC transition is prominent for the 1.0 – 2.5 eV region, within which there is an crossover point ($\hbar\omega \cong 1.4$ eV). Since the temperature modulation range nearby T_c was quite narrow (± 5 K), it is believed that the peculiarity nearby T_c is jumplike in character. It should be noted that by the data on reflection shown in Fig. 5 the jump scale is $\Delta R/R \cong 0.3\%$ while by our data on absorption (Fig. 4) it is equal to $\Delta\alpha/\alpha \cong 1$ – 2% .

The data shown suggest an idea of the T -induced correlation redistribution between VIS and MIR spectra and the strong coupling of oscillators at CT and MIR transitions. Our

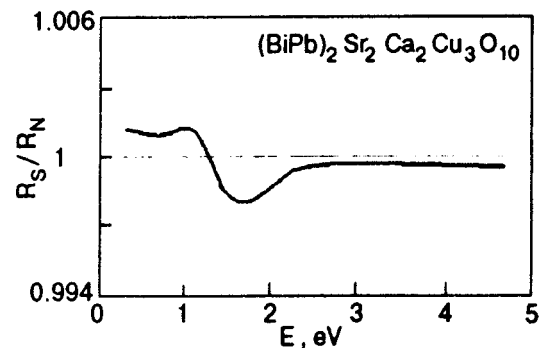


FIG. 5. The superconducting to normal-state reflectance ratio, R_s/R_n of Bi-contained HTSC at $T=90$ K (R_s/R_n deviates significantly from unity at energies 0.5 – 2.5 eV).¹⁴

data are interesting because they were obtained at LT under the conditions where the charge transfer between CuO_2 and CuO_x planes is hindered. It is known that with decrease in temperature down to the pseudogap state, the interaction between the CuO_2 and the CuO_x planes is sharply diminished (there occurs a strengthening of the two-dimensionality of the CuO_2 plane), as evidenced by the considerable reduction in the optical conductivity along the c axis at frequencies of the scale of the pseudogap value $\hbar\omega < 40$ meV.⁶ It is obvious that this process reflects the freezing of charge transfer between the different planes of the YBCO cell.

So, there exists an optical response of all the spectral functions at frequencies hundreds times higher than the superconducting gap which is opened under the transition of HTSC systems to a superconducting state. It may be assumed that this nonconventional effect in HTSC is responsible for by a high ratio $(\Delta/\varepsilon_F)^2 \cong 10^{-2}$ which determines the effect scale and is hundreds times more than that in conventional BCS materials. The optical response mechanism was considered theoretically from different viewpoints in Refs. 15 and 16 and still remains debatable. Moreover, the sensitivity of spectral functions to T_c occurs against the background of temperature-induced correlation mixture low- and high-frequency excitations. Therefore, the optical response suggests that either (i) superconductivity stimulates an extra additional correlation redistribution of excitations or (ii) high-frequency excitations of 1 eV are directly involved in the mechanism of high- T_c superconductivity.

PHOTODOPING AT LOW TEMPERATURES

One of the important questions of the optical spectroscopy of HTSC is the question of photoirradiation critical dose, D_0 , and the threshold spectral energy, $\hbar\omega_{th}$, which determine permissible doses and energies of photoirradiation without persistent photoinduced effects in the lattice structure and in the current characteristics. It is known that a HTSC material is sensitive to exposure dose in VIS with the threshold spectral energy $\hbar\omega_{th} > \hbar\omega_g$ (in the region of the CT transitions) and with the doses $D > D_0 \cong 10^{19-20}$ photon/cm². That is, using these conditions of photoirradiation at RT it becomes possible to observe an enhancement of T_c in HTSC underdoped samples after photopumping.^{5,17,18} The accepted explanation of the photoinduced conductivity is based on the assumption that the photoexcitation at RT causes the ordering of oxygen vacancies in the CuO_x chains that in turn leads to a subsequent transfer of electrons between the CuO_2 and the CuO_x planes and the emergence of excess holes in CuO_2 .¹⁷

At the same time in some works it is found that the threshold dose of photoinduced effects become less by about two orders of magnitude if photopumping is carried out at low temperatures, $D_0 \approx 10^{17}$ photon/cm².^{9,19} The progressive increase of photodoping and the LT photoinduced phase transition of $\text{Y}_1\text{Ba}_2\text{Cu}_3\text{O}_{6.35}$ from the dielectric to a metallic state can be traced by the dose dependence of the absorption coefficient. Figure 6 shows the changes in the absorption coefficient as compared to the initial moment of irradiation with a light of $J = 2 \times 10^{13}$ photon·s⁻¹ cm⁻² at 80 K of

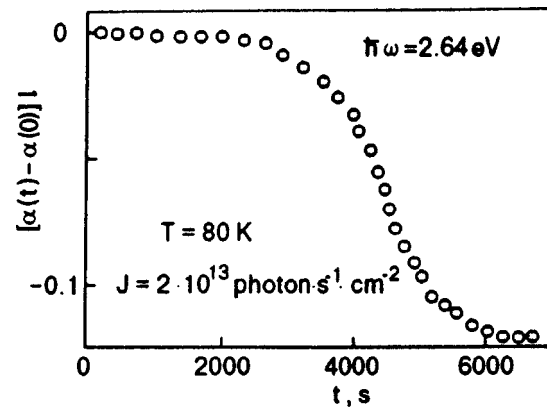


FIG. 6. Dose dependence of the absorption in YBCO with $r=0.35$ under irradiation and at measurements with $\hbar\omega=2.64$ eV. At doses $D=Jt > 10^{17}$ photon·cm⁻² the sharp decrease of VIS absorption occurs due to photoinduced insulator-metal phase transition.

$\text{Y}_1\text{Ba}_2\text{Cu}_3\text{O}_{6+x}$ ($x=0.35$). As is evident, there occurs a sharp passage of the dependence $\Delta\alpha_\omega(t)$ to saturation at $D > Jt \approx 10^{17}$ photon·cm⁻², suggesting the insulator—metal phase transition. It should be mentioned that the phase transition under LT photopumping follows the pattern of the second-kind phase transition. In Fig. 7 the process manifestation of YBaCuO metallization under LT photopumping is seen from the temperature dependence of the absorption coefficient. The upper curve (on cooling the sample) corresponds to the dielectric state of YBaCuO with $x=0.35$ prior photopumping. As is evident, in this case the behavior of $\alpha(T)$ is temperature independent, which is typical of the insulator phase. After exposure of the sample to the light flux of $D=10^{17}$ photon·cm⁻² at 80 K and with subsequent increase in temperature, one can observe a temperature dependence of absorption typical of HTSC metals (compare with Fig. 2b). At $T=135$ K a sharp reduction in the photopumped holes occurs due to their recombination with electrons so that the sample reverts to the original initial insulator state. The temperature of the reduction in the photopumped carriers (the threshold temperature) is dependent on doping of samples. The threshold temperature $T_{th}=135$ K was also

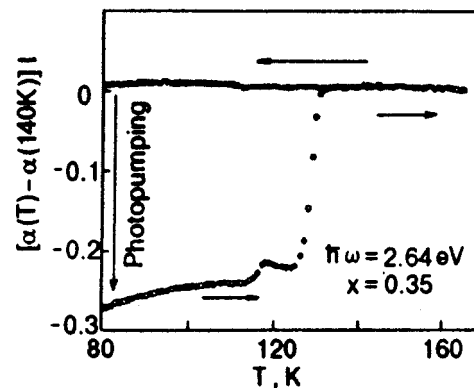


FIG. 7. Temperature dependences of the differential absorption coefficient in YBCO with $x=0.35$ before (the upper curve) and after (the lower curve) LT photopumping with $\hbar\omega=2.64$ eV, $D=10^{17}$ photon·cm⁻².

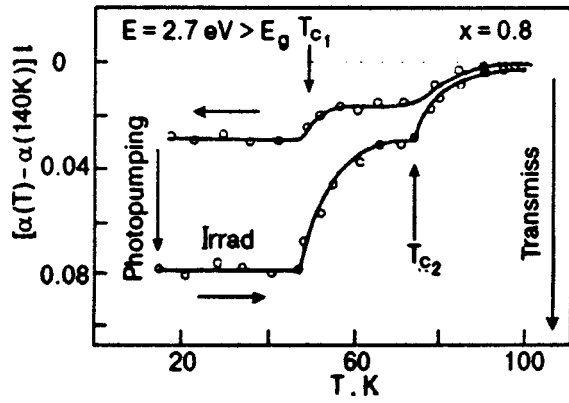


FIG. 8. Temperature dependences of the absorption in YBCO with $x=0.8$ before (the upper curve) and after (the lower curve) LT photopumping into SC phase with $\hbar\omega=2.7$ eV, $D \geq 10^{17}$ photon·cm⁻².

observed in⁴ by the decrease weakening of metallization on the curves $\alpha(T)$.

The effect of photodoping is also observed at immediate pumping into the superconducting phase. The experimental results for a two-phase sample with SC transitions at $T_{c1}=50$ K and $T_{c2}=75$ K are illustrated in Fig. 8. After the LT photopumping the sample is seen to become more transparent and with subsequent heating it returns to the initial state. The sharp decrease in the nonequilibrium concentration of photopumped holes is occurring at superconducting transition temperatures. We assume that the superconducting state is favorable to the retention of photopumped holes. As is seen from Fig. 9, the photopumping results in the correlation spectral weight redistribution between VIS and MIR, i.e., it acts like chemical doping. We can see a decrease in the integral absorption coefficient in $Y_1Ba_2Cu_3O_{6.8}$ after LT photopumping, i.e., due to the generation of nonequilibrium extra holes.

Our understanding of the process of persistent photodoping at LT is distinguished from the accepted ones at RT and is as follows. We think that the photoinduced holes appear in the valence band as a result of the charge-transfer

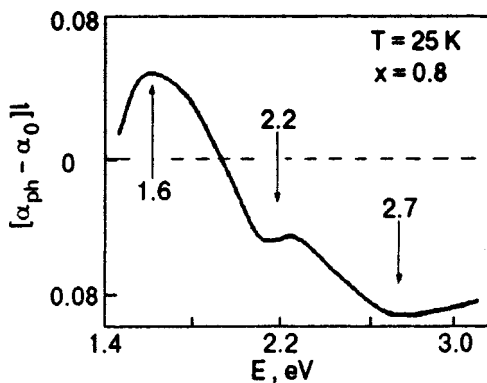


FIG. 9. The differential absorption spectra of YBCO with $x=0.8$ in the CT interband region of frequencies after LT photopumping.

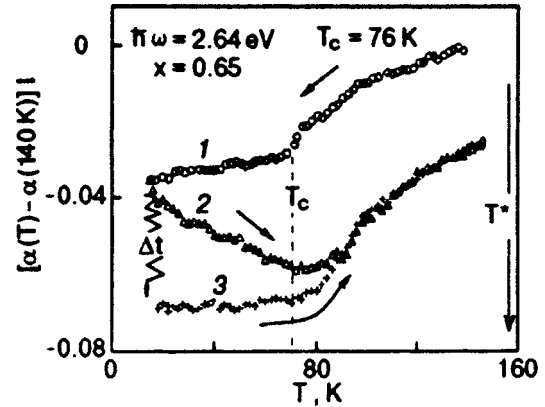


FIG. 10. Nonreversible effect in VIS absorption upon cooling and heating of the underdoped YBCO. Curves 1 and 2 were measured with uninterrupted cooling and heating. Curve 3 was measured after a long pause at 20 K ($\Delta t \approx 40$ min before heating).

excitations in the CuO_2 plane with $\hbar\omega > E_g = 1.6$ eV ($Cu^{2+}O^{2+} \rightarrow Cu^+O^-$). Thus photopumping will be persistent if some obstacles to a reversible process exist. We suggest that a new process arises at LT photopumping that hampers the reversible recombination. This new process is considered in²⁰. It is based on the concept of appropriate generation of low-temperature heavy quasi-particles—fluctuons. The physical concept of fluctuons was first introduced in the physics of solids by I. Lifshitz,²¹ and their phenomenological model was developed in Ref. 22. In HTSC systems a hole fluctuon in the active CuO_2 plane is easily generated through hole trapping by spin fluctuations inherent in the pseudogap state at $T < T^*$. In the 2D case particularly deep fluctuon wells are generated with reduction in temperature, the well depth increasing as T^{-2} .²⁰ It is the hole trapping by these spin fluctuons that results in the retention and accumulation of photoinduced holes. As the number of photoinduced holes increases, the fluctuon-fluctuon interaction determines a non-linear process of photopumping (Fig. 6) and gives rise to an infinite metallic cluster following the pattern of the second-order phase transition.

So, the LT photopumping of HTSC at $T < T^* \approx 150-200$ K (in the pseudogap state) with reduced threshold doses may be attributed to the effective hole trapping by spin fluctuations followed by generation of heavy fluctuons. It is likely that it is heavy fluctuons that determines a temperature- and photo-dependent addition to the spectral weight of the MIR region at LT, resulting in the correlation redistribution in the CuO_2 plane.

THE LT RELAXATION IN YBCO SAMPLES OBSERVED IN OPTICAL SPECTROSCOPY

Yet another low-temperature peculiarity in the behavior of spectral functions of HTSC at $T < T^*$ was observed with varying direction and velocity of T scanning of the samples, namely, hysteresis effects in absorption and reflection. The hysteresis loop under cooling and heating of YBaCuO was mentioned in our former work for VIS absorption (Fig. 10)¹²

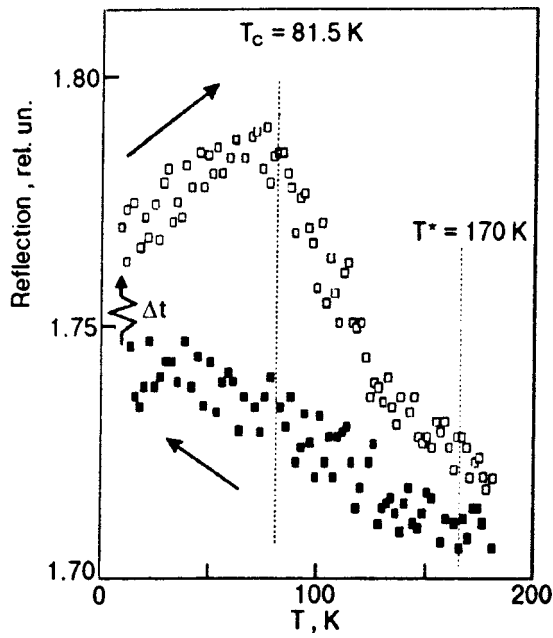


FIG. 11. The reflection spectra of YBCO in MIR region at $\hbar\omega = 0.6$ eV upon cooling and heating.

and then subsequently the same effect was observed in measurements of MIR absorption (Fig. 2) and reflection (Fig. 11). As is evident from Figs. 10 and 11, as the samples are cooled, there occurs an accumulation of nonequilibrium that may be discarded (completely or partially) if the sample is held at LT for Δt . The set of our data suggests that the upper temperature boundary of instability is a temperature in the vicinity of the phase transition from the pseudogap state to states with disordered spins, T^* . The most pronounced hysteresis (electron-structure instability) is displayed by underdoped samples. With increasing doping, the loop area in the spectral function-temperature coordinates reduces, and the loop itself shifts towards lower temperatures. For samples of optimal doping, the hysteresis effects are minimum and may be observed with rather fast temperature cycling between the SC and N phases solely within the $T < T_c$ range. Generally speaking, the occurrence of hysteresis effects is associated with the existence of relaxation processes within a hysteresis loop temperature range. It is important to stress that the hysteresis loop in the MIR spectra is temperature inverse to that of the VIS spectral measurements. This means that the absorption (reflection) coefficient undergoes changes in different directions in VIS and MIR during relaxation (Figs. 10 and 11). All the experiments with instabilities of spectra were performed with low light doses ($D < D_0$). We also carried out a special test-measurement with a dark window during relaxation and therefore we are convinced that the instabilities observed are not associated with the photoinduced effect. Note that the resistive measurements in different HTSC films exhibited no hysteresis effects with a loop span of several percents.

The differential spectra of VIS absorption of a sample with $x = 0.4$ (in the vicinity of dielectric—metal transition) measured for two relaxation times ($t_1 = 5700$ s and $t_2 = 7200$ s) after cooling from 220 to 88 K are plotted

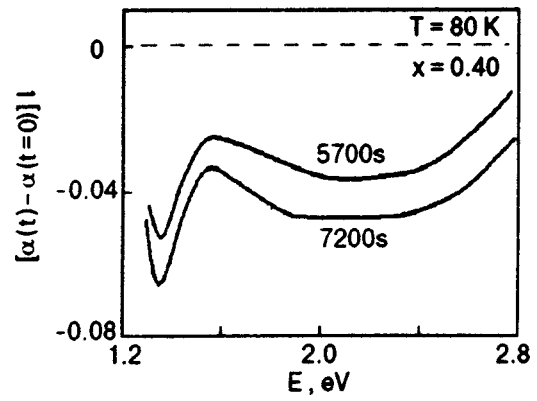


FIG. 12. The differential absorption spectra of YBCO with $x = 0.4$ in CT interband region of frequencies at different time of relaxation after fast cooling.

in Fig. 12. It can be seen that the absorption decreases through the whole VIS region, i.e., the integral bleaching of the CT transitions occurs. The characteristic time of LT-relaxation could be estimated as $\tau \approx (1-2) \cdot 10^3$ s. Time modifications in the absorption and reflection spectra are also observed in the MIR region after rapid cooling down to a certain temperature. These modifications occur with increasing both the integral MIR absorption and the MIR reflection, i.e., during relaxation the MIR and VIS optical characteristics undergo changes in different directions just as it occurs under chemical or photodoping. At the same time, in the near UV region for $\hbar\omega = 4.1$ eV, in which there are optical transitions ($3d-4p$) on local centers of Cu^+ , one cannot observe relaxation effects in absorption at LT, i.e., the concentration of monovalent Cu^+ ions in the chain structure of CuO_x remains unchanged after temperature variations in the $T < T^*$ region (Fig. 13).

Figure 14 presents relaxation curves for the underdoped metal film of $\text{Y}_1\text{Ba}_2\text{Cu}_3\text{O}_{6+x}$ with $x = 0.7$ at $T_c = 70$ K. The data for different temperatures were obtained in sequential measurements upon cooling from 250 K. Differential absorption $\Delta\alpha l = (\alpha^f - \alpha^i)$ vs. T is plotted relative to the initial moment of temperature stabilization (T_i) of $\alpha_i(t=0)$. After each previous case where the curve (t) reached saturation at a

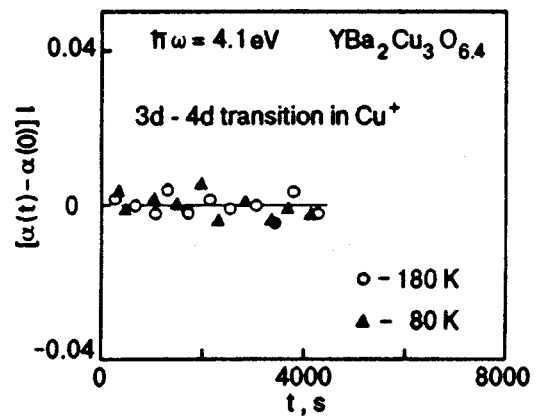


FIG. 13. Time dependence of the differential absorption coefficient at $\hbar\omega = 4.1$ eV after fast cooling of YBCO from 220 K to 180 K (○) and to 80 K (▲).

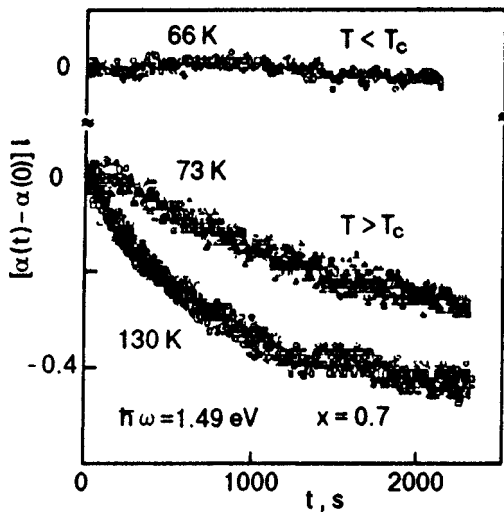


FIG. 14. Time dependences of the differential absorption coefficient at $\hbar\omega = 1.49$ eV in process of relaxation after cooling to different temperatures $T > T_c = 70$ K and $T < T_c$.

certain temperature, the temperature was quickly decreased to a next level and relaxation was measured once again and so on. On this slow cooling, upon reaching the equilibrium state (saturation) one can see that relaxation is absent below $T < T_c$.

It seems to be likely that the T -induced time instability revealed in VIS optical absorption of CT transitions, which belong to the CuO_2 plane, reflects the inherent electron (spin)-structure relaxation in the active CuO_2 plane at LT variations. In the course of this relaxation the spectral weight redistribution from the VIS to the MIR region occurs. If we accept this assumption, two questions arise immediately: 1) what is the nature of the electron-structure relaxation at low temperatures? 2) what is the reason why the LT relaxation is not so clearly observed in experiments on the dc resistivity?

Let us remember that the T -induced structure relaxation resulting in ortho-ordering and variations of spectral functions of HTSC samples after fast cooling from high temperature (400 °C) down to RT are described in a series of papers.^{3,23} The commonly accepted model of RT relaxation of an order parameter is based on the mechanism of diffusion rearrangement of oxygen vacancies making the copper-oxygen chain (Cu–O–Cu) along the b -axis in CuO_x longer and following the charge transfer between the CuO_x and CuO_2 planes. One of the arguments in favor of this model was the evidence for the variations of the Cu^+ concentration (the variations observed in the optical reflection of the $(3d - 4d)$ transitions of the Cu^+ ions at 4.1 eV vs. time³).

In contrast to the RT relaxation of the spectral functions, the LT relaxation of the CT interband and MIR intraband spectral weights is not accompanied by variations of the Cu^+ concentration (Fig. 13). This result is against the electron-structure rearrangement in CuO_x , where the Cu^+ ions reside, and the evidences that the LT relaxation occurs exactly in the CuO_2 plane without any charge transfer between the planes (the interplane charge transfer is likely to be hindered at LT). We assume that the most reliable explanation of the LT relaxation of the spectral functions in VIS and MIR is the

temperature-induced spin structure rearrangement in the Cu^+ plane due to the formation of hole-spin fluctuons at LT. Strong influence of the system prehistory and its cooling rate on the LT state and long relaxation times in underdoped HTSC suggest that these are similar to irreversible effects in nonergodic systems with competing interactions (for example, to structural or spin glasses²⁴). From this viewpoint, the transition to the pseudogap state at T^* may be considered as a transition to a nonergodic system where ordering regions alternate with disordering ones. In the fluctuon model the ordering occurs within a region round a hole trapped by spins. Note also that the concept of holes trapped in a spin bag²⁵ as well as the concept of holes trapped in the \langle string \rangle potential created by AF background,²⁶ or the model of stripes, that is the subject of wide speculation,²⁷ are not dramatically different from our pattern of hole-spin fluctuons.

Thus, we think it quite reasonable to associate the LT instability of optical spectra and the effective photodoping at low temperatures with two processes—the hole trapping by spin fluctuons at low temperature and the induced spectral weight redistribution from VIS to MIR (due to strong correlation).

In parallel with the fluctuon domains where the trapped heavy holes reside, there exists a current network for light holes. Therefore, the light and heavy holes are in dynamic equilibrium resulting from the competition between the superexchange energy lost near a trapped hole and its kinetic energy. The spectral weight of intraband transitions is distributed between the contributions from light and heavy carriers. Note that in the MIR region the contribution from heavy holes is dominant while in the far low-frequency region ($\omega \rightarrow 0$) the contribution from light holes is prevalent. The measurements of HTSC sample resistivity ($\omega \rightarrow 0$) reveal mainly the contribution of light carriers not related to the spin-structure relaxation. d.c. conductivity $\sigma(0)$ is defined by plasma frequency $\omega_p^2 \sim n_L(T, t)$ and damping $\Gamma(T, t)$ (where n_L is the number of light carriers): $\sigma(0) \sim n/\Gamma$. The relative changes $\Delta\sigma/\sigma$ in the experiments with varying T (or due to relaxation) are $\Delta\sigma/\sigma = \Delta n/n - \Delta\Gamma/\Gamma$. As is evident from the optical measurements, $\Delta n/n \sim \Delta\alpha/\alpha \approx 5\%$. At the same time $\Delta\Gamma/\Gamma \sim \Delta T/T$ and amounts to 50%. Therefore, unlike the optical measurements, the resistive ones do not sense relaxation and temperature variations associated with the number of carriers and show mainly the T variations in damping of light carriers.

So, the optical data reveal the dramatic effects of non-equilibrium inherent in HTSC systems after their fast cooling to the pseudogap state region below T^* . The effects are most pronounced for underdoped samples and much weaker for the optimal doping regime. Generally speaking, the high nonequilibrium resulted from the competitive interactions occurring in the HTSC system which bring two types of carriers (holes) with different spin surrounding into dynamic coexistence: light (coherent) holes and heavy holes trapped in a spin bag. As a result, the optical conductivity is determined by two contributions—a coherent part at the expense of Drude-like light carriers and a noncoherent one at the expense of heavy hole fluctuons. The optical relaxation observed arises from the self-consistent hole trapping by spin

fluctuations and the subsequent spin ordering inside a fluctuation. In this case the ordering time is supposed to be $\tau \approx \exp(a\sqrt{N})$, where $N \gg 1$, the number of spins in a fluctuation, may be rather high.

CONCLUSION

After the discovery of high- T_c superconductivity a great number of works were concentrated on the problem of adequate description of the behavior of electrons in anisotropic cuprates. For the analysis of the above optical results we used the consequences of the theoretical concepts developed in a series of theoretical works as a basis. These works are directly or indirectly connected with a broader Hubbard-like model of strongly correlated 2D electrons submerged in spin media.^{26,28–33} One of the important general results of these theories is that the behavior of holes in the AF background is accounted for by the competition between the superexchange energy lost near a hole and its kinetic energy. Thus, the Hubbard-like model evidences that there is a dynamical coexistence of mobile (coherent) holes and heavy holes trapped in a spin bag. The impressive calculations of the temperature evolution of DOS in terms of the Hubbard model are carried out in.³³ Away from half-filling of a lower Hubbard band a sharp resonance peak appears near the chemical potential. As the doping is increased the resonance width also increases and it starts to merge with the lower Hubbard band. For the overdoping regime, both low-energy peaks are indistinguishable, implying that the system has become an uncorrelated ordinary metal. The narrow peak in DOS evolves like the MIR band in the optical spectra. The narrow peak appears to be strongly temperature dependent, thus it is pronounced only in the region of low temperatures and within a regime that extends from underdoping to optical doping.

Recent low-temperature experimental and theoretical works have made it clear that in HTSC materials there appears a state below $T < T^*$ that is precursory to superconductivity. The temperature T^* coincides with the temperature of the pseudogap opening with spin singlet ordering. This LT precursory region turns out to be optically active in the absorption and reflection spectra. Using the basic consequences of the theory of correlated electrons and the optical experimental findings, we propose the following principal ansatz:

1. The consistent concept of strongly correlated hole excitations interacting with spin fluctuations in the CuO_2 plane is attractive for understanding and interpreting the anomalous optical effects in HTSC at LT having no analogue with conventional BCS superconductors (the sensitivity to T_c , the T -induced spectral weight redistribution, the LT relaxation of optical functions, the LT-enhanced photodoping).

2. A nontrivial consequence of the correlation model in the intermediate regime is the coexistence of light (Drude-like) and heavy (hole-spin-fluctuations) holes, the latter being generated in the LT region below the temperature of spin ordering (opening spin gap). Thus, the high- T_c superconductive scenario is realized in dynamical two-component systems of carriers.

3. Subsystems of light and heavy carriers are in dynamical equilibrium upon doping or T variations. If the doping of

HTSC is increased the localization effects are weakened, while if the temperature is decreased, the localization effects become stronger and the density of heavy trapped holes increases. Thus, the temperature serves as fine tuning for high- T_c superconductivity.

ACKNOWLEDGMENTS

We are pleased to express our deep gratitude to Prof. G. Saemann-Ischenko and his colleagues for their useful scientific cooperation and preparation of HTSC samples for our optical measurements. We are grateful to Prof. H. Kinder and Dr. P. Berberich for providing the samples for the MIR measurement. The authors wish to express their thanks to S. Uytunov for his help during optical measurements. Some of results of this work were delivered at the NATO-ASI Conference ‘‘Materials Science, Fundamental Properties and Future Electronic Applications of High- T_c Superconductors’’ (September, 1998).

¹S. Uchida, I. Ido, H. Takagi, T. Arima, Y. Tokura, and S. Tojima, Phys. Rev. B **43**, 7942 (1991).

²S. L. Cooper, D. Reznik, A. Kotz, M. A. Karlow, R. Liu, M. V. Klein, and W. C. Lee, Phys. Rev. B **47**, 8233 (1993).

³J. Kircher, M. Cardona, A. Zibold, K. Widder, H. P. Geserich, J. Giapintzakis, D. M. Ginsberg, B. W. Veal, and A. P. Paulikas, Phys. Rev. B **48**, 9684 (1993).

⁴G. Yu, C. H. Lee, D. Mihailovic, A. J. Heeger, C. Fincher, N. Herron, and E. M. McCarron, Phys. Rev. B **48**, 7545 (1993).

⁵V. Kudinov, A. Kirilyuk, N. Kreines, R. Laiha, and E. Lahderanta, Phys. Lett. A **151**, 358 (1990).

⁶A. V. Puchkov, D. N. Basov, and T. J. Timusk, J. Phys.: Condens. Matter **8**, 10049 (1996).

⁷C. M. Varma, Int. J. Mod. Phys. B **3**, 2083 (1989).

⁸I. Fugol and V. Samovarov, in *Studies of HTSC (Advances in Research and Applications)*, v. 22 A. Narlikar (Ed). Nova Science, Commack, New York (1997).

⁹I. Fugol, G. Saemann-Ischenko, V. Samovarov, Yu. Rybalko, V. Zhuravlev, Y. Strobel, B. Holzappel, and P. Berberich, Solid State Commun. **80**, 201 (1991).

¹⁰H. L. Dewing and E. K. H. Salje, Supercond. Sci. Technol. **5**, 50 (1992); J. Solid State Chem. **100**, 363 (1992).

¹¹C. H. Ruscher, M. Gotte, B. Schmidt, C. Quitmann, and G. Guntherodt, Physica C **204**, 30 (1992).

¹²I. Fugol, V. Samovarov, A. Ratner, V. Zhuravlev, and G. Saemann-Ischenko, Solid State Commun. **86**, 385 (1993); Physica C **216**, 391 (1993).

¹³I. Fugol, C. Politis, A. Ratner, V. Samovarov, and V. Zhuravlev, J. Lumin. **62**, 291 (1994).

¹⁴H. J. Holcomb, C. L. Perry, J. P. Collman, and W. A. Little, Phys. Rev. B **53**, 6734 (1996).

¹⁵J. E. Hirsch, Physica C **199**, 305 (1992); *ibid.* **201**, 347 (1992).

¹⁶A. S. Alexandrov, A. M. Bratkovshy, N. F. Mott, and E. K. H. Salje, Physica C **215**, 359 (1993).

¹⁷E. Osquiquil, M. Maenhoudt, and B. Wayts, Phys. Rev. B **49**, 3675 (1994).

¹⁸V. M. Dmitriev, V. V. Eremenko, I. S. Kachur, V. G. Piryatinskaya, O. R. Prikhod'ko, A. M. Ratner, E. V. Khristenko, and V. V. Shapiro, Fiz. Nizk. Temp. **21**, 219 (1995), [Low Temp. Phys. **21**, 168 (1995)].

¹⁹G. Yu, C. H. Lee, A. J. Heeger, N. Herron, E. M. McCarron, and Lin Cong, Phys. Rev. B **45**, 4964 (1992).

²⁰L. Kukuschkin, V. Samovarov, M. Libin, and I. Fugol, Fiz. Nizk. Temp. **22**, 375 (1996) [Low Temp. Phys. **22**, 290 (1996)].

²¹I. M. Lifshitz and S. Gredeskul, Zh. Éskp. Teor. Fiz. **57**, 2209 (1969) [Sov. Phys. JETP **30**, 1197 (1969)].

²²M. Krivogla, Uspekhi. Fiz. Nauk. **111**, 617 (1973) [Sov. Phys. Usp. **16**, 856 (1974)].

- ²³H. Shaked, J. Jorgensen, B. Hunter, R. Hittermen, A. Paulikas, and B. Veal, Phys. Rev. B **51**, 547 (1995).
- ²⁴S. L. Ginzberg, in *Irreversible Phenomena of Spin Glasses*, Nauka, Moscow (1989).
- ²⁵J. R. Schrieffer, X.-G. Wen, and S.-C. Zhang, Phys. Rev. B **39**, 11 663 (1989).
- ²⁶E. Dagotto, Rev. Mod. Phys. **66**, 763 (1994).
- ²⁷B. Levi, Phys. Today, June, 19 (1998).
- ²⁸H. Eskes, M. Meinders, and G. Sawatzky, Phys. Rev. Lett. **67**, 1035 (1991).
- ²⁹B. Stojkovic and D. Pines, Phys. Rev. B **55**, 8575 (1997).
- ³⁰S. M. Quinlan, P. J. Hirschfeld, and D. J. Scalapino, Phys. Rev. B **53**, 8575 (1996).
- ³¹A. Sherman and M. Schreiber, Phys. Rev. B **50**, 12 887 (1994).
- ³²V. M. Loktev, Fiz. Nizk. Temp. **22**, 3 (1996) [Low Temp. Phys. **22**, 1 (1996)].
- ³³Th. Pruschke, M. Jarrell, and J. K. Freerecks, Adv. Phys. **44**, 187 (1995).

This article was published in English in the original Russian journal. It was edited by R. T. Beyer.

LOW-TEMPERATURE MAGNETISM

Critical properties of the model of antiferromagnet Cr_2O_3

A. K. Murtazaev

*Institute of Physics, Dagestan Science Center, Russian Academy of Sciences, 367003 Makhachkala, Russia**

(Submitted September 8, 1998; revised December 14, 1998)

Fiz. Nizk. Temp. **25**, 469–477 (May 1999)

The critical properties of the model of real antiferromagnet Cr_2O_3 are investigated by the Monte Carlo method. The static critical exponents α , β , and γ are calculated for systems with periodic boundary conditions containing from 500 to 4000 spins. It is shown that the values of critical exponents, the type of critical behavior, and crossover effects are determined to a considerable extent by the relation between the interaction and anisotropy constants. The results are compared with the theoretical data and with the results of laboratory investigations of Cr_2O_3 . The critical parameters calculated by approximating the data by traditional exponential functions are compared with the values obtained on the basis of the finite-size scaling theory. © 1999 American Institute of Physics. [S1063-777X(99)00705-7]

INTRODUCTION

An analysis of phase transitions and critical phenomena on the basis of three-dimensional microscopic Hamiltonians remains a central problem in modern statistical physics.^{1,2} In recent years, the attention of the researches has been diverted towards more realistic models which take into account peculiarities existing in real systems but disregarded in the simplest models (such as classical Ising and Heisenberg models). We are speaking of the effects associated with the presence of various types of anisotropy, dipole–dipole, and many-spin interaction and a number of other phenomena. The inclusion of such factors becomes especially important near critical temperatures. A rigorous investigation of three-dimensional microscopic Hamiltonians of complex real systems by the methods of modern theoretical physics is an extremely complicated problem.

In this connection, the role of the computational methods such as the Monte Carlo (MC) method increases significantly.³ These methods make it possible to investigate (to a high degree of accuracy and over a wide range of various physical parameters systems that are not accessible easily for theoretical investigations. Till recently, the critical region for various systems undergoing phase transitions was investigated by the methods of numerical experiment only at a qualitative level. In recent years, MC methods have also been used for studying the critical region for an analysis of critical exponents (CE) and critical amplitudes (CA). The accuracy attained is not worse, and is sometimes even better, than in best results obtained by other methods.^{4–8} Such impressive results naturally could not be ensured only by improving computational abilities of modern computers without application of some new ideas and approaches, among which we must mention the development of powerful cluster algorithms of the MC method^{9–11} and histogram methods of data analysis^{12–14} on one hand and the application of the

ideas underlying the theory of finite-size scaling (FSS) for calculating critical parameters.^{15–17}

Till now, ordinary ferromagnetic systems with interaction between nearest neighbors and with simple lattices have mainly been investigated,^{5–7} while more complex and realistic antiferromagnetic models and the models for specific magnetic materials taking into account their peculiarities and specific properties were studied less comprehensively.

Another important aspect of an analysis of models of real magnetic materials by the MC methods is associated with the possibility of comparing the results of numerical analysis not only with theoretical predictions, but also with experimental results. This is especially important when the results of laboratory investigations of critical phenomena are contradictory and cannot provide an unambiguous answer to some important questions.

In this paper, we analyze critical phenomena in models of the real antiferromagnet Cr_2O_3 . The interest to this material is due to the following circumstances.

- (1) Cr_2O_3 is a multisublattice uniaxial weakly anisotropic AFM with a complex crystallographic structure, in which the interactions of each Cr ion (spin) not only with first, but also with second nearest neighbors are significant. Critical phenomena of this type virtually have not been investigated by the numerical experiment method.
- (2) The AFM Cr_2O_3 has a phase-transition temperature $T_N=307$ K convenient for laboratory experiments and has been studied in detail. However, the results of laboratory investigations of the critical properties of Cr_2O_3 do not lead to a complete and rigorous pattern of the critical behavior of Cr_2O_3 ^{18,19} and do not allow us to determine the dependence of critical parameters on thermodynamic quantities. This problem can be solved by a

numerical experiment in which all the quantities are controlled.

MODEL AND METHOD OF INVESTIGATIONS

It was found that Cr₂O₃ is an AFM of the easy-axis type with the Neel temperature ~307 K. It has the structure of corundum and a rhombohedral unit cell. Four magnetic Cr ions are located on the spatial diagonal [111], and the easy magnetization axis *z* coincides with this direction.^{18,19} It was found from the experiments on neutron scattering and the spin wave theory that interactions between first and second nearest neighbors are most significant in Cr₂O₃.²⁰ Taking into account these peculiarities, we can write the Hamiltonian of Cr₂O₃ in zero magnetic field in the form^{21,22}

$$H = -\frac{1}{2} \sum_{i,j} J_1(\mu_i \mu_j) - \frac{1}{2} \sum_{k,l} J_2(\mu_k \mu_l) - D \sum_i (\mu_i^z)^2, \quad (1)$$

$$|\mu| = 1,$$

where *J*₁ is the parameter of exchange interaction of each Cr ion with a nearest neighbor at a distance *r*_{ij} = 2.65 Å and *J*₂ a similar parameter of interaction with three next neighbors at a distance *r*_{kl} = 2.89 Å (*J*₁ = 2.2*J*₂, *J*₁ < 0, *J*₂ < 0).²⁰ Foner²³ proved that the anisotropy in Cr₂O₃ is due to dipole-dipole interaction and magnetic crystallographic anisotropy, while calculations made by Artman *et al.*²⁴ demonstrated that the second type of anisotropy is almost twice as strong as the first type. For this reason, relativistic interactions of various types were approximated by the effective single-ion anisotropy *D* > 0.

In our opinion, it is necessary to consider the following values of the ratio of anisotropy *D* and exchange *J*₁:

D/*J*₁ = 2.5 · 10⁻⁴, corresponding to real Cr₂O₃ samples and *D*/*J*₁ = 2.5 × 10⁻², typical of small magnetic systems with axial anisotropy and a size of a few tens of angstroms.^{24,25}

The former case will be referred to as model I and the latter as model II. All crystallographic, exchange, and other data used for model I correspond to real Cr₂O₃ samples. In model II, the value of anisotropy constant *D* corresponds to small magnetic systems (particles) since the system simulated by the MC method have finite linear dimensions (*L* ≪ ∞, *L* ∝ *N*^{1/3}) in spite of periodic boundary conditions (PBC) imposed on them and exhibit some properties typical of small systems.

The calculations were made for systems with PBC by the Monte Carlo method on the basis of the standard Metropolis algorithm.³ The systems under investigation contain *N* = 500, 864, 1372, 2048, 2916, and 4000 spins. In order to attain thermodynamic equilibrium in each system, we cut off a segment of Markov's chain having a length up to 3 × 10⁴ MC steps/spin, which is longer than the nonequilibrium segment by a factor of several units. Then averaging was carried out over an equilibrium region of 12 × 10⁵ MC steps/spin. The accuracy of the results was controlled by carrying out test experiments in which these values were doubled. A noticeable improvement of the results of calculations was not observed.

RESULTS OF CALCULATIONS

The temperature dependence of heat capacity *C* and susceptibility *χ* were analyzed by using the following expressions based on the fluctuation-dissipation theorem:⁶

$$C = (NK^2)(\langle U^2 \rangle - \langle U \rangle^2), \quad (2)$$

$$\chi = (NK)(\langle m^2 \rangle - \langle m \rangle^2), \quad (3)$$

where *K* = |*J*₁|/*k_BT*, *U* is the internal energy, and *m* the sublattice magnetization.

Figure 1 shows the dependences of heat capacity *C* and susceptibility *χ* for systems with different number of spin on temperature *T* (here and below, the temperature is given in the units for which *k_B*/*J*₁ = 1). It can be seen from Fig. 1a that the maximum values of heat capacity *C*_{max} for systems with different number of spins in the Cr₂O₃ model coincide on the temperature scale to within experimental error. As the value of *N* increases, only the absolute values of *C*_{max} become higher. Similar peculiarities are also manifested in susceptibility (see Fig. 1b). Such systems usually exhibit effects associated with a displacement of *C*_{max} and *χ*_{max} upon a change in the number *N* of spins (or *L* ∝ *N*^{1/3}) even under PBC. The absence of such peculiarities indicates the the method of imposing PBC used by us successfully removes various boundary effects. Nevertheless, the temperatures corresponding to the peaks of heat capacity *C*_{max} and susceptibility *χ*_{max} do not coincide. Figure 2 shows the dependence of the sublattice magnetization *m* on the temperature *T* for two systems with *N* = 864 and 2916. We observe a monotonic decrease in *m*. It should be noted that the effects associated with a finite number *N* of spins (including residual magnetization in the high-temperature phase, are weakened strongly with increasing *N*. The critical temperature determined from the data presented in Figs. 1 and 2 contains a large error.

In the general case, the MC method also encounters considerable difficulties in determining the true phase-transition temperature *T_c* (*L* = ∞) in such systems. This is also due to the fact that the effective transition temperature *T_c* is often a function of *L* even in the presence of PBC. Besides, the values of *T_c* determined from the peaks of heat capacity *T_c*(*C*_{max}) and susceptibility *T_c*(*χ*_{max}) virtually do not coincide as in our case. Various difficulties are encountered when *T_c* is determined by other methods.

Obviously, the situation has changed since Binder²⁵ proposed the method of fourth-order cumulants of magnetization *U_L* for determining *T_c*:

$$U_L = 1 - \frac{\langle m^4 \rangle}{3\langle m^2 \rangle^2}, \quad (4)$$

where *m* is the magnetization per spin.

This method can be used for determining the transition temperature of systems with different linear sizes. As a matter of fact, the cumulants *U_L* calculated accurately for systems of any size must intersect at a point with temperature *T* = *T_c*(*L*) according to the finite-size scaling (FSS) theory.¹⁵⁻¹⁷ Many aspects of determination of *T_c* by this

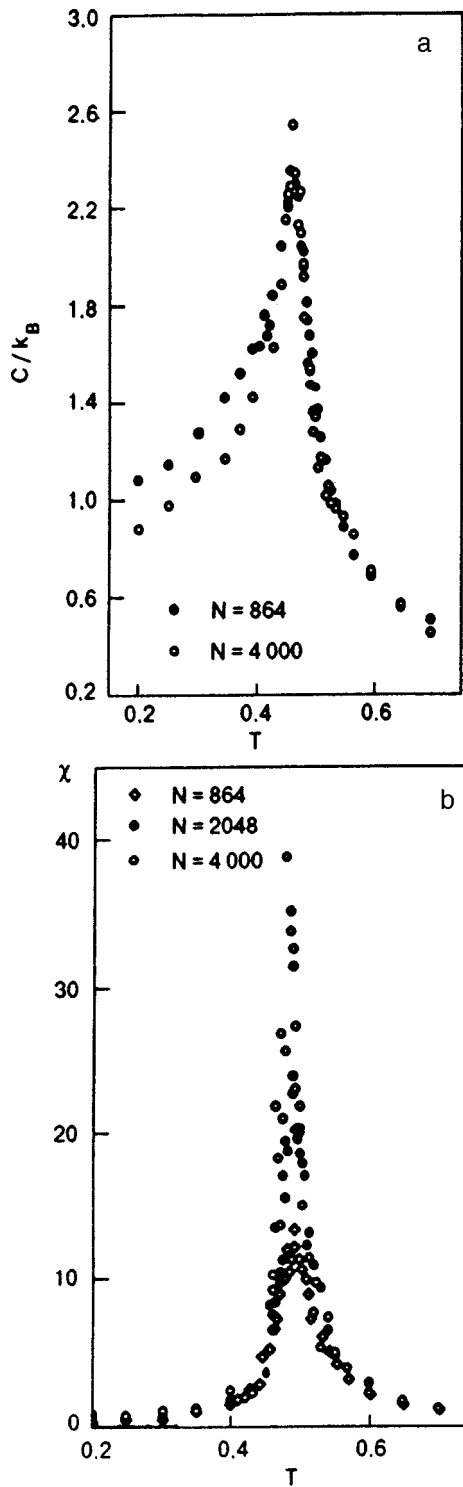


FIG. 1. Dependences of the heat capacity C/k_B (a) and susceptibility χ (b) (model II) on normalized temperature T for systems with different number N of spins.

method are considered in Refs. 5 and 6 for ferromagnetic Ising and Heisenberg models with interactions between near-est neighbors.

For the model considered by us, the temperature dependence of Binder's cumulant for two systems with $N=500$ and 4000 (model I) is shown in Fig. 3. A similar dependence is also observed for model II. Transition temperatures deter-

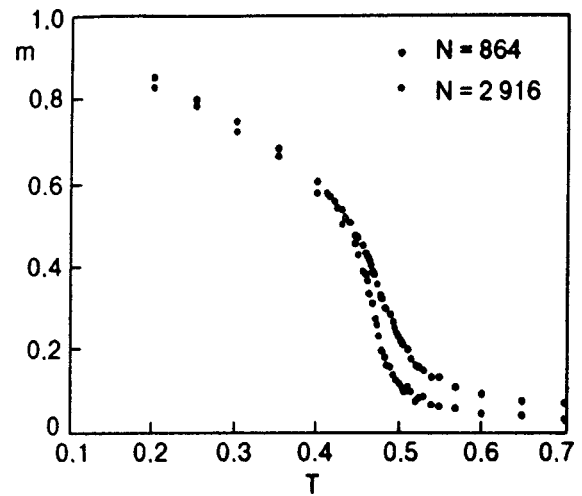


FIG. 2. Dependence of sublattice magnetization m on temperature T (model II).

mined in this way for models I and II have the values $T_N=0.466(2)$ and $0.480(2)$. These values of temperature were used by us here as the critical temperatures. The slight increase in the value of T_N for model II is in accord with the well-known fact that the value of T_c for Ising systems is higher than for Heisenberg systems. The value of anisotropy $D/|J_1|=2.5 \cdot 10^{-2}$ used for model II enhances Ising properties of the model and will affect the values of all critical parameters (see below).

In order to approximate the critical behavior of heat capacity, we used the following expressions:¹⁹⁻²⁸

$$C = \frac{A}{\alpha} |t|^{-\alpha} (1 + D_s |t|^x), \tag{5}$$

$$C = \frac{A}{\alpha} (|t|^{-\alpha} - 1) + D_s |t|^x, \tag{6}$$

where $t = (T - T_N)/T_N$, and α , A , and D_s , are the critical exponent of heat capacity, critical amplitude, and the amplitude of correction to scaling respectively. The value of x was assumed to be equal to 0.55, which corresponds to the Heisenberg model.²⁹

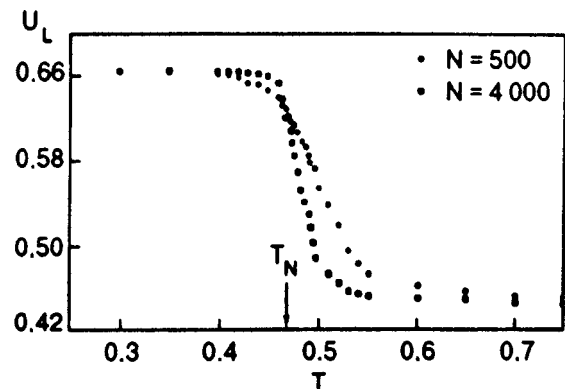


FIG. 3. Dependence of cumulant U_L on temperature T (model I).

TABLE I. Effective values of critical exponent α and critical amplitudes A and A' in the interval of reduced temperatures $5 \times 10^{-3} \leq t \leq 7.5 \times 10^{-1}$.

Number of spins N	$D/ J_1 =2.5 \times 10^{-4}$			$D/ J_1 =2.5 \times 10^{-2}$		
	α	A	A'	α	A	A'
500	-0.15(3)	0.61(2)	0.60(2)	0.11(3)	0.53(3)	0.70(3)
864	-0.15	0.56	0.56	0.12	0.43	0.61
1372	-0.16	0.51	0.49	0.10	0.44	0.57
2048	-0.12	0.47	0.46	0.13	0.44	0.52
2916	-0.15	0.53	0.53	0.10	0.38	0.42
4000	-0.14	0.47	0.48	0.15	0.42	0.43

The data obtained by the MC method were processed by the nonlinear least-squares method. The values minimizing the sum of mean square deviations were used as optimal values of α , A , and D_s .

The results of approximation of the data obtained on the basis of formulas (5) and (6) correlate well. However, preference was given to formula (6) which ensured a higher accuracy of the results. The values of α , A , and A' calculated for models I and II are given in Table I (the value of A' for $T < T_N$ was calculated by using the prediction of static scaling $\alpha' = \alpha$).¹ All values of α in model I have the negative sign typical of the Heisenberg model, are virtually independent of the number of spins in the system, and are in good agreement with the theoretical value $\alpha = -0.126(28)$ obtained for the isotropic Heisenberg model with short-range forces.²⁹ The ratio of the critical amplitudes A and A' determined according to the above algorithm belong to the interval $0.90 \leq A/A' \leq 1.10$ for all the systems. The situation changes radically for model II in which the values of α are positive as in the Ising model. The theoretical value of α in the Ising model obtained on the basis of ϵ -expansion is $0.108(9)$.²⁹ Obviously, the relatively high value of one-ion anisotropy typical of small magnetic particles^{25,26} and assumed by us for model II allows us to treat systems with PBC as Ising systems. It should be noted that systems with free surfaces with the same value of anisotropy preserved the Heisenberg type of critical behavior.²² The ratio of critical amplitudes belong to the interval $0.75 \leq A/A' \leq 0.9$.

The values of critical exponent α for Cr_2O_3 determined from the results of laboratory experiments are quite contradictory and vary from 0.14 ³⁰ to -0.12 ⁹ depending on the method of investigation, the interval of variation of t , the choice of T_N , and some other parameters.

The Hamiltonian under investigation contains one-ion anisotropy, and hence such a system must exhibit a crossover from the Heisenberg critical behavior to the Ising behavior for $t \rightarrow 0$.¹ The theoretical values of the crossover temperatures for models I and II calculated from our results are equal to $t_{\text{cr}} \approx 0.0013$ and 0.052 respectively. The values of α obtained in model I do not exhibit a crossover for $5 \times 10^{-3} \leq t \leq 7.5 \times 10^{-1}$. Model II is of the Ising type in all temperature intervals.

In order to get a more clear idea of the critical behavior of the models under investigation, we must consider temperature dependences of the sublattice magnetization and susceptibility. Both these quantities are inconvenient for investigations by the MC method.²² Figure 2 shows that the magnetization decreases monotonically upon an increase in temperature, but differs from zero even for values of T much higher than T_N .

The approximation of the critical behavior of m was based on the expression

$$m = B|t|^\beta(1 + a_m|t|^x), \tag{7}$$

where β , B , and a_m are the critical exponent, critical amplitude, and the amplitude of scaling correction respectively.

Table II contains values of β for different temperature ranges t . It should be noted that the value of β in model I for the same temperature interval is slightly higher than in model II. In contrast to the other two exponents (α and γ), the exponent β has the following two peculiarities:

- (1) the absolute value of β increases with N , and
- (2) the values of β increases with t_{min} also.

Both these peculiarities are apparently associated with short-range effects which are manifested in high-temperature magnetization ‘‘tails’’ in Fig. 2.

The dependence of the sublattice magnetization m on the reduced temperature t plotted on the log-log scale in model I at $t_{\text{cr}} \approx 0.05$ displays a kink typical of crossover. This dependence is presented in Fig. 4a for two values of $\beta \approx 0.31(2)$ at $t \leq t_{\text{cr}}$ and $\beta \approx 0.36(2)$ at $t > t_{\text{cr}}$ for a system with $N = 1372$. In model I, a similar situation is observed for all systems irrespective of N . These data probably indicate a crossover from the Heisenberg critical behavior in model I with $\beta \approx 0.36$ (the theoretical value of β for the Heisenberg model is $\beta \approx 0.367$)²⁹ to the Ising behavior with $\beta \approx 0.31$ ($\beta = 0.326$ for

TABLE II. Effective values of critical exponent β , $t_{\text{max}} = 7.5 \times 10^{-1}$.

Number of spins N	$D/ J_1 =2.5 \times 10^{-4}$				$D/ J_1 =2.5 \times 10^{-2}$					
	5×10^{-3}	1×10^{-2}	2×10^{-2}	4×10^{-2}	t_{min}		1×10^{-2}	2×10^{-2}	4×10^{-2}	8×10^{-2}
					8×10^{-2}	5×10^{-3}				
500	0.24(3)	0.25	0.26	0.28	0.28	0.18	0.21	0.23	0.24	0.25
864	0.25	0.26	0.27	0.29	0.29	0.20	0.23	0.24	0.25	0.26
1372	0.27	0.29	0.32	0.35	0.36	0.21	0.24	0.25	0.26	0.27
2048	0.28	0.28	0.32	0.33	0.34	0.21	0.24	0.25	0.26	0.28
2916	0.31	0.34	0.35	0.36	0.37	0.25	0.26	0.27	0.29	0.30
4000	0.33	0.35	0.36	0.38	0.38	0.27	0.27	0.28	0.29	0.31

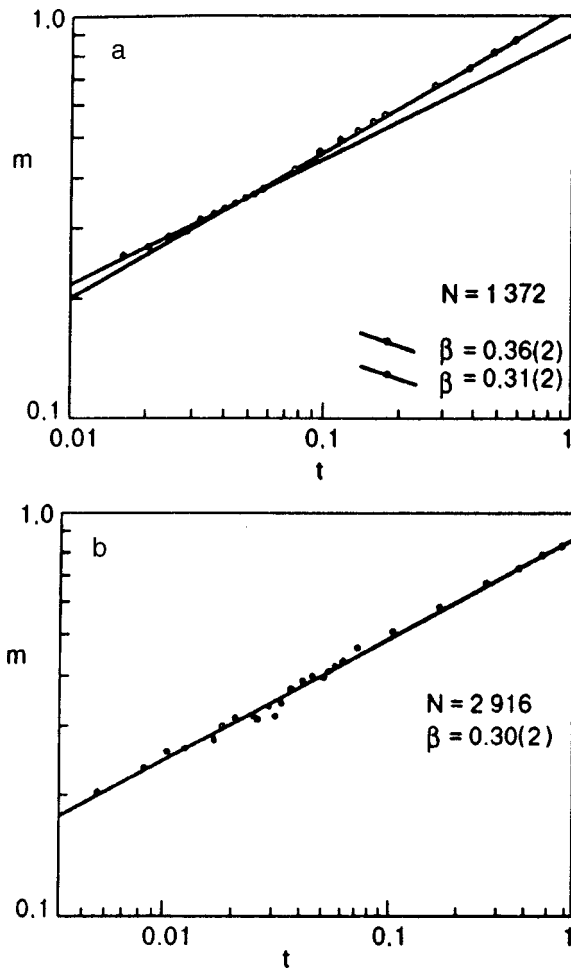


FIG. 4. Dependence of sublattice magnetization m on reduced temperature t on the log-log scale: model I (a) and model II (b), $t = (T - T_N)/T_N$.

the Ising model),²⁹ which is not observed in the behavior of heat capacity.

Figure 4b shows the characteristic dependence of m on t in model II for a system with $N = 2916$. It can be seen that no peculiarities typical of model I are observed in this case. The value of $\beta \approx 0.30(2)$ obtained for this model are quite close to the theoretically predicted values for the Ising model.

The experimental value of β in the temperature range $3 \times 10^{-5} \leq t \leq 3 \times 10^{-2}$ amounts to 0.35³¹ and is close to the

theoretical value obtained for the Heisenberg model as well as to the precrossover value calculated by us in model I.

Typical dependences of susceptibility χ on temperature T are presented in Fig. 1b. These dependences were approximated by using the simple power function

$$\chi = \Gamma |t|^{-\gamma}, \tag{8}$$

where γ and Γ are the critical exponent and the critical amplitude of susceptibility. Table III contains the values of γ and γ' obtained in model I on the basis of formula (8) irrespective of each other from the data obtained at $T > T_N$ and $T < T_N$ respectively. It should be noted that γ and γ' as well as α are independent of the number N of spins in the system under investigation, but their values increase with t_{\min} . It is difficult to judge whether the critical behavior of susceptibility is of the Heisenberg ($\gamma = 1.39$)²⁹ or the Ising type ($\gamma = 1.24$)²⁹ from the absolute values of γ and γ' . Similar data obtained in model II coincide with those from Table III within the admissible error. Such a behavior of γ and γ' is probably associated with the insufficient resolution of the method of processing of a strongly fluctuating quantity such as susceptibility. It will be proved in the next section that an analysis of the same results on the basis of another approach gives a more clear pattern of the critical behavior of susceptibility.

FINITE-SIZE SCALING

Basic concepts of the theory of finite-size scaling (FSS) are reduced to taking into account finite ($L \ll \infty$) size of the systems being simulated since the systems analyzed by the MC method are just of this type. Such systems reproduce successfully the thermodynamic properties of infinitely large systems as long as the correlation length ξ is smaller than the linear size L of the system. In the vicinity of the critical point $\xi \geq L$, the properties of the systems depend considerably on the type of periodic boundary conditions. In the case of PBC, fluctuations can be “switched” to opposite sides which is not observed in real systems. This results in “rounding” effects, e.g., long-range effects above T_c , smoothing of heat capacity and susceptibility peaks, and their displacement on the temperature scale. The ideas underlying the FSS theory make it possible to extrapolate the MC data obtained for finite-size systems to the thermodynamic limit ($N = L^3$

TABLE III. Effective values of critical exponents γ and γ' for a system with PBC, $t_{\max} = 7.5 \times 10^{-1}$, $D/|J_1| = 2.5 \times 10^{-2}$.

Number of spins N	γ			γ'				
	1×10^{-2}	2×10^{-2}	4×10^{-2}	t_{\min}				
				8×10^{-2}	1×10^{-2}	2×10^{-2}	4×10^{-2}	8×10^{-2}
500	0.86	1.05	1.08	1.17	0.92	1.07	1.15	1.29(4)
864	0.87	1.07	1.10	1.17	0.93	1.08	1.20	1.31
1372	0.89	1.09	1.13	1.19	0.94	1.10	1.15	1.32
2048	0.90	1.11	1.15	1.21	0.96	1.12	1.19	1.31
2916	0.89	1.10	1.11	1.18	1.03	1.14	1.21	1.34
4000	0.93	1.12	1.17	1.23	1.03	1.15	1.22	1.33

$\rightarrow\infty$) and are used widely.⁵⁻¹¹ According to this theory, the free energy for a large system with PBC at a temperature close enough to the transition temperature T_c can be scaled as follows:¹⁵⁻¹⁷

$$F(T,L) = L^{-d} F(tL^{1/\nu}), \quad (9)$$

where $T_c = T_c(L \rightarrow \infty)$, d is the dimension of the space, and ν the static critical exponent of the correlation length of an infinitely large system ($L = \infty$). Expression (9) leads to similar dependences for heat capacity, magnetization, and susceptibility per spin:

$$C(T,L) - L^{\alpha/\nu} C_0(tL^{1/\nu}), \quad (10)$$

$$m(T,L) - L^{-\beta/\nu} m_0(tL^{1/\nu}), \quad (11)$$

$$\chi(T,L) - L^{\gamma/\nu} \chi_0(tL^{1/\nu}), \quad (12)$$

where α , β , and γ are static critical exponents connected through the hyperscaling relations $2 - \alpha = d\nu = 2\beta - \gamma$.¹ Equations (10)–(12) successfully reproduce the critical behavior of infinite systems for large $tL^{1/\nu}$ ($t \ll 1$ and $L \rightarrow \infty$). The validity of basic concepts of the FSS theory was proved by many authors.⁵⁻⁸

According to this theory, the magnetization and susceptibility of a system of size $L \times L \times L$ at $T = T_N$ and large values of L satisfy the relations

$$m \sim L^{-\beta/\nu}, \quad (13)$$

$$\chi \sim L^{\gamma/\nu}. \quad (14)$$

An analysis of our results on the basis of relations (13) and (14) also makes it possible to determine the values of β and γ . For this purpose, the dependences of m and χ on the linear lattice size L were plotted on the log–log scale. The slope of the straight line determines the value of β/ν and γ/ν . The values of the ratios obtained in this way in model I are $\beta/\nu = 0.544$ and $\gamma/\nu = 1.985$. If we assume that model I exhibits a clearly manifested Heisenberg behavior and that $\nu = 0.706$,²⁹ we obtain $\beta = 0.38(2)$ and $\gamma = 1.38(2)$. It should be noted that these values of β and γ are in accord with the theoretical values calculated for the Heisenberg model ($\beta = 0.368$ and $\gamma = 1.39$).²⁹ For model II, we have $\beta/\nu = 0.426$ and $\gamma/\nu = 1.791$. Since this model exhibits the Ising behavior, while the initial Hamiltonian is of the Heisenberg type, we determine the exponents both for $\nu = 0.706$ (Heisenberg model) and for $\nu = 0.63$ (Ising model).²⁹ Thus, $\beta = 0.30(2)$, $\gamma = 1.26(3)$, for $\nu = 0.706$ and $\beta = 0.27(2)$, $\gamma = 1.13(3)$ for $\nu = 0.63$. It should be noted that the results obtained in model II for any ν is closer to the theoretical values of the Ising model ($\beta = 0.326$ and $\gamma = 1.24$)²⁹ although they do not completely coincide with them.

For a clearly manifested peak-type shape of heat capacity, the following expression is normally used for scaling^{6,32} C_{\max} :

$$C_{\max}(L) = C_{\max}(L = \infty) - aL^{\alpha/\nu}, \quad (15)$$

where a is a certain coefficient. Approximation of the data on the basis of formula (15) gives the value of critical exponent $\alpha = -0.14(3)$ in model I and $\alpha = 0.16(3)$ for $\nu = 0.706$ and $\alpha = 0.14(3)$ for $\nu = 0.63$ in model II. These results are also in

good agreement with the data obtained for the Heisenberg ($\alpha = -0.126$)²⁹ and Ising model ($\alpha = 0.108$)²⁹ as well as with the results of analysis of the data given by MC calculations on the basis of traditional power functions.

CONCLUSION

Our results obtained by the MC method applied to investigations of models of the real antiferromagnet Cr_2O_3 indicate that model I with anisotropy $D/|J_1| = 2.5 \cdot 10^{-4}$ exhibits Heisenberg critical behavior. The critical exponents α of heat capacity determined by approximating the data by power functions and from the relations of the FSS theory are in good agreement with each other and with theoretical values.

The exponents β and γ determined by traditional methods from formulas (7) and (8) exhibit peculiarities typical of MC data and can hardly be used to determine the type of the critical behavior. The results obtained for α , β , and γ from the processing of the same data in accordance with the FSS theory indicate unambiguously that model I belongs to the Heisenberg class of universality with the critical exponents $\alpha = -0.14(3)$, $\beta = 0.38(2)$, $\gamma = 1.38(2)$.

An analysis of the results obtained for $D/|J_1| = 2.5 \cdot 10^{-2}$ (model II) and processed by using both approaches indicates that model II exhibits the Ising mode of critical behavior.

It should be noted that although the values of critical exponents α , β , and γ obtained on the basis of the FSS theory are in better agreement with the theoretical and experimental results, the analysis of the same data based on approximation by power functions makes it possible to obtain rich additional information. In our opinion, an analysis of the results of the results of MC simulation by these two methods is required for the formation of the most complete pattern of the critical behavior of such systems.

The author is grateful to I. K. Kamilov, Corresponding Member of the Russian Academy of Sciences, and Profs. Kh. K. Aliev and P. N. Vorontsov-Vel'yaminov for their support and fruitful discussions.

*E-mail: kamilov@datacom.ru

¹S. Ma, *Modern Theory of Critical Phenomena*, Benjamin-Cummings, Reading (USA) (1976).

²K. Binder and D. V. Heerman, *Simulation by Monte Carlo Method in Statistical Physics* [Russian transl.], Mir, Moscow (1995).

³K. Binder (ed), *Monte Carlo Methods in Statistical Physics*, Springer, Heidelberg (1979).

⁴D. P. Landau, *Physics* **A205**, 41 (1994).

⁵A. M. Ferrenberg and D. P. Landau, *Phys. Rev. B* **44**, 5081 (1991).

⁶P. Peczak, A. M. Ferrenberg, and D. P. Landau, *Phys. Rev. B* **43**, 6087 (1991).

⁷Kun Chen, A. M. Ferrenberg, and D. P. Landau, *Phys. Rev. B* **48**, 3249 (1993).

⁸D. Ledue, D. P. Landau, and J. Tillet, *Phys. Rev. B* **49**, 12 523 (1995).

⁹R. N. Swendsen and J.-Sh. Wang, *Phys. Rev. Lett.* **58**, 86 (1987).

¹⁰V. Wolf, *Phys. Rev. Lett.* **62**, 361 (1989).

¹¹V. Wolf, *Nucl. Phys. B* **322**, 759 (1989).

¹²A. M. Ferrenberg and R. N. Swendsen, *Phys. Rev. Lett.* **61**, 2635 (1988).

¹³A. M. Ferrenberg and R. N. Swendsen, *Phys. Rev. Lett.* **63**, 1195 (1989).

¹⁴N. A. Alves, B. A. Berg, and R. Villanova, *Phys. Rev. B* **43**, 5846 (1991).

¹⁵A. E. Ferdinand and M. E. Fisher, *Phys. Rev.* **185**, 832 (1969).

- ¹⁶M. N. Barber, in *Phase Transitions and Critical Phenomena*, vol. 8, Academic Press, New York (1983).
- ¹⁷N. Privman (Ed.), *Finite-Size Scaling and Numerical Simulation*, World Scientific, Singapore (1990).
- ¹⁸R. H. Bruce and D. S. Cannel, *Phys. Rev. B* **15**, 4451 (1977).
- ¹⁹M. Marinelli, F. Mercury, U. Zammit *et al.*, *Phys. Rev. B* **49**, 9523 (1994).
- ²⁰E. J. Samuelsen, M. T. Hutchings, and G. Shirane, *Physica* **48**, 13 (1970).
- ²¹A. K. Murtazaev and I. A. Favorskii, *Fiz. Nizk. Temp.* **19**, 160 (1993) [*Low Temp. Phys.* **19**, 113 (1993)].
- ²²A. K. Murtazaev, Kh. K. Aliev, I. K. Kamilov, and K. Sh. Khizriev, *Fiz. Nizk. Temp.* **24**, 462 (1998) [*Low Temp. Phys.* **24**, 349 (1998)].
- ²³S. Foner, *Phys. Rev.* **30**, 183 (1963).
- ²⁴J. O. Artman, J. C. Murphy, and S. Foner, *Phys. Rev. A* **138A**, 912 (1965).
- ²⁵L. J. Dormann, D. Fiorani, and E. Trone, *Adv. Chem. Phys.* **98**, 283 (1997).
- ²⁶P. V. Hendriksen, S. Linderoth, and P.-A. Lindgard, *Phys. Rev. B* **48**, 7259 (1993).
- ²⁷K. Binder, *Z. Phys. B* **43**, 119 (1981).
- ²⁸G. Bernarz, D. J. W. Geldern, and M. A. White, *Phys. Rev. B* **47**, 14247 (1993).
- ²⁹J. C. LeGuillou and J. Zinn-Justin, *Phys. Lett.* **46A**, L137 (1985).
- ³⁰A. Barchellerie and C. H. Frenois, *J. Phys. (Paris)* **35**, 30 (1974).
- ³¹E. Fisher, G. Gorodetsky, and S. Shtrikman, *J. Phys. Colloq.* **32**, 1 (1971).
- ³²Th. T. A. Paaau, A. Compagner, and D. Bedeaux, *Physica A* **79**, 1 (1975).

Translated by R. S. Wadhwa

Photoinduced changes in magnetostriction of $Y_3Fe_5O_{12}$ single crystals

N. V. Vorob'eva and R. A. Doroshenko

*Ufa Research Center, Institute of Physics of Molecules and Crystals, Russian Academy of Sciences, 450075 Ufa, Russia**

(Submitted October 13, 1998; revised December 8, 1998)

Fiz. Nizk. Temp. **25**, 478–480 (May 1999)

A decrease in the value of the magnetostriction constant λ_{111} is observed at 78 K in YIG(Ba) and YIG(Si) single crystals exposed to light in the spectral range 0.65–2 μm . Exposure to infrared light leads to a decrease in the value of λ_{111} for YIG(Si), but causes no change for YIG(Ba). © 1999 American Institute of Physics. [S1063-777X(99)00805-1]

The magnetic and optical properties of yttrium iron garnets (YIG) change as a result of exposure to light. Earlier, we reported on the spectral sensitivity of the photoinduced optical effect¹ as well as a change in the permeability² of $Y_3Ba_xFe_{5-x}O_{12}$ (YIG(Ba)) and $Y_3Si_xFe_{5-x}O_{12}$ (YIG(Si)) single crystals. In this work, we present the results of investigation of the photoinduced variation of magnetostriction of monocrystalline YIG samples with different dopings exposed to light of different spectral composition.

EXPERIMENTAL TECHNIQUE AND SAMPLES

Measurements were made by the bridge technique using film-type chromium strain gauges formed directly on the surfaces of monocrystalline disks (110) in $\langle 111 \rangle$ -type directions. Single crystals of $Y_3Fe_5O_{12}$ grown from $BaO-B_2O_3$ (YAG(Ba)) and $PbO-PbF_2:SiO_2$ (YAG(Si)) solutions in the melt were investigated. The samples were immersed in liquid nitrogen in the course of the experiments. YIG(Si) was illuminated by light passing from a KGM 12-100 lamp through a condenser and optical filters IKS-3 (transmission range 1–2 μm) and KS-3 (transmission range 0.65–2 μm). An IKS filter from the monochromator MDR-12 (transmission range 1.5–2.5 μm) or KS 17 was used for YIG(Ba). The main aim of the experiments was to obtain the dependence of the magnetostrictive deformation $(\Delta L/L)^{\langle 111 \rangle}$ on the direction of the applied constant saturating field H in the (110) plane. The direction of H was defined by the angle ψ measured from the [001] direction.

The angular dependences of $(\Delta L/L)^{\langle 111 \rangle} - (\Delta L/L)_{\psi}^{\langle 111 \rangle}$, i.e., the change in relative elongation of the sample in the [111] direction upon a rotation of the saturating field in the (110) plane were measured.

The curves were plotted after initial and repeated exposure to red and infrared light, as well as to the infrared light alone. Samples were exposed for 15 minutes in a saturating magnetic field oriented along the [001] direction in the sample cut plane. The experimental conditions correspond to the largest photoinduced variation of magnetostriction constants obtained earlier for YIG(Si).³ The saturation of photoinduced effects in these crystals was attained in a period of about three minutes,¹ but a more prolonged exposure makes it possible to avoid the effect of time dependences. The main condition determining the experimental results is that the

saturating magnetic field $H = 2000$ Oe be directed along the [001] axis during illumination to ensure a symmetrization of the arrangement of photoactive centers along the trigonal axes.

EXPERIMENTAL RESULTS

Figure 1 shows the dependence of the variation of the magnetostriction $\Delta L/L$ for YIG(Si) along [111] direction as a result of magnetization along the direction ψ in the (110) plane of the sample. The shape of the curve changes under illumination: it can be seen that the amplitude of the peak (separation between the end points along the ordinate axis) decreases as a result of exposure to red and infrared radiation, while exposure to infrared light alone causes an increase in the peak amplitude. The obtained experimental dependences can be described by the expression⁴

$$\begin{aligned} \Delta L/L^{\langle 111 \rangle} - \Delta L/L_{\psi}^{\langle 111 \rangle} = & \lambda_{\sigma} \left(\frac{2}{3} - \sin^2 \psi \right) \\ & + \lambda_{111} \left(-\frac{\sqrt{2}}{2} \sin 2\psi - \frac{1}{2} \sin^2 \psi \right), \end{aligned}$$

where λ_{σ} is a coefficient and λ_{111} is the magnetostriction constant.

For YIG(Si), the magnetostriction constant λ_{111} decreases upon exposure to red light: $\lambda_{111}^d = -0.11 \times 10^{-5}$ and $\lambda_{111}^l = -0.09 \times 10^{-5}$ before and after the action of light from KS-17. Exposure to infrared radiation through the optical filter IKS-3 increases the value of λ_{111} : $\lambda_{111}^l = -0.13 \times 10^{-5}$. The dark value of the coefficient λ_{σ} for unexposed (dark) sample is $\lambda_{\sigma}^d = -0.13 \times 10^{-5}$, while the coefficient is equal to $\lambda_{\sigma}^l = -0.11 \times 10^{-5}$ under simultaneous exposure to red and infrared light, and $\lambda_{\sigma}^l = -0.14 \times 10^{-5}$ upon exposure to infrared light only. Partial reproducibility of the effect is observed upon an alternation of optical filters. The experimental data were processed with the help of the Sigma Plot software, and the standard error in determining the constants did not exceed 0.5%.

The action of red light together with IR radiation on YIG(Ba) is analogous to the effect of white light. No change was observed experimentally in the magnetostriction constants for YIG(Ba) after exposure to light in the spectral range 1.5–2.5 μm .

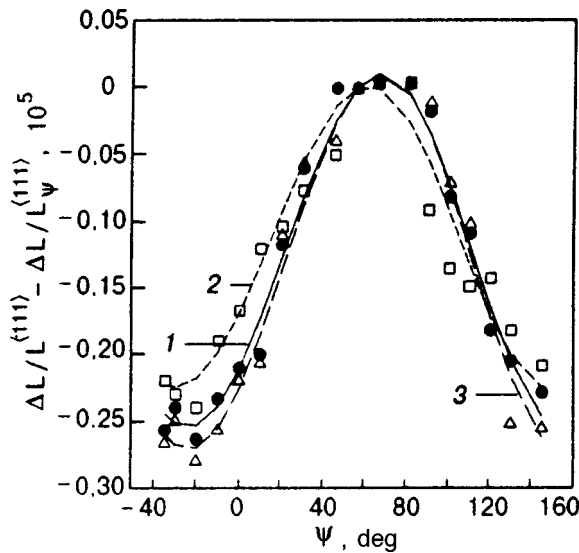


FIG. 1. Angular dependences of magnetostriction for YIG(Si): $\Delta L/L^{(111)} - \Delta L/L_{\psi}^{(111)}$ recorded during rotation of field in the (110) plane. The symbols correspond to the experimental results and the curves to theory (curve 1 – dark curve before illumination (●); curve 2 – after primary action of red light (□); and curve 3 – after primary exposure to infrared light (Δ). Exposure time 15 min; $T=78$ K.

DISCUSSION OF RESULTS

The obtained experimental results can be interpreted as photoinduced variation of internal elastic stresses produced by heterovalent Fe ions occupying octahedral positions. Zaikova and Shur⁵ studied the effect of internal elastic stresses on magnetostriction variations by considering the example of iron silicide single crystals. Heterovalent Fe ions in YIG produce local elastic stresses which affect the magnetoelastic properties of the surrounding Fe^{3+} ions. A magnetoelastic center containing a heterovalent Fe^{2+} (Fe^{4+}) ion and the surrounding Fe^{3+} ions can be treated as a macroscopic center. The averaging of nonuniform macroscopic stresses and the possibility of their replacement by mean elastic stress parameters was considered theoretically by Livshits.⁶

The dependence of the magnetostriction constants in YIG on elastic stresses along trigonal and tetragonal crystallographic axes resulting from the emergence or redistribution of magnetoelastic centers was obtained earlier by us³:

$$\lambda_{111} = \lambda_{111}^* + \frac{2}{9} \Delta \left(\frac{1}{6c_{44}} - \frac{1}{c_{11} - c_{12}} \right) + \frac{4}{27} \frac{K}{c_{44}},$$

where λ_{111}^* is the magnetostriction constant for a sample without elastic stresses caused by heterovalent ions, K is the symmetric part of the stresses $\sigma_i = K_i \cos^2 \theta$ along trigonal axes ($K_1 = K$, $K_2 = K + \Delta$, $K_3 = K_4 = K + \varepsilon$; θ is the angle between the direction of the magnetic field and i th diagonal of the cube), Δ the asymmetry of stresses along the trigonal axes in the (110) plane, and c_{11}, c_{12} and c_{44} are the elastic moduli.

The value of the constant λ_{σ} depends only on nonuniform distribution of the number of magnetoelastic centers over octahedral and tetrahedral sites³:

$$\lambda_{\sigma} = \frac{2}{9} (\varepsilon - \Delta) \left(\frac{1}{6c_{44}} - \frac{1}{c_{11} - c_{12}} \right) + \frac{1}{c_{11} - c_{12}} \frac{4}{3} \varepsilon',$$

where ε is the asymmetry of stresses along trigonal axes not belonging to the (110) plane, and ε' is the asymmetry of stresses along tetragonal axes.

The change in the cubic constant λ_{111} as a result of illumination of YIG(Ba) and YIG(Si) is determined by the change in the symmetric part of the trigonal elastic stresses K . An increase or decrease in the total number of centers in octahedral positions leads to a change in the value of K and hence of λ_{111} .

The quantity λ_{σ} changes as a result of variation of the asymmetry Δ, ε , distribution of magnetoelastic centers between trigonal axes for YIG(Ba) and YIG(Si), and due to a possible variation of the asymmetry in tetragonal stresses ε' . Upon an increase in the asymmetry of stresses, the number of centers distributed equiprobably along the axes decreases, leading to a corresponding variation in K and λ_{111} .

For YIG(Si), the magnetostriction constant λ_{111} decreases as a result of exposure to both red and white light.

According to the conclusions drawn by Dillon *et al.*,⁷ an increase in the occupancy of positions by Fe^{2+} ions in YIG(Si) leads to an elongation of the sample placed in a saturating magnetic field along the trigonal axis for which the number of active centers increases. In other words, a decrease in magnetostriction is observed. It was also shown by us³ that $K > 0$ for YIG(Si). This means that heterovalent Fe ions in YIG(Si) produce a tensile stress. The value of λ_{111} decreases upon an increase in the value of K , which means that the tensile stress increases along all trigonal axes upon exposure to red or white light. This corresponds to an increase in the total number of Fe^{2+} ions occupying octahedral positions. Exposure to infrared radiation causes an increase in the value of λ_{111} , i.e., to a decrease in the internal elastic stresses.

CONCLUSION

It can be assumed on the basis of the experimental data obtained for YIG(Si) that redistribution of heterovalent iron ions from “near” and “far” positions under the action of IR radiation leads to a decrease in internal trigonal equiprobable and symmetric stresses in the crystal and to an increase in the value of λ_{111} .

Mack and Smith⁸ have studied the effect of close proximity of Fe^{2+} and Si^{4+} ions on the minimization of elastic energy and magnetostriction. They found that the magnetostriction increases upon annealing along the $\langle 100 \rangle$ direction on account of the possibility of redistribution of active centers at 78 K, thus indicating a difference in the magnetoelastic properties of Fe^{2+} ions “near” and “far” from the Si^{4+} ions.

An increase in the number of photoactive centers in “near” positions for YIG(Si) under the action of red light leads to an increase in trigonal stresses and a decrease in the value of λ_{111} . The formation of heterovalent iron ions under the action of red light leads to a decrease in internal stresses

in YIG(Ba). The smallness of the effect may hamper the observation of the influence of IR radiation on this sample.

*E-mail: imcp@anrb.ru

¹M. D. Nadezhdin and R. A. Doroshenko, in *Structural, Magnetoelastic and Dynamic Effects in Ordered Media* [in Russian], BGU, Ufa (1997), p. 149.

²R. A. Doroshenko, M. D. Nadezhdin, R. Z. Khalilov, and N. V. Vorob'eva, in *Abstracts of Papers to XVI Intern. Seminar. Cum School on New Materials in Magnetolectronics*, Part II (1998), p. 654.

³R. A. Doroshenko and N. V. Vorob'eva, in *Structural, Magnetoelastic and Dynamic Effects in Ordered Media* [in Russian], BGU, Ufa (1997), p. 36.

⁴V. G. Veselago, N. V. Vorob'eva, and R. A. Doroshenko, *Pis'ma Zh. Éksp. Teor. Fiz.* **45**, 402 (1987) [*JETP Lett.* **45**, 512 (1987)].

⁵V. A. Zaikova and Ya. S. Shur, *Fiz. Met. Metalloved.* **16**, 614 (1963).

⁶I. M. Livshits, in *Physics of Real Crystals and Disordered Systems* [in Russian] Nauka, Moscow (1987).

⁷J. P. Dillon, E. M. Gyorgy, and J. P. Remeika, *Appl. Phys. Lett.* **15**, 221 (1969).

⁸D. R. Mack and J. Smith, *J. Appl. Phys.* **2**, 23 (1973).

Translated by R. S. Wadhwa

ELECTRONIC PROPERTIES OF METALS AND ALLOYS

On correlation effects in a narrow-band model with electron–hole asymmetry

L. D. Didukh and V. V. Hankevych

*Ternopol State Engineering University, 282001 Ternopol, Ukraine**

(Submitted June 29, 1998; revised December 14, 1998)

Fiz. Nizk. Temp. **25**, 481–486 (May 1999)

Some correlation effects are studied in a narrow-band model with electron–hole asymmetry. A peculiar feature of the model is that it takes into account the hopping integral associated with electron–electron interaction (correlated hopping). The method of Green’s functions is used to find the quasiparticle energy spectrum, as well as expressions for the upper and lower Hubbard subband widths. It is shown that the specific features of the model lead in a number of cases to consequences differing significantly from those following from the Hubbard model. The obtained results mainly illustrate the peculiarities of the model in the low-temperature region and are used for interpreting the physical properties of systems with narrow energy bands. © 1999 American Institute of Physics. [S1063-777X(99)00905-6]

INTRODUCTION

One of the characteristic properties of the Hubbard model¹ which is used widely for describing correlation effects in narrow conduction bands (review articles in Refs. 2–4, to mention a few) is the electron–hole symmetry: systems with $n < 1$ and $n > 1$ have identical physical properties (n is the electron concentration in the band). This symmetry is associated with the disregard of electron–electron interaction matrix elements

$$J(ikjk) = \iint \varphi^*(\mathbf{r}-\mathbf{R}_i)\varphi(\mathbf{r}-\mathbf{R}_j) \frac{e^2}{|\mathbf{r}-\mathbf{r}'|} \times |\varphi(\mathbf{r}'-\mathbf{R}_k)|^2 d\mathbf{r}d\mathbf{r}' \quad (1)$$

in the Hamiltonian of the model (the matrix elements (1) describe electron transitions between i th and j th crystal lattice sites, and φ -functions are the Wannier functions).

However, the experimental data reflecting the electron–hole asymmetry in narrow-band materials on the one hand, and the results of theoretical analysis on the other hand, point towards the need to take the correlated hopping (1) into account in the generalized Hubbard model.^{5,6} As a result, the hopping integrals describing transitions to the lower and upper Hubbard subbands in such a generalized Hubbard model differ from one another as well as from the hopping integral corresponding to transitions between Hubbard’s subbands (among other things, the lower and upper Hubbard subbands are not equivalent in this model). Such models have been studied quite intensively in recent years (see, for example, Refs. 7–9 and the literature cited therein).

In our earlier publications,¹⁰ we studied correlation effects and, in particular, metal–insulator transition in the narrow-band model with electron–hole asymmetry for a half-filled band ($n = 1$) and zero temperature, using the approach presented in Refs. 11 and 12. The approximation used

by us defines exact atomic and band boundaries in Hubbard’s model, and also describes the metal–insulator transition.

It seems interesting to continue these studies to narrow-band materials with partially filled narrow bands ($n \neq 1$). Such investigations should be useful from theoretical point of view (it was mentioned in Refs. 2–4 that this important case has not been analyzed quite extensively), as well as for a possible interpretation of the experimental data for some narrow-band materials. This is the main aim of the present research.

ONE-PARTICLE ENERGY SPECTRUM

The Hamiltonian of the model can be presented in the form¹¹

$$H = -\mu \sum_{i\sigma} a_{i\sigma}^+ a_{i\sigma} + (t_0 + nT_1) \sum_{ij\sigma} ' a_{i\sigma}^+ a_{j\sigma} + T_2 \sum_{ij\sigma} ' (a_{i\sigma}^+ a_{j\sigma} n_{i\bar{\sigma}} + \text{H.c.}) + U \sum_i n_{i\uparrow} n_{i\downarrow}, \quad (2)$$

where μ is the chemical potential, $a_{i\sigma}^+$ ($a_{i\sigma}$) the operator of creation (annihilation) of an electron with spin σ ($\sigma = \uparrow, \downarrow$) at the i th site ($\bar{\sigma}$ indicates spin projection opposite to σ , $n_{i\sigma} = a_{i\sigma}^+ a_{i\sigma}$ the operator of the number of electrons with spin σ at the i th lattice site, $n = \langle n_{i\uparrow} + n_{i\downarrow} \rangle$ the electron concentration at the site, U the intraatomic Coulomb repulsion, and

$$t_0 = \int \varphi^*(\mathbf{r}-\mathbf{R}_i) \sum_j V(\mathbf{r}-\mathbf{R}_j) \varphi(\mathbf{r}-\mathbf{R}_j) d\mathbf{r}, \quad (3)$$

$$T_1 = \sum_{\substack{k \neq i \\ k \neq j}} J(ikjk), \quad T_2 = J(iijj) \quad (4)$$

are the integrals of electron transitions between nearest neighbors at i th and j th lattice sites ($V(\mathbf{r}-\mathbf{R}_j)$ is the

potential energy of an electron in the field of an ion at the l th lattice site). The primes on the sums in Hamiltonian (2) indicate that $i \neq j$.

A distinguishing feature of Hamiltonian (2) is that it takes into account the correlated hopping T_1 , which leads to a concentration dependence of the transition integral $t_0 + nT_1$ in the proposed model of narrow-band materials with electron-hole asymmetry in contrast to the similar models considered in Refs. 6–9.

In order to determine the one-particle Green's function

$$G_{pp'}^\sigma(E) = \langle\langle a_{p\sigma} | a_{p'\sigma}^+ \rangle\rangle \quad (5)$$

we use the generalized version of the Hartree-Fock approximation^{13–15} proposed by us in Refs. 11 and 12. It should be observed that the use of the generalized Hartree-Fock approximation in the form¹³ in the range of energy parameters for which a metal-insulator transition can occur is fraught with considerable difficulties (see Refs. 15 and 16 for details of such problems). In the \mathbf{k} -representation, the Green's function (5) obtained in this way has the following form for the paramagnetic case:

$$G_{\mathbf{k}}(E) = \frac{1}{2\pi} \left(\frac{A_{\mathbf{k}}}{E - E_1(\mathbf{k})} + \frac{B_{\mathbf{k}}}{E - E_2(\mathbf{k})} \right), \quad (6)$$

$$A_{\mathbf{k}} = \frac{1}{2} - \frac{(n-1)(U - \varepsilon(\mathbf{k}) + \tilde{\varepsilon}(\mathbf{k})) - (2-n)\varepsilon_2(\mathbf{k}) - n\varepsilon_1(\mathbf{k})}{2Q(\mathbf{k})}, \quad (7)$$

$$B_{\mathbf{k}} = \frac{1}{2} + \frac{(n-1)(U - \varepsilon(\mathbf{k}) + \tilde{\varepsilon}(\mathbf{k})) - (2-n)\varepsilon_2(\mathbf{k}) - n\varepsilon_1(\mathbf{k})}{2Q(\mathbf{k})}, \quad (8)$$

$$E_{1,2}(\mathbf{k}) = -\mu + \frac{U}{2} + \frac{\varepsilon(\mathbf{k}) + \tilde{\varepsilon}(\mathbf{k})}{2} \mp \frac{1}{2} Q(\mathbf{k}), \quad (9)$$

$$Q(\mathbf{k}) = \sqrt{[\varepsilon(\mathbf{k}) - \tilde{\varepsilon}(\mathbf{k}) - U]^2 + 4\varepsilon_1(\mathbf{k})\varepsilon_2(\mathbf{k})}. \quad (10)$$

The Fourier transforms of the quantities determining formulas (7)–(10) can be defined by the expressions

$$\begin{aligned} \varepsilon(\mathbf{k}) &= \alpha t_{\mathbf{k}}(n), & \tilde{\varepsilon}(\mathbf{k}) &= \tilde{\alpha} \tilde{t}_{\mathbf{k}}(n), & \varepsilon_1(\mathbf{k}) &= \alpha_1 t'_{\mathbf{k}}(n), \\ \varepsilon_2(\mathbf{k}) &= \alpha_2 t'_{\mathbf{k}}(n), \end{aligned} \quad (11)$$

$$\alpha = -n + 2d + \frac{2(1-d)^2}{2-n} - \frac{2d(d-n+1)}{2-n} \frac{\tilde{t}(n)}{t(n)}, \quad (12)$$

$$\tilde{\alpha} = n - 2d + \frac{2d^2}{n} - \frac{2d(d-n+1)}{n} \frac{t(n)}{\tilde{t}(n)}, \quad (13)$$

$$\alpha_1 = n - 1 - \frac{2d}{n}, \quad \alpha_2 = -1 - n + \frac{2(1-d)}{2-n}, \quad (14)$$

where $E_1(\mathbf{k})$ ($E_2(\mathbf{k})$) is the electron energy in lower (upper) Hubbard subband, d is the concentration of doubly occupied sites (doublons), $t(n) = t_0 + nT_1$ and $\tilde{t}(n) = t(n) + 2T_2$ describe the transitions of quasiparticles to the lower and upper Hubbard subbands respectively (hopping of holes and doublons), and $t'(n) = t(n) + T_2$ is the integral of transition of quasiparticles between the lower and upper subbands (processes of creation and annihilation of pairs of holes and

doublons). In the model described by the Hamiltonian (2), the following four states can exist: the state $|0\rangle$ of a site not occupied by an electron corresponds to a hole, $|\sigma\rangle \equiv a_{i\sigma}^+(0)$ is the state of a site occupied by an electron with spin σ , and $|2\rangle \equiv a_{i\uparrow}^+ a_{i\downarrow}^+ |0\rangle$ is the state of a lattice site (doublon) with double occupancy (two electrons with opposite spins).

The chemical potential is defined by the expression

$$\frac{n}{2} = \frac{1}{N} \sum_{\mathbf{k}} \int_{-\infty}^{+\infty} J_{\mathbf{k}}(E) dE, \quad (15)$$

where $J_{\mathbf{k}}(E)$ is the spectral intensity of Green's function (6).

Let us consider now the common features of formulas (6) and (9). For $n < 1$ and $U \rightarrow \infty$, we obtain

$$E_1(\mathbf{k}) = -\mu + \left(\frac{2}{2-n} - n \right) t_{\mathbf{k}}(n) \quad (16)$$

(lower Hubbard subband). If $n > 1$ and only the upper Hubbard subband is important, we obtain

$$E_2(\mathbf{k}) = -\mu + U + \left(\frac{2}{n} - 2 + n \right) \tilde{t}_{\mathbf{k}}(n). \quad (17)$$

For the Hubbard model, $(t(n) = \tilde{t}(n) = t'(n) = t_0) E_1(\mathbf{k})$ for $n \rightarrow 0$ and $E_2(\mathbf{k})$ for $n \rightarrow 2$ acquire a band form. Moreover, formulas (6) and (9) describe the exact atomic boundary for $t_0 = 0$ and the band situation for $U = 0$.

The following important situation is worth noting. Owing to a difference in the hopping integrals $t(n)$ and $\tilde{t}(n)$, the energy width of the upper subband may be much smaller, and the effective mass of carriers in this subband much larger, than for the lower subband. Thus, the concepts of "narrow" and "wide" subbands, "light" and "heavy" charge carriers are introduced in a natural way (as a consequence of electron-electron interactions) in the model under consideration.

The peculiarity of the common expression for the quasi-particle energy spectrum (9) is the dependence on doublon concentration (and hence on temperature).

The doublon concentration is defined by the equation

$$\begin{aligned} d &= \frac{1}{N} \sum_{\mathbf{k}} \int_{-\infty}^{+\infty} \tilde{J}_{\mathbf{k}}(E) dE \\ &= \frac{1}{2N} \sum_{\mathbf{k}} \left(\frac{C_{\mathbf{k}}}{\exp(E_1(\mathbf{k})/\theta) + 1} + \frac{D_{\mathbf{k}}}{\exp(E_2(\mathbf{k})/\theta) + 1} \right), \end{aligned} \quad (18)$$

where

$$\begin{aligned} C_{\mathbf{k}} &= \frac{1}{2} - \frac{U + \tilde{\varepsilon}(\mathbf{k}) - \varepsilon(\mathbf{k})}{2Q(\mathbf{k})}; \\ D_{\mathbf{k}} &= \frac{1}{2} + \frac{U + \tilde{\varepsilon}(\mathbf{k}) - \varepsilon(\mathbf{k})}{2Q(\mathbf{k})}; \end{aligned} \quad (19)$$

$\theta = k_B T$, N is the number of sites in the crystal lattice, and $\tilde{J}_{\mathbf{k}}(E)$ the spectral intensity of the Green's function

$$\langle\langle a_{i\sigma} n_{i\bar{\sigma}} | a_{i\sigma}^+ \rangle\rangle_{\mathbf{k}} = \frac{n/2}{2\pi} \left(\frac{C_{\mathbf{k}}}{E - E_1(\mathbf{k})} + \frac{D_{\mathbf{k}}}{E - E_2(\mathbf{k})} \right). \quad (20)$$

We assume that the density of states is rectangular

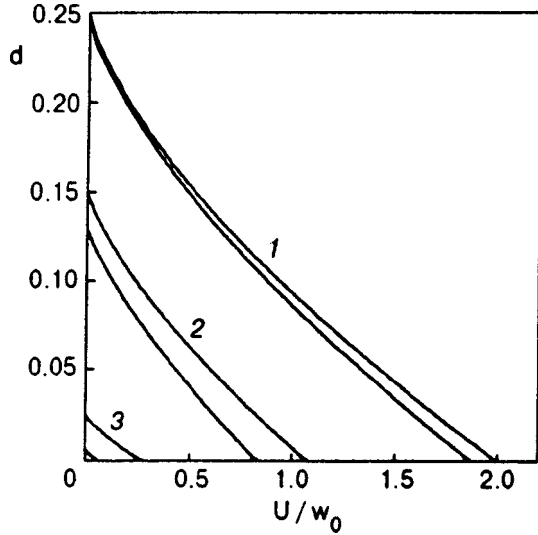


FIG. 1. Dependence of doublon concentration d on U/w_0 for various electron concentrations n : 1.2 (1), 0.8 (2), and 0.5 (3). The upper curves correspond to $\tau_1 = \tau_2 = 0$ (Hubbard's model), and the lower ones to $\tau_1 = \tau_2 = 0.2$.

$$\frac{1}{N} \sum_{\mathbf{k}} \delta(E - t(\mathbf{k})) = \frac{1}{2w} \theta(w^2 - E^2) \quad (21)$$

$\theta(x) = 1(x > 0)$ and $\theta(x) = 0(x < 0)$; $w = z|t(n)|$; z is the number of nearest neighbors of a lattice site. Formula (18) leads to an equation describing the doublon concentration ($d \geq 0$) at $T = 0$:

$$\left[\frac{2(1-d)}{2-n} - 1 \right] \frac{4}{n} - 2 = \frac{\beta}{\beta^2 + \gamma} \frac{Q(\varepsilon_1) - Q(\varepsilon_2)}{w} + \frac{U}{w} \frac{\gamma}{[(\beta^2 + \gamma)^3]^{1/2}} \times \ln \left| \frac{\sqrt{\beta^2 + \gamma} Q(\varepsilon_2) + (\beta^2 + \gamma)\varepsilon_2 - U\beta}{\sqrt{\beta^2 + \gamma} Q(\varepsilon_1) + (\beta^2 + \gamma)\varepsilon_1 - U\beta} \right|, \quad (22)$$

where $E_{1,2}(\varepsilon), Q(\varepsilon)$ are obtained from formulas (9) and (10) as a result of the substitution $t_{\mathbf{k}}(n) \rightarrow \varepsilon, \tilde{t}_{\mathbf{k}}(n) \rightarrow [\tilde{t}(n)/t(n)]\varepsilon; t'_{\mathbf{k}}(n) \rightarrow [t'(n)/t(n)]\varepsilon; \beta = \alpha - \tilde{\alpha}[\tilde{t}(n)/t(n)]; \gamma = 4\alpha_1\alpha_2[t'(n)/t(n)]^2; \varepsilon_1, \varepsilon_2$ are the roots of the equations $E_{1,2}(\varepsilon) = 0$, and $\varepsilon_2 > \varepsilon_1$.

The hole concentration c is defined by the expression $c = d - n + 1$, which is obtained from two conditions $c + d + n^\uparrow + n^\downarrow = 1$ and $n^\uparrow + n^\downarrow + 2d = n$, n^\uparrow and n^\downarrow being the concentrations of sites occupied singly (by electrons with spin $\sigma = \uparrow$ and $\sigma = \downarrow$ respectively).

Figure 1 shows the dependence of the doublon concentration d on the parameter U/w_0 , where $w_0 = z|t_0|$, for different values of n . The parameters $\tau_1 = T_1/|t_0|, \tau_2 = T_2/|t_0|$ characterize the magnitude of the correlated hopping (1). It can be seen that the doublon concentration d decreases rapidly with increasing U/w_0 for $n < 1$.

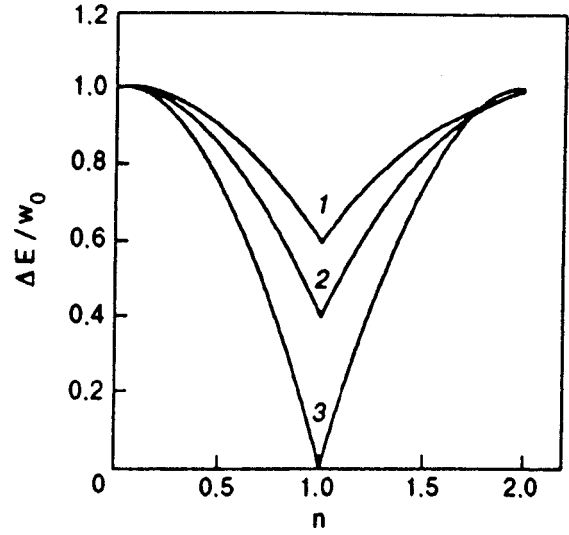


FIG. 2. Concentration dependence of ΔE for $U/w_0 = 2$; $\tau_1 = \tau_2 = 0.3$ (curve 1), $\tau_1 = \tau_2 = 0.2$ (curve 2), and $\tau_1 = \tau_2 = 0$ (Hubbard's model) (curve 3).

SOME CORRELATION EFFECTS IN NARROW ENERGY BANDS

Let us consider some of the consequences of the above results.

1. Using formula (9), we obtain the energy difference between the bottom of the upper and top of the lower Hubbard subbands for the quasistatic energy spectrum:

$$\Delta E = -(\alpha w + \tilde{\alpha} \tilde{w}) + \frac{1}{2}(Q_1 + Q_2), \quad (23)$$

$$Q_1 = \sqrt{(\alpha w - \tilde{\alpha} \tilde{w} + U)^2 + 4\alpha_1\alpha_2[z t'(n)]^2}, \quad (24)$$

$$Q_2 = \sqrt{(\alpha w - \tilde{\alpha} \tilde{w} - U)^2 + 4\alpha_1\alpha_2[z t'(n)]^2}, \quad (25)$$

where $\tilde{w} = z|\tilde{t}(n)|$.

At zero temperature and for $n = 1$, the energy gap (23) vanishes for

$$U \leq w + \tilde{w}, \quad (26)$$

in accordance with Mott's general physical considerations.¹⁷ For $t' = 0$ (i.e., for $t = -T_2$), the exact criterion for the metal-insulator transition was obtained by several authors.¹⁸ The condition (26) obtained by us coincides with this exact result. For $t' \neq 0 (t \neq -T_2)$, the metal-insulator transition criterion has not been determined so far (see, for example, Refs. 8 and 9). Gagliano *et al.*⁸ obtained a criterion for the metal-insulator transition, which coincides with (26). Using the methods of auxiliary bosons,¹⁹ Bulka⁹ found that the system goes over from metallic to insulating state for $U_c = 4z|t + T_2|$. However, this leads to the natural problem of matching the result with the exact criterion for metal-insulator transition obtained in Ref. 18 (for $t = -T_2$). It is also worthwhile to note that as in the Hubbard model, the use of Hubbard's approximation-1¹ in this model does not lead to a description of the metal-insulator transition.

The dependence of ΔE on the electron concentration n at $T = 0$ is shown in Fig. 2. It can be seen that for values of n close to 0 and 2, the difference in the energies between the

bottom of the upper and the top of the lower Hubbard subbands depends weakly on the correlated hopping parameters τ_1 and τ_2 . For $n \approx 1$, ΔE depends significantly on τ_1 and τ_2 . The value of ΔE increases upon a departure from half-filling (ΔE has a minimum for $n=1$). Hence it is easy to understand that in the metallic phase, the “metallic” nature of vanadium oxides V_kO_{2k-1} ($k \geq 3$) with a nonintegral number of electrons per cation is manifested less strongly than in oxides VO_2 and V_2O_3 (having an integral number of electrons per lattice site).²⁰

On account of the dependence of ΔE on the doublon concentration, the energy gap (23) depends on temperature. The dependence $\Delta E(T)$ shows that an increase in temperature may lead to a transition from the state with $\Delta E \leq 0$ to the state with $\Delta E > 0$. It should be noted in this connection that a transition from the paramagnetic metallic state to the state of a paramagnetic Mott-Hubbard insulator is observed in NiS_2 upon an increase in temperature.²¹

The model (2) can be used for describing doped narrow-band materials. Apparently, it can be assumed (see, for example, Refs. 2, 4 and 22) that in transition metal compounds of the type $(M_1)_{1-x}(M_2)_xX(M_1, M_2)$ denote the transition metal and X stands for oxygen, sulphur, selenium), the main effect of substitution $M_1 \rightarrow M_2$, where M_1 and M_2 are neighbors in the Periodic Table, boils down to a variation of the electron concentration in the narrow d -band (especially for small values of x). Thus, the obtained temperature dependence of the energy gap (23) can be used for explaining the metal-insulator transition observed upon an increase in temperature in the paramagnetic phase of the compound $(V_{1-x}Cr_x)_2O_3$ ^{17,23} for $x=0.04$.

2. Using the one-particle energy spectrum (16) and (17), we find that in the state with $U \rightarrow \infty$, the lower Hubbard subband has a width

$$\Delta E_1 = E_1(w) - E_1(-w) = 2w \left(\frac{2}{2-n} - n \right), \quad (27)$$

for $n < 1$, while the width of the upper subband for $n > 1$ is

$$\Delta E_2 = E_2(\tilde{w}) - E_2(-\tilde{w}) = 2\tilde{w}(n - 2 + 2/n). \quad (28)$$

These two formulas lead to a dependence of the energy width of subbands on electron concentration (Fig. 3). The concentration dependence of subbands is associated, in the first place, with the correlation effect of narrowing of subbands (the expression within brackets in formulas (27) and (28)), and in the second place by the concentration dependence of hopping integrals in the lower ($t(n)$) and upper ($\tilde{t}(n)$) Hubbard subbands (a peculiarity of the model under consideration). It can be seen that if we take into account the correlated hopping (1), the subbands become considerably narrower, the decrease in the width increasing with electron concentration. It can also be seen from Fig. 3 that in contrast to the electron-hole symmetry in the Hubbard model, the cases with $n < 1$ and $n > 1$ are not equivalent in the model under consideration.

A peculiar feature of formulas (27) and (28) for the concentration dependence of energy widths of subbands is the existence of minima shown in Fig. 3 (for the Hubbard model,

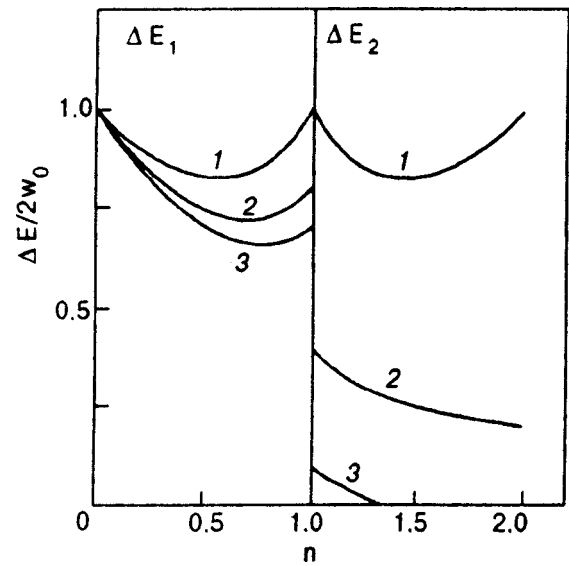


FIG. 3. Dependence of the energy width of lower (ΔE_1) and upper (ΔE_2) subbands on electron concentration n : $\tau_1 = \tau_2 = 0$ (curve 1), $\tau_1 = \tau_2 = 0.2$ (curve 2), and $\tau_1 = \tau_2 = 0.3$ (curve 3).

in the case when $\tau_1 = \tau_2 = 0$, for $n_1 \approx 0.6$ and $n_2 \approx 1.4$). The observed variation of the energy subband widths can be explained as follows. In the concentration range $0 < n < n_1$, transitions to the lower Hubbard subband can be interpreted as a hopping of the $|\sigma\rangle$ -states with effective hopping integral whose value increases (and hence ΔE_1 also increases). In other words, the electron-type conductivity changes into hole-type conductivity for $n = n_1$. The concentration dependence of the width of the upper Hubbard subband can be explained in a similar manner. Such an interpretation of dependences shown in Fig. 3 is in complete accord with the concentration dependence of the conductivity in partially filled narrow energy bands described in Ref. 11.

In the case of weak electron-electron interactions, the Hamiltonian (2) also leads to a number of serious departures from the Hubbard model, as was shown in Refs. 6 and 11. Among other things, the use of Eq. (2) allows us to explain the dependence of the binding energy of $3d$ -systems on the concentration of d -electrons, viz., the existence of a minimum for Mn and two nonequivalent peaks (V, Co) (resulting from a consideration of the correlated hopping (1)).¹¹

CONCLUSION

We have studied some correlation effects in the narrow-band model with electron-hole asymmetry with the help of the technique proposed in Refs. 11 and 12. A characteristic feature of this model is a systematic consideration of electron-electron interactions describing the hopping of electrons (correlated hopping).

The one-particle Green's function and the energy spectrum of quasiparticles are determined. A distinguishing feature of these expressions is the dependence on doublon or hole concentration (and hence on temperature), and the non-equivalence of concentration-dependent widths of upper and lower Hubbard subbands.

The quasiparticle energy spectrum is used for determining the expressions for the energy gap (the difference between energy values corresponding to the top of the lower and the bottom of the upper Hubbard subbands) and the widths of the upper and lower subbands.

It is shown that the energy gap increases upon a departure from the half-occupancy.

The temperature dependence of the energy gap can be used for studying the temperature-induced metal–insulator transition.

The concentration dependence of the width of Hubbard subbands is studied. It is found that a consideration of the correlated hopping (1) leads to a considerable narrowing of the subbands, the effect associated with this factor intensifying with the electron concentration.

The obtained results can be used to explain certain experimental data for narrow-band materials.

The authors are indebted to Prof. D. Khomskii for a discussion of some of the results presented in this work.

E-mail: didukh@tu.edu.te.ua

¹J. Hubbard, Proc. Roy. Soc. **A276**, 238 (1963).

²A. Georges, G. Kotliar, W. Krauth, and M. Rozenberg, Rev. Mod. Phys. **68**, 13 (1996).

³Yu. A. Izyumov, Usp. Fiz. Nauk **165**, 403 (1995) [*sic*].

⁴F. Gebhard, *The Mott Metal-Insulator Transition: Models and Methods*, Springer, Berlin (1997).

⁵L. D. Didukh, Fiz. Tverd. Tela **19**, 1217 (1977) [Sov. Phys. Solid State **19**, 711 (1977)].

⁶J. E. Hirsch, Physica C **158**, 326 (1989); Physica B **199-200**, 366 (1994).

⁷H. Q. Lin and J. E. Hirsch, Phys. Rev. B **52**, 16155 (1995); J. C. Amador and J. E. Hirsch, Phys. Rev. B **54**, 6364 (1996).

⁸E. R. Gagliano, A. A. Aligia, L. Arrachea, and V. Avignon, Phys. Rev. B **51**, 14012 (1995); L. Arrachea, E. R. Gagliano, and A. A. Aligia, Phys. Rev. B **55**, 1173 (1997).

⁹B. R. Bulka, Phys. Rev. B **57**, 10303 (1998); condmat/9703040.

¹⁰L. Didukh, V. Hankevych, and Yu. Dovgopyatii, Zh. Fiziich. Doslidzhen' **2**, 362 (1998); L. Didukh and V. Hankevych, cond-mat./9811213.

¹¹L. Didukh, Zh. Fiziich. Doslidzhen' **1**, 241 (1997).

¹²L. Didukh, Phys. Status Solidi B **206**, R5 (1998).

¹³L. M. Roth, Phys. Rev. Lett. **20**, 1431 (1968); Phys. Rev. **184**, 451 (1969).

¹⁴D. N. Zubarev and Yu. G. Rudoi, Usp. Fiz. Nauk **163**, 103 (1993) [Phys. Usp. **36**, 744 (1993)].

¹⁵Yu. A. Izyumov and N. I. Chashchin, Fiz. Metal. Metalloved. **84**, 16 (1997).

¹⁶B. Mehligh, H. Eskes, R. Hayn, and M. Meinders, Phys. Rev. B **52**, 2463 (1995); J. Beenen and D. M. Edwards, Phys. Rev. B **52**, 13636 (1995).

¹⁷N. F. Mott, *Metal-Insulator Transitions*, Taylor and Francis, London (1990).

¹⁸R. Strack and D. Vollhardt, Phys. Rev. Lett. **70**, 2637 (1993); A. A. Ovchinnikov, J. Phys.: Condens. Matter **6**, 11057 (1994); A. A. Aligia, L. Arrachea, and E. R. Gagliano, Phys. Rev. B **51**, 13774 (1995); J. de Boer and A. Schadschneider, Phys. Rev. Lett. **75**, 4298 (1995).

¹⁹G. Kotliar and A. E. Ruckenstein, Phys. Rev. Lett. **57**, 1362 (1986).

²⁰K. Kosuge, H. Okinaka, and S. Kachi, IEEE Trans. Magn. **Mag-8**, 581 (1972); R. O. Zaitsev, E. V. Kuz'min, and S. G. Ovchinnikov, Usp. Fiz. Nauk **148**, 603 (1986) [Sov. Phys. Usp. **29**, 322 (1986)].

²¹J. A. Wilson, *The Metallic and Nonmetallic States of Matter*, Taylor and Francis, London (1985).

²²H. Kajueter, G. Kotliar, and G. Moeller, Phys. Rev. B **53**, 16214 (1996).

²³D. B. Mc Whan, J. B. Remeika, T. M. Rice *et al.*, Phys. Rev. Lett. **27**, 941 (1971).

Translated by R. S. Wadhwa

Generation of nonequilibrium phonons and phonon–electron drag in bismuth

Vit. B. Krasovitskiĭ and S. V. Bengus

*B. Verkin Institute for Low Temperature Physics and Engineering, National Academy of Sciences of the Ukraine, 310164 Kharkov, Ukraine**

(Submitted December 2, 1998)

Fiz. Nizk. Temp. **25**, 487–495 (May 1999)

A directed flow of nonequilibrium phonons generated in crossed electric and magnetic field during supersonic drift of charge carriers in a high-quality bismuth single crystal is observed directly for the first time. Special geometry of the experiment makes it possible to measure the signal of acoustomagnetolectric effect which is a result of the drag of charge carriers by nonequilibrium phonons. The measurement of acoustomagnetolectric effect enables us to determine the part of electric power supplied to the sample, which is transformed into acoustic power. © 1999 American Institute of Physics. [S1063-777X(99)01005-1]

INTRODUCTION

The acoustoelectric effect is a manifestation of the phonon–electron interaction.^{1,2} Local electric fields emerging in a conducting medium under the action of a propagating acoustic wave trap charge carriers and lead to the excitation of a direct electric current in the direction of wave propagation as a result of momentum (and energy) transfer. The relation connecting the acousto-emf E^{ae} and the coefficient α_e of electron absorption of sound was derived by Weinreich³ from elementary considerations of conservation of total momentum of the electron and phonon systems and is valid both in the hydrodynamic ($ql \gg 1$) and in the collisionless ($ql \ll 1$) approximation (q is the acoustic wave vector and l the electron mean free path):

$$\alpha_e I_s = ne v_s E^{ae}, \quad (1)$$

where $\alpha_e I_s$ is the power per unit volume, supplied by the acoustic wave to conduction electrons. It was assumed that each phonon transfers to an electron the momentum $\hbar \omega / v_s$ (ω and v_s are the frequency and velocity of acoustic wave respectively). The density of induced electric current $j^{ae} = ne(\hbar \omega / v_s m)$, and the acoustic wave intensity is $I_s = \hbar \omega N_q v_s$ (N_q is the number of phonons per unit volume) and $\alpha_e = n / N_q v_s \tau$.

The number of electrons in bismuth is equal to the number of holes, and hence the resulting acoustoelectric current (for a closed circuit) or acousto-emf (for a disconnected circuit) is small since they are determined only by the difference between electron and hole mobilities. However, electrons and holes dragged by an acoustic wave in a magnetic field \mathbf{H} applied perpendicularly to the direction of propagation of sound are deflected in opposite directions at right angles to the direction of sound and to the magnetic field, creating the resultant emf (acoustomagnetolectric (AME) effect).

The AME effect was investigated theoretically in Refs. 4–7 and was observed experimentally for the first time in bismuth.⁶ The expression for the acousto-emf in the AME effect derived by Jamada⁶ under the conditions $ql \gg 1$, when

the acoustic wave propagates along the direction \mathbf{Y} and the static magnetic field is parallel to direction \mathbf{Z} has the form

$$E_x^{ame} = -\mu H \frac{S}{\rho v_s^3} \frac{\mu}{D} \left(\frac{\Sigma_n - \Sigma_p}{e} \right)^2 \frac{\omega \tau_R}{1 + \omega^2 \tau_R^2}, \quad (2)$$

where ρ is the density, $\mu = (\mu_n^{-1} + \mu_p^{-1})^{-1}$ and $D = (\mu_n D_p + \mu_p D_n)(\mu_n + \mu_p)^{-1}$ are the ambipolar mobility and diffusion coefficient (the subscripts n and p correspond respectively to electrons and holes), Σ_n and Σ_p are the deformation potential constants for electrons and holes, τ_R is the effective relaxation time, and S the acoustic energy density. A comparison of formula (2) with the expression for the acoustoelectric field calculated by Weinreich³ carried out by Jamada⁶ leads to the relation $E^{ame} = -\mu H E^{ae}$ for the AME field and accordingly to the relation with the electron absorption coefficient (modified Weinreich relation)

$$\alpha_e I_s = -ne v_s E^{ame} / \mu H. \quad (3)$$

This relation remains valid in a constant electric field E_0 parallel to \mathbf{X} . In this case, we have

$$\alpha_e = \frac{ne}{S} \frac{E^{ame}}{\mu H} = \frac{ne}{\rho v_s^3} \left(\frac{\Sigma_n - \Sigma_p}{e} \right)^2 \frac{\mu}{D} \frac{\omega \omega_{\text{eff}} \tau_R}{1 + \omega_{\text{eff}}^2 \tau_R^2}, \quad (4)$$

where $\omega_{\text{eff}} = \omega[1 - (E_0/H)/v_s]$. It can be seen from formula (4) that the electron absorption coefficient α_e reverses its sign when the electron moves at the supersonic velocity $v_d = E_0/H > v_s$, i.e., the absorption of sound by electrons is replaced by its enhancement, and the acousto-emf in the AME effect also changes its sign.

If no acoustic power is supplied to the crystal, the motion of charge carriers at a supersonic velocity is accompanied by spontaneous emission of phonons,⁸ leading, among other things, to a change in the conduction, and hence to nonlinearity in the current–voltage characteristics (IVC). Nonlinear current–voltage characteristics were observed for the first time in bismuth by Esaki:^{9,10} the transverse magnetoconductivity increases abruptly, while the velocity of charge carriers in the direction $[\mathbf{E} \times \mathbf{H}]$ of Hall drift attains the value of the velocity of sound. This fact enabled Esaki to

propose a hypothesis concerning the interrelation between the observed effect and the generation of phonons in bismuth. In experiments^{11,12} aimed at direct observation of phonon generation in bismuth, acoustic noise was detected in principle when the condition $v_d \approx v_s$ was satisfied. The interpretation of the results was complicated by the fact that the duration of the ultrasonic signal was larger than the duration of the driving current pulse by a factor of several units. Later, many authors¹³⁻¹⁶ proposed different versions of theoretical substantiation of the Esaki effect, which, however, described IVC nonlinearity only qualitatively. Bogod and Valeev¹⁷ proposed a phenomenological model of the Esaki effect, which successfully explained the experimentally observed peculiarities in the magnetoresistance of bismuth under nonlinear conditions. The model is based on the concept of acousto-emf associated with the number of nonequilibrium phonons. Bogod and Valeev¹⁷ used the Weinreich relation (1) in which the flux density of acoustic energy incident on the sample is replaced by the average power γW liberated by electrons during the generation of nonequilibrium phonons, i.e., $E^{ae} = \gamma W / nev_s$ (γ is the generation coefficient indicating the fraction of electric power supplied to the sample, which is transformed into acoustic flux). In a large number of publications devoted to experimental investigation of bismuth under nonlinear conductivity conditions (see, for example, Refs. 18-22), a large body of new information concerning the Esaki effect was obtained by measuring either the longitudinal voltage drop in the sample, or Hall voltage depending on various extrinsic parameters. It should be noted, however, that these experiments have a considerable drawback: the information on the system of nonequilibrium phonons gained from these experiments is only indirect.

In the present work, the directed flow of nonequilibrium phonons generated during supersonic drift of charge carriers and propagating in a sample is observed directly for the first time. We propose a special experimental geometry that makes it possible to observe in the same samples of Bi a negative AME signal, which is associated with the generation of acoustic power by charge carriers, as well as a positive AME signal, which is a result of drag of charge carriers by the flow of nonequilibrium phonons. The measurement of the magnitude of the AME effect allowed us to determine directly the fraction of electric power supplied to the sample, which is transformed into acoustic power.

EXPERIMENTAL RESULTS

Measurements were made at 4.2 K and involved the detection of the response signal formed as a result of passage through the sample of a solitary current pulse of the rectangular (with an elevation front $\sim 0.3 \mu\text{s}$) or saw-tooth shape (increasing linearly with time) of duration t_p from 2 to 20 μs on a storage oscilloscope, followed by the recording on an xy recorder.

The sample was cut from a high-quality bismuth single crystal (the ratio of resistances at room and helium temperatures was ~ 300) and had the shape of a rectangular bar with a size $4.5 \times 6.5 \times 2 \text{ mm}$ along the bisector ($C_1 \parallel X$), binary ($C_2 \parallel Y$), and trigonal ($C_3 \parallel Z$) crystallographic axes.

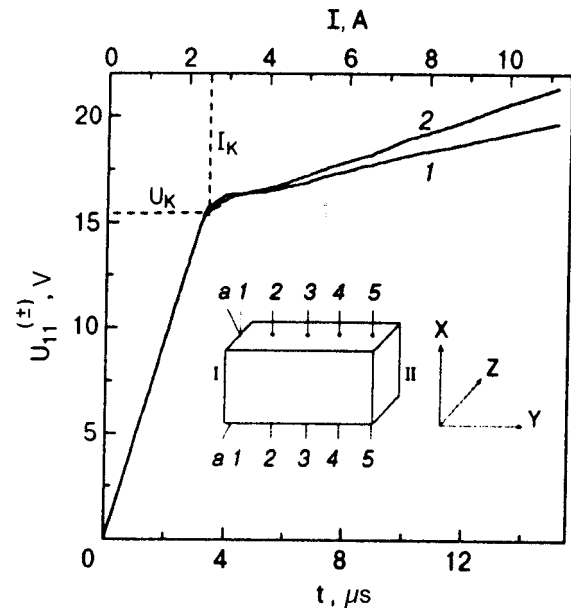


FIG. 1. Copies of oscillograms of $U_{11}^{(\pm)}$ signals: $-v_d$ (curve 1) and $+v_d$ (curve 2); $H=4.1 \text{ T}$. The upper scale corresponds to values of current proportional to time sweep, U_K and I_K are the voltage and current corresponding to the onset of the transition to the nonlinear conductivity mode. The inset shows the experimental geometry, 1-1, ..., 5-5 are pairs of potential contacts, a-a are current contacts.

The experimental geometry is shown in Fig. 1. The magnetic field is oriented along the third-order crystallographic axis. Digits 1-1, ..., 5-5 denote pairs of potential contacts distributed uniformly along the sample, and a-a are current contacts.

The employment of a-a contacts fixed at the endface of the sample as current contacts naturally leads to nonuniformity of electric current. The current density at face I near the current contacts (see Fig. 1) is always higher, and for $d \ll L$ is much higher than at face II at the opposite end of the sample (d is the separation between current contacts and L the sample length). With such an experimental geometry, the electric field strength E , and hence the drift velocity $v_d = cE/H$ of charge carriers in the sample, are position functions, and the condition $v_d > v_s$ for a transition to acoustoelectronic nonlinearity is realized only in the range of electric field $E > E_k$ near the endface I (E_k corresponds to the onset of the transition to nonlinear conductivity). At the same time, the linear dependence of current on voltage, i.e., Ohm's law, is preserved in the remaining part of the sample. Thus, the conductivity of the sample becomes nonuniform for a certain current $I > I_k$.¹⁾

The asymmetry of the experiments in the above sense determined two versions of measurements characterized by opposite directions of the drift velocity vector. Reversing the direction of current and magnetic field, the drift velocity vector for charge carriers $\mathbf{v}_d = c[\mathbf{E} \times \mathbf{H}] / H^2$, and accordingly the flow of nonequilibrium phonons generated by charge carriers for $v_d > v_s$ were directed either to the endface I ($-v_d$) containing current contacts or to the opposite endface II ($+v_d$). Figure 1 shows copies of oscillograms of potentials $U_{11}^{(\pm)}$ measured across contacts 1-1 with the help of "saw-tooth" current pulses for $\pm v_d$, i.e., directly in the region of

current contacts *a-a*. The time *t* laid along the abscissa axis is proportional to the measuring current *I*, and oscillograms are in fact current–voltage characteristics $U_{11}^{(\pm)}(I)$. The $U_{11}^{(\pm)}(I)$ dependences have a characteristic inflection associated with the generation of phonons in the direction of Hall drift of charge carriers for $v_d > v_s$. The slight mismatching of IVC in Fig. 1 is determined by the so-called nonreciprocity effect (NE),²⁰ i.e., nonreproducibility of the nonlinear region of IVC upon inversion of the drift velocity vector of charge carriers. The nonreciprocity effect was observed earlier in the conventional experimental geometry,²⁰ when the electric current is uniformly distributed along the sample, and in the case of nonuniform flow of current.^{22,23} It should be noted in this connection that a kink was also observed on the oscillograms $U_{ii}^{(-)}(t)$ ($i \geq 2$) measured together with $U_{11}(t)$, but not on oscillograms $U_{ii}^{(+)}(t)$ (this will be proved below). This kink, however, should not be identified with the generation of nonequilibrium phonons in the corresponding region of the sample. As a matter of fact, the emergence of a region of nonlinear (higher) conductivity near the current contacts *a-a* limiting the voltage drop to $\sim U_k$ (Fig. 1) and “accumulating” the major part of current for $I = I_k$ leads to restriction of the part of current flowing through the periphery region of the sample, while the response signals $U_{ii}^{(\pm)}$ are recorded on the oscillograph as a function of time *t*, i.e., of the total current *I*.

Figures 2 and 3 give examples of copies of oscillograms for nonlinear response signals $U_{ii}^{(\pm)}$ measured by passing through the sample the rectangular current pulses of amplitude 7.2 A corresponding to the nonlinear segment of IVC (see Fig. 1). Voltage drop at the beginning of the response signal corresponds to relaxation process of transition to a nonlinear regime and is characterized by the time τ_b .^{20,24} Response signals $U_{ii}^{(-)}$ ($i \geq 1$, Figs. 2a and 3a) have the same shape similar to the shape of current pulse (except the relaxation maximum at the beginning of response signals) and the amplitude decreasing monotonically with increasing distance between potential and current contacts. The horizontal segment of the response signal following the relaxation voltage drop characterizes the stationary mode of nonlinear conductivity.²⁾

A completely different situation is observed for response signals $U_{ii}^{(+)}$ ($i \geq 2$, Figs. 2b and 3b). Their shape differs from that of the current pulse: instead of the flat peak, we observe an increase in voltage after the relaxation voltage drop (in time t_b after the beginning of the pulse) (Fig. 2b, segment *b-m*). As the distance between the measuring potential and current contacts increases, the time t_{bm} during which the voltage increases to the maximum value increase monotonically, and the peak amplitude decreases (however, much more slowly than the amplitude of the response signal $U_{ii}^{(-)}$). Besides, response signals $U_{ii}^{(+)}$ can still be registered during a certain time t_{ps} while the response signals $U_{ii}^{(-)}$ cease upon switching off the current, the value of t_{ps} increases (like the time t_{bm}) with increasing number *i-i* of the measuring pair of potential contacts. Figure 3 shows for comparison the copies of oscillograms $U_{11}^{(\pm)}$ and $U_{55}^{(\pm)}$. It can be clearly seen that small difference (of the order of a few percent) between the signals $U_{11}^{(\pm)}$, i.e., the nonreciprocity

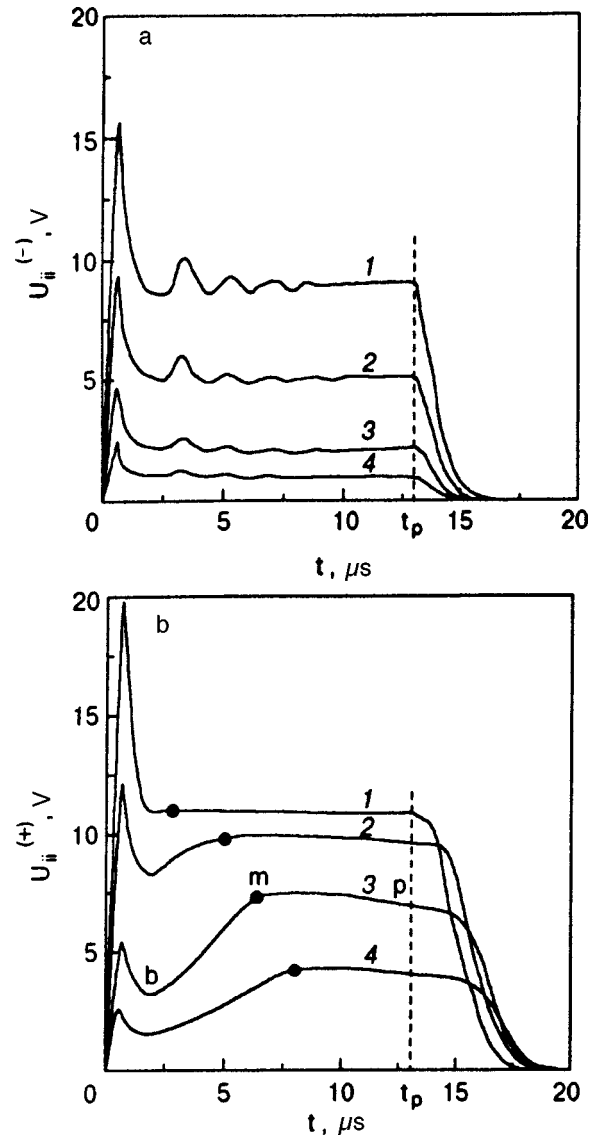


FIG. 2. Copies of oscillograms of $U_{ii}^{(-)}$ (a) and $U_{ii}^{(+)}$ (b) signals: U_{22} (curve 1), U_{33} (curve 2), U_{44} (curve 3), U_{55} (curve 4), t_p is the instant of switching-off the current, $H = 4.1$ T, $I = 7.2$ A.

effect, attain 400% for $U_{55}^{(\pm)}$ signals. Figure 3b also shows the time delay t_{ps} on the $U_{55}^{(+)}$ signal.

The degree of nonuniformity of current in the sample can be judged from the ratio $U_{ii}(i \geq 2)/U_{11}$ of signals measured in the range of currents $I < I_k$ corresponding to linear conductivity (see Fig. 1): 0.5, 0.29, 0.12, and 0.06 respectively for contacts 2–2, ..., 5–5. Almost the same ratios are also preserved between response signals $U_{ii}^{(-)}$ for $I > I_k$ (see Figs. 2a and 3a). However, similar relations between response signals $U_{ii}^{(+)}$ for $I > I_k$ are not observed. The values of $U_{ii}^{(+)}$ are always higher than the corresponding values of $U_{ii}^{(-)}$, the difference increasing significantly with increasing distance between potential contacts and the region of nonlinear conductivity (Figs. 2 and 3).

An unexpected result was obtained during measurements of response signals $U_{34}^{(+)}$ at contacts 3–4 arranged along the sample. The copies of oscillograms $U_{34}^{(\pm)}$ are shown in Fig. 4. It can be clearly seen that the signal $U_{34}^{(+)}$ can still be

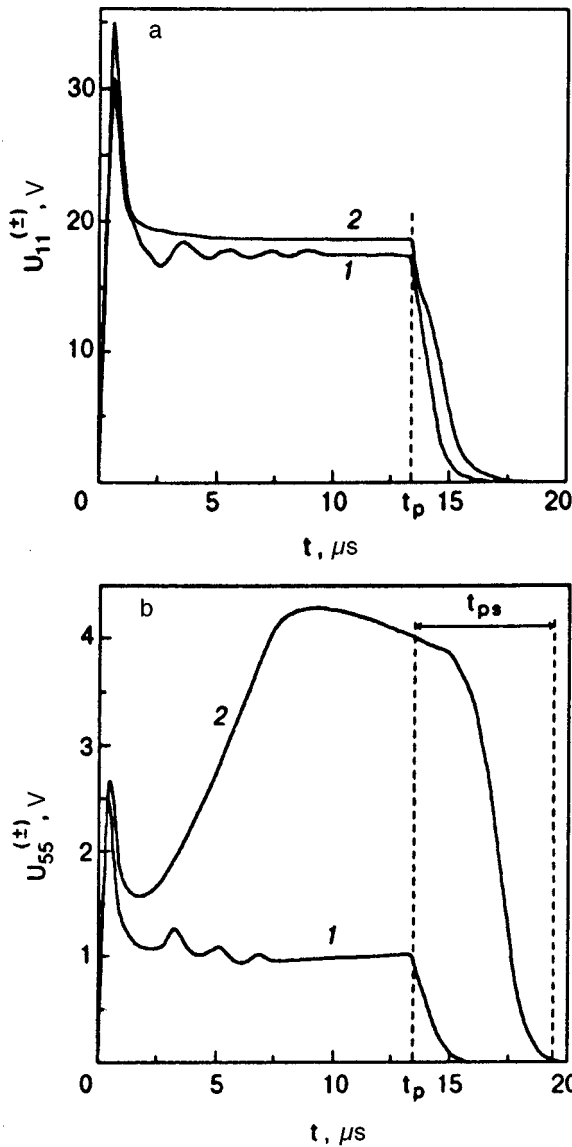


FIG. 3. Copies of oscillograms of $U_{11}^{(\pm)}$ (a) and $U_{55}^{(\pm)}$ (b) signals: $-v_d$ (curve 1) and $+v_d$ (curve 2); $H=4.1$ T, $I=7.2$ A.

registered during the time t_{ps} after switching off the current, but it does not become zero as a result of decrease (as in the case of the signal $U_{ii}^{(+)}$), passing through zero and reversing its sign.

DISCUSSION OF RESULTS

The experimental results concerning the behavior of nonlinear response signals $U_{ii}^{(+)}$ ($i > 1$) can be explained by making the following assumptions that are quite natural for bismuth.

- (1) Nonlinear conductivity regime is formed in the sample region directly adjoining current contacts. (This region at the endface of the sample will be henceforth referred to as the nonlinear conductivity region (NCR), and the remaining part as the linear conductivity region (LCR). The mechanisms of instability stabilization upon a

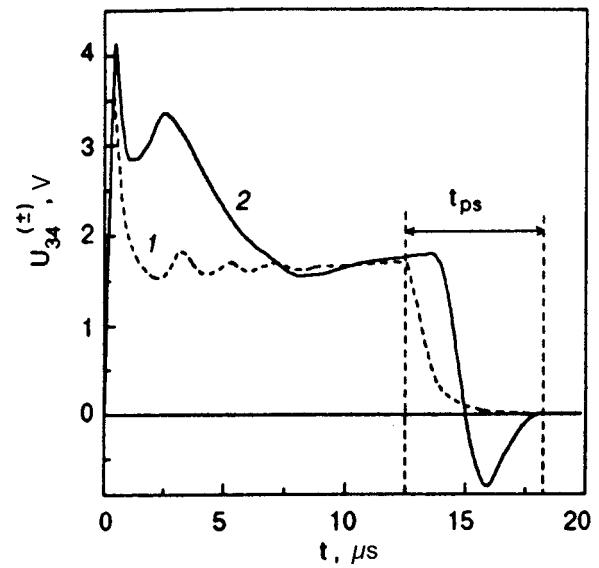


FIG. 4. Copies of oscillograms of $U_{34}^{(\pm)}$ signals: $-v_d$ (curve 1) and $+v_d$ (curve 2); $H=4.1$ T, $I=7.2$ A.

transition to the phonon generation mode and the size of the NCR in a similar experimental geometry are considered in detail in Ref. 23.)

- (2) A front ($\sim 0.5 \mu s$) of the acoustic pulse propagating in the sample in the direction of the endface II is formed in the NCR during the time interval equal to the time $t_b \approx 1 - 2 \mu s$ of relaxation to the nonlinear mode.^{20,25}
- (3) Bismuth exhibits a strong phonon–electron interaction leading to the drag of charge carriers by nonequilibrium phonons.
- (4) The energy of an acoustic pulse attenuates during its propagation along the sample.

Thus, having created two regions with different conductivity in the sample and treating NCR as a generator of acoustic pulse probing LCR, we obtain a standard geometry for observing the acoustomagnetolectric effect: an acoustomagnetolectric voltage is formed in the direction \mathbf{X} as the acoustic pulse propagates along the direction \mathbf{Y} in the presence of the magnetic field $\mathbf{H} \parallel \mathbf{Z}$.

The nonuniformity of potential distribution in the sample is determined by the experimental geometry at the initial instant and almost till the end of relaxation to the nonlinear regime, i.e., during the time t_b (see Fig. 2b, index b). However, starting from the instant $t_b \approx \tau_b$, the acoustic wave front begins to form in the LCR an acoustomagnetolectric signal which is stronger (see Figs. 2 and 3) than the corresponding signal associated with the initial ($t < \tau_b$) nonuniformity of the current flow. In other words, starting from the instant t_b , the potential distribution in the sample varies significantly, and the magnitudes of voltages $U_{ii}^{(+)}$ ($i > 1$) being measured are determined completely by the AME effect. The time t_{bm} of the increase in the AME voltage to its maximum value (dark circles m in Fig. 2b) is determined just by the propagation of the front of the acoustic wave formed in the NCR region. The values of time t_{bm} observed experimentally at contacts $i-i$ ($i > 1$) correlate with the corresponding values

calculated from the relation $t_{bm} = L_i/v_s$, where L_i is the distance between the NCR to the contacts $i-i$, and $v_s = 0.85 \times 10^5$ cm/s is the velocity of sound for the direction $\mathbf{Y} \parallel \mathbf{C}_2$.²⁶

The measured values of voltage $U_{ii}^{(+)} (i > 1)$ are completely determined just by the AME effect rather than by percolation currents since, in contrast to the response signals $U_{ii}^{(-)} (i \geq 1)$, switching-off the current (index p in Fig. 2b) is manifested in response signals $U_{ii}^{(+)} (i > 1)$ not immediately, but only after a time t_{ps} (see Figs. 2b and 3b). During the time t_{ps} , the rear front of the acoustic pulse formed after switching-off the current traverses the distance from the NCR region to the given pair of contacts $i-i$. The observed phenomenon is typical of ‘‘postsounding’’ effect whose manifestation in our case can be formulated as follows. After the removal of electric field whose value $E \geq E_k$ corresponds to supersonic drift of charge carriers, and hence to the completion of generation of the acoustic pulse in the NCR, the potential difference observed in the LCR and caused by the drag of charge carriers by sound can still be detected during the time of existence of acoustic flux in the sample. The values of ‘‘postsounding’’ time t_{ps} observed experimentally at contacts $i-i (i > 1)$ correlate with corresponding values calculated from the relation $t_{ps} = L_i/v_s$. It should also be noted that the values of time t_{bm} and t_{ps} required for the leading and rear fronts of an acoustic pulse to traverse the relevant distances L_i are close, i.e., $t_{bm} \approx t_{ps}$ (see Figs. 2b and 3b).

Since the duration of current pulse ($\sim t_p - t_b$) in our case is longer than the time of its passage through the sample (L/v_s), an increase in voltage to the maximum value after the relaxation to the nonlinear mode at response signals $U_{ii}^{(+)} (i > 1)$ corresponds to the stabilization of the stationary value of voltage of the AME effect, and hence a horizontal plateau must be observed in the response signals down to zero values of current. It can be seen from Figs. 2b and 3b, however, that the voltage decreases monotonically after attaining its maximum value. Experiments show^{20,22,23} that in such experimental conditions (magnitudes of current and magnetic field as well as size and quality of the sample) Joule heating starts being manifested in nonlinear response signal after the time interval $\sim 7-10 \mu s$, which is manifested in deviation of the voltage being measured from the stationary value towards higher values²³ (suppression of nonlinearity). Indeed, Joule heating is manifested in nonlinear response signals $U_{ii}^{(-)}$ determined by the NCR in the form of a typical increase in voltage at the end of the pulse (see Figs. 2a and 3a). At the same time, the decrease in the acoustic power emitted from the NCR upon heating must lead to a corresponding suppression of the AME effect, which is actually observed in the signals $U_{ii}^{(+)} (i > 1)$. This statement is also confirmed in Fig. 5 containing oscillograms of response signals $U_{55}^{(\pm)}$ measured in different magnetic field. As the magnetic field increases, the condition for a transition to nonlinear conductivity mode ($v_d = cE/H \geq v_s$) is satisfied in stronger electric fields.⁹ This leads to an increase in the power supplied to the sample and to a stronger heating of the sample for a given current. It can easily be seen from Fig. 5 that an increase in magnetic field leads to a stronger decrease in the $U_{55}^{(+)}$ after attaining the peak value and to a stronger

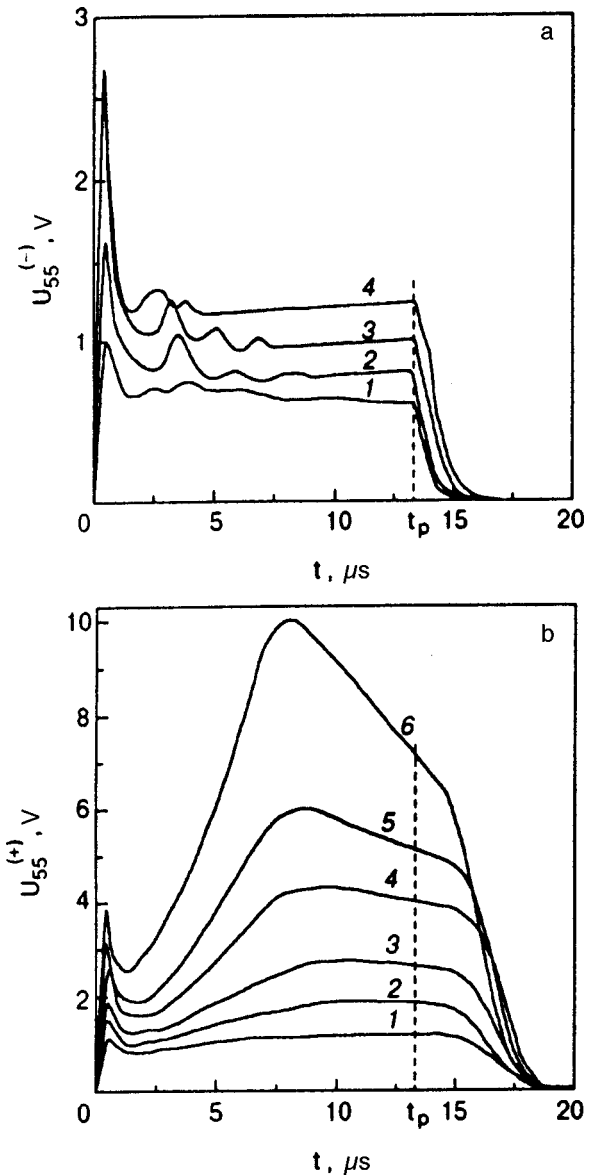


FIG. 5. Copies of oscillograms of $U_{55}^{(-)}$ (a) and $U_{55}^{(+)}$ (b) signals recorded for $I = 7.2$ A and different values of magnetic field, T: 1.76 (curve 1), 2.93 (curve 2), 4.1 (curve 3), and 8.79 (curve 4) (a) and 1.76 (curve 1), 2.34 (curve 2), 2.93 (curve 3), 4.1 (curve 4), 5.86 (curve 5), and 8.79 (curve 6) (b).

increase in the signal $U_{55}^{(-)}$. It should be noted that basically different response of the signals $U_{ii}^{(-)}$ and $U_{ii}^{(+)}$ to Joule heating of the sample confirms once again the correctness of the above interpretation of experimental results.

The above arguments explain the experimental result presented in Fig. 4, where the positive ‘‘postsounding’’ signal measured on longitudinal contacts 3–4 changes to a negative signal. The presence of a nonzero signal $U_{34}^{(+)}$ is a direct consequence of attenuation of acoustic pulse as a result of its propagation along the sample and corresponds to the difference in the AME effect $U_{33}^{(+)}$ and $U_{44}^{(+)}$; before and immediately after switching-off the current, $U_{33}^{(+)} > U_{44}^{(+)}$ (see Fig. 2b). However, this relation, and hence the signal $U_{34}^{(+)}$ reverse sign when the rear front of the acoustic pulse passes through the line of contacts 3–3.

Analyzing processes associated with the generation of sound by charge carriers drifting with ultrasonic velocities, we must know the part of electric power supplied to the sample, which is transformed into the acoustic power. For example, the introduction into the expression for IVC^{17,20} of the sound generation coefficient in explicit form

$$j \approx \sigma_H E (1 + \Gamma c E / H v_s) \quad (5)$$

has made it possible to explain a number of electric properties of bismuth¹⁷⁻¹⁹ associated with the transition to the nonlinear conductivity mode. (Here σ_H is the linear magnetoconductivity, $\Gamma = \gamma - \delta$, δ being the coefficient associated with attenuation of sound). Experimental data on IVC obtained by Bogod *et al.*^{18,19} at different temperatures and magnetic fields, as well as relation (5) provided rich but unfortunately indirect information on the generation coefficient. Although the value of Γ is always smaller than unity by definition, its absolute values calculated by Bogod and Valeev¹⁷ at helium temperature proved to be absurdly high (1-10). In Ref. 23, where we studied transverse galvanothermomagnetic (Ettingshausen) effect during the transition of bismuth to the phonon generation mode, the value of the experimentally determined sound generation coefficient was ~ 0.3 . The experimental values of AME voltage obtained by us here allow us in principle to determine directly the value of acoustic power generated in the sample in the nonlinear conductivity region. For this purpose, we can use the value of $U_{22}^{(+)}$ measured in the sample region directly adjoining the source of sound, i.e., NCR, and formula (2) connecting the acoustic energy density with the AME signal, as well as the results obtained by Jamada⁶ who measured the ratio of the acoustic power supplied to the sample to the corresponding AME signal in a similar experimental geometry and in Bi samples of the same degree of purity as in our experiments. In our calculations, we assume that the ambipolar mobility for $\mathbf{H} \parallel \mathbf{C}_3 \mu^{-1} = 1/2(\mu_x^{-1} + \mu_y^{-1}) + \nu_x^{-1} = 2.3 \times 10^6 \text{ cm}^2 / (\text{V} \cdot \text{s})$, is where μ_x, μ_y , and ν_x are the components of the mobility tensors for electrons and holes,²⁷ the velocity of sound for the direction $\mathbf{Y} \parallel \mathbf{C}_2$ is $v_s = 0.85 \times 10^5 \text{ cm/s}$,²⁶ $D/\mu = (2/3e)(\varepsilon_F^n + \varepsilon_F^p)$, where $\varepsilon_F^n = 25 \text{ meV}$ and $\varepsilon_F^p = 12 \text{ meV}$ are the Fermi energies for electrons and holes,²⁸ $\tau_R \approx \tau = 3 \times 10^{-8} \text{ s}$,²⁹ $\omega \tau_R \gg 1$, the difference between the deformation potential constants for electrons and holes for $\mathbf{q} \parallel \mathbf{C}_2$ determined experimentally by Jamada⁶ is $\Sigma_n - \Sigma_p = 0.3 \text{ eV}$, and the density $\rho = 10 \text{ g/cm}^3$. As a result, we obtain the intensity of sound $I_s = S v_s = 700 \text{ W/cm}^2$ for $U_{22}^{(+)} = 12 \text{ V}$ and $H = 4.1 \text{ T}$. The corresponding electric power supplied to the sample (see IVC in Fig. 1) is equal to 130 W or, if we assume that the entire supplied power is transformed into the acoustic flux, $I_0 = 1300 \text{ W/cm}^2$ for the cross-sectional area of the sample $\sim 0.1 \text{ cm}^2$. Thus, the generation coefficient is $\gamma = I_s / I_0 \approx 0.5$.

Let us consider again the $U_{ii}^{(-)}$ signals measured in the case when the drift velocity vector for charge carriers, and hence the flow of nonequilibrium phonons generated by charge carriers in the NCR, was directed to the endface I of the sample. In this situation, the AME effect associated with the sound reflected at the endface I could be observed in principle in the LCR. However, no AME voltage is observed

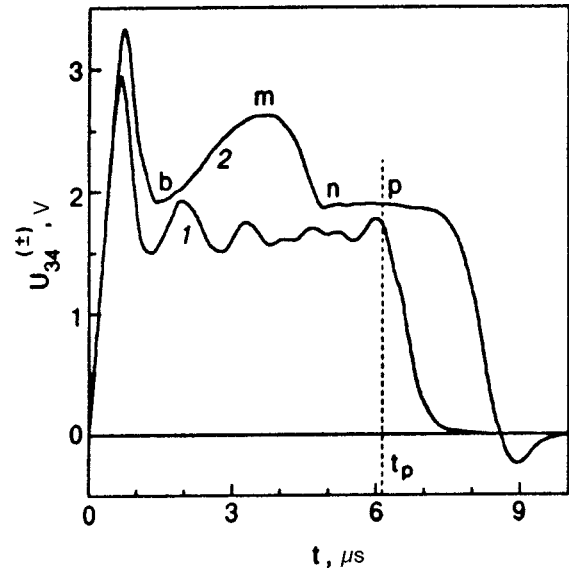


FIG. 6. Copies of oscillograms of $U_{34}^{(\pm)}$ signals: $-\mathbf{v}_d$ (curve 1) and $+\mathbf{v}_d$ (curve 2); $I_{25} = 7.2 \text{ A}$.

at $U_{ii}^{(-)}$ ($i \geq 2$) signals (see Fig. 2a). It should also be noted that no peculiarities associated with the acoustic momentum reflected at the endface II of the sample are observed at signals $U_{ii}^{(+)}$ ($i \geq 2$) either. In this case, additional AME voltage could be manifested in the main signal in the form of a voltage decrease following the peak (point *m* in Fig. 2b) after a time required for the acoustic pulse front to traverse the distance from the corresponding pair of contacts to face II and back. We assume that the absence of the AME effect associated with the sound reflected at the endfaces is first of all a consequence of strong dissipation of sound at roughnesses. The endfaces of the sample usually contain a larger number of crystal lattice defects emerging during its electric-spark erosion and leading to the formation of a rough surface after subsequent etching.

In order to confirm the correctness of the interpretation of the above results, we made an additional experiment on the same sample in a different geometry. A current pulse was passed through a pair of contacts 2-5 at the lateral (long) face of the sample, while contacts 3-4 mounted on the opposite face (Fig. 1) were used as potential contacts. It was assumed that the small separation between the source of nonequilibrium phonons (NCR between the current contacts 2-5) and the opposite face of the sample on which the potential contacts 3-4 are mounted will enable us to observe in the given experimental geometry an AME signal associated with phonons emitted directly in the LCR as well as with phonons reflected from the sample surface. These expectations were also based on the fact that unlike endfaces, the lateral surfaces are smooth and do not contain roughnesses. The results of experiments are presented in Fig. 6. As in the previous experiments, the response signal $U_{34}^{(-)}$ is similar in shape to the current pulse. At the same time, the signal $U_{34}^{(+)}$ has a complex shape which, however, can easily be calculated on the basis of the treatment of experimental data proposed above. After the initial voltage drop corresponding to the transition to the regime of generation of nonequilibrium

phonons, the oscillogram displays a nonmonotonic region $b-n-m-p$ demonstrating the process of stabilization of AME voltage in the LCR. The increase in the AME voltage (segment $b-m$) is a consequence of the propagation of acoustic front from the NCR region to the opposite face of the sample, while the subsequent decrease in voltage (segment $m-n$) is associated with the motion of acoustic pulse reflected from the sample surface and with the corresponding compensation of the part of the main AME signal. Pay attention to the fact that the time periods t_{bm} and t_{mn} corresponding to an increase and decrease in the AME voltage are virtually equal: $t_{bm} \approx t_{mn}$. The next flat segment corresponds to stabilized AME voltage in the sample. A comparison with the total signal amplitude $U_{34}^{(+)}$ (point m in Fig. 6) and the amplitude of the compensating part $m-n$ shows that approximately 20% of the incident phonon flux is reflected from the sample surface. The existence of a noticeable reflected phonon flux and the AME voltage associated with it also follows from the fact that after switching-off the current (point p in Fig. 6), not only a positive, but also a negative “postsounding” signal is observed on the $U_{34}^{(+)}$ signal. In analogy with experiments in the main geometry, no AME voltage is observed in the $U_{34}^{(-)}$ signal. In all probability, not more than 5% of nonequilibrium phonons emitted in the NCR attained in this case the sample surface containing potential contacts according to our estimates. While obtaining the estimate, we assumed that the sample surface containing current contacts reflects approximately 20% of emitted acoustic power, which subsequently attenuates over a length of 4.5 mm (sample width) to 1/4 of the initial value (in analogy with the ratio of the signals $U_{22}^{(+)}$ and $U_{55}^{(+)}$ in Fig. 2b). Naturally, such a small value of the AME voltage is not manifested in the much stronger signal $U_{34}^{(-)}$ whose value is determined by the voltage drop associated with nonuniform current flow in the sample, i.e., the sample geometry.

The authors are grateful to V. D. Fil' for critical remarks.

*E-mail: krasovitsky@ilt.kharkov.ua

¹⁾Detailed experimental investigation of bismuth in the acoustoelectric nonlinearity mode under the conditions of nonuniform distribution of electric field was carried out in Ref. 22. The distribution of potential for a semi-infinite plate into which the direct current flows and leaves the sample through a pair of contacts is also calculated in Ref. 22.

²⁾For all response signals $U_{ii}^{(-)}$ (Fig. 2a), a transient effect associated with a periodic time dependence of voltage across the sample is observed. Similar voltage oscillations were observed and analyzed in Refs. 9, 17, 20 and 25

devoted to investigation of electrical properties of bismuth in the regime of elastic wave generation. In Ref. 22, it is shown experimentally that acoustoelectric oscillations emerge in the case of a nonuniform current flow through the sample, when charge carriers drift to the surface containing current contacts. Oscillations obtained in this way can be observed for an arbitrary combination of current, magnetic field, and temperature corresponding to the conditions for the existence of nonlinear conductivity mode in the sample.

¹R. N. Parmenter, Phys. Rev. **89**, 990 (1953).

²G. Weinreich, T. Sanders, Jr., and H. G. White, Phys. Rev. **114**, 33 (1959).

³G. Weinreich, Phys. Rev. **107**, 317 (1957).

⁴A. A. Grinberg, Fiz. Tverd. Tela **6**, 2010 (1964) [Sov. Phys. Solid State **6**, 1586 (1964)].

⁵A. A. Grinberg and N. I. Kramer, Dokl. Akad. Nauk SSSR **157**, 79 (1964) [Sov. Phys. Dokl. **9**, 552 (1964)].

⁶T. Jamada, J. Phys. Soc. Jpn. **20**, 1424 (1965).

⁷M. I. Kaganov, Sh. T. Mevlyut, and I. M. Suslov, Zh. Éksp. Teor. Fiz. **78**, 376 (1980) [Sov. Phys. JETP **51**, 189 (1980)].

⁸V. I. Pustovoit, Usp. Fiz. Nauk **97**, 257 (1969) [Sov. Phys. Usp. **12**, 105 (1969)].

⁹L. Esaki, Phys. Rev. Lett. **8**, 4 (1962).

¹⁰L. Esaki, Proc. IEEE **50**, 322 (1962).

¹¹A. M. Toxen and S. Tansal, Phys. Rev. Lett. **10**, 481 (1963).

¹²K. Walther, Phys. Rev. Lett. **15**, 706 (1965).

¹³J. I. Hopfield, Phys. Rev. Lett. **8**, 311 (1962).

¹⁴S. J. Miyake and R. Kubo, Phys. Rev. Lett. **9**, 62 (1962).

¹⁵R. Abe, Prog. Theor. Phys. **30**, 149 (1963).

¹⁶V. P. Kalashnikov, Fiz. Met. Metalloved. **18**, 171 (1964).

¹⁷Yu. A. Bogod and R. G. Valeev, Fiz. Nizk. Temp. **3**, 874 (1977) [Sov. J. Low Temp. Phys. **3**, 424 (1977)].

¹⁸Yu. A. Bogod, R. G. Valeev, and G. P. Onokienko, Fiz. Nizk. Temp. **1**, 636 (1975) [sic].

¹⁹Yu. A. Bogod and R. G. Valeev, Fiz. Nizk. Temp. **2**, 897 (1976) [Sov. J. Low Temp. Phys. **2**, 441 (1976)].

²⁰Yu. A. Bogod, Fiz. Nizk. Temp. **8**, 787 (1982) [Sov. J. Low Temp. Phys. **8**, 393 (1982)].

²¹S. V. Bengus, Yu. A. Bogod, and P. E. Finkel', Fiz. Nizk. Temp. **16**, 738 (1990) [Sov. J. Low Temp. Phys. **16**, 434 (1990)].

²²S. V. Bengus, Vit. B. Krasovitskiĭ, and P. E. Finkel', Fiz. Nizk. Temp. **18**, 30 (1992) [Sov. J. Low Temp. Phys. **18**, 19 (1992)].

²³Vit. B. Krasovitskiĭ and S. V. Bengus, Fiz. Nizk. Temp. **19**, 805 (1993) [Low Temp. Phys. **19**, 576 (1993)].

²⁴T. Jamada, J. Phys. Soc. Jpn. **20**, 1647 (1965).

²⁵P. Finkel, S. V. Bengus, and Vit. B. Krasovitskiy, Physica B **194–196**, 435 (1994).

²⁶G. Eckstein, A. W. Lawson, and D. H. Reneker, J. Appl. Phys. **31**, 1534 (1960).

²⁷Yu. A. Bogod and Vit. B. Krasovitskiĭ, in *Physics of Condensed State* [in Russian], Khar'kov (1974), p. 37.

²⁸V. S. Edel'man, Usp. Fiz. Nauk **123**, 257 (1977) [Sov. Phys. Usp. **20**, 819 (1977)].

²⁹R. N. Zitter, Phys. Rev. Lett. **14**, 14 (1965).

LOW-DIMENSIONAL AND DISORDERED SYSTEMS

On vortex phase of systems with pairing of spatially separated electrons and holes

S. I. Shevchenko and V. A. Bezuglyĭ

*B. Verkin Institute for Low Temperature Physics and Engineering, National Academy of Sciences of the Ukraine, 310164 Kharkov, Ukraine**

(Submitted December 4, 1998)

Fiz. Nizk. Temp. **25**, 496–508 (May 1999)

The possibility of the emergence of a macroscopic amount of planar vortices with identical circulation in systems with pairing of spatially separated electrons and holes was predicted by us recently [S. I. Shevchenko, Phys. Rev. **B56**, 10355 (1997); *ibid.* **B57**, 14809 (1998)]. In the present work, we consider a structure formed by planar vortices in a disk-shaped sample in a magnetic field whose two-dimensional divergence differs from zero. The total number of vortices and the energy of a system of vortices are determined as functions of the external magnetic field and the sample size. It is found that the energy of the vortex structure is proportional to the volume of the system, and hence a vortex state is a new thermodynamic phase of the investigated system (analogous to the Shubnikov phase in conventional superconductors).

© 1999 American Institute of Physics. [S1063-777X(99)01105-6]

1. INTRODUCTION

In recent years, several publications have appeared which contain the results of experimental investigations of double-layered 2D-electron-hole and electron-electron systems and report on the observation of several effects probably associated with the emergence of spontaneous interlayer coherence (“condenser” superconductivity) in these systems. Thus, Cooper *et al.*¹ have attributed the increase in the longitudinal resistance of three-layered InAs/GaSb/AlSb heterostructures for identical densities of electrons in the InAs layer and holes in the AlSb layer to the formation of bound electron-hole pairs. Lilly *et al.*² have studied the drag of electrons in one layer by the current of electrons in the other layer in the system GaAs/Al_xGa_{1-x}As in a strong magnetic field for a half-filled lower Landau level in each layer. They observed a number of anomalies in the drag current and attributed them to a strong correlation between electrons in adjacent layers. Butov *et al.*^{3,4} studied the time evolution of luminescence of indirect excitons in double quantum wells AlAs/GaAs after pulse laser excitation in strong magnetic fields ($B \leq 12$ T) at low temperatures ($T \geq 1.3$ K). Butov *et al.*³ observed an anomalous increase in the diffusion coefficient with increasing field and decreasing temperature, and interpreted it as the onset of superfluidity of excitons as a result of their condensation. The anomalously rapid transport of indirect excitons detected by Butov and Filin⁴ was also attributed by them to the emergence of superfluidity of excitons.

Many authors have reported the results of theoretical investigations of systems with spontaneous interlayer correlations. The possibility of superfluidity of electron-hole pairs in systems with pairing of spatially separated electrons and holes (PSSEH) was predicted about two decades ago⁵⁻⁷ (see also Ref. 8). A large number of theoretical works⁹⁻³⁰ have

been published in recent years describing the effect of a strong uniform magnetic field on pairing of spatially separated electrons and holes, as well as the peculiarities of superfluidity in such fields. However, the fact that a nonuniform magnetic field can produce qualitatively new effects remained unnoticed.

One of the authors of the present work^{31,32} studied the behavior of systems with PSSEH in a magnetic field below the point of transition of electron-hole pairs into superfluid state and showed that a nonuniform magnetic field with a nonzero two-dimensional divergence ($\text{div}_2 \mathbf{H}$) may produce in the system a macroscopic amount of planar vortices with identical circulation. The term planar vortex stands for a vortex in which electron-hole pairs rotate as a single entity in the plane of the structure. Although planar vortices are in many respects similar to the well-known Onsager-Feynman vortices or Abrikosov vortices, they do not form a lattice unlike these vortices. It was shown in Refs. 31 and 32 that in the limit when planar vortices can be treated as continuously distributed, their density is proportional to $\text{div}_2 \mathbf{H}$. It follows hence that the total number of planar vortices is proportional to the magnetic flux across the sample boundary. The latter quantity is proportional to the perimeter of the system and not its area, and hence one can ask whether the predicted effect of emergence of planar vortices in superconducting systems with PSSEH is two- or three-dimensional. It will be shown in the present work that this effect is three-dimensional, and hence the vortex state is a new thermodynamic phase analogous to the Shubnikov Phase in conventional superconductors.

Returning to the problem of experimental confirmation of the transition of indirect excitons to the superfluid state, it must be remarked that certain difficulties are encountered in the direct measurement of conductivity of each layer. In this

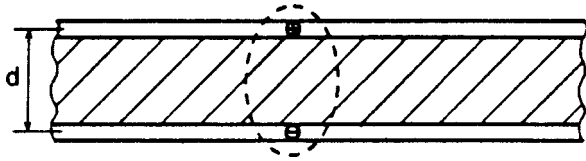


FIG. 1. Electron-hole pair in a system with PSSEH (schematic diagram).

respect, the emergence of planar vortices is also interesting because it may provide a direct evidence for the transition of electron-hole pairs to the superfluid state since planar vortices carry a magnetic flux^{31,32} which may be detected by contactless method.

It was shown in Ref. 31 and 32 that the energy of the superconducting phase in a magnetic field in systems with PSSEH is defined by the expression

$$E = \int \left[\frac{\hbar^2 n_s}{2M} (\nabla \varphi)^2 - \frac{\hbar n_s e d}{Mc} \nabla \varphi (\mathbf{H} \times \hat{\mathbf{z}}) \right] d^2 \rho. \quad (1)$$

Here n_s is the superfluid density of pairs, M their mass, φ the phase of the order parameter, d the separation between layers with electron and hole conductivity, and $\hat{\mathbf{z}}$ a unit vector along the normal to the conducting layers.

Let us explain the emergence of the second term in formula (1). If electrons and holes are separated in space, the electron-hole pairs form a system of dipoles (see Fig. 1) whose dipole moments are parallel (or antiparallel) to the z -axis. In a magnetic field \mathbf{H} , the energy of a dipole moving with a velocity \mathbf{v}_s is equal to $\mathbf{v}_s(e\mathbf{d} \times \mathbf{H})/c$ (plus the kinetic energy $Mv_s^2/2$). Since the velocity \mathbf{v}_s can be assumed to be equal to $(\hbar/M)\nabla\varphi$ within the accuracy desired by us, we arrive at the required result (after replacing \mathbf{d} by $d\hat{\mathbf{z}}$). It is the presence of the second term in (1) that may lead to the emergence of a macroscopic number of vortices with identical circulation in superconducting systems with PSSEH. Indeed, assuming that the field \mathbf{H} is a two-dimensional ‘‘hedgehog’’ (i.e., the magnetic field diverges radially from a certain center), we find that the second term makes the emergence of circular currents around this center more advantageous from the energy point of view (for a quite large value of H). However, since the phase φ may acquire only a quantum increment $2\pi n$ (where n is an integer), the mechanism of realization of these circular current loops involves the emergence of quantized planar vortices with identical circulation in the system.

As in our previous works,^{31,32} we consider an exactly solvable case in which a system with PSSEH is placed in an external magnetic field produced by a two-dimensional circular current loops. We assume that the electron-hole system is a disk of radius R , and consider the case when the circular currents producing the field lie in a plane parallel to the plane of the disk, and the axis around which they circulate passes through the center of the disk (Fig. 2). Let us consider some important properties of such a magnetic field. Let a system of circular current loops with a constant azimuthal component of the two-dimensional current density $I = \text{const}$ fill a circle of radius R' . In this case, at distances much smaller than R' from the plane in which the currents flow, the components of

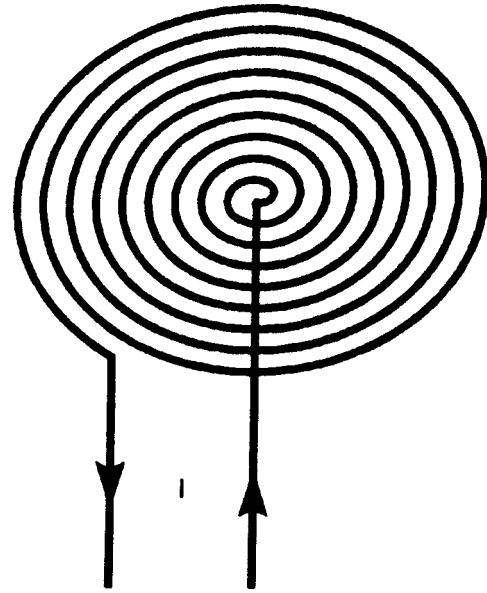


FIG. 2. Schematic diagram of a two-dimensional circular current loop.

the magnetic field will be equal to $H_\theta = 0$ and $H_\rho = 2\pi I/c = \text{const}$ everywhere except in small regions at the center of the circle and at its periphery where the edge effects become significant (Fig. 3). Such a current also leads to the emergence of the component H_z which, however, does not affect the value of the superfluid velocity. As in Refs. 31 and 32, we consider the case $R \ll R'$ (in order to eliminate the effect of the boundary of the system of circular current loops), and assume that the distance between the plane of the currents and the disk-shaped sample is much smaller than R but much larger than d .

Using formula (1), it can be shown^{31,32} that the energy of a solitary vortex at a distance ρ from the center of the disk is defined as

$$E_v(\rho) = \frac{\pi \hbar^2 n_s}{M} \left(\ln \frac{R^2 - \rho^2}{R\xi} - \frac{R - \rho}{\lambda} \right), \quad (2)$$

where ξ is the size of the vortex core. The magnetic field appears in this expression through the length λ defined by the relation

$$\lambda^{-1} = \frac{4\pi I e d}{\hbar c^2}, \quad (3)$$

where I is the two-dimensional density of circular currents.

Assuming that the first quantum vortex emerges at the center of the disk (i.e., for $\rho=0$) and equating $E_v(0)$ to zero,

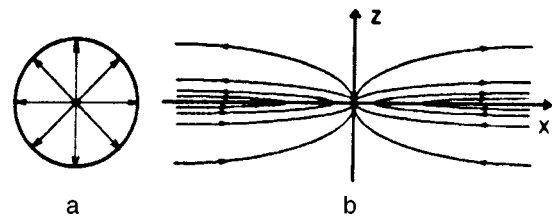


FIG. 3. Magnetic field of the current shown in Fig. 2: top view (a), and sectional view (b).

we obtain the critical current I_{c1} beyond which the emergence of vortices in the system becomes advantageous. It can be verified easily that the current I_{c1} satisfies the relation

$$\lambda_{c1}^{-1} \equiv \frac{4\pi I_{c1} e d}{\hbar c^2} = \frac{1}{R} \ln \frac{R}{\xi}. \tag{4}$$

This current is quite small. Thus, in the particular case when the separation \mathbf{d} between the conducting layers is of the order of 10^{-6} cm and the disk radius $R \approx 1$ cm, the magnetic field $H = 2\pi I/c$ corresponding to the current I_{c1} is of the order of 1 G.

For $I > I_{c1}$, the number of vortices and their distribution in space are determined by the interaction of vortices with a magnetic field as well as with one another. It is obvious from symmetry considerations that in the magnetic field produced by circular current loops, the vortices must lie on circles which are concentric with the disk. The energy of a system of vortices in which the radius of the i th circle is equal to ρ_i and the number of vortices on this circle is equal to N_i can be defined by the following expression if the inequality $N_i \gg 1$ is satisfied.^{31,32}

$$E = \sum_i \left\{ E_v(\rho_i) + \frac{\pi \hbar^2 n_s}{M} \left[2 \sum_{j(<i)} N_j \left(\ln \frac{R}{\rho_i} + \frac{1}{N_i} \ln \frac{1 - \exp(-N_i \ln(R^2/\rho_i \rho_j))}{1 - \exp(-N_i \ln(\rho_i/\rho_j))} \right) - \ln N_i + (N_i - 1) \ln \frac{R}{\rho_i} + \ln \left(1 - \exp \left(-2N_i \ln \frac{R}{\rho_i} \right) \right) - \ln \left(1 - \frac{\rho_i^2}{R^2} \right) \right] \right\} N_i. \tag{5}$$

Note that the last term in braces was not taken into account in our earlier work.^{31,32} However, this term becomes significant only in a narrow region $R - \rho_i \ll R$ near the edge of the disk, and can be disregarded in an analysis of the problems in which we are interested.

2. VORTEX STRUCTURE AS A FUNCTION OF MAGNETIC FIELD

The main difference between the planar vortices considered here and the familiar Onsager-Feynman or Abrikosov vortices lies in that the structure formed by them is spatially inhomogeneous. It will be shown below that if the current I exceeds the lower critical current I_{c1} but is quite close to it, the energetically advantageous situation is one in which planar vortices are formed not all over the disk, but only near its center. In order to find such currents, we shall consider below only the case $R \gg \rho_i \gg \lambda$. This leads to a much simpler expression (5) for vortex energy which can be presented in the form

$$E = \frac{\pi \hbar^2 n_s}{M} \sum_i \left\{ \ln \frac{\rho_i}{\xi} - \frac{R - \rho_i}{\lambda} - \ln N_i + \left(N_i + 2 \sum_{j(<i)} N_j \right) \ln \frac{R}{\rho_i} - 2 \sum_{j(<i)} \frac{N_j}{N_i} \times \ln \left[1 - \exp \left(-N_i \ln \frac{\rho_i}{\rho_j} \right) \right] \right\} N_i. \tag{6}$$

The dependence of the radius ρ_i of the i th circle and the number N_i of vortices on this circle on i can be obtained from condition (6) of minimum energy with respect to ρ_i and N_i . The first minimization condition gives

$$\frac{\rho_i}{\lambda} = 2 \sum_{j(\leq i)} N_j - N_i - 1 + 2 \sum_{j(<i)} \frac{N_j}{\exp\{N_i \ln(\rho_i/\rho_j)\} - 1} - 2 \sum_{j(>i)} \frac{N_j}{\exp\{N_j \ln(\rho_j/\rho_i)\} - 1}. \tag{7}$$

while the minimization condition for the energy E with respect to the number N_i of vortices leads to the equation

$$\frac{R - \rho_i}{\lambda} - \ln \frac{\rho_i}{\xi} = -\ln N_i - 1 + 2 \sum_{j(\leq i)} N_j \ln \frac{R}{\rho_i} + 2 \sum_{j(>i)} N_j \ln \frac{R}{\rho_j} - 2 \sum_{j(<i)} \frac{N_j \ln(\rho_i/\rho_j)}{\exp\{N_i \ln(\rho_i/\rho_j)\} - 1} - 2 \sum_{j(>i)} \ln \left[1 - \exp \left(-N_j \ln \frac{\rho_j}{\rho_i} \right) \right]. \tag{8}$$

The system of equations (7) and (8) can be analyzed quite easily by writing an equation analogous to (8) for the $(i + 1)$ th circle and subtracting Eq. (8) from it. As a result, we obtain

$$\frac{\rho_{i+1} - \rho_i}{\lambda} - \left(2 \sum_{j(\leq i)} N_j - 1 \right) \ln \frac{\rho_{i+1}}{\rho_i} = \ln \frac{N_{i+1}}{N_i} + 2 \sum_{j(<i+1)} \frac{N_j \ln(\rho_{i+1}/\rho_j)}{\exp\{N_{i+1} \ln(\rho_{i+1}/\rho_j)\} - 1} - 2 \sum_{j(<i)} \frac{N_j \ln(\rho_i/\rho_j)}{\exp\{N_i \ln(\rho_i/\rho_j)\} - 1} + 2 \sum_{j(>i+1)} \times \ln \left[1 - \exp \left(-N_j \ln \frac{\rho_j}{\rho_{i+1}} \right) \right] - 2 \sum_{j(>i)} \times \ln \left[1 - \exp \left(-N_j \ln \frac{\rho_j}{\rho_i} \right) \right]. \tag{9}$$

Let us write down the solution of the system of equations (7) and (9). Denoting the last two terms on the right-hand side of (7) as $2S_i$, we can write Eq. (7) in the form

$$\frac{\rho_i}{\lambda} = 2 \sum_{j(\leq i)} N_j - N_i - 1 + 2S_i. \tag{10}$$

Assuming that the functions $N(i)$ and $\rho(i)$ vary insignificantly in one step, i.e., $(N_{i+1} - N_i) \ll N_i$ and $(\rho_{i+1} - \rho_i) \ll \rho_i$ we can show (see Appendix 1) that

$$S_i = 2 \left[N_i \frac{d^2 \rho_i}{di^2} - \frac{N_i}{\rho_i} \left(\frac{d\rho_i}{di} \right)^2 + \frac{dN_i}{di} \frac{d\rho_i}{di} \frac{N_i}{\rho_i} - \frac{dN_i}{di} \right] \times \exp \left(- \frac{N_i}{\rho_i} \frac{d\rho_i}{di} \right). \tag{11}$$

This expression can be simplified considerably. It was found in Refs. 31 and 32 that $N_i = (\rho_{i+1} - \rho_i) / 2\lambda + O(1)$ and $(\rho_{i+1} - \rho_i)^2 \sim \lambda \rho_i$ for the discrete model. A dependence of the same type (but with a different coefficient) was obtained in the continual approximation also. We shall use these results and present them in the following form:

$$N_i = \alpha \frac{\rho_{i+1} - \rho_i}{2\lambda} + O(1); \tag{12}$$

$$2 \sum_{j(\leq i)} N_j = \beta N_i^2; \tag{13}$$

$$(\rho_{i+1} - \rho_i)^2 = \gamma \lambda \rho_i. \tag{14}$$

It is assumed that the coefficients α , β , and γ are of the order of unity.

Formula (13) can be obtained from (12) and (14), and hence coefficients α, β, γ are interrelated. Indeed, it follows from (12) that

$$2 \sum_{j(\leq i)} N_j = 2 \frac{\alpha}{2\lambda} \sum_{j(\leq i)} (\rho_{i+1} - \rho_i) = \alpha \frac{\rho_i}{\lambda},$$

while from (12) and (14) we obtain

$$\beta N_i^2 = \beta \alpha^2 \frac{(\rho_{i+1} - \rho_i)^2}{4\lambda^2} = \beta \alpha^2 \frac{\gamma \rho_i}{4\lambda}.$$

Taking into consideration Eq. (13), we obtain from the above system of equations

$$\alpha \beta \gamma = 4. \tag{15}$$

It can be shown with the help of (12) and (14) that the following relations hold in the main approximation:

$$\rho_i = \frac{\gamma \lambda}{4} i^2; \tag{16}$$

$$N_i = \frac{\alpha \gamma}{4} i. \tag{17}$$

For this purpose, it is sufficient to replace $(\rho_{i+1} - \rho_i)$ by $d\rho(i)/di$ in (14) and solve the resulting differential equation. The solution of this equation is given by (16). Substituting this equation into (12) and disregarding the small correction, we obtain formula (17).

Substituting (16) and (17) into (11) and the obtained result for S_i into (10), we obtain the first of the equations describing the structure of the system of vortices (instead of Eq. (7)):

$$\frac{\rho_i}{\lambda} = 2 \sum_{j(\leq i)} N_j - N_i - 1 - \alpha \gamma e^{-\alpha \gamma / 2}. \tag{18}$$

This equation is much simpler than the initial equation (7). It contains two unknown constants, one of which can be determined straightaway. We write Eq. (18) for the $(i+1)$ th circle and subtract (18) for the i th circle from the obtained equation. This gives

$$N_{i+1} + N_i = \frac{\rho_{i+1} - \rho_i}{\lambda}. \tag{19}$$

Hence, taking into consideration the slow variation of N_i with number i , we obtain

$$N_i = \frac{\rho_{i+1} - \rho_i}{2\lambda} + O(1). \tag{20}$$

A comparison of (20) and (12) leads to the conclusion that $\alpha = 1$. In this case, it follows from (15) that $\beta \gamma = 4$.

We can simplify Eq. (9) in an analogous manner (see Appendix 2). As a result, we can replace the cumbersome equation (9) by

$$\frac{\rho_{i+1} - \rho_i}{\lambda} - \left(2 \sum_{j(\leq i)} N_j - 1 \right) \ln \frac{\rho_{i+1}}{\rho_i} = \ln \frac{N_{i+1}}{N_i} - \frac{\gamma^2}{4N_i} (\gamma - 2) e^{-\gamma/2}. \tag{21}$$

The system of equations (18) and (21) leads to an equation for the coefficient γ (see Appendix 3):

$$\frac{1}{12} + (\gamma - 4) e^{-\gamma/2} = \frac{1}{\gamma}. \tag{22}$$

This equation can be solved numerically. It has one root which is given by

$$\gamma = 5.55, \tag{23}$$

correct to the second significant digit. Accordingly, for $\beta = 4/\gamma$ we obtain

$$\beta = 0.72. \tag{24}$$

Substituting (23) into (14), we arrive at the final expression describing the law of variation of distance between adjacent circles upon a change in the radius of the circle:

$$(\rho_{i+1} - \rho_i)^2 = 5.55 \lambda \rho_i. \tag{25}$$

Thus, we have derived the laws of variation of the radius ρ_i of i th circle and of the number N_i of vortices on this circle with the circle number i (formulas (20) and (25)). It follows from these expressions that the vortex density at the i th circle decreases with increasing i (since $N_i / 2\pi \rho_i \sim (\lambda \rho_i)^{-1/2}$), while it follows from (25) that the density of circles also decreases with increasing i (since the separation between adjacent circles increases with i).

The dependence of the number of vortices on a circle on the number of this circle can be obtained explicitly by using the obtained values of α and γ in (17):

$$N_i = 1.4i. \tag{26}$$

This result indicates that the number of vortices on a circle increases with i by 1.4 on the average ($N_{i+1} - N_i = 1.4$). Such a seemingly paradoxical result (ΔN_i is not an integer) was obtained on account of the fact that while

deriving Eq. (8) we assumed the variable N_i to be continuous, which is actually a correct assumption under the conditions $N_i \gg 1$ and $\Delta N_i \ll N_i$. Naturally, the number of vortices will increase by an integer (1 or 2) as we go over from one circle to the next, and the system itself will choose an alternation of $\Delta N_i^{(1)} = 1$ and $\Delta N_i^{(2)} = 2$ which is more advantageous from the energy point of view (computations can be made only numerically). The continuous variables ρ_i will be slightly "tuned." This indeterminacy is taken into consideration in the exact formula (19) as follows:

$$N_{i+1} + N_i \pm 1 = \frac{\rho_{i+1} - \rho_i}{\lambda} \pm \frac{\Delta(\rho_{i+1} - \rho_i)}{\lambda}.$$

It follows from this formula that the "tuning" of the radius of one circle relative to the adjacent circle is quite small:

$$\Delta(\rho_{i+1} - \rho_i) \sim \frac{1}{N_i} (\rho_{i+1} - \rho_i),$$

which means that the error associated with such a "tuning" is just a small correction in formulas (20) and (25) describing the structure of a system of vortices.

Let us now consider the problem of mutual arrangement of vortex chains on adjacent circles. It is well known that the lattice structure of Abrikosov vortices in a uniform magnetic field is determined to a considerable extent by the energy of interaction of a vortex with the nearest neighbors. In the present work, we consider planar vortices in a nonuniform magnetic field having a central symmetry, and assume that vortices lie on concentric circles. The vortex chains on a circle can rotate relative to each other as a single entity, choosing a mutual arrangement that is most advantageous from the energy point of view. While deriving formula (5) in our earlier works,^{31,32} we disregarded the term associated with such a rotation of one circle relative to another as a small correction. In the present work, however, the small term (last term in (6)) which was disregarded in Refs. 31 and 32) plays a significant role in the derivation of Eq. (22) for the coefficient γ . Hence we must make an order-of-magnitude estimate for the contribution to the energy (5) made by the correction associated with the mutual arrangement of vortices on adjacent circles. It can be seen (see Appendix 4) that this correction is equal to

$$\Delta E = \frac{\pi \hbar^2 n_s}{M} \sum_i \left\{ 2 \sum_{j(<i)} N_j \left[\frac{\pi^2 a^2}{N_i^3} \exp\left(-N_i \ln \frac{\rho_i}{\rho_j}\right) \right] \right\} N_i,$$

where a is a coefficient of the order of unity. It can be seen that the quantity ΔE is smaller than the smallest term in (6) by a factor of $(N_i/\pi a)^2$. Thus, the correction to the energy (ΔE) considered here is negligible.

The following important circumstance is worth noting. The gain in energy due to the emergence of vortices is associated with the interaction of electron-hole dipoles with the magnetic field. The corresponding term in formula (6) for energy (i.e., the second term) decreases with increasing ρ_i . Hence, for a current $I \sim I_{c1}$, it is advantageous from the energy point of view if the vortex structure occupies only a part of the disk. Consequently, the obtained solution for ρ_i and N_i

will be valid only for values of ρ_i smaller than a certain critical value ρ_m which can be found easily with the help of Eq. (8) if we consider that all $N_i = 0$ for $\rho_i > \rho_m$. In this case, Eq. (8) assumes the following form for the m th circle:

$$-\ln N_m + 2 \sum_{j(\leq m)} N_j \ln \frac{R}{\rho_m} = \frac{R - \rho_m}{\lambda} - \ln \frac{\rho_m}{\xi}. \quad (27)$$

We have disregarded the second and fifth terms on the right-hand side of (8) as small corrections. Using (18), we can write this equation in the form

$$-\ln N_m + 2 \left(N_m + \frac{\rho_m}{\lambda} \right) \ln \frac{R}{\rho_m} = \frac{R - \rho_m}{\lambda} - \ln \frac{\rho_m}{\xi}. \quad (28)$$

Since $N_m \propto (\rho_m/\lambda)^{1/2}$ in view of (20) and (25), it can be seen easily that the following inequalities are satisfied:

$$\frac{\rho_m}{\lambda} \gg N_m \gg \ln N_m \gg 1.$$

Taking these inequalities into consideration and using the definition of λ_{c1} from (4), we obtain from (28)

$$\rho_m = \frac{\lambda_{c1} - \lambda}{\lambda_{c1}} \frac{R}{1 + \ln R/\rho_m}. \quad (29)$$

It can be seen from the above equation that the quantity ρ_m is actually proportional to the radius R of the disk (perimeter of the sample) since the term $\ln R/\rho_m$ in the denominator varies only slightly with increasing R , and we can assume in the main approximation that this logarithm is constant. It also follows from (29) that ρ_m depends on the magnetic field H appearing in the equation through the parameter λ . As the current producing the magnetic field increases, the parameter λ decreases while the radius of the outer circle ρ_m increases. The dependence of ρ_m on the current I is hyperbolic.

3. ENERGY OF THE VORTEX SYSTEM

Thus, we have a complete picture of the vortex structure in the system under consideration: planar vortices are situated on concentric circles, filling the disk from the center to a certain outer circle of radius ρ_m (see Fig. 4) which increases with magnetic field in accordance with (29). The number of vortices on a circle, the radius of the circle, and the separation between two adjacent circles are connected through relations (20) and (25).

We can now determine the total number of vortices in the system:

$$N = \sum_{i=1}^m N_i.$$

Such a sum can be evaluated easily by using formula (20). As a result, we obtain

$$N = \sum_{i=1}^m \frac{\rho_{i+1} - \rho_i}{2\lambda} = \frac{\rho_m}{2\lambda}. \quad (30)$$

Here, we have omitted the term $\rho_1/2\lambda$, assuming that $\rho_m \gg \rho_1$. Substituting (29) into (30), we arrive at the required dependence of the number of vortices on the sample size:

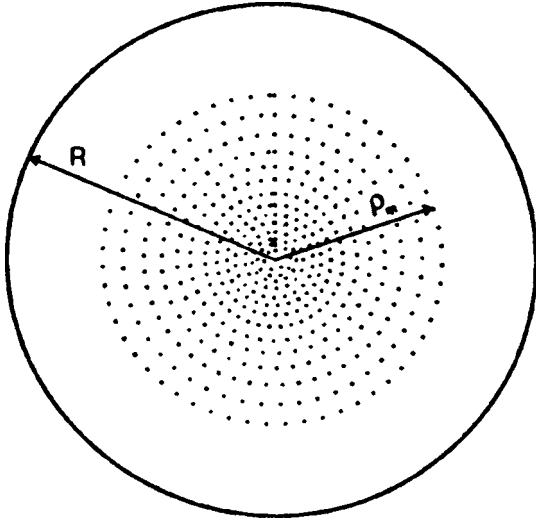


FIG. 4. Vortex structure in the field of a circular current.

$$N = \frac{\lambda_{c1} - \lambda}{\lambda_{c1}} \frac{R}{2\lambda \ln eR/\rho_m}. \quad (31)$$

Thus, the total number of vortices is indeed proportional to the perimeter of the sample.

Let us now compute the energy of the system of vortices. In order to calculate the energy in the main approximation, we can neglect the third and the last terms in formula (6), and also the quantity N_i in comparison with $\sum_{j < (i)} N_j = \beta N_i^2$. The expression for energy then assumes the form

$$E = \frac{\pi \hbar^2 n_s}{M} \sum_i \left(\ln \frac{\rho_i}{\xi} - \frac{R - \rho_i}{\lambda} + \beta N_i^2 \ln \frac{R}{\rho_i} \right) N_i. \quad (32)$$

These sums can be evaluated exactly. However, we can go over from summation over the circle numbers to integration with respect to the continuous variable i since the evaluation of sums in the main approximation does not differ in any way from integration (see Appendix 5). As a result of integration, we obtain

$$E = \frac{\pi \hbar^2 n_s}{M} \int_1^m \left(\ln \frac{\rho_i}{\xi} - \frac{R - \rho_i}{\lambda} + \beta N_i^2 \ln \frac{R}{\rho_i} \right) N_i di$$

$$= - \frac{\pi \hbar^2 n_s}{M} \frac{\rho_m^2}{2\lambda^2} \left(\frac{\lambda_{c1}}{\lambda} \ln \frac{eR}{\rho_m} - \frac{3}{4} \right). \quad (33)$$

Obviously, the energy of the system of vortices is always negative. Indeed, even for values of λ close to λ_{c1} (i.e., for $(\lambda_{c1} - \lambda) \ll \lambda_{c1}$), we have

$$\frac{\lambda_{c1}}{\lambda} \ln \frac{eR}{\rho_m} \approx \frac{\lambda_{c1}}{\lambda} \ln \frac{\lambda_{c1}}{\lambda_{c1} - \lambda} > 1,$$

while the expression within parentheses on the right-hand side of (33) increases with current I , i.e., with decreasing λ .

Substituting (29) into (33), we arrive at the required expression for the energy of the system of vortices:

$$E = - \frac{\pi \hbar^2 n_s}{2M} R^2 \left(\frac{1}{\lambda} - \frac{1}{\lambda_{c1}} \right)^2 \left(\frac{\lambda_{c1}}{\lambda} \ln \frac{eR}{\rho_m} - \frac{3}{4} \right) \ln^{-2} \frac{eR}{\rho_m}. \quad (34)$$

Let us analyze the obtained result. The energy of the system of vortices is negative for $I > I_{c1}$, i.e., the emergence of vortices is indeed advantageous from the energy point of view if the current I exceeds the critical value I_{c1} . The magnitude of the energy increase upon an increase in the current I (i.e., upon a decrease in the parameter λ). Finally, the energy of the system of vortices is proportional to R^2 , i.e., to the ‘‘volume’’ of a two-dimensional sample, and it can be stated that the vortex state is a new thermodynamic phase of the system under consideration.

4. CONCLUSIONS

We have shown in this work that the emergence of a macroscopic quantity of planar vortices with identical circulation becomes energetically advantageous in a system with PSSEH at temperatures below the superconducting transition temperature and in a nonuniform magnetic field (in the form of a two-dimensional ‘‘hedgehog’’) when the current producing this field exceeds a certain critical value I_{c1} . In a disk-shaped sample of radius R , vortices lie on circles whose centers coincide with the center of the disk, thus filling the disk from the center to a certain value ρ_m (radius of the biggest circle) defined by formula (29). The quantity ρ_m increases linearly with the sample radius R , as well as with the current I , i.e., the vortex system expands from the center of the disk towards its edges upon an increase in I . The number of vortices on a circle, the radius of the circle, and the separation between two adjacent circles are connected through relations (20) and (25). The total number of vortices and the energy of a system of vortices are determined (formulas (31) and (34)) and it is shown that although the total number of vortices is proportional to the perimeter of the sample, the energy of the system of vortices is proportional to R^2 , i.e., the effect under consideration is not a surface effect, but a bulk effect and hence the vortex state is a new thermodynamic phase of the system under consideration.

This research was supported by INTAS (Grant No. 97-0972).

APPENDIX 1

In accordance with the notation introduced in Sec. 2, we can write

$$S_i = \sum_{j < (i)} \frac{N_j}{\exp\{N_i \ln(\rho_i/\rho_j)\} - 1}$$

$$- \sum_{j > (i)} \frac{N_j}{\exp\{N_j \ln(\rho_j/\rho_i)\} - 1}.$$

Because of the presence of an exponential factor in the denominator, the main contribution to these sums comes from terms with numbers j that are close to i , hence we obtain in the main approximation

$$S_i = \sum_{k=1}^p \left[\frac{N_{i-k}}{\exp\{N_i \ln(\rho_i/\rho_{i-k})\} - 1} - \frac{N_{i+k}}{\exp\{N_{i+k} \ln(\rho_{i+k}/\rho_i)\} - 1} \right], \tag{A1.1}$$

where the upper limit of summation p must be quite small ($p \ll i$) since we shall carry out an expansion of i -dependent

$$S_i = \sum_{k=1}^p \frac{e^{c_i k} \left[\left(\frac{N_i}{\rho_i} \frac{d^2 \rho_i}{di^2} - \frac{N_i}{\rho_i^2} \left(\frac{d\rho_i}{di} \right)^2 + \frac{1}{\rho_i} \frac{dN_i}{di} \frac{d\rho_i}{di} \right) N_i k^2 - 2 \frac{dN_i}{di} k \right] + 2 \frac{dN_i}{di} k}{(\exp\{N_i \ln(\rho_i/\rho_{i-k})\} - 1)(\exp\{N_{i+k} \ln(\rho_{i+k}/\rho_i)\} - 1)}, \tag{A1.2}$$

where we have introduced the notation

$$c_i = \frac{N_i}{\rho_i} \frac{d\rho_i}{di}. \tag{A1.3}$$

In order to calculate the sum S_i in the main approximation, we disregard the last term in the numerator of (A1.2) (since $c_i > 2$ which can be verified by substituting (16) and (17) and (23) into (A1.3), and by equating the denominator to $\exp(2c_i k)$). For calculating S_i in this approximation, we can make the upper limit of summation tend to infinity. The series simplified in this way can be evaluated easily by differentiating with respect to the parameter. As a result, we arrive at formula (11).

$$S_2(i) = \sum_{j(<i)} \frac{\frac{1}{\rho_i} \frac{d\rho_i}{di} (i-j) \exp \left\{ \frac{N_i}{\rho_i} \frac{d\rho_i}{di} (i-j) \right\} \left[\frac{dN_i}{di} - \frac{N_i}{\rho_i} \frac{dN_i}{di} \frac{d\rho_i}{di} (i-j) \right]}{(\exp\{N_{i+1} \ln(\rho_{i+1}/\rho_{j+1})\} - 1)(\exp\{N_i \ln(\rho_i/\rho_j)\} - 1)}$$

$$= \sum_{k=1}^p \frac{\frac{1}{\rho_i} \frac{d\rho_i}{di} \exp \left\{ \frac{N_i}{\rho_i} \frac{d\rho_i}{di} k \right\} \left[\frac{dN_i}{di} - \frac{N_i}{\rho_i} \frac{dN_i}{di} \frac{d\rho_i}{di} k \right] k}{(\exp\{N_{i+1} \ln(\rho_{i+1}/\rho_{i-k+1})\} - 1)(\exp\{N_i \ln(\rho_i/\rho_{i-k})\} - 1)}. \tag{A2.2}$$

In order to calculate the sum $S_2(i)$ in the main approximation, we can use the expressions (16) and (17) and equate the numerator to $\exp(2c_i k)$. Making the upper limit of summation on the right-hand side of (A2.2) tend to infinity, we can evaluate the series obtained in this way by differentiating with respect to the parameter. As a result, we arrive at a formula for $S_2(i)$:

$$S_2(i) = -\frac{\gamma}{2i} (\gamma - 1) e^{-\gamma/2} = -\frac{\gamma^2}{8N_i} (\gamma - 1) e^{-\gamma/2}. \tag{A2.3}$$

functions into a Taylor series in the small increment k . However, the limit p must be large enough so that the disregarded part of the series is negligible. Estimates show that the optimal value of p is equal to six.

Expanding the expression within brackets in (A1.1) into a Taylor series, we obtain after cancellation of the first approximation terms

APPENDIX 2

For the second and third terms on the right-hand side of (9), we introduce the notation $2S_2(i)$. This gives

$$S_2(i) = \sum_{j(<i)} \frac{N_{j+1} \ln(\rho_{i+1}/\rho_{j+1})}{\exp\{N_{i+1} \ln(\rho_{i+1}/\rho_{j+1})\} - 1} - \frac{N_j \ln(\rho_i/\rho_j)}{\exp\{N_i \ln(\rho_i/\rho_j)\} - 1}. \tag{A2.1}$$

As in Appendix 1, we shall use the fact that the functions $N(i)$ and $\rho(i)$ vary slowly over one step, and the main contribution to these sums comes from terms with numbers j that are close to i on account of the presence of an exponential in the denominator. Reducing the fractions in (A2.1) to a common denominator and expanding the i -dependent functions into a Taylor series in the small increment $|i-j| \ll i$, we obtain

Let us now consider the last two terms on the right-hand side of (9), and denote them by $2S_3(i)$:

$$S_3(i) = \sum_{j(>i)} \left[\ln \left(1 - \exp \left\{ -N_{j+1} \ln \frac{\rho_{j+1}}{\rho_{i+1}} \right\} \right) - \ln \left(1 - \exp \left\{ -N_j \ln \frac{\rho_j}{\rho_i} \right\} \right) \right].$$

Using the smallness of the exponent in comparison with unity and expanding into a Taylor series as above, we obtain

$$S_3(i) = \sum_{k=1}^p \frac{1}{\rho_i} \frac{dN_i}{di} \frac{d\rho_i}{di} k e^{-c_i k}.$$

Making the upper limit of summation tend to infinity, we can evaluate the infinite series obtained in this way by differentiating with respect to the parameter. Using (16) and (17), we obtain

$$S_3(i) = \frac{\gamma}{2i} e^{-\gamma/2} = \frac{\gamma^2}{8N_i} e^{-\gamma/2}. \tag{A2.4}$$

Substituting (A2.3) and (A2.4) into (9), we arrive at (21).

APPENDIX 3

The system of equations (18) and (21) leads to the equation

$$\begin{aligned} N_{i+1} + N_i - \left(2 \sum_{j(\leq i)} N_j - 1 \right) \ln & \\ \times \frac{2 \sum_{j(\leq i+1)} N_j - N_{i+1} - 1 - \gamma e^{-\gamma/2}}{2 \sum_{j(\leq i)} N_j - N_i - 1 - \gamma e^{-\gamma/2}} & \\ = \ln \frac{N_{i+1}}{N_i} - \frac{\gamma^2}{4N_i} (\gamma - 2) e^{-\gamma/2}. & \end{aligned} \tag{A3.1}$$

Expanding the logarithm of the left-hand side of this equation

$$\begin{aligned} \ln \frac{2 \sum_{j(\leq i+1)} N_j - N_{i+1} - 1 - \gamma e^{-\gamma/2}}{2 \sum_{j(\leq i)} N_j - N_i - 1 - \gamma e^{-\gamma/2}} & \\ = \ln \left(1 + \frac{N_{i+1} + N_i}{2 \sum_{j(\leq i)} N_j - N_i - 1 - \gamma e^{-\gamma/2}} \right) & \end{aligned}$$

into a Taylor series up to third-order terms, and the fraction

$$\begin{aligned} \frac{1}{2 \sum_{j(\leq i)} N_j - N_i - 1 - \gamma e^{-\gamma/2}} & \\ = \frac{1}{2 \sum_{j(\leq i)} N_j - 1} \frac{1}{1 - (N_i + \gamma e^{-\gamma/2}) / (2 \sum_{j(\leq i)} N_j - 1)} & \end{aligned}$$

up to second order terms, we substitute the result into (A3.1). After reducing like terms on the left-hand side of (A3.1), terms of the order of N_i and terms of the order of unity will cancel out, leaving only terms of the same order as on the right-hand side of (A3.1). Expanding the logarithm on the right-hand side into a series in the small increment

$$\ln \frac{N_{i+1}}{N_i} = \frac{N_{i+1} - N_i}{N_i}$$

and using formula (17), we arrive at Eq. (22).

APPENDIX 4

While calculating the interaction energy for vortices belonging to different circles,^{31,32} we encountered the term

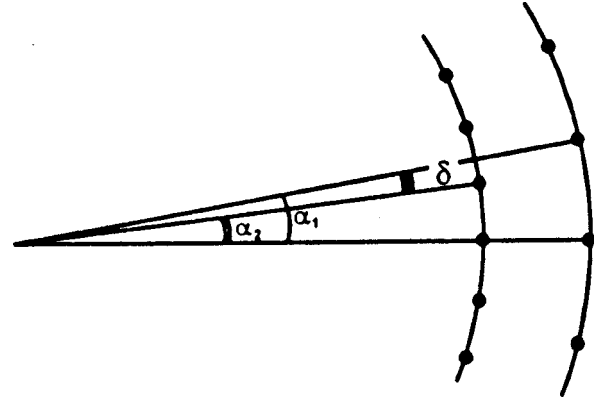


FIG. 5. Fragment of the vortex structure for two adjacent circles.

$$\begin{aligned} \frac{\pi \hbar^2 n_s}{2M} \sum_{i,j} \sum_{n_j=1}^{N_j} \sum_{n_i=1}^{N_i} \ln \left[1 - 2 \frac{\rho_j}{\rho_i} \cos(\theta(n_i) - \theta(n_j)) + \frac{\rho_j^2}{\rho_i^2} \right] & \\ = \frac{\pi \hbar^2 n_s}{M} \sum_i \sum_{j(<i)} N_j \sum_{n_i=1}^{N_i} \ln \left[1 - 2 \frac{\rho_j}{\rho_i} \cos \left(\frac{2\pi n_i}{N_i} \right. \right. & \\ \left. \left. - \alpha_i(n_j) \right) + \frac{\rho_j^2}{\rho_i^2} \right], & \end{aligned} \tag{A4.1}$$

where $\alpha_i(n_j)$ is the minimum angle between radii drawn at the vortex center on both vortices. The quantity $\alpha_i(n_j)$ lies in the interval between 0 and $\alpha_{\max}(i)$. The value of $\alpha_{\max}(i)$ can be determined as follows.

The energy of interaction of vortices belonging to different circles decreases exponentially with increasing distance (in proportion to $\exp\{-N_i \ln(\rho_i/\rho_j)\}$), hence it is sufficient to consider vortices from the nearest circles. We shall consider two circles with N_i and $N_i - a$ vortices, where a is a coefficient of the order of unity. The radius drawn from the vortex center to one of the circles in Fig. 5 passes through the vortex center on the other circle also, i.e., $\alpha_i(n_j) = 0$. The minimum angle δ through which one of the circles must be turned relative to the other so that the vortices lie on the same radius again is given by the expression

$$\delta = \alpha_1 - \alpha_2 = \frac{2\pi}{N_i - a} - \frac{2\pi}{N_i} \approx \frac{2\pi a}{N_i^2},$$

while the angle $\alpha_{\max}(i)$ is equal to half this angle. In order to obtain the ‘‘upper’’ estimate of the correction to the energy associated with the tuning of the vortex chain of one circle to the other, we replace the angles $\alpha_i(n_j)$ in (A4.1) by their maximum values $\alpha_{\max}(i)$. In this case, the expression (A4.1) can be presented in the form

$$\begin{aligned} \frac{\pi \hbar^2 n_s}{M} \sum_i \sum_{j(<i)} N_j \sum_{n_i=1}^{N_i} \ln \left[1 - 2x \left(\cos \frac{2\pi n_i}{N_i} \cos \frac{\pi a}{N_i^2} \right. \right. & \\ \left. \left. + \sin \frac{2\pi n_i}{N_i} \sin \frac{\pi a}{N_i^2} \right) + x^2 \right], & \end{aligned} \tag{A4.2}$$

where we have introduced the notation $x = \rho_j/\rho_i$. In order to isolate in this expression the energy increment in which we are interested, we must note that $(\pi a/N_i^2) \ll 1$ and expand

$\sin(\pi a/N_i^2)$ and $\cos(\pi a/N_i^2)$ into a power series in $(\pi a/N_i^2)$, after which we expand the logarithm into a Taylor series in the small increment

$$-2x \frac{\pi a}{N_i^2} \sin \frac{2\pi n_i}{N_i} + x \left(\frac{\pi a}{N_i^2} \right)^2 \cos \frac{2\pi n_i}{N_i}$$

up to second-order terms. As a result, we find that the correction to energy associated with the mutual arrangement of vortex chains at the adjacent circles does not exceed

$$\begin{aligned} \Delta E = & \frac{\pi \hbar^2 n_s}{M} \sum_i \sum_{j(<i)} N_j \sum_{n_i=1}^{N_i} \left[-2x \frac{\pi a}{N_i^2} \right. \\ & \times \frac{\sin(2\pi n_i/N_i)}{1-2x \cos(2\pi n_i/N_i) + x^2} \\ & + x \left(\frac{\pi a}{N_i^2} \right)^2 \frac{\cos(2\pi n_i/N_i)}{1-2x \cos(2\pi n_i/N_i) + x^2} \\ & \left. - 2x^2 \left(\frac{\pi a}{N_i^2} \right)^2 \frac{\sin^2(2\pi n_i/N_i)}{(1-2x \cos(2\pi n_i/N_i) + x^2)^2} \right]. \end{aligned} \quad (\text{A4.3})$$

Let us compute the sums appearing in this expression. For the first term in brackets, we can write

$$-2x \frac{\pi a}{N^2} \sum_{n=1}^N \frac{\sin(2\pi n/N)}{1-2x \cos(2\pi n/N) + x^2} = 0, \quad (\text{A4.4})$$

since the summation is carried out over a periodic odd function over its period. For the summation of second and third terms in (A4.3), we use Poisson's sum rule. In particular, we obtain for the second term

$$\begin{aligned} & x \left(\frac{\pi a}{N^2} \right)^2 \sum_{n=1}^N \frac{\cos(2\pi n/N)}{1-2x \cos(2\pi n/N) + x^2} \\ & = x \left(\frac{\pi a}{N^2} \right)^2 \int_0^N \frac{\cos(2\pi n/N) dn}{1-2x \cos(2\pi n/N) + x^2} + 2x \left(\frac{\pi a}{N^2} \right)^2 \\ & \quad \times \sum_{k=1}^{\infty} \int_0^N \frac{\cos(2\pi kn) \cos(2\pi n/N) dn}{1-2x \cos(2\pi n/N) + x^2}. \end{aligned} \quad (\text{A4.5})$$

The third term can be written in an identical manner. After this, we integrate both terms in (A4.5) in parts and add the result to the expression for the third term. The obtained expression is integrated by parts once again. This gives

$$\begin{aligned} & - \left(\frac{\pi a}{N} \right)^2 \sum_{k=1}^{\infty} k^2 \int_0^N \cos(2\pi kn) \ln(1 \\ & \quad - 2x \cos(2\pi n/N) + x^2) dn. \end{aligned} \quad (\text{A4.6})$$

Considering that³³

$$\begin{aligned} & \int_0^N \cos(2\pi kn) \ln(1-2x \cos(2\pi n/N) + x^2) dn \\ & = -\frac{1}{k} \exp(-kN|\ln x|), \end{aligned}$$

we can write (A4.6) in the form

$$\begin{aligned} & \left(\frac{\pi a}{N} \right)^2 \sum_{k=1}^{\infty} k \exp(-kN|\ln x|) \\ & \approx \left(\frac{\pi a}{N} \right)^2 \exp(-N|\ln x|). \end{aligned} \quad (\text{A4.7})$$

Substitution of (A4.7) and (A4.3) finally gives

$$\Delta E = \frac{\pi \hbar^2 n_s}{M} \sum_i \left\{ 2 \sum_{j(<i)} N_j \left(\frac{\pi^2 a^2}{N_i^3} \exp \left\{ -N_i \ln \frac{\rho_i}{\rho_j} \right\} \right) \right\} N_i.$$

APPENDIX 5

For the first term, we obtain from Eq. (32)

$$\sum_i N_i \ln \frac{\rho_i}{\xi} = \sum_i N_i \ln \frac{\rho_i}{\lambda} + \frac{\rho_m}{2\lambda} \ln \frac{\lambda}{\xi}, \quad (\text{A5.1})$$

where we have used the result (30). Using the expression (20), we can present the first term in (A5.1) in the form

$$\sum_i N_i \ln \frac{\rho_i}{\lambda} = \frac{1}{2\lambda} \left(\sum_i \rho_{i+1} \ln \frac{\rho_i}{\lambda} - \sum_i \rho_i \ln \frac{\rho_i}{\lambda} \right).$$

However, for $\rho_{i+1} - \rho_i \ll \rho_{i+1}$, we have

$$\ln \frac{\rho_i}{\lambda} = \ln \frac{\rho_{i+1}}{\lambda} + \ln \left(1 - \frac{\rho_{i+1} - \rho_i}{\rho_{i+1}} \right) \approx \ln \frac{\rho_{i+1}}{\lambda} - \frac{\rho_{i+1} - \rho_i}{\rho_{i+1}},$$

and hence

$$\begin{aligned} \sum_i N_i \ln \frac{\rho_i}{\lambda} & = \frac{1}{2\lambda} \left[\sum_i \left(\rho_{i+1} \ln \frac{\rho_{i+1}}{\lambda} - \rho_i \ln \frac{\rho_i}{\lambda} \right) \right. \\ & \quad \left. - \sum_i (\rho_{i+1} - \rho_i) \right] \\ & = \frac{\rho_m}{2\lambda} \ln \frac{\rho_m}{\lambda} - \frac{\rho_m}{2\lambda}. \end{aligned} \quad (\text{A5.2})$$

Substituting (A5.2) into (A5.1) and using Eqs. (4) and (29), we finally obtain

$$\sum_i N_i \ln \frac{\rho_i}{\xi} = \frac{R\rho_m}{2\lambda\lambda_{c1}}. \quad (\text{A5.3})$$

The same result can be obtained by going over from summation to integration. In this case,

$$\sum_i N_i \ln \frac{\rho_i}{\xi} = \int_1^m N(i) \ln \frac{\rho(i)}{\xi} di.$$

Using formulas (4), (16), (17), and (29), we obtain

$$\int_1^m N(i) \ln \frac{\rho(i)}{\xi} di = \frac{R\rho_m}{2\lambda\lambda_{c1}}. \quad (\text{A5.4})$$

It can be seen that the results (A5.3) and (A5.4) coincide.

*E-mail: shevchenko@ilt.kharkov.ua

¹L. J. Cooper, N. K. Patel, V. Drouot *et al.*, Phys. Rev. B **57**, 11915 (1998).

²M. P. Lilly, J. P. Eisenstein, L. N. Pfeiffer, and K. W. West, Phys. Rev. Lett. **80**, 1714 (1998)

- ³L. V. Butov, A. Z. Zrener, M. Hang *et al.*, Surf. Sci. **361-362**, 2434 (1996).
- ⁴L. V. Butov and A. I. Filin, Zh. Éksp. Teor. Fiz **114**, 1115 (1998) [JETP **87**, 608 (1998)].
- ⁵S. I. Shevchenko, Fiz. Nizk. Temp. **2**, 505 (1976) [Sov. J. Low Temp. Phys. **2**, 251 (1976)].
- ⁶Yu. E. Lozovik and V. I. Yudson, Zh. Éksp. Teor. Fiz **71**, 738 (1976) [Sov. Phys. JETP **44**, 389 (1976)].
- ⁷Yu. E. Lozovik and V. N. Nishanov, Fiz Tverd Tela (Leningrad) **18**, 3267 (1976) [Sov. Phys. Solid State **18**, 1905 (1976)].
- ⁸S. I. Shevchenko, Phys. Rev. Lett. **72**, 3242 (1994).
- ⁹A. B. Dzyubenko and Yu. E. Lozovik, Fiz Tverd Tela (Leningrad) **25**, 1519 (1983) [Sov. Phys. Solid State **25**, 874 (1983)].
- ¹⁰A. B. Dzyubenko and Yu. E. Lozovik, Fiz Tverd Tela (Leningrad) **26**, 1540 (1984) [Sov. Phys. Solid State **26**, 938 (1984)].
- ¹¹H. A. Fertig, Phys. Rev. B **40**, 1087 (1989).
- ¹²D. Yoshioka and A. H. MacDonald, J. Phys. Soc. Jpn. **59**, 4211 (1990).
- ¹³A. H. MacDonald, P. M. Platzman, and G. S. Boebinger, Phys. Rev. Lett. **65**, 757 (1990).
- ¹⁴X. M. Chen and J. J. Quinn, Phys. Rev. Lett. **67**, 895 (1991).
- ¹⁵R. Cote, L. Brey, and A. H. MacDonald, Phys. Rev. B **46**, 10239 (1992).
- ¹⁶S. R. Renn, Phys. Rev. Lett. **68**, 658 (1992).
- ¹⁷X. G. Wen and A. Zee, Phys. Rev. Lett. **69**, 1087 (1992).
- ¹⁸Z. F. Ezawa and A. Iwazaki, Phys. Rev. Lett. **70**, 3119 (1993).
- ¹⁹X. M. Chen and J. J. Quinn, Phys. Rev. Lett. **70**, 2130 (1993).
- ²⁰Kun Yang, K. Moon, L. Zheng *et al.*, Phys. Rev. Lett. **72**, 732 (1994).
- ²¹Tin-Lun Ho, Phys. Rev. Lett. **73**, 874 (1994).
- ²²J. Szymanski, L. Swierkowski, and D. Nielson, Phys. Rev. B **50**, 11002 (1994).
- ²³L. Swierkowski, J. Szymanski, and Z. W. Gortel, Phys. Rev. Lett. **74**, 3245 (1995).
- ²⁴X. Zhu, P. B. Littlewood, M. S. Hybertsen, and T. M. Rice, Phys. Rev. Lett. **74**, 1633 (1995).
- ²⁵A. B. Dzyubenko and G. E. W. Bauer, Phys. Rev. B **51**, 14524 (1995).
- ²⁶K. Moon, H. Mori, Kung Yang *et al.*, Phys. Rev. B **51**, 5138 (1995).
- ²⁷Kung Yang, K. Moon, Lotfi Belkhir *et al.*, Phys. Rev. B **54**, 11644 (1996).
- ²⁸L. Brey, H. A. Fertig, R. Cote, and A. H. MacDonald, Phys. Rev. B **54**, 16888 (1996).
- ²⁹G. Vignale and A. H. MacDonald, Phys. Rev. Lett. **76**, 2786 (1996).
- ³⁰Z. F. Ezawa, Phys. Rev. B **55**, 7771 (1997).
- ³¹S. I. Shevchenko, Phys. Rev. B **56**, 10355 (1997).
- ³²S. I. Shevchenko, Phys. Rev. B **57**, 14809 (1998).
- ³³I. S. Gradshteĭn and I. M. Ryzhik, *Tables of Integrals, Sums, Series, and Products* [in Russian], Fizmatgiz, Moscow (1963).

Translated by R. S. Wadhwa

BRIEF COMMUNICATIONS**Misfit dislocation superlattices in IV–VI multilayered compounds as zero-dimensional quantum boxes**

A. Yu. Sipatov

*Kharkov State Polytechnic University, 21 Frunze St., Kharkov, 310002, Ukraine**

(Submitted June 20, 1998; revised December 8, 1998)

Fiz. Nizk. Temp. **25**, 509–511 (May 1999)

Quantum dots can be generated by a new method based on the formation of misfit dislocations in a perfectly periodic array network during the epitaxial growth of IV–VI compound superlattices. Infrared photoluminescence spectra of IV–VI superlattices are measured at temperatures $T=5-90$ K. A large blue shift and temperature independent line positions and width were observed in PbSe–PbS/(001)KCl superlattices with a three-dimensional periodic arrays of misfit dislocations. It is supposed that these features are due to quantum dot luminescence.

© 1999 American Institute of Physics. [S1063-777X(99)01205-0]

1. INTRODUCTION

Any new attempt to create quantum dots is great importance because, compared with 2D-structures, it is more difficult to build up both 0D and 1D objects. Recently a new way has been found to create quantum dots of InAs with help of self-organizing processes in Stranski–Krastanov island growth during molecular beam epitaxy on a GaAs substrate.¹ Another example is the creation of 1D wires by dislocation slipping induced reduction in dimensionality of 2D structure down to one dimension.² The present contribution is devoted to the investigation of the photoluminescence spectra of IV–VI superlattices with features due to lattice misfit dislocation. These superlattices reveal the specific properties of 0D systems such as a remarkable blue shift and temperature independent line positions and width. Thus it is a new way of creating quantum dots in IV–VI superlattices via misfit dislocation generation during the epitaxial growth process. It is known that there exists a nearly ideal periodic grid of interface misfit dislocations (MD) in strained IV–VI superlattices.^{3,4} The lead and rare-earth chalcogenides are quite suitable for preparation of such misfit dislocation superlattices. These materials have NaCl-crystal structure, and provide a wide range of lattice misfit ($f=0.5-13\%$) as well as of misfit dislocation periods ($D=3-50$ nm).

2. SAMPLE CHARACTERIZATION

The multilayers were prepared by thermal or electron beam evaporation of lead and rare-earth chalcogenides in vacuum ($10^{-4}-10^{-5}$ Pa) and alternate deposition of two compounds onto a (001)KCl substrate at the temperature 500–550 K. The layer thickness and the growth rate were controlled by quartz resonator. Superlattices with periods 5–500 nm and number of periods $N=2-50$ were grown. Structure investigation by X-ray diffraction (XRD) and transmission electron microscopy (TEM) shows that growth in $\langle 001 \rangle$ direction is going on to the layer-by-layer (Frank–

van der Merwe) mechanism and square grids of misfit dislocations are formed at the interfaces with a period $D=3-50$ nm. The MD grid periodicity is much better for a sufficiently large layer lattice misfit ($f>2\%$). Such MD grid may be considered as a new kind of superlattice—misfit dislocation superlattice (MDSL). The MDSL is the 3-dimensional superlattice with periodic modulation by misfit dislocation arrays in the plane of multilayer structure and composition modulation along growth direction. The MDSL of above type with multilayers of PbSe–PbS was prepared by thermal evaporation and alternate deposition of PbSe and PbS on (001)KCl substrate. The specimen has 40 layers, each 7.0 nm in thickness, and MD periodic grids with $D=13.5$ nm. The structural properties were checked by XRD and TEM. X-ray diffraction investigations supported the evidence of periodicity along the superlattice growth direction and where a TEM proved the existence of high quality inplane MD grids and thus gave evidence for further dimension reduction. The electron microscope image of two-layer PbSe–PbS film with thickness PbSe—30 nm and PbS—30 nm is shown in Fig. 1a. X-ray diffraction patterns of PbSe–PbS superlattices with different periods are shown in Fig. 1b–1d.

3. RESULTS OF MEASUREMENTS AND DISCUSSION

Photoluminescence spectra of PbSe–PbS superlattices were earlier discussed in Ref. 5 for $T=80$ K where two-dimensional size quantizing effects were observed (blue shift in photoluminescence spectra). In the above paper only PbSe–PbS/(111) superlattices without misfit dislocations were investigated. In the present work the infrared photoluminescence spectra at $T=5-90$ K in (001)-oriented superlattices with misfit dislocation grids are investigated and the results are shown in Fig. 2. There are four main lines, whose positions and widths do not depend on temperature for the temperature range in which they exist. A MDSL has a com-

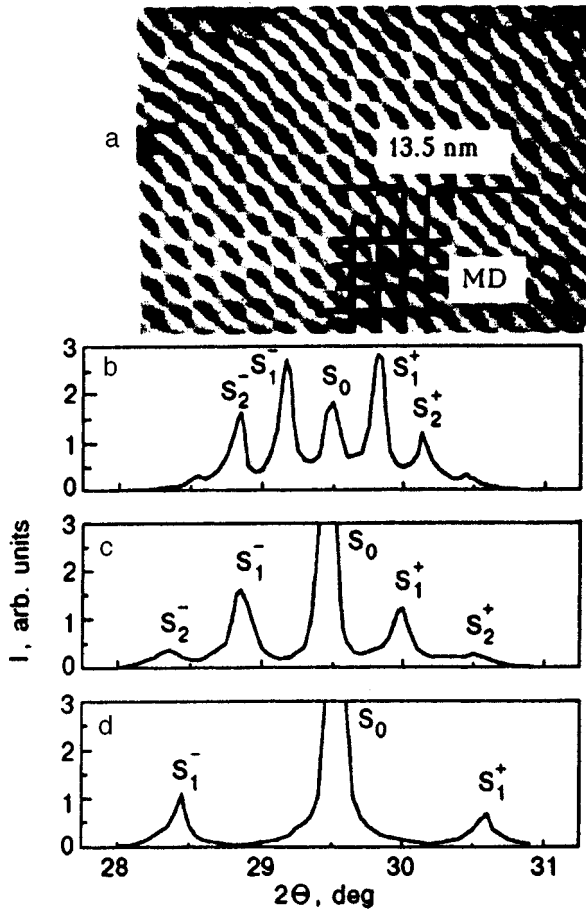


FIG. 1. Electron-microscope image of two-layer PbSe-PbS film (a) with thickness of PbSe and PbS equal to 30 nm and (200) x-ray diffraction pattern of PbSe-PbS superlattices with periods $D_{SL}=28$ nm (b), 15.8 nm (c), 8.1 nm (d). S_n —satellite reflections, MD—misfit dislocations.

positional modulation along the plane normal to superlattice and additionally a deformation induced, band gap modulation by periodic MD arrays in the plane. The MD stresses have been calculated using methodics⁴ and it appears that the amplitude of the oscillations of the MD stresses near the interface are as high as 10^9 Pa (Fig. 3.a). The local position dependence of the energy gap is schematically shown in Fig. 3b. The coordinates (x,y) demote the position in the interface plane and in the perpendicular direction, respectively. One can see from this picture that lattice deformation and gap modulation decrease with distance from the interface y . The strain variation of the band gap width $\Delta E_g = (\delta E / \delta P) \sigma_{11}$, where $(\delta E / \delta P)$ for PbSe equals $-8 \cdot 10^{-11}$ eV/Pa.⁶ From the above estimation it is clear that if we consider the real values of normal strain σ_{11} near interface PbSe-PbS (Fig. 3a) the variation in the magnitude of the band gap width ΔE_g PbSe (Fig. 3b) can achieve 30%–15% for distance from interface 1 nm and 2 nm, respectively. That is why the modulation of the energy gap is deep enough to form a quantum well in the interface plane and confines particles in 0D quantum boxes. It is very important that, for a certain sign of the misfit in PbSe-PbS interfaces, the deformation-changed PbSe energy gap has minima in between two dislocation lines that are separated by a distance

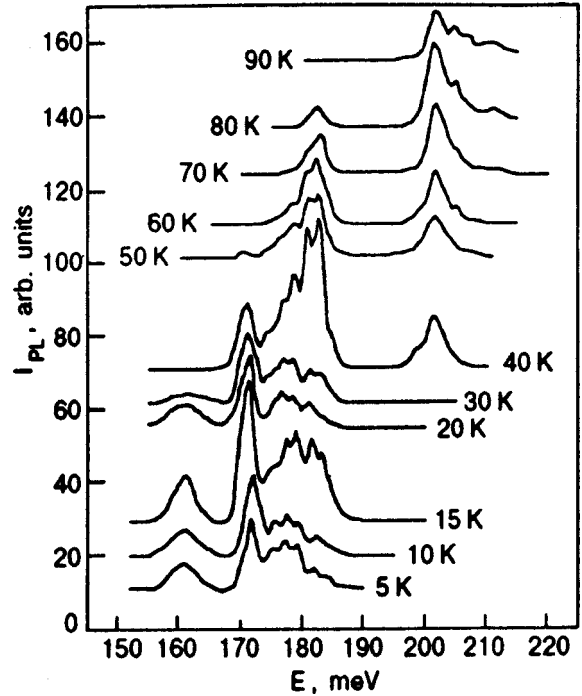


FIG. 2. Photoluminescence emission spectra of PbSe-PbS superlattice at temperature $T=5-90$ K. The superlattice period $D_{SL}=d_{PbSe}+d_{PbS}$ = 14 nm ($d_{PbSe}=d_{PbS}$), the number of periods—20.

of 13.5 nm. It means that each optically active PbSe region, bounded by four MD planes and two interface planes, is free of traps that are placed close along to dislocation lines and thus the properties are sufficient for photoluminescence signal observation. The blue shifts of reference $E_g(T)$ on 15–30

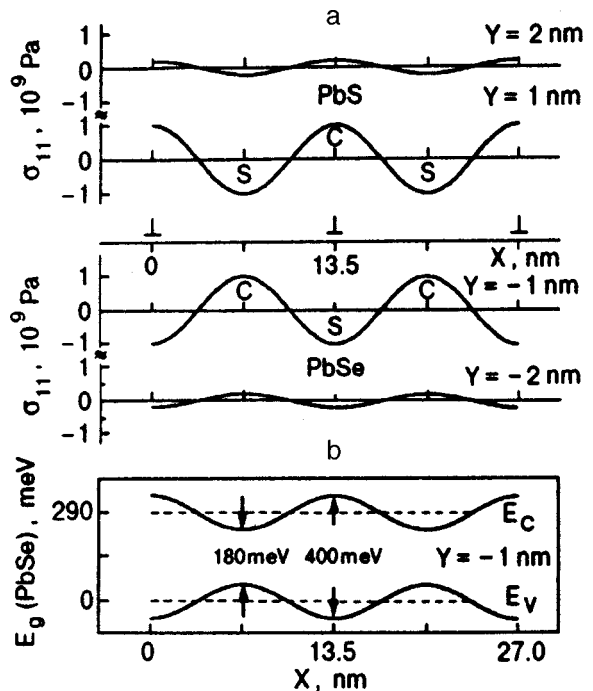


FIG. 3. Normal stress σ_{11} distribution (a) in two-layer PbSe-PbS film near the interface and PbSe energy band gap modulation (b) by misfit dislocation stresses at 300 K. Y —distance from PbSe-PbS interface; \perp —position of the misfit dislocation; C—compressed region; S—stretch region.

meV were observed in the emission spectra of superlattices in Fig. 2 ($E_g=145$ meV for bulk unstrained PbSe at $T=5-10$ K). The positions as well as the width of the four lines observed in luminescence spectra do not depend on temperature, which is probably due to the $0D$ size quantization of the PbSe quantum boxes. In the model of quantum dots⁷ there exist four “intraband” dipole transitions which change only the state of one particle in the electron-hole pairs. The energy of such transitions should not depend on the band gap $E_g(T)$ and consequently on the temperature. It is reasonable to suppose that the width of the lines is caused mainly by quantum dot size fluctuations and does not depend on temperature. A temperature increase leads to more effective phonon-induced suppression of photoluminescence such that low-lying excitations have not been observed in the emission spectra at high temperature (Fig. 2). Thus it is possible to consider the epitaxial growth induced dislocation superlattices as an interesting new object of extremely reduced dimensionality. The MDSL described above require further investigation to make clear not only the optical properties but the set of special properties which have been observed as, for instance, unusual high T_C -like superconductivity in IV–VI MDSL.^{8–10}

The author wishes to thank K. M. Herrmann and J. W. Tomm from Humboldt University of Berlin for help in photoluminescence measurements.

*E-mail: sipat@kpi.kharkov.ua

-
- ¹D. Bimberg, M. Grundmann, N. N. Ledentsov, S. S. Ruvimov, P. Werner, U. Richter, U. Gosele, J. Heydenreich, V. M. Ustinov, A. Yu. Egorov, A. E. Zhukov, P. S. Kop'ev, and Zh. I. Alferov, *Abstracts of Workshop on MBE Growth Physics and Technology*, Warsaw, Poland (1994), p. 12.
- ²C. Guasch, F. Voillot, M. Goiran, J. P. Peyrade, E. Bedel, C. Fontaine, H. Atmani, and A. Rocher, *Solid-State Electron.* **37**, 567 (1994).
- ³L. S. Palatnik and A. I. Fedorenko, *J. Cryst. Growth* **52**, 917 (1981).
- ⁴I. F. Michailov, B. A. Savitskii, A. Yu. Sipatov, A. I. Fedorenko, and L. P. Shpakuvskaya, *Fiz. Tverd. Tela.* **25**, 1166 (1983) [*Sov. Phys. Solid State* **25**, 668 (1983)].
- ⁵I. V. Kolesnikov, A. N. Kovalev, A. Yu. Sipatov, V. I. Paramonov, A. I. Fedorenko, and A. E. Yunovich, *Fiz. Tekh. Poluprovodn.* **23**, 960 (1989) [sic].
- ⁶Yu. I. Ravich, B. A. Efimova, and I. A. Smirnov, *Investigation Methods of Semiconductors Applied to Lead Chalcogenides*, PbTe, PbSe, PbS, Nauka, Moscow (1968).
- ⁷H. Haug and S. W. Koch, *Quantum Theory of the Optical and Electronic Properties of Semiconductors*, World Scientific, Singapore (1990).
- ⁸O. A. Mironov, O. N. Makarovskii, A. I. Fedorenko, A. Yu. Sipatov, O. N. Nashchekina, I. M. Zaritskii, and A. A. Konchits, *Acta Phys. Pol. A* **85**, 603 (1994).
- ⁹N. Ya. Fogel, A. Yu. Sipatov, A. I. Fedorenko, V. N. Rybalchenko, and V. G. Cherkasova, *Fiz. Nizh. Temp.* **20**, 1142 (1994) [*Low Temp. Phys.* **20**, 897 (1994)].
- ¹⁰N. Ya. Fogel, V. G. Cherkasova, A. S. Pokhila, A. Yu. Sipatov, and A. I. Fedorenko, *Czech. J. Phys.* **46**, 727 (1996).

This article was published in English in the original Russian journal. It was edited by R. T. Beyer.

Determination of low-energy electronic levels of the Tm^{3+} ion in the compound $\text{KTm}(\text{MoO}_4)_2$

M. I. Kobets, V. V. Kurnosov, V. A. Pashchenko, and E. N. Khats'ko

*B. Verkin Institute for Low Temperature Physics and Engineering, National Academy of Sciences of the Ukraine, 310164 Kharkov, Ukraine**

(Submitted December 2, 1998; revised January 4, 1999)

Fiz. Nizk. Temp. **25**, 512–514 (May 1999)

A complex measuring technique is used for reconstructing the structure of electron energy levels of the Tm^{3+} ion in a $\text{KTm}(\text{MoO}_4)_2$ crystal in the frequency range $0\text{--}300\text{ cm}^{-1}$. It is shown that the first excited state is very close to the ground state ($\Delta E = 2.3\text{ cm}^{-1}$). © 1999 American Institute of Physics. [S1063-777X(99)01305-5]

INTRODUCTION

The compound $\text{KTm}(\text{MoO}_4)_2$ belongs to the class of layered low-symmetry magnetically concentrated magnets of the type $\text{MRE}(\text{MoO}_4)_2$, where $\text{M}=\text{K}, \text{Cs}, \text{Li}, \dots$, $\text{RE}=\text{Gd}, \text{Dy}, \text{Er}, \text{Yb}, \text{Ho}, \dots$. One of the main problems encountered in the theoretical and experimental investigations of magnetically concentrated crystals belonging to this family is the restoration of their energy spectrum, since the ground state is characterized by orbital and spin quantum numbers other than 0 and 1/2 respectively. However, the calculation of the energy spectrum of concentrated crystals taking into account all possible types of contributions is severely hampered.

Under the effect of temperature or external magnetic fields, low-temperature structural phase transformations are observed in these compounds,^{1,2} where the low-lying electron energy states of rare-earth ion play the dominating role. The present paper aims at using experimental methods for obtaining quantitative information about the energy gap ΔE between the ground state and excited levels of the electron spectrum of the compound $\text{KTm}(\text{MoO}_4)_2$. The authors have not come across any information concerning the low-lying electron energy levels of the Tm^{3+} ion in the compound $\text{KTm}(\text{MoO}_4)_2$.

EXPERIMENTAL TECHNIQUE

Single crystals of $\text{KTm}(\text{MoO}_4)_2$ were grown by the method of spontaneous crystallization from solution in the melt.³ The obtained samples were in the form of laminated plates (like mica) of light-green color and had a very high degree of structural perfection. X-ray studies of $\text{KTm}(\text{MoO}_4)_2$ were carried out by Klevtsova and Borisov⁴ and by Spitsyn and Trunov.⁵ The crystal belongs to the class D_{2h}^{14} of rhombic type with the following parameters of the unit cell: $a=5.05\text{ \AA}$, $b=18.31\text{ \AA}$, $c=7.89\text{ \AA}$, $z=4$. The Tm^{3+} ion belongs to the category $4f^{12}$ of ions with an even number of electrons and the ground state $^3\text{H}_6(L=5, S=1, J=6)$. Measurements of the angular dependence of the EPR spectra showed that the symmetry of local environment of the Tm^{3+} ion in $\text{KTm}(\text{MoO}_4)_2$ is not higher than rhombic. In a crystal field of such a low symmetry, the degeneracy of Stark levels of the Tm^{3+} ion is completely removed. The energy

spectrum of the electron excitations of the Tm^{3+} ion in the $\text{KTm}(\text{MoO}_4)_2$ crystal was reconstructed by using the results of measurements based on various experimental techniques. Low-frequency measurements (25–180 GHz) of the EPR spectrum of the $\text{KTm}(\text{MoO}_4)_2$ crystal were made by using a reflection-type radiospectrometer with detachable resonator cells. Raman scattering of light was used in the quest for electron excitations in the $\text{KTm}(\text{MoO}_4)_2$ crystal in the frequency interval $2\text{--}10\text{ cm}^{-1}$. Raman spectrum in the sample was excited by using a 40 mW He–Ne laser, and was recorded by using the Jobin Yvon U1000 spectrometer equipped with a cooled photoelectric multiplier and a photon counter circuit. The excited energy levels in the frequency interval $10\text{--}300\text{ cm}^{-1}$ were sought by using a Fourier spectrometer whose spectral resolution was 1 cm^{-1} .

EXPERIMENTAL RESULTS

The EPR energy spectrum of the ion Tm^{3+} was not observed in the frequency interval 25–65 GHz. An undistorted magnetic resonance line in $\text{KTm}(\text{MoO}_4)_2$ was observed only at a frequency 76 GHz for an external magnetic field orientation along the c -axis. The condition of resonance is the orientation of the ultrahigh-frequency (UHF) field \mathbf{h} perpendicular to the static field \mathbf{H} . A very narrow absorption line ($\Delta H=450\text{ Oe}$) is observed. Such a small linewidth is unusual for magnetically concentrated paramagnets of this family, in which strong local dipole fields considerably broaden the EPR lines. Hence their analysis requires the use of millimeter and submillimeter frequencies. Our subsequent experimental studies of the EPR spectrum of the Tm^{3+} ion in the frequency interval 75–190 GHz showed that the EPR linewidth is practically independent of frequency. Figure 1 shows the dependence of the square of frequency on the square of resonance field obtained from EPR spectral studies in $\text{KTm}(\text{MoO}_4)_2$ along the c -axis. This dependence can be described quite satisfactorily by the model formula $\nu^2 = \Delta^2 + (gH/2)^2$. The ‘‘intercept’’ on the Y -axis defines the numerical value of the separation from the first excited level in $\text{KTm}(\text{MoO}_4)_2$: $\Delta = 69.95\text{ GHz}(2.3\text{ cm}^{-1})$. This means that the ground state of the Tm^{3+} ion is a split ‘‘quasidoublet,’’ and the observed EPR spectrum is associated with transitions

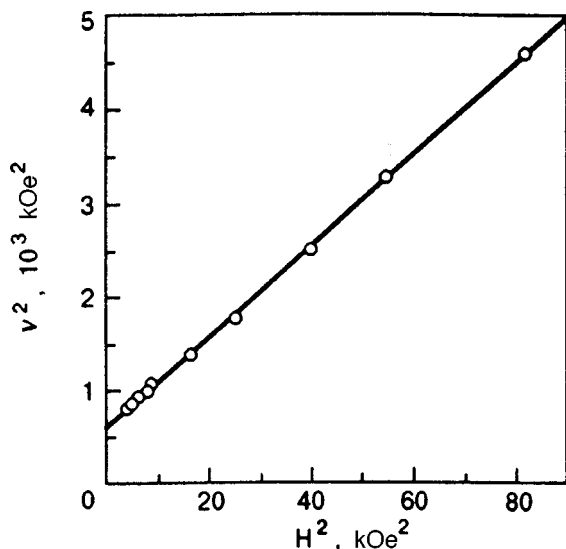


FIG. 1. Frequency vs. field dependence of the EPR spectrum of the Tm^{3+} ion in the compound $\text{KTm}(\text{MoO}_4)_2$ ($T=4.2$ K, $\mathbf{H}\parallel c$). The straight line corresponds to the formula $\nu^2 = \Delta^2 + (gH/2)^2$ with the parameters $\Delta=25$ kOe and $g=13.95$.

between components of the principal "quasidoublet." The slope of the straight line gives the effective g -factor $g_c = 13.95 \pm 0.05$ for the c -axis of the crystal.

In order to verify the results and to obtain new data in $\text{KTm}(\text{MoO}_4)_2$, we made a quest for electron excitations of the Tm^{3+} ion by using the Raman spectrum technique in frequency interval $2\text{--}10\text{ cm}^{-1}$ at $T=2$ K. The results of these experiments are shown in Fig. 2. The hatched region corresponding to the interval $3\text{ cm}^{-1} \pm 0.5\text{ cm}^{-1}$ is attributed to the electron excitation in $\text{KTm}(\text{MoO}_4)_2$, since optical phonons with such a low energy were not observed in inorganic crystals, and the absence of scattering by acoustic phonons at the temperature of superfluid helium is associated not only with a strong symmetry prohibition for the Raman process near the center of the Brillouin zone, but also with the fact that the frequency position of such peaks cannot exceed 1 cm^{-1} for the investigated compound. The slight discrepancy between Raman and EPR frequencies may be caused, for example, by a strong dispersion of the electron branch near the center of the Brillouin zone. In this case, the difference in the real wave vector for EPR and Raman spectra comes into play. Such an analysis was carried out by Hsu and Staut,⁶ who interpreted the difference in the IR and Raman frequencies of electron transitions as the momentum dependence of the transition frequency. We did not observe any other excitations in this frequency range.

The IR spectra of the $\text{KTm}(\text{MoO}_4)_2$ crystal were studied in the frequency interval between 10 and 300 cm^{-1} at a temperature $T=4.2$ K and for a magnetic field orientation along

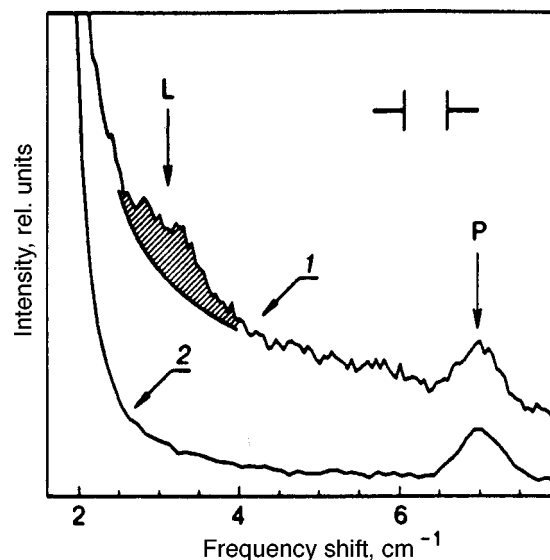


FIG. 2. Raman scattering spectral region for $\text{KTm}(\text{MoO}_4)_2$ at $T=2$ K. Curve 1 corresponds to the polarization of the incident and scattered radiation of the type $aa(bb)+ab$, and curve 2 to $ac+bc$. Symbol P on the spectra indicates the percolating line of the gaseous plasma laser, while L denotes the low-frequency scattering line referred to the electron excitation.

the c -axis. The results of measurements carried out in the IR region using a Fourier spectrometer indicate the presence of an absorption band (200 cm^{-1}) which is sensitive to the applied magnetic field.

Thus, summarizing the experimental results, it can be stated that two electron energy levels (2.3 and 200 cm^{-1}) of the Tm^{3+} ion in the compound $\text{KTm}(\text{MoO}_4)_2$ exist in the frequency interval $0\text{--}300\text{ cm}^{-1}$. An extremely small value of the splitting $\Delta E=2.3\text{ cm}^{-1}$ allows us to assume that for a certain orientation of the applied magnetic field ($H\parallel a$ in the present case), a structural phase transition can be induced by the applied magnetic field in this compound, as in other compounds of this family such as $\text{KEr}(\text{MoO}_4)_2$, $\text{CsEr}(\text{MoO}_4)_2$, $\text{K Dy}(\text{MoO}_4)_2$. Further experimental investigations are certainly called for in this direction.

*E-mail: khatsko@ilt.kharkov.ua

¹V. I. Kut'ko, V. A. Pashchenko, and M. I. Kobets, *Fiz. Nizk. Temp.* **19**, 1354 (1993) [*Low Temp. Phys.* **19**, 962 (1993)].

²A. I. Zvyagin, S. D. El'chaninova, T. S. Stetsenko *et al.*, *Fiz. Nizk. Temp.* **1**, 79 (1975) [*Sov. J. Low Temp. Phys.* **1**, 39 (1975)].

³A. A. Evdokimov, V. A. Efremov, V. K. Trunov *et al.*, *Rare-Earth Molybdates and Tungstates* [in Russian], Nauka, Moscow (1991).

⁴R. F. Klevtsova and S. V. Borisov, *Sov. Phys. Dokl. Dokl. Akad. Nauk SSSR* **117**, 1334 (1967).

⁵V. I. Spitsyn and V. K. Trunov, *Sov. Phys. Dokl. Dokl. Akad. Nauk SSSR* **185**, 854 (1969).

⁶E. C. Hsu and J. W. Staut, *J. Chem. Phys.* **59**, 502 (1973).

Translated by R. S. Wadhwa

LETTERS TO THE EDITOR

On a possible reason behind the anisotropy observed in the superconducting properties of underdoped cupratesV. M. Loktev,^{1,2} R. M. Quick,² and S. G. Sharapov^{1,3}¹*N. N. Bogoliubov Institute of Theoretical Physics, National Academy of Sciences of the Ukraine, 252143 Kiev, Ukraine;* *²*National Engineering University "KPI," 252056 Kiev, Ukraine;* ³*Department of Physics, University of Pretoria, 0002 Pretoria, South Africa*
(Submitted December 14, 1998)Fiz. Nizk. Temp. **25**, 515–518 (May 1999)

An attempt is made to interpret the experiments in which the superconducting transition temperature in underdoped HTSC was found to depend on the direction of the current passing through the sample. It is suggested that one (higher) temperature approximately corresponds to the point T_{BKT} of the two-dimensional transition, while the other is the temperature T_c corresponding to 3D ordering between layers. For conditions when $T_c \geq T_{BKT}$ (relatively high values of carrier concentration and interlayer coupling), the anisotropy of the superconducting properties becomes negligible and the layered system possesses only one critical temperature.

© 1999 American Institute of Physics. [S1063-777X(99)01405-X]

1. During investigations of the electrical resistance of $\text{Bi}_2\text{Sr}_3\text{Ca}_x\text{Cu}_2\text{O}_{8+\delta}$ ¹ and $\text{YBa}_2\text{Cu}_3\text{O}_{7-\delta}$ ² single crystals underdoped in oxygen (or, in other words, with a less-than-optimal concentration of delocalized holes), a “splitting” of the superconducting transition (SCT) temperature was observed: its value for the current \mathbf{j} in the CuO_2 layers ($\mathbf{j} \perp \mathbf{c}$) exceeds noticeably the corresponding value for $\mathbf{j} \parallel \mathbf{c}$. Such a behavior was predicted by Friedel³ and must be manifested in layered SC with Josephson-type coupling between layers. At the same time, it was shown by Korshunov⁴ and Rodriguez⁵ that the necessary condition for the emergence of different values of T_c (depending on the direction of \mathbf{j}) in stacks of planes with Josephson-type of tunneling of carriers between them is a random distribution (inequivalence) of SC properties of layers. However, these authors did not discuss any concentration dependences of the above-mentioned anisotropy.

In this work, we shall use the results of our earlier publication⁶ to provide a different interpretation of the phenomenon observed in Refs. 1 and 2. According to this interpretation, one SCT (for $\mathbf{j} \perp \mathbf{c}$) which, however, is not accompanied by a spontaneous symmetry breaking (see Ref. 7), may be caused by Berezinsky–Kosterlitz–Thouless transition at the crossover temperature T_{BKT} . In this case, the SC correlations in layers decrease according to a power law, while the correlations between layers decrease exponentially. A consideration of the three-dimensionalization, which always occurs even in strongly anisotropic (including layered) media restores T_c or, in other words, leads to the formation of a condensate with long-range 3D-order and breaking of charge symmetry. Although it was shown long ago (on an example of quasi-one-dimensional conductors) that three-dimensionalizing one-particle tunneling rapidly makes the BCS (mean-field) theory (in which $T_c \approx T_c^{MF}$) valid for

describing SCT, two-dimensional phenomena may still persist in a finite range of parameters ensuring three-dimensionalization. Thus, 2D- (near T_{BKT}) and 3D- (at T_c) SC states may be formed separately in principle in quasi-two-dimensional systems (if the parameters carrier concentration and tunneling constant are such that $T_c < T_{BKT}$).

2. The simplest model Hamiltonian of a regular layered metallic system can be presented in the form

$$H = -\psi_\sigma^+(x) \left[\frac{\nabla_{2D}^2}{2m_\perp} + \frac{1}{m_\parallel d^2} \cos(i\nabla_\parallel d) + \mu \right] \psi_\sigma(x) - V \psi_\uparrow^+(x) \psi_\downarrow^+(x) \psi_\downarrow(x) \psi_\uparrow(x), \quad (1)$$

where $\psi_\sigma(x)$ is the Fermi field with spin σ ; $x \equiv \tau, \mathbf{r}_{2D}, z; m_\perp$ and m_\parallel are effective carrier masses in a layer and along the \mathbf{c} -direction respectively, V is the attraction constant, d the separation between layers, and μ the chemical potential defining the fermion density $n_f^{3D} (\equiv n_f^{2D}/d)$. We also assume that $m_\parallel \gg m_\perp$ (weak tunneling) and $\hbar = k_B = 1$. Note that Eq. (1) does not consider incoherent (Josephson) tunneling (which is often used for stabilizing 2D-fluctuations) for at least two reasons. In the first place, this is done in order to show (in contrast to the conclusions drawn in Refs. 3–5) that even coherent one-particle transition between planes can ensure the anisotropy observed in Refs. 1 and 2. Second, the true nature of tunneling of particles between cuprate layers of HTSC compounds has not been established so far, and hence it is justified to consider both types of tunneling on the model level.

Further calculations do not differ significantly from those carried out in Ref. 6, where the effective thermodynamic potential Ω of the system was determined by using the standard Hubbard–Stratanovich technique in which auxiliary Bose-fields $\varphi(x) = V \psi_\downarrow \psi_\uparrow$ and their conjugates are used

instead of the Fermi fields. After eliminating the latter, we obtain the following expression for the density of the potential part Ω :

$$\Omega_{\text{pot}}(\mu, T, |\varphi|^2) \cong \Omega_{\text{pot}}^{MF}(\mu, T, |\varphi|^2) + \Omega_{\text{fl}}^{(1)}(\mu, T, |\varphi|^2), \quad (2)$$

where $\Omega_{\text{pot}}^{M,F} = \Omega(\mu, T, \varphi(x), \varphi^*(x))|_{\varphi, \varphi^* = \text{const}}$ is the mean-field potential obtained in the tree approximation, and

$$\Omega_{\text{fl}}^{(1)}(\mu, T, |\varphi|^2) = \frac{T}{2} (\text{Tr} \text{Ln} \Gamma_+^{-1} + \text{Tr} \text{Ln} \Gamma_-^{-1}) \quad (3)$$

is the one-loop correction, in which

$$\Gamma_{\pm}^{-1}(x) = \frac{1}{T} \left[\frac{\delta^2 \Omega}{\delta \varphi^*(x) \delta \varphi(0)} \pm \frac{\delta^2 \Omega}{\delta \varphi^*(x) \delta \varphi^*(0)} \right]_{\varphi = \varphi^* = |\varphi| = \text{const}} \quad (4)$$

It must be noted that factorization (3) is valid only for low frequencies and momenta,¹⁰ while representation (2) can be used conveniently for describing phases with a long-range order. In the absence of such an order (e.g., in the 2D-case, when $T_c = 0$), potential (2) is found to be insufficient and the system can be described in the parametrization $\varphi(x) = \rho(x) \exp(i\Theta(x))$, taking into consideration its kinetic part. Being a function of $\nabla_{2D} \Theta(x)$, such a parametrization leads to an equation defining the SCT temperature in a 2D metal.⁶ In the general case, both T_{BKT} and T_c^{MF} are sublinear functions of ε_F , where $\varepsilon_F = \pi n_f^{2D} / m_{\perp}$ is the Fermi energy of free fermions. In this case, $T_{BKT} \sim \varepsilon_F$, $T_c^{MF} \sim \varepsilon_F^{1/2}$, in the local pairing region, and $T_{BKT} \rightarrow T_c^{MF} \sim \varepsilon_F^{1/2}$ for Cooper pairing. It must be noted that in spite of the fact that the temperature is the same, BKT-type SCT occur in different planes independently (the differences between their phases $\Theta(x)$ are coincidental). The effect of tunneling on T_{BKT} and its renormalization were studied in Ref. 11.

3. In order to find the critical temperature of a 3D SCT, we must use potential (2) corresponding to a quasi-2D system and presented in the Gaussian approximation. In this case, the required equation for T_c has the form

$$\frac{\partial \Omega_{\text{pot}}^{MF}(\mu, T_c, |\varphi|^2)}{\partial |\varphi|^2} + \frac{\partial \Omega_{\text{fl}}^{(1)}(\mu, T_c, |\varphi|^2)}{\partial |\varphi|^2} \Big|_{\varphi = \varphi^* = 0} = 0, \quad (5)$$

where μ is an unknown parameter defined by the equality¹²

$$n_F^{3D}(\mu, T_c) + 2n_B^{3D}(\mu, T_c) = n_f^{3D}. \quad (6)$$

It can be seen that the retention of fluctuational terms in Eq. (2) (see Eqs. (3) and (4)) modifies the equation for the gap, while Eq. (6) shows that the Fermi subsystem is divided into intrinsic fermions with density n_f^{3D} and Bose fluctuations with density n_B^{3D} (the expressions for n_f^{3D} and n_B^{3D} are presented in Ref. (13)).

The complete solution of the self-consistent system (5) and (6) can be obtained only numerically; an analytic solution requires approximations that are controlled by the condition $T_c \rightarrow 0$ for $m_{\parallel} \rightarrow \infty$. Thus, in the Bose limit, where $\mu < 0$ and $n_f^{3D} = 0$, formula (5) leads to an expression for T_c which coincides with the temperature of condensation of an ideal quasi-2D Bose gas.¹⁴

However, a more important situation closer to the real HTSC materials arises when the condition $\mu = \varepsilon_F$ is satisfied. This means that T_c for these materials is determined by Eq. (5) whose first term is the same as the BCS equation and leads to the mean-field value $T_c^{MF} = (\gamma/\pi)(2\varepsilon_F|\varepsilon_b|)^{1/2}$ [Ref. 6] (here, γ is the Euler constant, and ε_b is the energy of a two-particle bound state which is always nonzero in 2D systems with attraction). The fluctuational contribution can be estimated in the longwave approximation. In this case, the Fourier transform

$$\Gamma_-^{-1}(0, \mathbf{K})|_{\varphi = \varphi_{\text{min}}} = \frac{m_{\perp}}{2\pi d} [a\mathbf{K}_{\perp}^2 + b(1 - \cos K_{\parallel}d)];$$

$$a = \frac{7\zeta(3)}{(4\pi)^2} \frac{\varepsilon_F}{m_{\perp} T^2}; \quad b = \frac{7\zeta(3)}{(4\pi)^2} \frac{1}{m_{\parallel}^2 d^4 T^2} \quad (7)$$

of the principal function from (4) at the minimum Ω_{pot} can be used to determine the derivative

$$\frac{\partial \Gamma_-^{-1}(0, \mathbf{K})}{\partial \varphi^2} \Big|_{\varphi = \varphi_{\text{min}}} \approx \frac{m_{\perp} c}{2\pi d}; \quad c = \frac{7\zeta(3)}{8\pi^2 T^2} \quad (8)$$

($\zeta(3)$ in Eqs. (7) and (8) is the Riemann function.) Integrating with respect to \mathbf{K} , we first arrive at the required correction

$$\left| \frac{\partial \Omega_{\text{fl}}^{(1)}(\varepsilon_F, T, |\varphi|^2)}{\partial \varphi^2} \right|_{\varphi = \varphi_{\text{min}}} \approx \frac{m_{\perp}}{4\pi d} \frac{T}{\varepsilon_F} |\ln \kappa|, \quad (9)$$

and then, after its substitution into (5), at the final equation

$$T_c = 2 \frac{|\ln(T_c/T_c^{MF})|}{|\ln \kappa|} \varepsilon_F, \quad (10)$$

where the dimensionless parameter κ is defined by

$$\kappa^{-1} = 4\sqrt{2} m_{\parallel}^2 d^4 |\varepsilon_b|^{1/2} \varepsilon^{3/2}. \quad (11)$$

It can be easily verified that Eq. (10) leads to the dependence of T_c on n_f^{3D} with a fairly high degree of precision. This dependence is found to be nearly linear, which is in accord with the dependence $T_c(n_f^{3D})$ in underdoped HTSC compounds.¹⁵ For the present communication, the fact that T_c may turn out to be lower than T_{BKT} (see Eqs. (10) and (11)) is more significant. This may be due to a weak tunneling constant (large values of m_{\parallel} or d) since the slope of the curve $T_c(n_f^{3D})$ is defined by this constant,¹⁾ or (which is undoubtedly more significant) to a decrease in the carrier concentration n_f^{3D} which can be varied rather easily in HTSC compounds. Hence the same HTSC compound with a given (but small) amplitude of hopping between planes may be characterized by the anisotropy in the SC properties ($T_c < T_{BKT}$) or by its absence ($T_c \rightarrow T_{BKT}$) for different doping levels of the compound. Note that if the initial constant of (coherent or incoherent) tunneling turns out to be large, the above anisotropy does not appear in such a compound irrespective of doping, since T_c is always higher than T_{BKT} in this case.

4. Naturally, the interpretation presented in this work is only qualitative. The theory of SC properties of real HTSC must also take into account their other properties also, viz., strong correlation between electrons, spin degrees of

freedom, pairing anisotropy, etc. However, the sharply manifested two-dimensionality of electronic properties cannot be disregarded either. We have analyzed here one of the consequences of this circumstance.

Eventually, we consider the region of algebraic order in quasi-2D metals whose existence is determined entirely by the carrier concentration in these materials. If such a region does exist, the sample resistance to the current in the plane must vanish before the resistance in the perpendicular direction. The model considered by us does not require any assumption concerning the inequivalence of planes for such an effect,^{4,5} or about the Josephson nature of coupling between the layers.³

*E-mail: vloktev@bitp.kiev.ua

¹⁾An identical result was obtained in Ref. 16 for the case of Josephson (bifermion) tunneling between layers.

¹V. L. Arbutov, O. M. Bakunin, A. E. Davletshin, *et al.*, Pis'ma Zh. Éksp. Teor. Fiz. **48**, 399 (1988) [JETP Lett. **48**, 440 (1988)].

²V. N. Zverev, D. V. Shovkun, and A. G. Naumenko, Pis'ma Zh. Éksp. Teor. Fiz. **68**, 309 (1998) [JETP Lett. **68**, 332 (1998)].

³J. Friedel, J. Phys. (Paris) **49**, 1561 (1988).

⁴S. T. Korshunov, Europhys. Lett. **11**, 757 (1990).

⁵J. P. Rodriguez, Europhys. Lett. **31**, 479 (1995).

⁶V. P. Gusynin, V. M. Loktev, and S. G. Sharapov, Fiz. Nizk. Temp. **23**, 816 (1997) [Low Temp. Phys. **23**, 612 (1997)].

⁷L. N. Bulaevskii, Int. J. Mod. Phys. B **4**, 1849 (1990).

⁸I. E. Dzyaloshinskii and E. I. Kats, Zh. Eksp. Teor. Fiz. **55**, 2373 (1968) [Sov. Phys. JETP **28**, 1259 (1968)].

⁹K. B. Efetov and A. I. Larkin, Zh. Eksp. Teor. Fiz. **66**, 2290 (1974) [Sov. Phys. JETP **39**, 1129 (1974)].

¹⁰V. N. Popov, *Functional Integrals in Quantum Field Theory*, Kluwer, Dordrecht (1983).

¹¹R. M. Quick and S. G. Sharapov, Physica C **301**, 262 (1998).

¹²P. Nozieres and S. Schmitt-Rink, J. Low Temp. Phys. **59**, 195 (1985).

¹³V. M. Loktev and S. G. Sharapov, Comments Nucl. Part. Phys. **11**, 131 (1997).

¹⁴X.-G. Wen and R. Kan, Phys. Rev. B **37**, 595 (1988).

¹⁵Y. J. Uemura, Preprint, cond-mat/9706151.

¹⁶V. I. Loktev and V. M. Turkovskii, Fiz. Nizk. Temp. **24**, 767 (1998) [Low Temp. Phys. **24**, 578 (1998)].

Translated by R. S. Wadhwa

Microwave transmittance of a high- T_c superconductor film in a magnetic field

V. V. Eremenko, V. A. Novosad, and V. V. Pishko*

B. I. Verkin Institute for Low Temperature Physics and Engineering, National Academy of Sciences of Ukraine, 47, Lenin Ave., 310164, Kharkov, Ukraine

C. Falco

University of Arizona, PO Box 210077, Tucson, Arizona, USA

V. M. Rashkovan

State Aerospace University, 310070, 17 Chkalova St., Kharkov, Ukraine

(Submitted December 30, 1998; revised January 28, 1999)

Fiz. Nizk. Temp. **25**, 519–520 (May 1999)

The results of microwave transmittance measurements of crystalline high- T_c YBaCuO film under the influence of an external magnetic field are presented. Generally, in high- T_c superconductors dissipation mechanisms different from those in conventional superconductors may take place as well as transport current. Josephson-junction and anisotropy resistance-connected processes. Measurements of transmittance induced by the magnetic field demonstrate the dominance of flux flow dissipation mechanism and nonlinear transmittance dependence when approaching T_c . This makes possible to detect and characterize all the mechanisms mentioned above. © 1999 American Institute of Physics. [S1063-777X(99)01505-4]

Our measurements were carried out in the 2-mm wave range. Under these conditions the transmittance is sensitive to the presence of “normal” electrons, whereas infrared measurements sense the superconducting energy gap. The backward-wave tube was used as a microwave generator, with the radiation channeled through a measurement cell that consists of two (in and out) symmetrical quasioptical waveguides inside the pulse solenoid. The sample was placed between the waveguides in the region of the maximum, homogeneous magnetic field. Finally, the radiation was detected after the measurement cell which was placed in a cryostat with special windows to transmit the microwaves. To obtain the best sensitivity a liquid helium cooled n -InSb detector was used.¹ Such a technique produces ultrahigh frequency (130–150 GHz) current densities in the sample which are much smaller in magnitude than the critical current, and thus avoids test current inside the sample that is a consequence of direct current investigations.

The sample under study was made using magnetron sputtering procedure. The 1000 Å YBaCuO (123) film, which was deposited on the surface of a 0.5 mm-thick SrTiO₃ substrate, exhibited a micro-twinned crystalline structure with its C -axis perpendicular to the surface. Preliminary testing determined a superconducting transition at 87.8 K with 1 K width.

The experimental dependences of the magnetic field-induced transmittance at different temperatures are shown in Fig. 1. As can be seen, the transmittance value rises monotonically when the temperature rises from 4.2 K to T_c . At low temperatures a linear behavior of the transmittance versus the external field with a slope of $1\% \cdot T^{-1}$ was exhibited, which is consistent with results reported in Refs. 3 and 4 where the bolometric and reflectance measurements were

performed. This linear dependence of microwave transmittance on magnetic field may be explained in terms of flux flow dissipation. In contrast, the slope value at temperatures approaching the T_c rised to $3\% \cdot T^{-1}$ and the behavior was strongly nonlinear. Evidently, this region is dominated by the influence of the magnetic field on the superconducting phase transition.

Normal electron transmittance includes dissipation resulting from the Lorentz-like force motion due to the transport current normal to applied magnetic field H . For the HTSC the microwave frequency range is higher than the depinning frequency. Consequently, electromagnetic interaction is much stronger than the pinning force, and the major source of the dissipation is due to the free-moving vortices.

In the London electrodynamics approach it is possible to represent the current density J as

$$J = -\frac{1}{i\omega\mu\lambda^2}(E - f\nu B), \quad (1)$$

where λ is the London penetration depth; E is the microwave electric field; f is the fraction free vortices.² Writing the vortex velocity as $\nu = Jf/n$, the expression for the flow resistivity may be obtained as

$$\rho = \varphi_0 \frac{fB}{\eta} - i\bar{\omega}\mu\lambda^2, \quad (2)$$

which is true for H smaller than critical field and temperatures that are not too high. Taking into account that a typical HTSC critical field is of order 100 T, the limit representation for surface resistance R_s demonstrates a linear dependence on H :

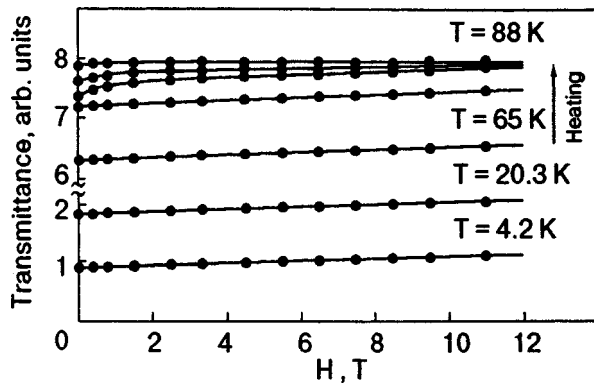


FIG. 1. Magnetic field effect on transmittance of the HTSC thin film at different temperatures.

$$R_s = \varphi_0 \frac{fB}{2\lambda\eta}. \tag{3}$$

This approximation is based on the pure flow regime and neglects the normal electron contribution, so the model is not valid in the region very close to T_c . A more detailed consideration of high frequency magneto-absorption was developed based on the equation of motion for a flux line in a sinusoidal pinning well under an alternating field and a random driving force due to thermal fluctuations.⁵

The granularity and various inhomogenities of the sample can produce a weak-like structure or, if there is an intrinsic Josephson junction inside, either effect may dominate in the microwave response. We assume the observed behavior of microwave properties near T_c may be due to the domination of dissipation effects from losses related to the Josephson junctions. To clarify this problem a set of additional measurements on other HTSC thin films are expected to be carried out. Attention will be given to the hysteresis phenomena due to the thermal and magnetic history of samples with different crystalline properties.

This work was supported by CRDF of USA and Government of Ukraine through the research project UP2-301 and by ONR N00014-92-J-1159.

*E-mail: pishko@ilt.kharkov.ua

- ¹V. V. Eremenko, S. A. Zvyagin, V. V. Pishko, Yu. A. Pashkevich, and V. V. Shakhov, *Fiz. Nizk. Temp.* **18**, 255 (1992) [*Sov. J. Low Temp. Phys.* **18**, 175 (1992)].
- ²A. M. Portis, K. W. Blazey, and K. A. Muller, *Europhys. Lett.* **5**, 467 (1988).
- ³Y. Masuda, N. P. Ong, Y. F. Yan, J. M. Harris, and J. B. Peterson, *Phys. Rev. B* **49**, 4380 (1994).
- ⁴P. B. Tharane, G. Dumas, C. Schlenker, and R. Buder, *Physica C* **127**, 147 (1997).
- ⁵M. W. Coffey and J. R. Clem, *Phys. Rev. Lett.* **58**, 1143 (1991).

This article published in English in the original Russian journal.